



Prepared in cooperation with the  
National Park Service

# Geophysical Characterization of Range-Front Faults, Snake Valley, Nevada

By Theodore H. Asch and Donald S. Sweetkind



Open-File Report 2010–1016

U.S. Department of the Interior  
U.S. Geological Survey

**U.S. Department of the Interior**  
KEN SALAZAR, Secretary

**U.S. Geological Survey**  
Marcia K. McNutt, Director

U.S. Geological Survey, Reston, Virginia: 2010

For product and ordering information:  
World Wide Web: <http://www.usgs.gov/pubprod>  
Telephone: 1-888-ASK-USGS

For more information on the USGS—the Federal source for science about the Earth,  
its natural and living resources, natural hazards, and the environment:  
World Wide Web: <http://www.usgs.gov>  
Telephone: 1-888-ASK-USGS

Suggested citation:  
Asch, T.H., Sweetkind, D.S., 2010, Geophysical characterization of range-front faults, Snake Valley,  
Nevada: U.S. Geological Survey Open-File Report 2010-1016, 226 p.

Any use of trade, product, or firm names is for descriptive purposes only and does not imply  
endorsement by the U.S. Government.

Although this report is in the public domain, permission must be secured from the individual  
copyright owners to reproduce any copyrighted material contained within this report.



## Contents

Introduction .....	1
Geologic Setting .....	4
Electrical Rock Properties.....	10
Magnetotellurics .....	11
Snake Valley Audio-Magnetotelluric Survey .....	12
Audio-Magnetotelluric Data Processing.....	17
2-D Modeling Analysis of the Audio-Magnetotelluric Data .....	19
Discussion .....	21
Line 1 .....	22
Surface Geologic Control .....	22
Subsurface Interpretation .....	23
Line 2 .....	31
Surface Geologic Control .....	31
Subsurface Interpretation .....	32
Summary and Conclusions.....	37
References Cited .....	40

## Appendixes

1. Audio-Magnetotelluric Data and Models.....	45
2. Survey Photographs.....	216

## Figures

1. Location of the study area and Great Basin National Park, east-central Nevada..	2
2. Geologic map of the study area and location of AMT lines.....	6
3. Stratigraphic column and expected range of resistivity for stratigraphic units.....	8
4. Schematic layout of the STRATAGEM system for Line 1 of the Snake Valley, Nevada AMT survey .....	14
5. Two-dimensional Audio-Magnetotelluric inversion modeling results for transverse-magnetic (TM) mode along line 1.....	25
6. Two-dimensional Audio-Magnetotelluric inversion modeling results for transverse-electric (TE) mode along line 1.....	28
7. Two-dimensional Audio-Magnetotelluric inversion modeling results for combined transverse-magnetic transverse-electric (TMTE) mode along line 1.....	29
8. Two-dimensional Audio-Magnetotelluric inversion modeling results for transverse-magnetic (TM) mode along line 2.....	33
9. Two-dimensional Audio-Magnetotelluric inversion modeling results for transverse-electric (TE) mode along line 2.....	34
10. Two-dimensional Audio-Magnetotelluric inversion modeling results for combined transverse-magnetic transverse-electric (TMTE) mode along line 2.....	36
11. Interpreted locations of mapped faults.....	39

## Tables

1. AMT station locations for line 1.....	15
2. AMT station locations for line 2.....	16
3. Inversion (RLM2DI) and forward (PW2D) numerical model meshes .....	21

## Conversion Factors

Multiply	By	To obtain
foot (ft)	0.3048	meter (m)
mile (mi)	1.609	kilometer (km)
centimeter (cm)	0.3937	inch (in.)
meter (m)	3.281	foot (ft)
kilometer (km)	0.6214	mile (mi)
Hz	1000	kHz

Vertical coordinate information is referenced to the North American Vertical Datum of 1988 (NAVD88).

Horizontal coordinate information is referenced to either the North American Datum of 1983 (NAD83).

Elevation, as used in this report, refers to distance above the vertical datum.

# **Geophysical Characterization of Range-Front Faults, Snake Valley, Nevada**

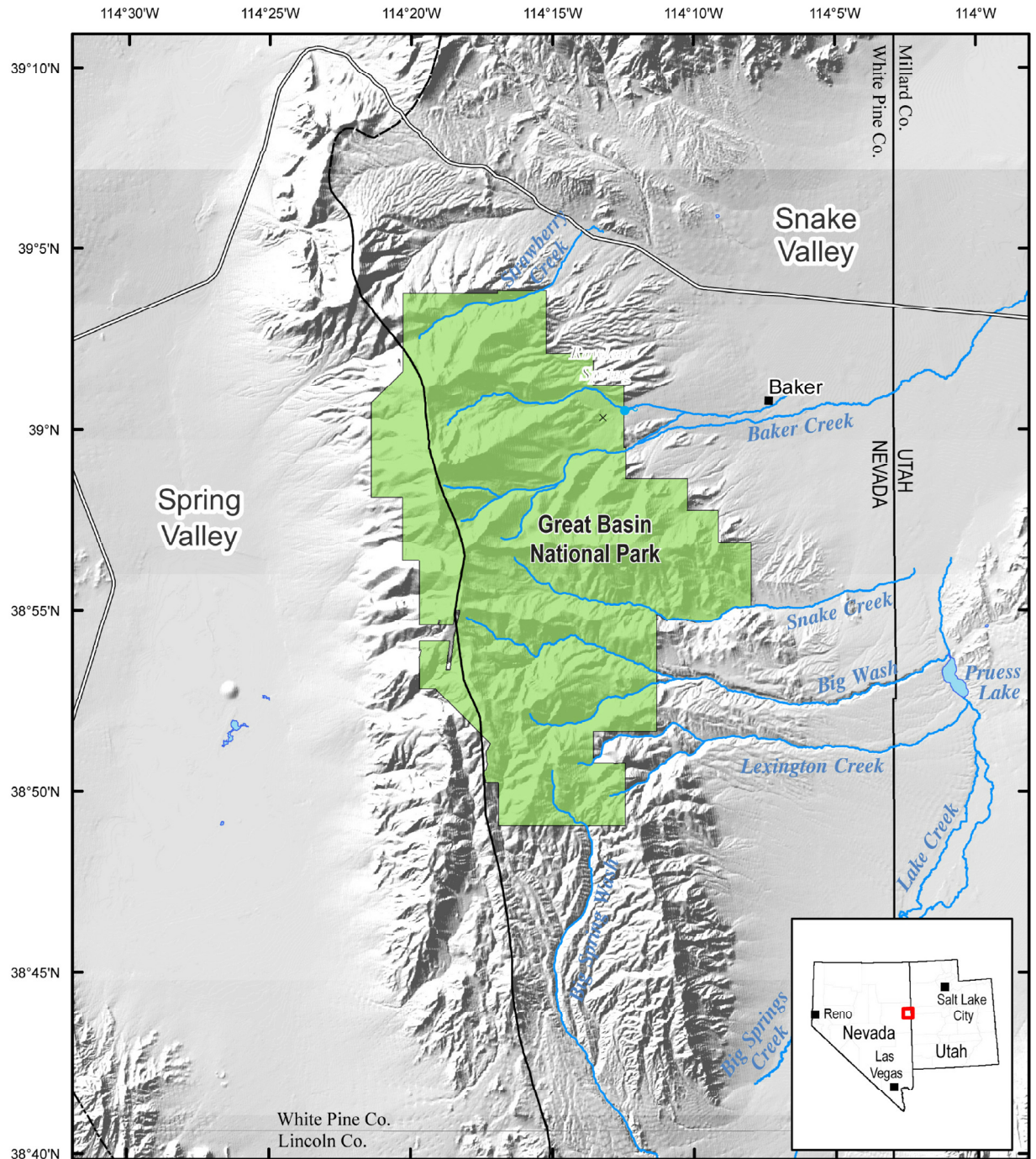
By Theodore H. Asch and Donald S. Sweetkind

## **Introduction**

Great Basin National Park encompasses about 310 square kilometers of mountainous terrain near the Nevada-Utah border in White Pine County, Nevada (fig. 1). The park lies in the southern part of the Snake Range and is bounded by Spring Valley on the west and Snake Valley on the east. Lehman Caves, the most visited natural resource feature within the park, and the Baker Creek cave system are located near the main entrance to the park in Snake Valley. Lehman Creek, Baker Creek, and Rowland Spring, which has the largest discharge of any spring in the park, also are located nearby (fig. 1), and they support abundant water-dependent flora and fauna along their riparian corridors.

Basin-fill and carbonate-rock aquifers beneath valleys in White Pine County provide water to springs, streams, pools, wetlands, limestone caves, and associated water-dependent ecosystems on Federal lands in the county. Because of increased demand for water supplies in Las Vegas and the surrounding region to support a rapidly growing population, the Southern Nevada Water Authority has applied for rights to withdraw large quantities of groundwater from Snake Valley adjacent to the park. A U.S. Geological Survey (USGS) study conducted in cooperation with the National Park Service (NPS) (Elliott and others, 2006)





Shaded relief base derived from 30 meter USGS National Elevation Dataset, 1999. Hydrology sourced from 1:24,000-scale National Hydrography Dataset, 1974-2009. Place names sourced from USGS Geographic Names Information System, 1974-2009. Great Basin National Park boundary sourced from Bureau of Land Management Surface Management Agency dataset, 2003. Universal Transverse Mercator Projection, Zone 11, NAD83.

0 2.5 5 10 Miles  
0 2.5 5 10 Kilometers

**Figure 1.** Location of the study area and Great Basin National Park, east-central Nevada. The red box in the lower right inset indicates the extent of figure 2.

indicated that streamflow, springs, and possibly water in caves in the area of Lehman and Baker Creeks near the Lehman Caves likely are susceptible to groundwater withdrawals from Snake Valley. The NPS has a mandate to preserve and protect the natural hydrologic processes that continue to form caves and that support water-dependent flora and fauna in the park. The continued formation of caves in some places likely is dependent on streamflow and groundwater in the alluvium and limestone.

The degree of susceptibility of the water resources in and near the National Park results from the interaction of the upland aquifer system in the southern Snake Range with the basin-fill and carbonate-rock aquifers beneath Snake Valley. The aquifer interaction is dependent on geologic units in the subsurface and their potential disruption along the range front by faulting. As such, understanding the presence, location, geometry, and amount of offset of faults that potentially lie between the mountain range front and the valleys is critical to understanding the degree of hydraulic connection and interaction between basin-fill and bedrock aquifers in Snake Valley and similar aquifers within the park. However, the location, age, amount of offset on, and even the presence of range-front faults here is controversial and difficult to document on the basis of surface mapping alone. Therefore, surface geophysical surveys were conducted to help delineate and characterize any range-bounding fault or faults in the subsurface in three dimensions. In this way, improved understanding of subsurface geologic conditions may thus assist in studies to determine the extent to which adjacent large-scale groundwater withdrawals adversely would affect water-resource features and cave-forming processes in the Park.

In September 2009, the U. S. Geological Survey (USGS), in cooperation with the NPS, collected controlled-source audio-magnetotelluric (AMT) data along two profiles in the Baker Creek drainage and nearby at Kiou Spring (fig. 2) to estimate the thicknesses and configuration

of geologic units and evaluate the presence of faults along the eastern range front of the Snake Range. The purpose of this report is to describe the AMT data collection in the vicinity of Great Basin National Park and present the results of the data analysis and subsequent AMT modeling of the subsurface geology in this area.

This study was performed in cooperation with the National Park Service, whose support is greatly appreciated. We are grateful to the field support provided by Toby Wellborn and Kip Allander. We thank the staff at Great Basin National Park for their help and cooperation in arranging the permits and permissions necessary for this study to go forward and for consultation with regards to access and logistics.

## **Geologic Setting**

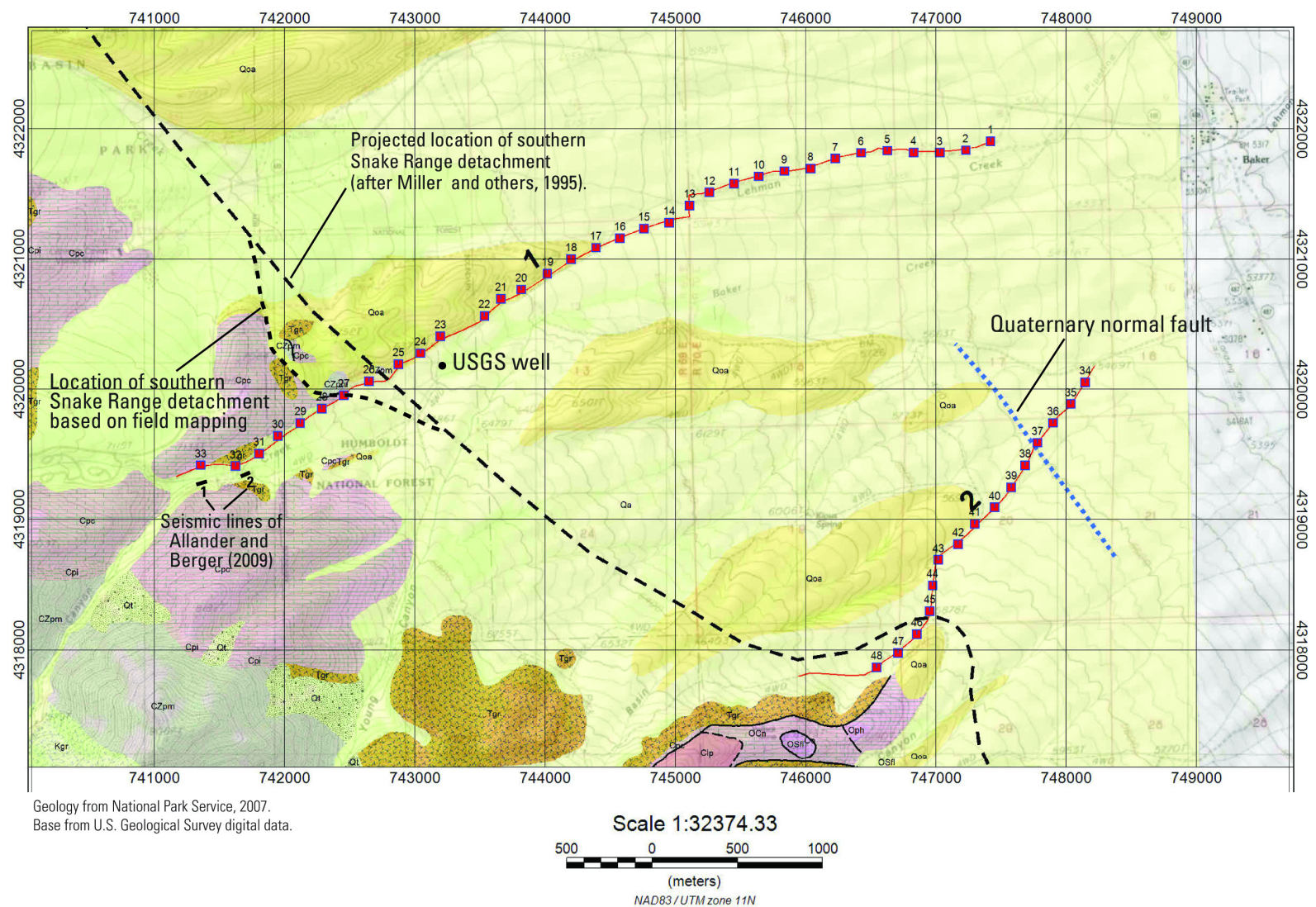
The geology of the Baker Creek and Kious basin area (figs. 2 and 3) consists of a thick section of Neoproterozoic and Cambrian quartzite that is successively overlain by relatively thin Cambrian shale and Cambrian limestone (Whitebread, 1969; McGrew and others, 1995; National Park Service, 2007). The thick (1.5 km) Neoproterozoic and Lower Cambrian Prospect Mountain Quartzite underlies a significant portion of the northern part of the southern Snake Range (Whitebread, 1969; National Park Service, 2007). The lower part of the formation consists of thickly bedded (0.3–1.5 m), coarse-grained quartzite, which grades upwards to thinner-bedded quartzite with occasional interbeds of silty quartzite and siltstone. Gradationally overlying the quartzite is the Lower Cambrian Pioche Shale, which has a maximum thickness of about 90 m and the unit is thinner where it was deformed. The Pioche Shale consists of thin-bedded dark siltstone and shale. Overlying the Pioche Shale is the Middle Cambrian Pole Canyon Limestone, a 500–550-m-thick, mostly massive limestone. Lehman Caves occurs in a fault-bounded block of Middle Cambrian Pole Canyon Limestone (Miller and others, 1995). Younger Paleozoic,

dominantly carbonate rocks are common at the south end of the southern Snake Range (Whitebread, 1969; National Park Service, 2007), but they do not crop out within the study area.

The Neoproterozoic and Cambrian siliciclastic and carbonate rocks were intruded by granitic rocks of Jurassic, Cretaceous, and Tertiary age (Whitebread, 1969; McGrew and others, 1995; National Park Service, 2007). Jurassic tonalitic to biotite-granite plutons are exposed south of the study area in the Snake Creek drainage. The Cretaceous Pole Canyon pluton occurs in the Kious Spring quadrangle (McGrew and others, 1995). The pluton belongs to a family of Cretaceous two-mica granites that form a north-trending band through eastern Nevada (Lee and others, 1981; Miller and others, 1989). The Tertiary [36 million years ago (Ma), Miller and others, 1989] Young Canyon pluton is a medium-grained equigranular granite and crops out along the southern edge of the study area (fig. 2).

Consolidated Miocene strata and unconsolidated Quaternary alluvium overlie these bedrock units. Miocene strata are composed in part of coarse-grained, often conglomeratic, moderately to well-cemented alluvial sediments that were derived from the Snake Range during middle Miocene ( $\approx 15$  Ma) uplift. The basal part of the section is composed of fine-grained, locally ash-rich lacustrine sedimentary rocks that have substantial amounts of limestone clasts. In the Sacramento Pass area, the Miocene section is 2-3 km thick. Large megablocks of Paleozoic rocks, some are one kilometer in dimension but usually smaller, were incorporated into the Miocene section during sedimentation (Grier, 1984; Miller and others, 1995; National Park Service, 2007). Miocene conglomerates and megabreccia deposits are best exposed on the low ridge that separates the Baker Creek and Lehman Creek drainages; however, elsewhere they are mantled by a thin cover of alluvial material and glacial outwash. Alluvium is subdivided into older and younger units.





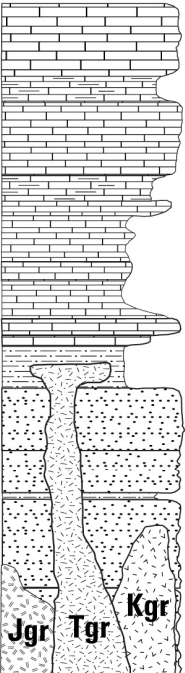
Older alluvium, which is Quaternary and possibly Pliocene in age, tends to cap ridges and form high-standing alluvial surfaces. The younger Quaternary alluvium, which includes some glacial outwash deposits, occupies active drainages and fans (Miller and others, 1995; National Park Service, 2007).

On the basis of mapping in bedrock and surficial materials (Whitebread, 1969; McGrew and others, 1995; National Park Service, 2007), in combination with interpretation of gravity and magnetic data (Watt and Ponce, 2007), two types of structures are inferred to have affected the eastern flank of the southern Snake Range. Both types of structures were capable of juxtaposing different bedrock and basin-fill units, and both have potential hydrologic significance.

Older, Miocene structures (fig. 2, long dashed black lines) were responsible for the uplift of the range and are the dominant structural features on the east side of the range. The main structure is the southern Snake Range detachment fault, which dips gently eastward beneath Snake Valley and separates consolidated bedrock from the overlying Miocene basin fill (McGrew, 1993; McGrew and others, 1995; Miller and others, 1999). The detachment fault largely is covered by Quaternary units in the study area, but it is exposed in a low ridge south-southwest of Kious Spring along the southern edge of the study area (fig. 2, dashed black lines) and shown in photo A2-18. Where the fault is exposed in the Snake Range, granitic rocks exhibit ductile to brittle deformational fabrics and hydrothermal chlorite immediately subjacent to the detachment; Paleozoic rocks exhibit low-grade metamorphism and ductile fabrics. The detachment approximately parallels the northeastern boundary of Great Basin National Park from Strawberry Creek southward to Snake Creek. Just to the north of the study area in the Sacramento Pass area, a 2- to 3-km-thick sequence of west-tilted middle Miocene rocks that overlie the central portion of Snake Range detachment are extensively exposed (Miller and

	<b>Stratigraphic unit<sup>1</sup></b>	<b>Potential resistivity range<sup>2</sup></b>
Quaternary sedimentary rocks	Younger (Qa) and older (Qoa) alluvium and terrace deposits (Qt)	10 - 1,000
Miocene sedimentary rocks	Miocene conglomerate, with megabreccia deposits (covered) (Lacustrine and volcanic rocks may also be present)	Wide range of values

Other Cambrian and Ordovician carbonate rocks (labeled €lp, O€n, Oph, and Osti) occur as local faulted blocks in the southern part of the study area. Younger Paleozoic rocks (Silurian through Permian) are not exposed in the AMT study area, but are possibly present in subsurface

Cambrian sedimentary rocks Mesozoic and Cenozoic igneous rocks		Pole Canyon Limestone (€pc)	5,000 - 10,000
		Pioche Shale (€pi)	0.1 - 100
		Prospect Mountain Quartzite (€Zpm)	5,000 - 10,000
		Jurassic (Jgr), Cretaceous (Kgr) and Tertiary (Tgr) plutonic rocks	>10,000 where unfractured; 1,000 - 5,000 fractured

<sup>1</sup>Unit abbreviations are for units depicted on geologic map (fig. 2).

<sup>2</sup>in ohm-m; modified after Telford and others (1976); ranges in resistivity represent general conditions and are not derived from the study area.

**Figure 3.** Stratigraphic column of the study area and typical range of electrical resistivities for geologic units.

others, 1995; National Park Service, 2007). The west-tilted section was repeated by east-dipping, east-side down normal faults, which are curved in map view and dip gently in cross-sectional view. The faults largely were contemporaneous with motion on the detachment, and they are inferred to merge at depth with the main detachment that underlies this basin (Miller and others, 1995; Miller and others, 1999). These relations are not exposed within the study area where younger alluvial units conceal the Miocene strata and faults, but both the strata and faults project southward towards the study area. As a result, the same structural situation likely is present in the subsurface beneath the study area.

The southern Snake Range detachment fault, as well as the east-dipping normal faults that formed above it, were active during the middle Miocene uplift of the southern Snake Range (Miller and others, 1999). After tectonic activity ceased in the late Miocene, a long period of erosion took place prior to the deposition of the Pliocene and younger sediments. Exposures in Big Wash, south of the study area, show that the erosion beveled the tops of the tilted Miocene strata and the east-dipping faults, creating a planar surface (an unconformity) onto which younger sediments eventually were deposited. The bedrock units were more resistant to erosion than were the Miocene strata, and much of the topographic relief of the current range front is a product of differential weathering rather than uplift related to a younger episode of faulting.

Young Quaternary faults (U.S. Geological Survey and Nevada Bureau of Mines and Geology, 2006) formed well east of the present range front and east of the eastern boundary of the park (fig. 2, dashed blue lines). They are not present along the geomorphic range front, which as noted above, has a more erosional origin. This location outboard of the range front also is coincidental with a gravity gradients that indicate an increase in thickness of the Miocene and younger basin fill (Watt and Ponce, 2007). Quaternary scarps are not well developed, appearing



as local gentle swales that affect the alluvial surfaces. In general, the geomorphic expression of the eastern flank of the southern Snake Range is not that of a young, active range front, in contrast to many other ranges in Nevada.

## **Electrical Rock Properties**

Electromagnetic geophysical methods detect variations in the electrical properties of rocks—in particular, electrical resistivity, or its inverse, electrical conductivity. Electrical resistivity can be correlated with geologic units on the surface (fig. 3) and at depth using lithologic logs to provide a three-dimensional (3-D) picture of subsurface geology. In the upper crust, the resistivities of geologic units are largely dependent upon their fluid content, pore-volume porosity, interconnected fracture porosity, and conductive mineral content (Keller, 1989). While there is not a one-to-one relation between lithology and resistivity, general correlations can be made using typical values, even though values can be found at other localities that may fall outside of the ranges presented herein (Palacky, 1987). Fluids within the pore spaces and fracture openings, especially if saline, can reduce electrical resistivities in what would otherwise be a resistive rock matrix. Resistivity also can be lowered by the presence of electrically conductive clay minerals, graphitic carbon, and metallic mineralization. It is common, for example, for altered volcanic rocks to contain replacement minerals that have resistivities 10 times lower than those of the surrounding, unaltered rocks (Nelson and Anderson, 1992). Fine-grained sediments, such as clay-rich alluvium, marine shales, and other mudstones, normally are conductive from a few ohm-meters to a few tens of ohm-meters (Keller, 1987; Palacky, 1987). Coarse-grained sediments are typically slightly more resistive, from a few ohm-meters to thousands of ohm-meters (Keller, 1987; Palacky, 1987). Metamorphic rocks (nongraphitic) and unaltered, unfractured igneous rocks are normally moderately to highly

resistive (a few hundreds to thousands of ohm-meters). Carbonate rocks can have similarly high resistivities depending on their fluid content, porosity, and impurities (Keller, 1987; Palacky, 1987). Fault zones may be moderately conductive (tens of ohm-meters) where fluid movement along fractures produced secondary, less-resistive minerals (Eberhart-Phillips and others, 1995). Higher subsurface temperatures cause higher ionic mobility that reduces rock resistivities (Keller, 1987; Palacky, 1987). Tables of electrical resistivity for a variety of rocks, minerals, and geological environments are in Keller (1987) and Palacky (1987).

## **Magnetotellurics**

The magnetotelluric (MT) method is a passive surface geophysical technique that uses the Earth's natural electromagnetic fields to investigate the electrical resistivity structure of the subsurface. The MT method can be used to probe the crust from depths of tens of meters to tens of kilometers (Vozoff, 1991). Natural variations of the Earth's magnetic and electric fields are recorded in two orthogonal, horizontal directions at each MT station. An optional third magnetometer measuring the vertical component of the magnetic field can help delineate vertical structures by helping to resolve the 90-degree ambiguity in the impedance rotation angle structures. The recorded time-series signals are used to derive apparent resistivities and phases. For a two-dimensional (2-D) Earth, the MT fields can be decoupled into transverse electric (TE) and transverse magnetic (TM) modes; 2-D modeling generally is done to fit both modes. When the geology satisfies the 2-D assumption, and the survey transect is oriented perpendicular to the geologic strike of interest, the MT data for the TE mode are for the electric field parallel to geologic strike (or perpendicular to the survey transect), and the data for the TM mode are for the electric field across strike (parallel to the survey transect). The MT method is well suited for studying complicated geological environments because the electric and magnetic relations are

sensitive to vertical and horizontal variations in resistivity. An introduction to the MT method and references for a more advanced understanding are in Dobrin and Savit (1988) and Vozoff (1991).

High-frequency audio-magnetotellurics (AMT) are MT signals in the range from approximately 10 Hz up to 100 kHz. Variations in ground electrical conductivity can be investigated from a few tens of meters to several 100 meters depth. The AMT technique can image range-front and interbasin faults, basin-fill alluvium, volcanic rocks, and carbonate versus clastic rocks. Generally, the AMT technique is limited by a natural paucity of MT signal from around 1 kHz to 5 kHz. However, the natural MT fields in this band can be augmented by providing additional signal power with a small battery-powered transmitter (the controlled source) which reduces the potential loss of resolution at what can be critical depths of investigation. This method, entitled CSAMT for controlled-source AMT, has been used effectively in adjacent Spring Valley, west of the park, to delineate subsurface geologic structure (McPhee and others, 2007).

## **Snake Valley Audio-Magnetotelluric Survey**

The purpose of this study was to evaluate the possible presence, location, geometry, and amount of offset of a buried range-bounding normal fault or faults along the east side of the southern Snake Range near Great Basin National Park. A CSAMT survey was performed west of Baker near the Park (fig. 1) September 9–14, 2009. For an AMT method to be successful, the geophysical data must be collected far (0.5 km to 1 km) from sources of anthropomorphic electronic signals generated by power lines, power generators, pumping wells, and moving vehicles. This eliminated data collection along the main paved road up the Lehman Creek drainage. Instead, AMT surveys were conducted in the Baker Creek drainage and near Kious

Spring (fig. 2). Photographs showing the southern Snake Range and the locations of the CSAMT lines are shown in Appendix 2. The location of Baker Creek AMT line 1 extends from the west end at the Baker Creek Narrows and runs eastward out of the park, generally following the Baker Creek drainage, to a point about 1.2 km east of the confluence of Baker and Lehman Creeks (fig. 2). Line 2 extends from southwest of the town of Baker westward towards the range front towards the vicinity of Kious Spring. A total of 48 AMT soundings were recorded progressing from approximately east to west. Table 1 lists the station locations for line 1 and table 2 lists the station locations for line 2.

The AMT system used in this investigation was the STRATAGEM EH4 by Geometrics, Inc. (2007). Photos of the system components and deployment are shown in Appendix 2. The STRATAGEM is a hybrid system that measures orthogonal arrays of electrical and magnetic fields over a nominal frequency range of 10 Hz to 100 kHz. The electrical resistivity of the subsurface as a function of this frequency is computed from the ratio of the electric field to the magnetic field. Electric field dipoles consisted of emplacement of five (2 each for X and Y directions and 1 ground) stainless-steel electrodes (fig. A2-6). Each electrode is about 1 cm (3/8-inch) in diameter and is hammered in about 0.25 m (10 inches) into the ground. Measurement of the ambient magnetic field is accomplished with two induction magnetometer coils (fig. A2-8) that are approximately 0.91-m (3 feet) long with diameters of about 5 cm (2 inches). Emplacement of these coils involves scraping a 2.54-cm (1 inch) trace about 1.07 m (3.5 feet) long into the surface into which the coil is placed and then covered with dirt (fig. A2-9). A small 400 Watt transmitter is used to supplement the received electromagnetic signal in the frequency range from 900 Hz to 23, 000 Hz. A schematic of the layout used for line 1 is shown in figure 4 and photos in figures A2-14 and A2-15.

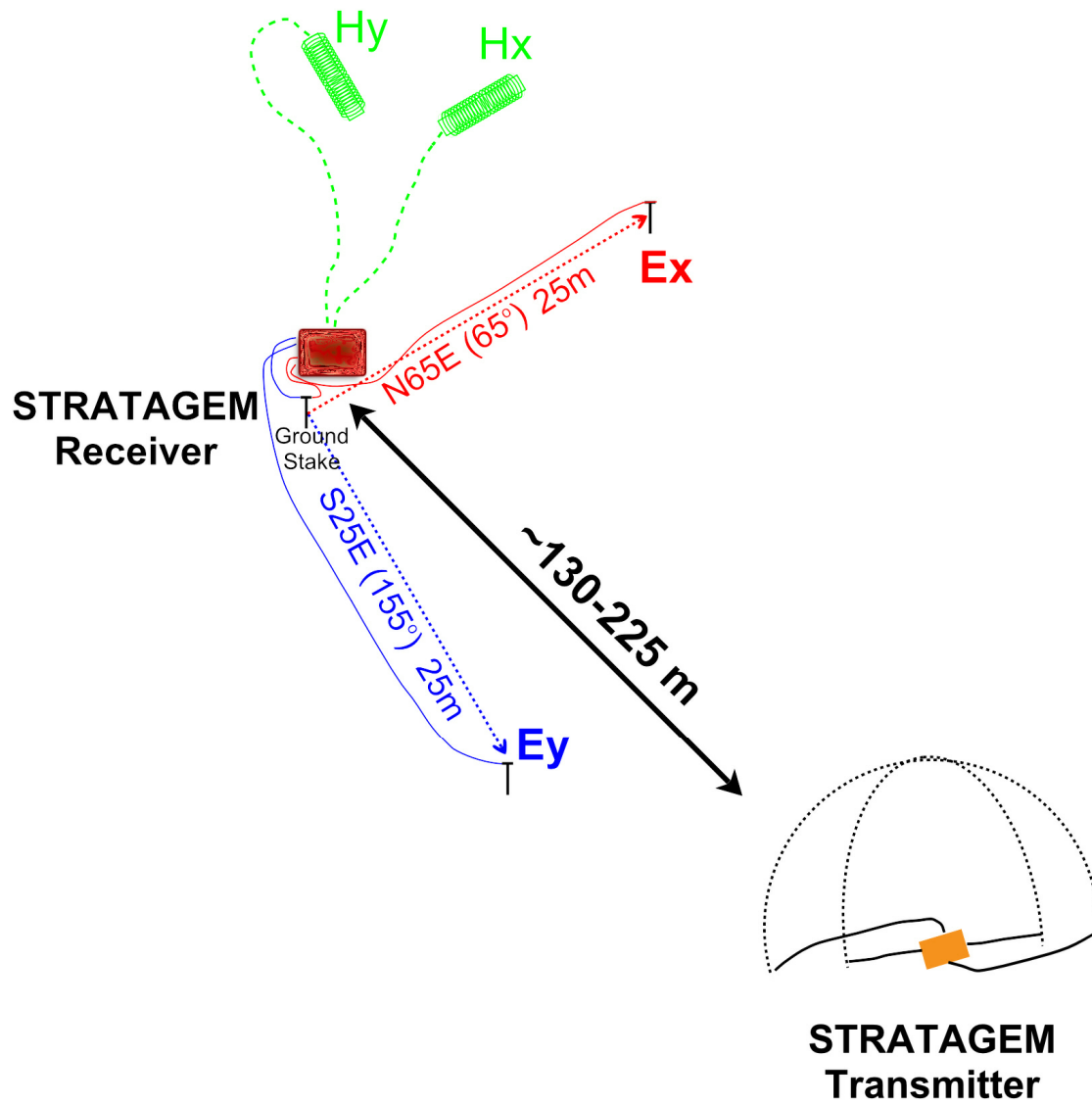


**Figure 4.** Schematic layout of the STRATAGEM system for Line 1 of the Snake Valley, Nevada AMT survey. Hx and Hy are horizontal induction coil magnetometers oriented in the X- and Y-directions, respectively. Ex and Ey are horizontal electric field dipoles also oriented in the X- and Y-directions.

**Table 1.** Audio-Magnetotelluric station locations for Line 1. Easting and Northing in North American Datum 1983 (NAD83), Universal Transverse Mercator (UTM), Zone 11 North, meters, and latitudes and longitudes in World Geodetic System (WGS) 1984.

Station	Date	Easting (m)	Northing (m)	Longitude (W)	Latitude (N)
1	09-Sep-09	747417	4321905	114° 08' 33"	39° 00' 40"
2	09-Sep-09	747227	4321838	114° 08' 41"	39° 00' 38"
3	09-Sep-09	747028	4321818	114° 08' 49"	39° 00' 38"
4	09-Sep-09	746825	4321819	114° 08' 58"	39° 00' 38"
5	09-Sep-09	746624	4321834	114° 09' 06"	39° 00' 39"
6	09-Sep-09	746423	4321817	114° 09' 14"	39° 00' 38"
7	09-Sep-09	746226	4321773	114° 09' 23"	39° 00' 37"
8	10-Sep-09	746035	4321696	114° 09' 31"	39° 00' 35"
9	10-Sep-09	745836	4321678	114° 09' 39"	39° 00' 35"
10	10-Sep-09	745639	4321636	114° 09' 47"	39° 00' 33"
11	10-Sep-09	745447	4321581	114° 09' 55"	39° 00' 32"
12	10-Sep-09	745258	4321514	114° 10' 03"	39° 00' 30"
13	10-Sep-09	745107	4321413	114° 10' 10"	39° 00' 27"
14	10-Sep-09	744950	4321281	114° 10' 16"	39° 00' 23"
15	10-Sep-09	744758	4321236	114° 10' 24"	39° 00' 21"
16	10-Sep-09	744571	4321162	114° 10' 32"	39° 00' 19"
17	11-Sep-09	744389	4321089	114° 10' 40"	39° 00' 17"
18	11-Sep-09	744198	4321001	114° 10' 48"	39° 00' 14"
19	11-Sep-09	744015	4320889	114° 10' 56"	39° 00' 11"
20	11-Sep-09	743816	4320768	114° 11' 04"	39° 00' 07"
21	11-Sep-09	743659	4320697	114° 11' 11"	39° 00' 05"
22	11-Sep-09	743533	4320564	114° 11' 16"	39° 00' 01"
23	11-Sep-09	743194	4320409	114° 11' 30"	38° 59' 56"
24	11-Sep-09	743042	4320279	114° 11' 37"	38° 59' 52"
25	12-Sep-09	742872	4320196	114° 11' 44"	38° 59' 50"
26	12-Sep-09	742647	4320063	114° 11' 54"	38° 59' 45"
27	12-Sep-09	742455	4319957	114° 12' 02"	38° 59' 42"
28	12-Sep-09	742286	4319853	114° 12' 09"	38° 59' 39"
29	12-Sep-09	742119	4319742	114° 12' 16"	38° 59' 36"
30	12-Sep-09	741949	4319643	114° 12' 23"	38° 59' 33"
31	12-Sep-09	741803	4319508	114° 12' 29"	38° 59' 28"
32	12-Sep-09	741623	4319412	114° 12' 37"	38° 59' 25"
33	12-Sep-09	741354	4319419	114° 12' 48"	38° 59' 26"

**Table 2.** Audio-Magnetotelluric station locations for Line 2. Easting and Northing in North American Datum 1983 (NAD83), Universal Transverse Mercator (UTM), Zone 11 North, meters, and latitudes and longitudes in World Geodetic System (WGS) 1984.

Station	Date	Easting (m)	Northing (m)	Longitude (W)	Latitude (N)
34	13-Sep-09	748144	4320054	114° 08' 05"	38° 59' 40"
35	13-Sep-09	748032	4319889	114° 08' 10"	38° 59' 34"
36	13-Sep-09	747897	4319744	114° 08' 16"	38° 59' 30"
37	13-Sep-09	747775	4319592	114° 08' 21"	38° 59' 25"
38	13-Sep-09	747681	4319417	114° 08' 25"	38° 59' 19"
39	13-Sep-09	747575	4319249	114° 08' 30"	38° 59' 14"
40	13-Sep-09	747448	4319095	114° 08' 35"	38° 59' 09"
41	13-Sep-09	747295	4318968	114° 08' 42"	38° 59' 05"
42	13-Sep-09	747167	4318813	114° 08' 47"	38° 59' 00"
43	13-Sep-09	747015	4318692	114° 08' 54"	38° 58' 57"
44	13-Sep-09	746972	4318497	114° 08' 56"	38° 58' 50"
45	14-Sep-09	746949	4318298	114° 08' 57"	38° 58' 44"
46	14-Sep-09	746851	4318123	114° 09' 01"	38° 58' 38"
47	14-Sep-09	746707	4317978	114° 09' 08"	38° 58' 34"
48	14-Sep-09	746542	4317868	114° 09' 15"	38° 58' 30"

AMT data were nominally measured every 200 m. The STRATAGEM does not use a third magnetometer to measure the vertical component. The general rule of thumb in magnetotelluric surveying is to use the right-hand rule (the X-direction, your fingers, curl towards the Y-direction using your right hand) with Z-positive (your thumb) in the downward direction. The survey X-direction was set along the generally northeast trend of the line and the Y-direction was set perpendicular to the line. For line 1 these directions were N65°E (X direction) and S25°E (Y direction) and for line 2 these directions were N35°E (X-direction) and S55°E (Y direction). Electric fields were measured using 25-m dipoles and the magnetic fields used EMI BF-6 high frequency magnetic induction coils (Geometrics, 2007). Time-series data are recorded and field-processed into cross powers in real time by the STRATAGEM acquisition software. This allows for almost immediate quality control field checks of the acquired data.



Each station required about 10 minutes for setup, 20 minutes for data acquisition, and about 10 minutes for pickup and moving to the next station with a crew of 2.

The effects of strong lateral inhomogeneities in near-surface materials can sometimes cause resistivity anomalies that demonstrate what are known as static shift effects in the data (Sternberg and others, 1988). Only stations 18, 19, and 20, which were located on the side of the hill on the north side of line 1, demonstrated minor static shift effects.

## **Audio-Magnetotelluric Data Processing**

In post-processing, the recorded AMT time-series data were transformed to the frequency domain and processed to determine a 2-D tensor apparent resistivity and phase at each station. Time-series data sets were selected for optimal signal-to-noise characteristics prior to the cross-power calculations. Noisy data in the time series, spectral, and resistivity data were culled out. Cross power and MT impedance data files were created with the STRATAGEM data acquisition program IMAGEM. These files are used as input to the 2-D inversion modeling program. Since the STRATAGEM is a single station MT sounding system, remote reference processing as discussed in Gamble and others (1979) and more advanced multistation processing (Egbert, 1997) could not be utilized. Active local lightning storms in Nevada and Utah provided high-quality signals during most of each day.

During the 2-D analysis and interpretation process, the impedance tensor at each station was rotated to a fixed angle that is determined by the perpendicular direction to the given nominal profile orientation. For line 1, this fixed angle was 155 degrees (-25 degrees), and a fixed angle of 125 degrees (-55 degrees) was applied to line 2 data. Rotation of the impedance tensor allows for decoupling into the TE and TM modes.

The raw AMT data and uninterpreted resistivity model AMT data are presented in Appendix 1. Included are the TM-, TE-, and TMTE-mode models for the Snake Valley AMT data with the measured and calculated apparent resistivity and phase curves, polar, skew, and impedance rotation and strike plots.

Apparent resistivity is the approximate ratio of the electric field strength to the magnetic field strength at a given frequency. The impedance phase is proportional to the slope of the apparent resistivity curve on a log-log plot, but from baselines at  $\pm 45$  degrees (Vozoff, 1991).

A measure of the dimensionality for AMT data is provided by the impedance skew of the impedance tensor (Vozoff, 1972). If the effective measured resistivity response to the geology beneath an AMT station truly is one or two dimensional, then the skew will be zero. Instrument and environmental sources of electrical noise can cause nonzero skew values. Skew values typically are small (about 0.1) for relatively low noise recordings in one- (1-D) or two-dimensional (2-D) geologic environments. Higher skews (above 0.2) are an indication of either 3-D geology or higher levels of noise. Manmade electrical noise, such as power lines, power generators, and moving vehicles and trains, can have a negative effect on AMT data quality. All of these local disturbances can produce incoherent noise that mainly affects frequencies above 1 Hz. Other manmade electrical noise, such as direct current electric trains and active cathodic protection of pipelines, produces coherent electromagnetic signals that mainly affect frequencies below 1 Hz which were not measured in this study.

The impedance polar diagrams provide a measure of AMT data dimensionality (Reddy and others, 1977). For 1-D resistivity structures, the principal impedance polar diagram (yellow-green line) is a circle. For 2-D or 3-D resistivity structures, the principal impedance polar diagram (yellow-green line) elongates either parallel or perpendicular to strike direction. Over

resistors, the principal impedance polar diagram elongates perpendicular to strike direction, and over conductors, it elongates parallel to strike direction. For 2-D resistivity structures, the additional impedance polar diagram (orange lines) attains the shape of a symmetric cloverleaf. For 3-D resistivity structures, the additional impedance polar diagram (orange line) elongates in one direction, and its amplitude is comparable to that of the principal impedance polar diagram.

## **2-D Modeling Analysis of the Audio-Magnetotelluric Data**

A two-dimensional forward and inverse modeling analysis of the Snake Valley AMT data has been completed. Wannamaker (1983) found that while some MT responses are fundamentally three-dimensional (3-D) in nature, for elongated structures 2-D modeling could be used to construct reasonable estimates of the resistivity cross sections along each profile. Wannamaker and others (1984) demonstrated that approximating 3-D structure beneath a centrally located measurement with 2-D modeling is best achieved when fitting the TM curve, even at the expense of a poor fit of the TE curve. However, because TM data are relatively insensitive to the depth extent of a subsurface body (Eberhart-Phillips and others, 1995), the depths to the base of the bodies in the model are not well constrained. Hence, mixed mode analysis (modeling the TMTE mode) may help clarify the modeling results for elongated geologic structures beneath the profile.

Two-dimensional resistivity models were constructed for the approximately 6.5-km-long line 1 and 2.8-km-long line 2. 2-D inversions of the audiomagnetotelluric data were conducted using the computer program RLM2DI (Mackie and others, 1997; Rodi and Mackie, 2001), from GEOTOOLS (Geotools, 1998), a shell program specifically designed to process and interpret MT and AMT data. This was followed by the application of the 2-D forward modeling algorithm program, PW2D, developed by Wannamaker and others (1987). The results of the RLM2DI 2-D

inversion were used as the initial input model for the forward modeling, PW2D, where a sensitivity analysis was performed on the conductive structures derived from the inversion results.

RLM2DI uses a finite-difference network analog to the Maxwell's equations governing magnetotellurics to calculate the forward solution and a nonlinear conjugate gradient optimization approach that is applied directly to the minimization of the objective function for the inverse problem. PW2D is a stable finite-element algorithm that simulates transverse electric and magnetic fields using a linear basis across each finite element. The inversion algorithm, RLM2DI, usually was allowed to batch run 25 iterations in order to reduce the root-mean-square error to a reasonable value between the measured field data and the numerical model calculated data. The number of iterations of forward modeling (PW2D) necessary for a sensitivity analysis of conductive structures depended on how complex the profile inversion results were from RLM2DI.

The RLM2DI inversion model meshes for the Snake Valley AMT data are listed in table 3. The number of horizontal and vertical nodes necessary for the iterative forward modeling (PW2D) algorithm to accurately model the subsurface resistivity distribution in the Snake Valley area was greater than the number of nodes required by the inversion algorithm. This is a function of some fundamental differences between how finite-difference and finite-element algorithms handle the numerical boundary conditions and, subsequently, how the electric and magnetic fields are calculated across the mesh.

The edges of the forward model were extended horizontally and vertically to minimize edge effects. The resolution of the resistivity boundaries used for each model is somewhat subjective. If different resistivities are used, then boundary positions and layer depths would

have to be adjusted to achieve similar fits to the observed data. The extreme case would be to use a model with a "continuous" resistivity gradient from low to high resistivities. The resolution of the resistivity boundaries also is, in part, a function of the model grid mesh design. We have attempted to keep each model simple. The AMT profiles' model depths are relative to the Earth's surface. Nine additional vertical nodes were added to model the overlying air layer.

**Table 3.** Inversion (RLM2DI) and forward (PW2D) numerical resistivity model meshes for each profile. The number of horizontal nodes (first number) and vertical nodes (second number) in each model mesh are listed.

Model	RLM2DI	PW2D
In1tm2	85 x 59	
In1tm2pw1		133 x 61
In1te2	85 x 59	
In1tmte2	85 x 59	
In1tmte2pw2		136 x 71
In2tm	79 x 59	
In2te	79 x 59	
In2tepw2		110 x 65
In2tmte	79 x 59	

## Discussion

Subsurface geologic interpretations of the Snake Valley AMT investigation are superimposed on the 2-D inversion and forward modeling results for the TM, TE, and the mixed TMTE modes that are presented in figures 5 to 7 for line 1 and figures 8 to 10 for line 2. As discussed above, for a 2-D Earth the MT fields can be decoupled into TE and TM modes. For optimal interpretation, the geology must satisfy the 2-D assumption that resistivity structure varies with depth and in a single lateral direction and the AMT survey should then be perpendicular to the geologic strike. Where these conditions are met, the AMT data for the TE mode represent the electric fields flowing parallel to geologic strike such that the resistivity

section emphasizes electrical variations perpendicular to the profile orientation. The data for the TM mode represent the electric fields across the geologic strike such that the resistivity section emphasizes electrical variations along the profile orientation. The TMTE model integrates these responses over a volume of rock. Because these modes are sensitive to the geometry and continuity of geologic units, all three modes show slightly different aspects of subsurface structure. The subsurface interpretations presented here were developed from using all three models, plus surface geologic control, the limited available well data, and reference to available gravity and magnetic data sets (Watt and Ponce, 2007). Because the interpretation was developed from all of these data, the interpretation is stronger than if it had been developed from only one data set. The final interpretation is superimposed on the AMT data for each of the three modes; as a result, the final interpretation may appear locally inconsistent with the results from a single mode inversion model.

## **Line 1**

### **Surface Geologic Control**

The west end of line 1 is just east of the Baker Creek Narrows adjacent to outcrops of Pole Canyon Limestone (figs. 2, A2-16, A2-17). The limestone in this area dips 40-50 degrees to the east-northeast, roughly parallel to the profile (Whitebread, 1969; National Park Service, 2007). Between stations 33 and 31, Tertiary granite crops out at road level, and this granite also appears in outcrop on the south side of Baker Creek (fig. 2). Between stations 30 and about 28, intact Pole Canyon Limestone forms scattered outcrops (Whitebread, 1969; National Park Service, 2007). AMT line 1 crosses the trace of the southern Snake Range detachment fault, the location of which was inferred from surface exposures, near station 27. West of that station are outcrops of cataclastically deformed and brecciated Pole Canyon Limestone. To the east are

large (up to 100 m) blocks of granite, carbonate, and quartzite within a dominantly conglomeratic section that is inferred to be Miocene in age; the large blocks likely are equivalent to the megablocks exposed in the Sacramento Pass section to the north and along Big Wash to the south (see Geologic Setting). The Miocene section is locally exposed in outcrop under thin alluvial cover eastward to about station 20 and is inferred to underlie the entire ridge north of Baker Creek (labeled Qoa on fig. 2). Young Quaternary alluvium (Qa on fig. 2) is present at the surface east of station 17.

### Subsurface Interpretation

The AMT modeling of this profile (figures 5, 6, and 7) may be divided into three general domains of electrical response: (1) a shallow (generally less than 150 m depth) domain of highly variable resistivity (10 ohm-m to 1,000 ohm-m), (2) an eastern domain in which resistivity character changes abruptly just to the east of station 10, and (3) a west-central deep domain characterized by generally high resistivity (1,000 ohm-m to greater than 10,000 ohm-m) with gradual resistivity changes across steeply dipping boundaries.

The shallow domain is characterized by highly variable resistivity conditions, generally between the surface and 100-150 m depth, in the interval between station 27 on west end and station 10 on the east. The resistivity consists of high-amplitude, short wavelength anomalies that cannot be traced for great distance along the section. While the heterogeneous electrical response is most prominent in the TE mode (fig. 6), the TM mode (fig. 5) also is highly variable, indicating that the electrical character is variable both along strike and across strike. This shallow, heterogeneous domain is interpreted as the conglomeratic Miocene section and the megabreccia blocks contained within it. This is based on consistency with adjacent outcrops and the highly variable nature of the electrical signal both along and across strike. This unit is

interpreted to thicken eastward from the interpreted surface trace of the detachment near station 27 to at least 250 m thick beneath station 10. A USGS water well was recently drilled (September 2009) about 200 m southeast of station 24 (fig. 2). The well was drilled to a depth of 18.3 meters (60 feet), penetrating 10.4 m (34 feet) of alluvium and a thin section of carbonate rock before entering rock interpreted to be Pioche Shale (David Prudic, USGS, written comm., September, 2009). It is likely that the well penetrated a megabreccia block within the Miocene section rather than actual carbonate and shale bedrock. This megablock relation is best observed under station 24 in figure 6 which shows the TE mode results. High-amplitude, short wavelength anomalies (figures 5, 6, and 7) within this shallow domain that are relatively conductive (2-10 ohm-m) could represent fractured blocks of Pioche Shale, whereas resistive anomalies may represent megabreccia blocks of Pole Canyon Limestone or granite.

The second domain is to the east of station 10, where there is an abrupt shift in electrical character from 10-50 ohm-m to more resistive values of 100-500 ohm-m in the upper 300 m of the section (figs. 5, 6, and 7). We interpret this change to be the result of a young, steeply east-dipping, east-side down normal fault. We interpret the Miocene section, which was shallow to the west, to have been down-dropped on the east side of the fault. The magnitude of post-Miocene offset could be as small as 100 m on the basis of short-wavelength anomalies with resistivity values of 50-100 ohm-m that occur at about 100 m depth to the east of the fault (figs. 5, 6, and 7). However, we do not observe the relatively conductive (2-10 ohm-m), high-amplitude, short wavelength anomalies that are common within this shallow domain just to the west of station 10 (figs. 6 and 7). In addition, if the offset on the steeply-dipping fault were only 100 m, we would expect to observe, to the east of the fault, an offset equivalent of the high-resistivity domain that dominates the deeper part of the section to the west of the fault. The



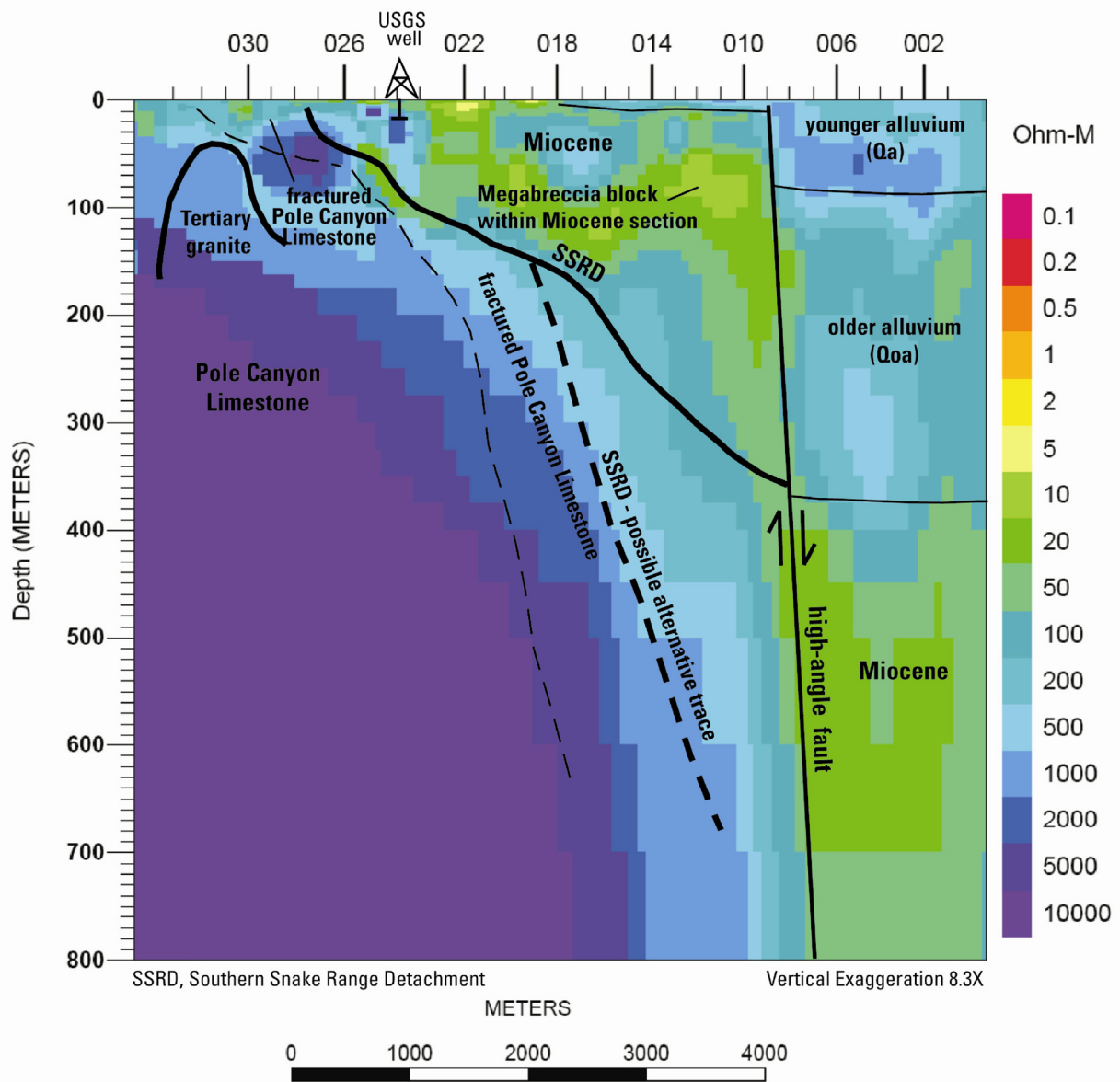


**Figure 5.** Two-dimensional Audio-Magnetotelluric forward modeling result for Transverse Magnetic (TM) mode inversion result along line 1. This forward model In1tm3pw1 (also in fig. A1-11) is derived from TM mode inversion model In1tm3 (fig. A1-1).

absence of such a high-resistivity domain to the east of the fault (fig. 5) leads us to suspect that the down-to-the-east offset on this fault may be significantly greater than 100 meters. It is more likely that the regions with resistivity values of 20-100 ohm-m that occur below 400 m depth to the east of the fault represent the down-dropped Miocene section (figs. 5, 6, and 7). Material between 100 m and 400 m depth with resistivity values of 100-1,000 ohm-m may be the buried equivalent to the older alluvium (Qoa, figs. 2 and 3) observed in outcrop.

An oil and gas exploration well drilled 4.6 km east of Baker penetrated about 425 m of coarse sand and gravel alluvium before entering a thick section of heterogeneous, clay-rich material that we interpret as the Miocene section. Lithologic descriptions, drilling rate, and geophysical logs indicate local intervals of quartzite and limestone within this section that may represent megabreccia blocks. The elevation of the top of this inferred Miocene section is consistent with the interpreted elevation of the down-dropped Miocene section on the east end of line 1. Water wells in the vicinity of Baker are mostly less than 100-m deep and penetrate sand and gravel deposits we interpret to be younger alluvium. Some wells penetrate cemented intervals that may be equivalent to the older alluvium (Qoa, figs. 2 and 3) observed in outcrop. The variably resistive nature of the shallow section to the east of the steeply-dipping fault may represent variable cementation conditions and varying amounts of clay in the young alluvial deposits.

No Quaternary fault is mapped at the surface at this location, but projections of Quaternary faults mapped to the south (crossing line 2) and to the north of line 1 (U.S. Geological Survey and Nevada Bureau of Mines and Geology, 2006) would pass exactly through this area. Based on the height of the Quaternary fault scarp that crosses line 2 (fig. 2), the amount of Quaternary offset may only be 2-3 m, although the surface scarp is not pristine and some

evidence for recent offset may not be preserved. This high-angle fault is thus interpreted as having from as little as 100 m to as great as 400 m of post-Miocene offset, of which at least a few meters is Quaternary in age.

The third domain is the deeper part of the section, characterized by a transition from very high resistivity on the west side (10,000 ohm-m) to lower resistivity on the east (10-100 ohm-m) and having a steeply east-dipping structure or grain (figs. 5, 6, and 7). Although the continuous bands of resistivity values appear nearly vertical on the 8.3x exaggerated section, on the 1:1 section the apparent dip is between 40 to 50 degrees to the east within the plane of the section. This approximates the dip of the Pole Canyon Limestone in nearby surface outcrops. We interpret the very resistive (1,000 – 10,000 ohm-m) unit at depth on the west side of the section (from the west end of the line to about station 26 on the TE section, fig. 6) to be the Pole Canyon Limestone. Seismic line 1 of Allander and Berger (2009) was collected near station 33. Results from that line suggested that consolidated rock, probably Pole Canyon Limestone, existed at an average depth of about 23 m (76 feet). This corresponds well to a change in resistivity on the TE section below station 33 from 100–200 ohm-m to a more resistive (500–1,000 ohm-m) unit (fig. 6). At the west end of the section, between stations 31 and 33, we infer a narrow granite body intruding the resistive limestone section based on the narrow domain of more electrically conductive material (200 ohm-m to 1,000 ohm-m) centered at about 100 m depth and the presence of granite outcrops near the line. Seismic line 2 of Allander and Berger (2009) was collected between stations 31 and 32. Results from that line suggested that consolidated rock, either Tertiary granite or Pole Canyon Limestone, existed at an average depth of about 26.5 meters (87 feet). Although the shape of the inferred granite body is uncertain because its

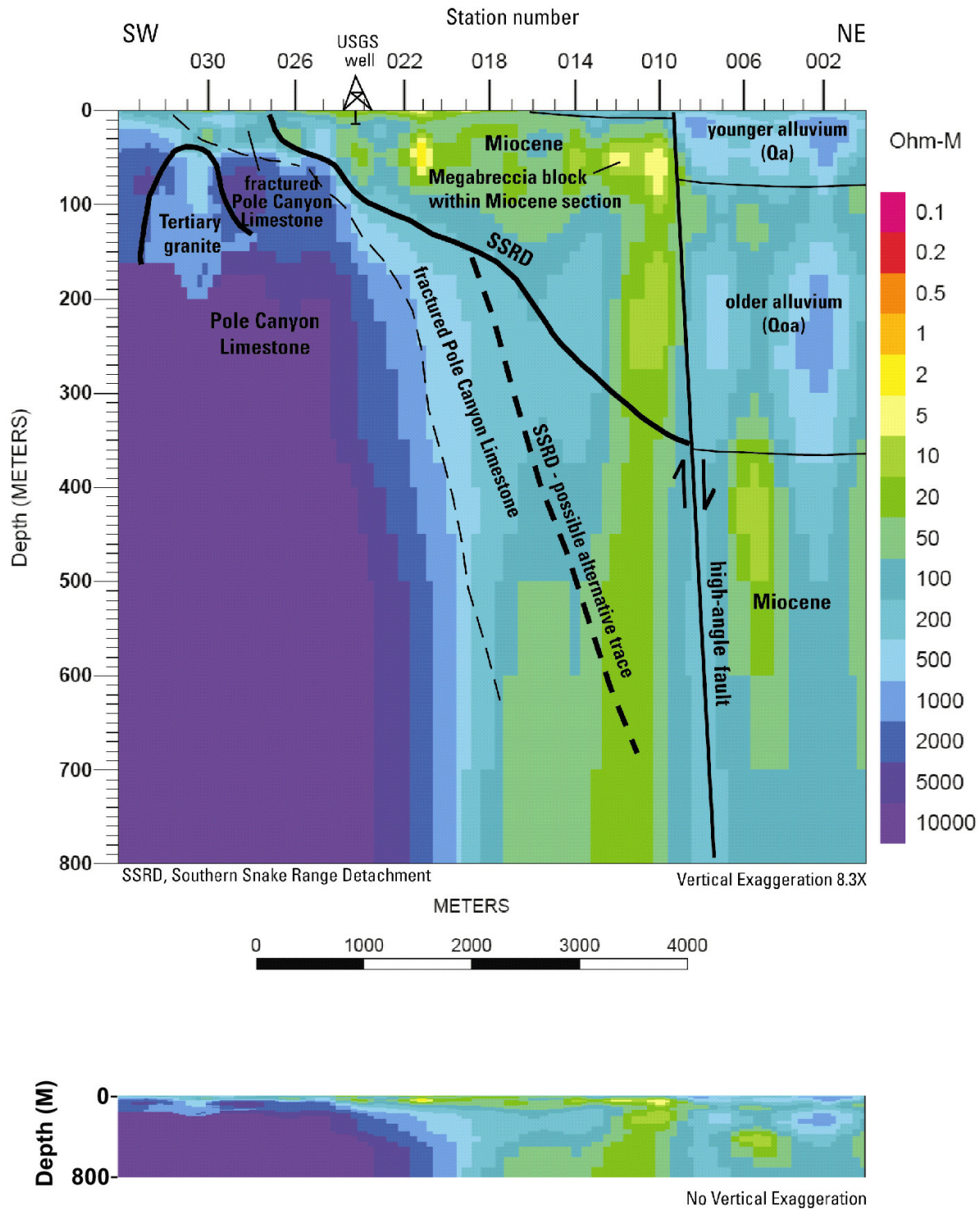


**Figure 6.** Two-dimensional Audio-Magnetotelluric forward modeling result for Transverse Electric (TE) mode inversion result along line 1. This forward model ln1te3pw1 (also in fig. A1-31) is derived from TE mode inversion model ln1tm3 (fig. A1-21).



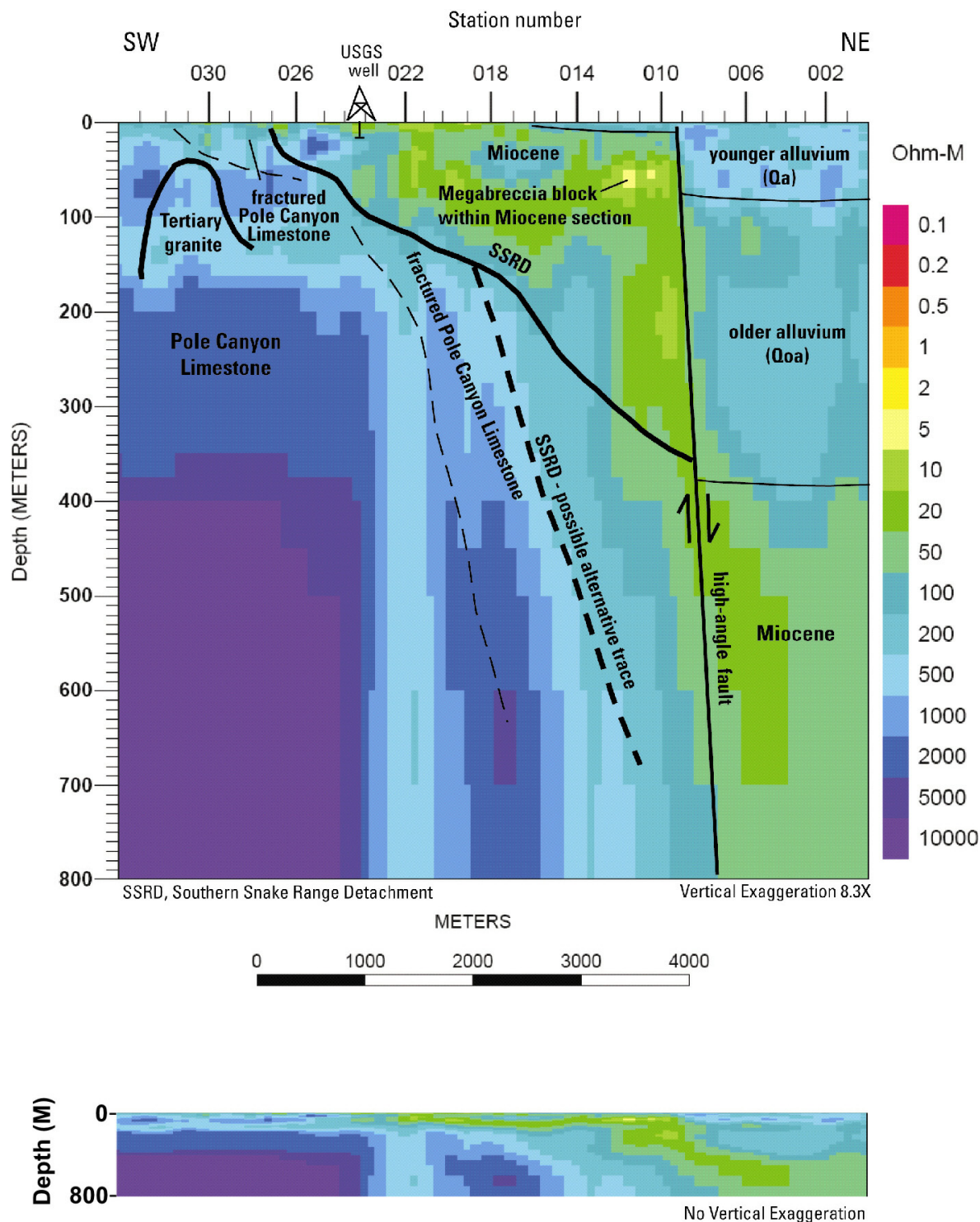


**Figure 7.** Two-dimensional Audio-Magnetotelluric inversion modeling results for combined Transverse Magnetic – Transverse Electric (TMTE) mode along line 1.

resistivity may be similar to the limestone, granite invades along the Pioche Shale elsewhere in the area as relatively narrow, sheet-like intrusions; we infer the granite near the west end of line 1 to be a similarly narrow intrusion. This also would explain the apparent absence of the granite at greater depths, as might be expected if the granite was a more vertical intrusive body.

The eastward gradational change to lower resistivity values in the deep section may be related to fracturing of the Pole Canyon Limestone beneath the detachment, the presence of other rock units in the subsurface, or both. On the surface, the upper part of the Pole Canyon Limestone that is immediately subjacent to the detachment is extensively fractured and brecciated. The gradual drop off in resistivity eastward and shallower from the area of highest resistivity may be the result of fault-related brecciation and fracturing in the upper portion of the limestone. This process could explain all of the gradational resistivity in the lower part of the section west of station 9. Alternatively, there may be additional Paleozoic units, not exposed at the surface, that exist at depth in the eastern part of the section. Although our preferred interpretation for the fault contact between the Miocene section and underlying bedrock is that of a relatively gently east-dipping surface, it is possible that the dip of the detachment surface steepens between stations 18 and 10. In this case, the Miocene section might be as much as 300-m thick below station 10 (figs. 5, 6, and 7).

Significantly, the relatively steep boundaries between western resistive crust and conductive eastern crust seen in the deep part of the section cannot be projected upwards through the interpreted Miocene section and the resistivity boundaries at depth have no counterparts within the shallow section. This is to be expected because the detachment, where exposed, separates footwall Paleozoic rocks from hanging-wall Miocene rocks, and it does not cut the Miocene strata. In addition, the continuity of the Miocene and older alluvial section on the ridge

to the north of the line precludes the projection of the detachment upwards through the Miocene units. The data do suggest that the detachment may steepen with increased depth. The only high-angle fault that cuts the Miocene units is the fault near station 10.

## **Line 2**

### **Surface Geologic Control**

The west end of line 2 (figs. 2 and A2-18) begins at the base of a hill that exposes the Tertiary granite of the Young Canyon pluton. There, a very gently east-dipping fault that is interpreted as the southern Snake Range detachment separates the pluton from overlying, faulted Cambrian and Ordovician carbonate rocks (McGrew and others, 1995). Line 2 runs northeastward along the southeastern edge of a hill mapped as older Quaternary alluvium (Qoa, fig. 2). Based on comparison with similar hills in the study area, this hill is inferred to be underlain by the Miocene strata that are covered by a thin veneer of older alluvium. Line 2 crosses over younger Quaternary alluvium at about station 40. The line crosses a mapped Quaternary scarp (U.S. Geological Survey and Nevada Bureau of Mines and Geology, 2006) at about station 37; this fault is expressed at the surface as a subtle 0.5-m-high swale in the alluvial surface (fig. A2-19). A single water well serves as subsurface geologic control on this line. This well is at the western end of the line near station 47. The well penetrated about 24 m (80 feet) of sediment (granitic boulders and sand) before penetrating what is interpreted to be fractured granite. The well is about 100-m (300 feet) deep and interpreted to be entirely within granite below the alluvium.

## Subsurface Interpretation

The geophysical response seen on this line is similar to that seen on line 1, again with three general domains of electrical response: a shallow (mostly less than 100-m deep) domain of highly variable resistivity, a deep domain characterized generally by high resistivity that gradually declines eastward to lower resistivity with a steeply-dipping grain or fabric, and an eastern domain in which resistivity character changes abruptly at all depths to the east of station 37 (figs. 8, 9, and 10). The TE mode (fig. 9) shows these three domains to their best effect, especially on the 1:1 ratio section at the bottom of the figure.

As on line 1, we interpret the shallow part of the AMT profile as being the Miocene section with megabreccia blocks, lying structurally above the southern Snake Range detachment. The west end of the line is underlain by Tertiary granites that are in the footwall of the detachment, with the gently east-dipping detachment present in outcrop on the hill above and to the south of the line (fig. 2). We infer that line 2 crosses the buried detachment near stations 46 or 47. West of station 45, we interpret the moderate (50-200 ohm-m) resistivity in the upper 100 m (300 feet) to be the result of highly fractured and chlorite-altered granite beneath the detachment fault, as supported by the granite found in the deeper part of the water well near station 47. The inferred Miocene section is interpreted to thicken to the northeast to about 140 m beneath station 40. This thickness is consistent with the modeled depth to basement (Watt and Ponce, 2007) at this location. The inferred detachment fault undulates and dips gently to the northeast. High-amplitude, very short wavelength anomalies (figures 8, 9, and 10) within this shallow domain that are relatively conductive (2-10 ohm-m) could represent fractured blocks of Pioche Shale, whereas resistive anomalies may represent megabreccia blocks of Pole Canyon Limestone or granite.



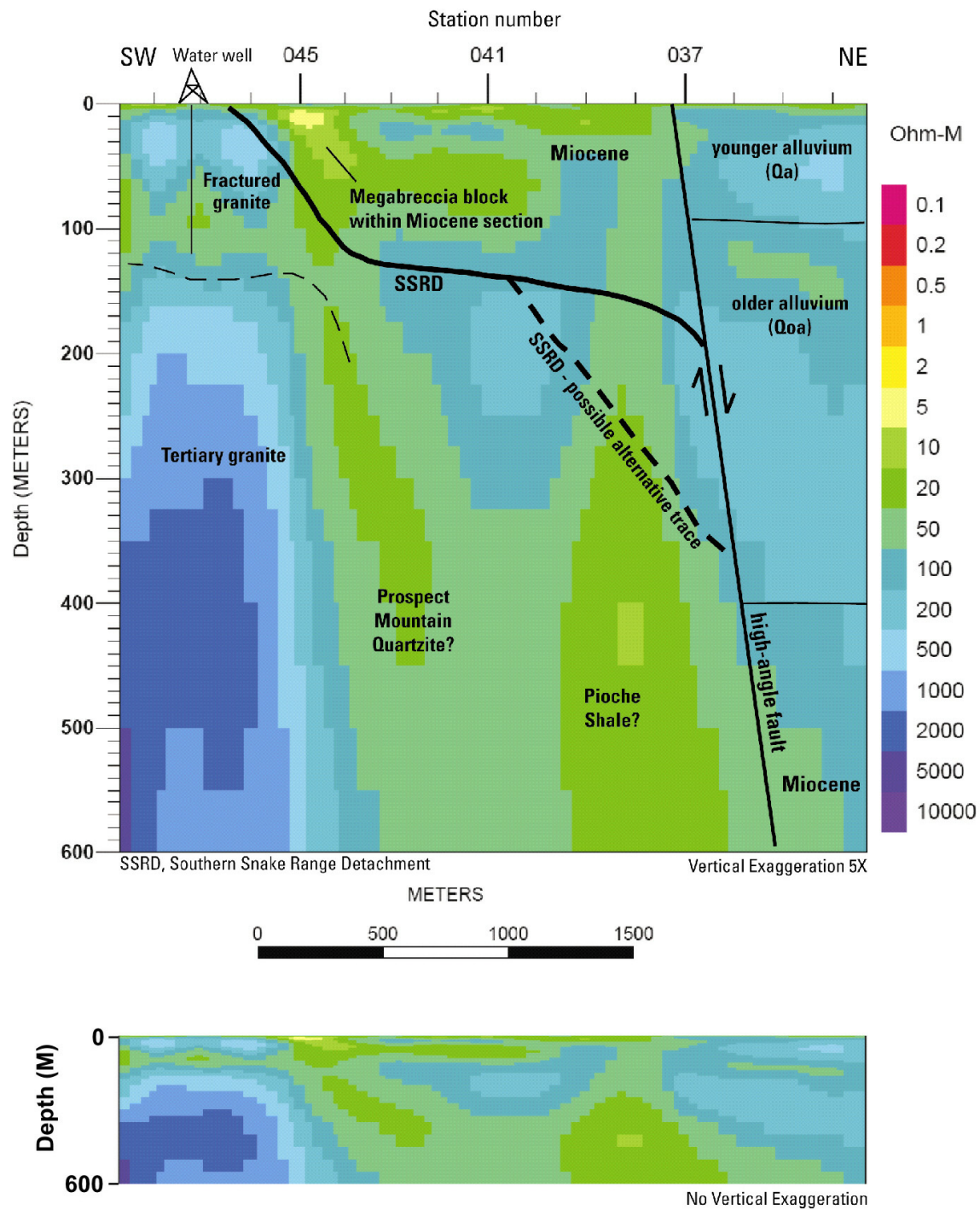


**Figure 8.** Two-dimensional Audio-Magnetotelluric inversion modeling results for the TM mode along line 2.

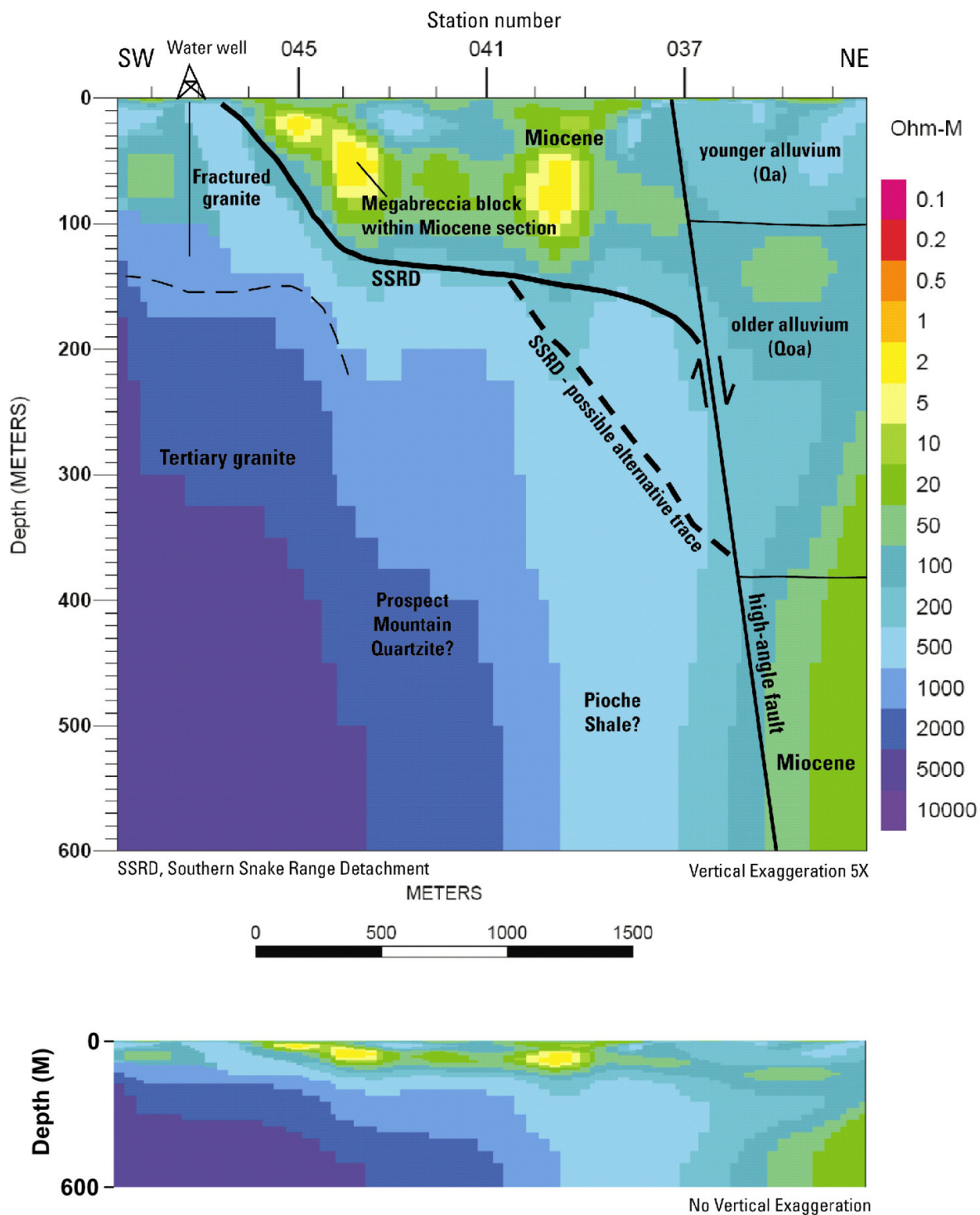


**Figure 9.** Two-dimensional Audio-Magnetotelluric forward modeling result for Transverse Electric (TE) mode inversion result along line 2. This forward model, In2te2pw1 (also in fig. A1-194), is derived from TE mode inversion model In2te2 (fig. A1-188).

The inferred shallow Miocene section is cut abruptly at about station 37 by an inferred steeply northeast-dipping fault, where there is an abrupt shift in electrical character from 50-100 ohm-m to more resistive values of 200-500 ohm-m, especially in the upper 100 m of the section (figs. 8, 9, and 10). We interpret this change to be the result of a young, steeply east-dipping, east-side down normal fault. We interpret the Miocene section, which was shallow to the west, to have been down-dropped on the east side of the fault. The magnitude of post-Miocene offset is difficult to definitively establish on this line. The offset could be as small as 100 m on the basis of short-wavelength anomalies with resistivity values of 50-100 ohm-m that occur at about 100 m depth east of the fault (figs. 8, 9, and 10). However, as on line 1, if the offset on the steeply dipping fault were only 100 m, we would expect to observe, to the east of the fault, an offset equivalent of the high-resistivity domain that dominates the deeper part of the section to the west of the fault. The absence of such a high-resistivity domain to the east of the fault (best expressed on fig. 9), combined with more definitive results from line 1, leads us to suspect that the down-to-the-east offset on this fault may be significantly greater. It is more likely that the regions with resistivity values of 50-100 ohm-m that occur at 400-500 m depth to the east of the fault represent the down-dropped Miocene section (figs. 8, 9, and 10).

The location of the steeply-dipping fault on the profile is consistent with the mapped surface trace of a Quaternary fault (figs. 2 and A2-19) (U.S. Geological Survey and Nevada Bureau of Mines and Geology, 2006). Based on the height of the Quaternary fault scarp that crosses line 2 (fig. A219), we infer that the amount of Quaternary offset is 2-3 m. As on line 1, our preferred interpretation is that this high-angle fault has up to 400 m of post-Miocene offset, of which a few meters is Quaternary in age.



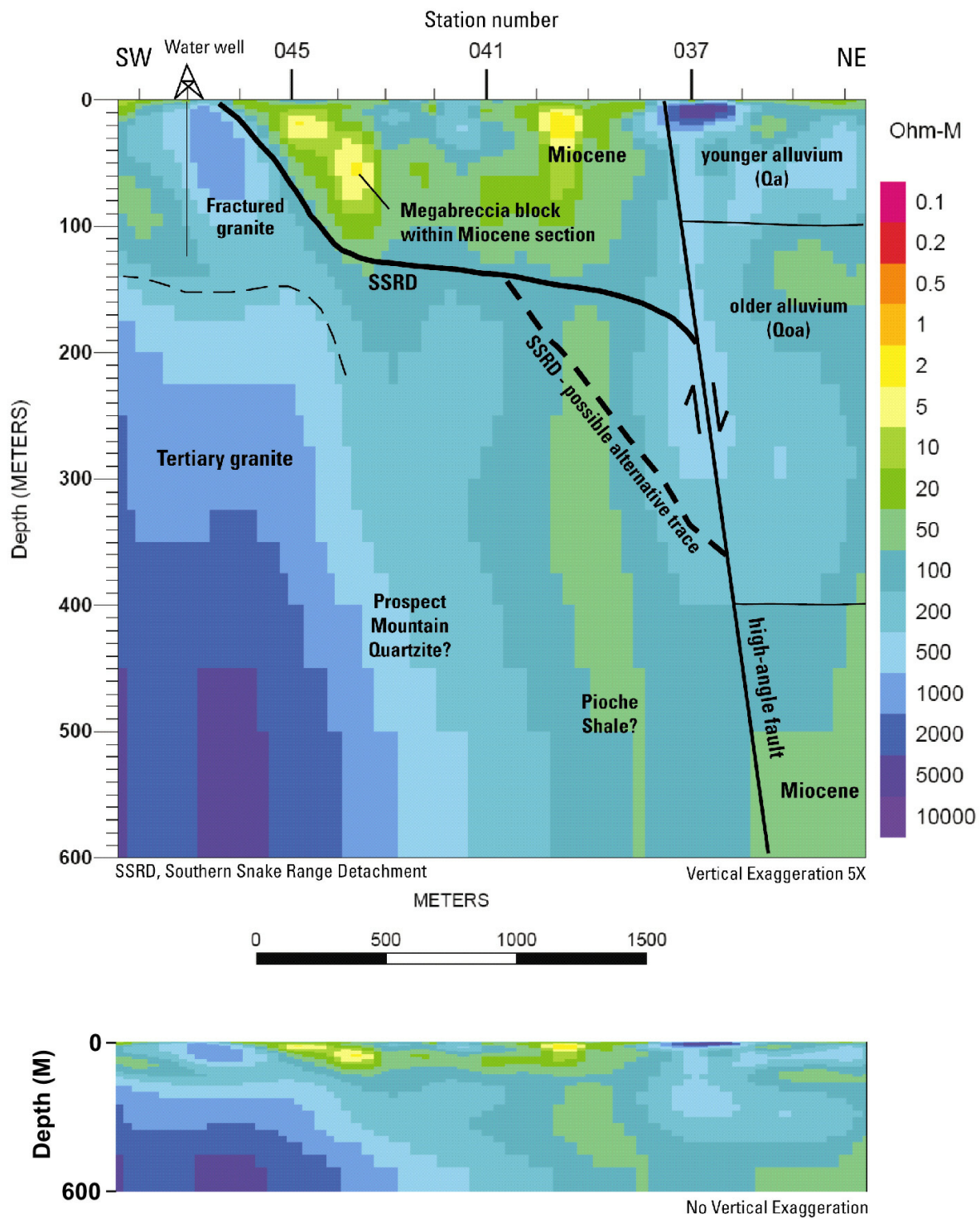


**Figure 10.** Two-dimensional Audio-Magnetotelluric inversion modeling results for combined Transverse Magnetic – Transverse Electric (TMTE) mode along line 2.

We infer that the high resistivity values (1,000-10,000 ohm-m) below 100-m depth of the western side of the section to be Tertiary granite (figs. 8, 9, and 10). The upward reduction in resistivity may be the result of ductile to brittle deformational fabrics and the formation of hydrothermal chlorite immediately subjacent to the detachment fault. It is possible that Prospect Mountain Quartzite also is present at depth because it is the country rock into which the granite was intruded in the Kious Springs quadrangle (McGrew and others, 1995). We speculate that the resistive (100 – 200 ohm-m) body beneath stations 41 and 42 from about 150- to 300-m depth and the conductive body beneath stations 38 and 39 from about 300- to at least 600-m depth may be Paleozoic rock units that are not exposed at the surface in the vicinity of the line. For example, the relatively conductive unit (10 – 50 ohm-m) beneath stations 38 and 39 could be the Pioche Shale at depth (figs. 8, 9, and 10). As on line 1, it is not possible to extend the resistivity boundaries that are seen deep in the section upward to the surface through the interpreted Miocene section. As such, it does not appear likely that any faults cut through the Miocene section west of the one Quaternary fault at station 37.

## **Summary and Conclusions**

In September 2009, the U.S. Geological Survey, in cooperation with the National Park Service, collected audiomagnetotelluric (AMT) data along two profiles on the eastern flank of the Snake Range to refine understanding of the subsurface geology. Line 1 was collected along Baker Creek, was approximately 6.7-km long, and recorded subsurface geologic conditions to approximately 800 m deep. Line 2, collected farther to the southeast in the vicinity of Kious Spring, was 2.8-km long, and imaged to depths of approximately 600 m. The two AMT lines are similar in their electrical response and are interpreted to show generally similar subsurface geologic conditions. The geophysical response seen on both lines may be described by three

general domains of electrical response: 1) a shallow (mostly less than 100-200 m deep) domain of highly variable resistivity, 2) a deep domain characterized by generally high resistivity that gradually declines eastward to lower resistivity with a steeply dipping grain or fabric, and 3) an eastern domain in which the resistivity character changes abruptly at all depths from that in the western domain. The shallow, highly variable domain is interpreted to be the result of a heterogeneous assemblage of Miocene conglomerate and incorporated megabreccia blocks overlying a shallowly eastward-dipping southern Snake Range detachment fault. The deep domain of generally higher resistivity is interpreted as Paleozoic sedimentary rocks (Pole Canyon limestone and Prospect Mountain Quartzite) and Mesozoic and Cenozoic plutonic rocks occurring beneath the detachment surface. The range of resistivity values within this deep domain may result from fracturing adjacent to the detachment, the presence of Paleozoic rock units of variable resistivities that do not crop out in the vicinity of the lines, or both.

The eastern geophysical domain is interpreted to be a section of Miocene strata at depth, overlain by Quaternary alluvial fill. These deposits lie east of a steeply east-dipping normal fault that cuts all units and has about 100 m of east-side-down offset. The surface expressions of the interpreted faults are shown in figure 11 by thick blue dashed lines near stations 10 and 27 on line1 and near station 46 on line 2.



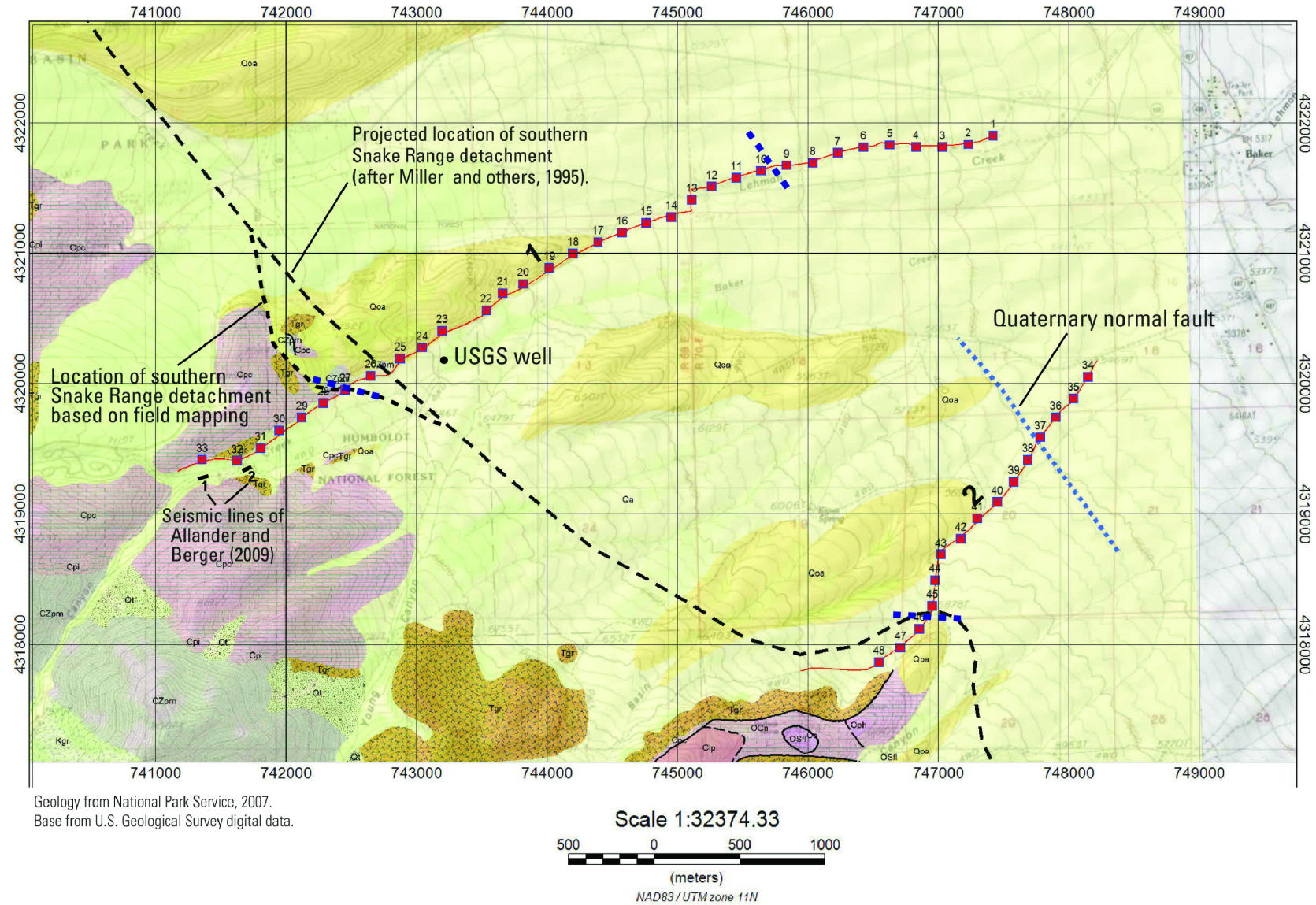


**Figure 11.** Interpreted locations of faults (thick blue dashed lines) based on geophysical results.

## References Cited

- Allander, K.K., and Berger, D.L., 2009, Seismic velocities and thicknesses of alluvial deposits along Baker Creek in the Great Basin National Park, east-central Nevada: U.S. Geological Survey Open-File Report 2009-1174, 14 p.
- Dobrin, M.D., and Savit, C.H., 1988, Introduction to geophysical prospecting (4th ed.): New York, McGraw-Hill, 867 p.
- Eberhart-Phillips, Donna, Stanley, W.D., Rodriguez, B.D., and Lutter, W.J., 1995, Surface seismic and electrical methods to detect fluids related to faulting: Journal of Geophysical Research, v. 100, no. B7, p. 12919-12936.
- Egbert, G.D., 1997, Robust multiple station magnetotelluric data processing: Geophysics Journal International, v. 130, p. 475–496.
- Elliott, P.W., Beck, D.A., and Prudic, D.E., 2006, Characterization of surface-water resources in the Great Basin National Park and their susceptibility to ground-water withdrawals in adjacent valleys, White Pine County, Nevada: U.S. Geological Survey Scientific Investigations Report 2005-5099, 156 p., accessed October 27, 2009, at <http://pubs.usgs.gov/sir/2006/5099/>.
- Gamble, T.D., Goubau, W.M., and Clarke, J., 1979, Error analysis for remote reference magnetotellurics: Geophysics, v. 44, no. 5, p. 959–968.
- Geometrics, Inc., 2007, STRATAGEM 26716-01 Rev. F, Operation manual for systems running IMAGEM ver. 2.19: Geometrics, Inc., 45 p.
- Geotools, 1998, Geotools MT User's Guide: Geotools Corporation, a division of AOA Geophysics, 450 p.



- Grier, S.P., 1984, Alluvial fan and lacustrine carbonate deposits in the Snake Range: A study of Tertiary sedimentation and associated tectonism: Stanford, Stanford University, Master's thesis, 61 p.
- Keller, G.V., 1987, Rock and mineral properties, *in* Nabighian, M.N., ed., Electromagnetic methods in applied geophysics theory: Tulsa, Okla., Society of Exploration Geophysicists, v. 1, p. 13-51.
- Keller, G.V., 1989, Electrical properties, *in* Carmichael, R.S., ed., Practical handbook of physical properties of rocks and minerals: Boca Raton, Fla., CRC Press, p. 359-427.
- Lee, D.E., Kistler, R.W., Friedman, I., and Van Loenen, R.E., 1981, Two-mica granites of northeastern Nevada: Journal of Geophysical Research, v. 86, p. 10607-10616.
- Mackie, R.L., Rieven, S., and Rodi, W., 1997, Users manual and software documentation for two-dimensional inversion of magnetotelluric data: GEOTOOLS User's Guide RLM2DI Supplement, 10 p.
- McGrew, A.J., 1993, The origin and evolution of the southern Snake Range décollement, east-central Nevada: Tectonics, v. 12, p. 21–34.
- McGrew, A.J., Miller, E.L., and Brown, J.L. (compiler), 1995, Geologic map of Kious Spring and Garrison 7.5' quadrangles, White Pine County, Nevada and Millard County, Utah: U.S. Geological Survey Open-File Report 95-10, scale 1:24,000.
- McPhee, D.K., Chuchel, B.A., and Pellerin, L., 2007, Audiomagnetotelluric data and two dimensional models from Spring, Snake, and Three Lakes Valleys, Nevada: U.S. Geological Survey Open-File Report 2007-1181, 47 p.

- Miller, E.L., Gans, P.B., Wright, J.E., and J.F. Sutter, 1989, Metamorphic history of the east-central Basin and Range province -- Tectonic setting and relationship to magmatism, *in* Ernst, W.G., ed., *Metamorphism and Crustal Evolution, Western Conterminous United States, Rubey Volume VII*: Englewood Cliffs, New Jersey, Prentice-Hall, p. 649-682.
- Miller, E.L., Grier, S.P., and Brown, J.L. (compiler), 1995, Geologic map of the Lehman Caves quadrangle, White Pine County, Nevada: U.S. Geological Survey Geologic Quadrangle Map 1758, scale 1:24,000.
- Miller, E.L., Dumitru, T.A., Brown, R.W., and Gans, P.B., 1999, Rapid Miocene slip on the Snake Range décollement, Geological Society of America Bulletin, v. 111, p. 886-905.
- National Park Service, 2007, Digital geologic map of Great Basin National Park and vicinity, Nevada: online digital geologic database, accessed October 27, 2009, at <http://science.nature.nps.gov/nrddata/datastore.cfm?ID=44849>.
- Nelson, P.H., and Anderson, L.A., 1992, Physical properties of ash flow tuff from Yucca Mountain, Nevada: Journal of Geophysical Research, v. 97, no. B5, p. 823–6841.
- Palacky, G.J., 1987, Resistivity characteristics of geologic targets, *in* Nabighian, M.N., ed., Electromagnetic methods in applied geophysics theory: Tulsa, Okla., Society of Exploration Geophysicists, v. 1, p. 53-129.
- Reddy, I.K., Rankin, D., and Phillips, R.J., 1977, Three-dimensional modeling in magnetotelluric and magnetic variational sounding: Geophysics Journal of the Royal Astronomical Society, v. 51, p. 313–325.
- Rodi, W., and Mackie, R.L., 2001, Nonlinear conjugate gradients algorithm for 2–D magnetotelluric inversion: Geophysics, v. 66, no. 1, p. 174–187.

- Sternberg, B.K., Washburne, J.C., and Pellerin, L., 1988, Correction for the static shift in magnetotellurics using transient electromagnetic soundings: *Geophysics*, v. 53, p. 1459–1468.
- Telford, W.M., Geldart, L.P., Sherriff, R.E., and Keys, D.A., 1976, *Applied Geophysics*: Cambridge University Press, Cambridge, England, 770 p.
- U.S. Geological Survey and Nevada Bureau of Mines and Geology, 2006, Quaternary fault and fold database for the United States, accessed October 27, 2009, from USGS web site: <http://earthquakes.usgs.gov/regional/qfaults/>.
- Vozoff, K., 1972, The magnetotelluric method in the exploration of sedimentary basins: *Geophysics*, v. 37, p. 980–141.
- Vozoff, K., 1991, The magnetotelluric method, *in* Nabighian, M.N., ed., *Electromagnetic methods in applied geophysics*: Tulsa, Oklahoma, Society of Exploration Geophysicists, v. 2, part. B, p. 641-711.
- Wannamaker, P.E., 1983, Resistivity structure of the northern Basin and Range, *in* Eaton, G. P., Ed., *The role of heat in development of energy and mineral resources in the northern Basin and Range Province*: Geothermal Resources Council, Special Report no. 13, p. 345 – 361.
- Wannamaker, P.E., Hohmann, G.W., and Ward, S.H., 1984, Magnetotelluric responses of three-dimensional bodies in layered earths: *Geophysics*, v. 49, no. 9, p. 1517–1533.
- Wannamaker, P.E., Stodt, J.A., and Rijo, L., 1987, PW2D— Finite element program for solution of magnetotelluric responses of two-dimensional earth resistivity structure, (User documentation): Earth Science Laboratory, University of Utah Research Institute, Salt Lake City, 40 p.
- Watt, J.T., and Ponce, D.A., 2007, Geophysical framework investigations influencing ground-water resources in east-central Nevada and west-central Utah, *with a section on* Geologic and

geophysical basin-by-basin descriptions by Wallace, A.R., Watt, J.T., and Ponce, D.A.: U.S. Geological Survey Open-File Report 2007-1163, 40 p., 2 plates, scale 1:750,000.

Whitebread, D.H., 1969, Geologic map of the Wheeler Peak and Garrison quadrangles, Nevada and Utah: U.S. Geological Survey Miscellaneous Geologic Investigations Map I-578, scale 1:48,000.

## APPENDIX 1 – Audio-Magnetotelluric Data and Models

### Line 1

Figure A1-1 - Figure A1-20	TM mode forward and inversion models, apparent resistivities, and phases.
Figure A1-21 - Figure A1-40	TE mode forward and inversion models, apparent resistivities, and phases.
Figure A1-41 - Figure A1-50	Combined TM and TE modes inversion models, apparent resistivities, and phases.
Figure A1-51 – Figure A1-83	Line 1 impedance skew data.
Figure A1-84 – Figure A1-116	Line 1 impedance strike data.
Figure A1-117 – Figure A1-181	Line 1 polar impedance data.

### Line 2

Figure A1-182 - Figure A1-187	TM mode inversion models, apparent resistivities, and phases.
Figure A1-188 - Figure A1-199	TE mode forward and inversion models, apparent resistivities, and phases.
Figure A1-200 - Figure A1-205	Combined TM and TE modes inversion models, apparent resistivities, and phases.
Figure A1-206 – Figure A1-220	Line 2 impedance skew data.
Figure A1-221 – Figure A1-233	Line 2 impedance strike data.
Figure A1-234 – Figure A1-263	Line 2 polar impedance data.

### NOTES:

1. For all impedance apparent resistivity and phase plots the yellow squares are measured TM mode, the orange squares are calculated TM mode, the black circles are measured TE mode, and the green circles are calculated TE mode.
2. For all the polar plot figures the yellowish-green line drawing is the  $Z_{xy}$  component and the orange line in the center is the  $Z_{xx}$  component. The black line in the polar plot diagrams originating from  $Z_{xx}$  in the center is the impedance strike rotation angle.

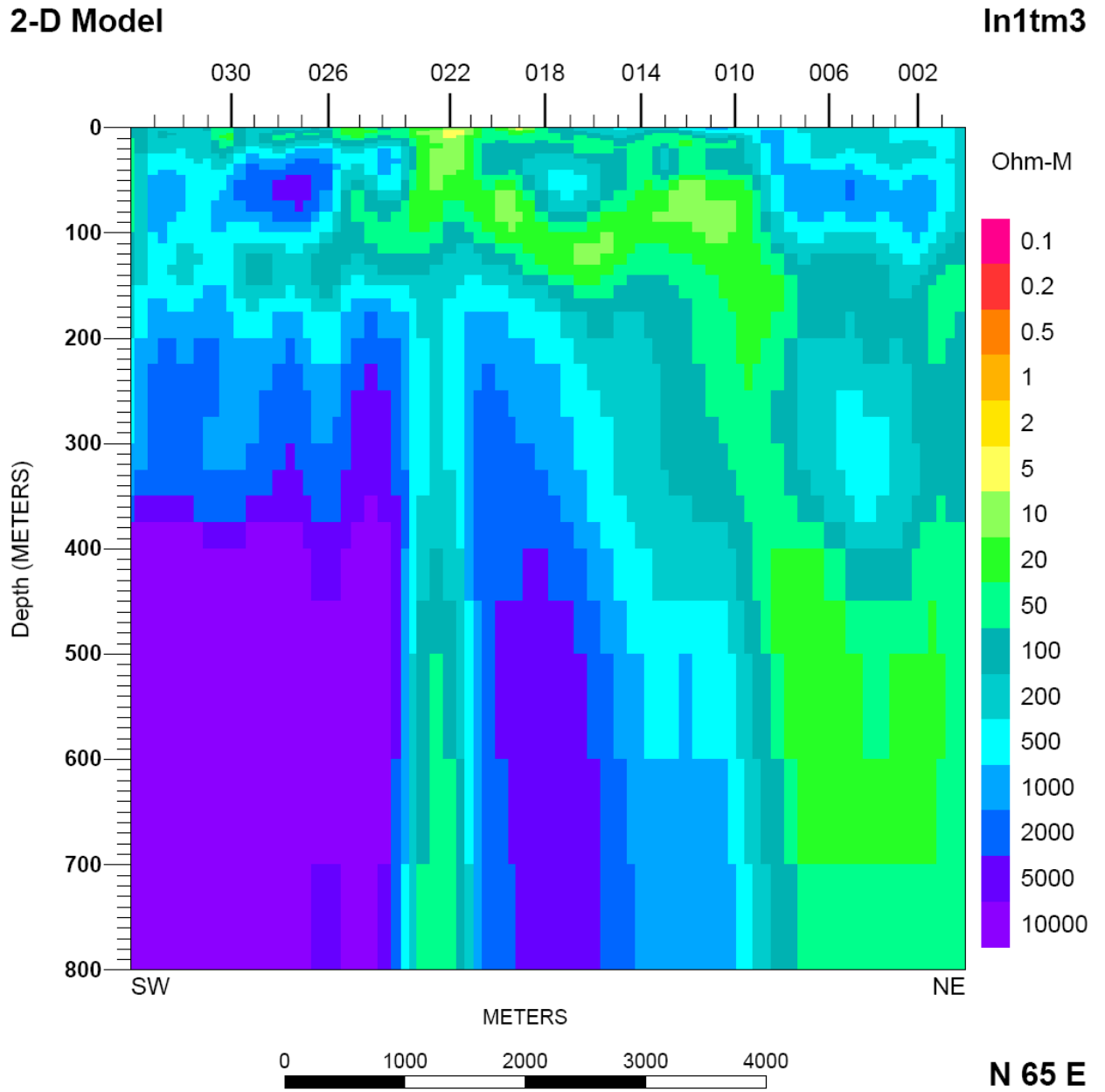


**Figure A1-1.** Line 1 2-D resistivity inversion modeling result for TM mode without model mesh. Tic marks at top of model are projected AMT station locations. Vertical exaggeration is 8.3:1.

## 2-D Model

In1tm3

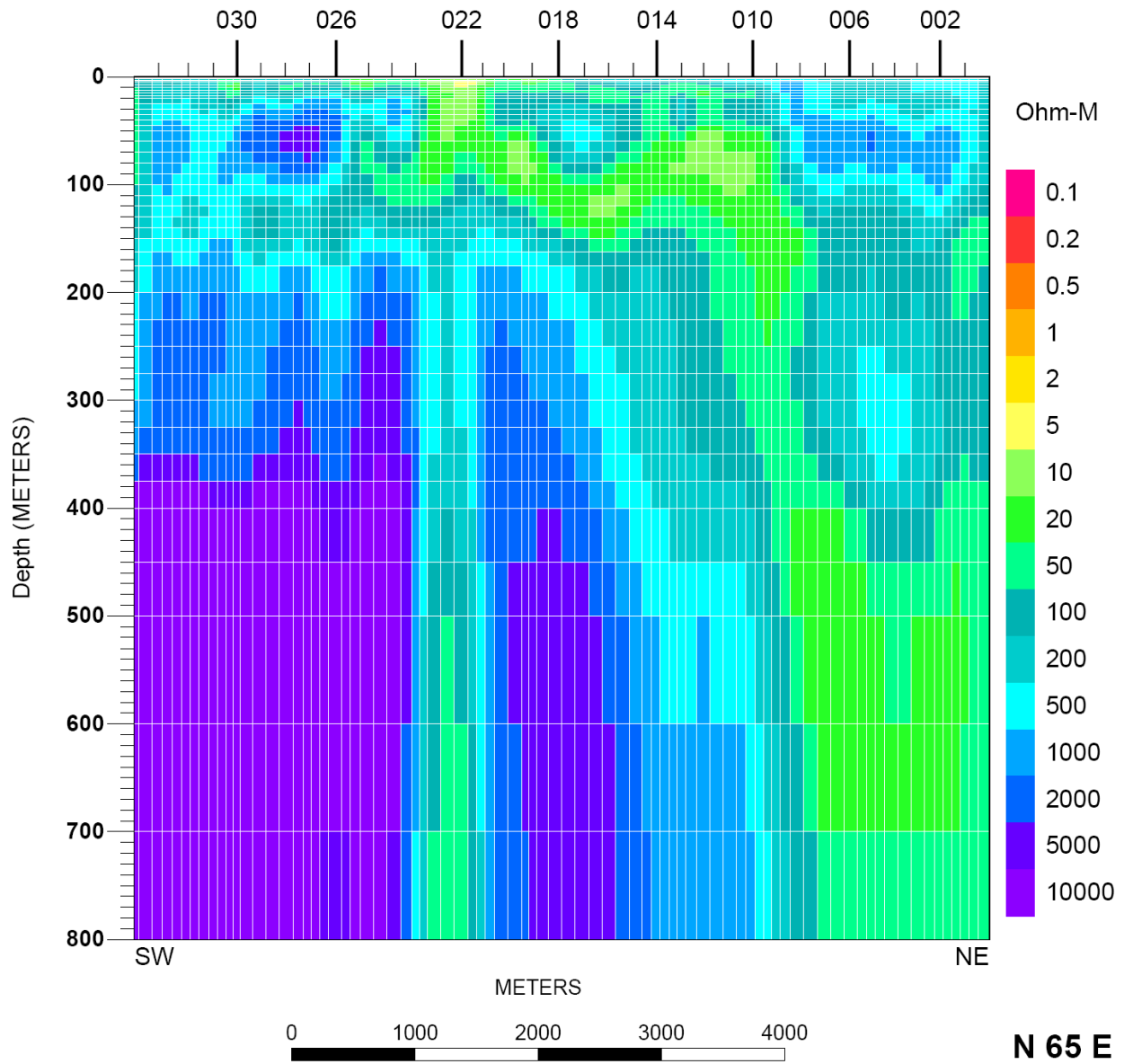


**Figure A1-2.** Line 1 2-D inversion modeling result for TM mode with white model mesh lines. Tic marks at top of model are projected AMT station locations. Vertical exaggeration is 8.3:1.

## Appendix 1 – Audio-Magnetotelluric Data and Models

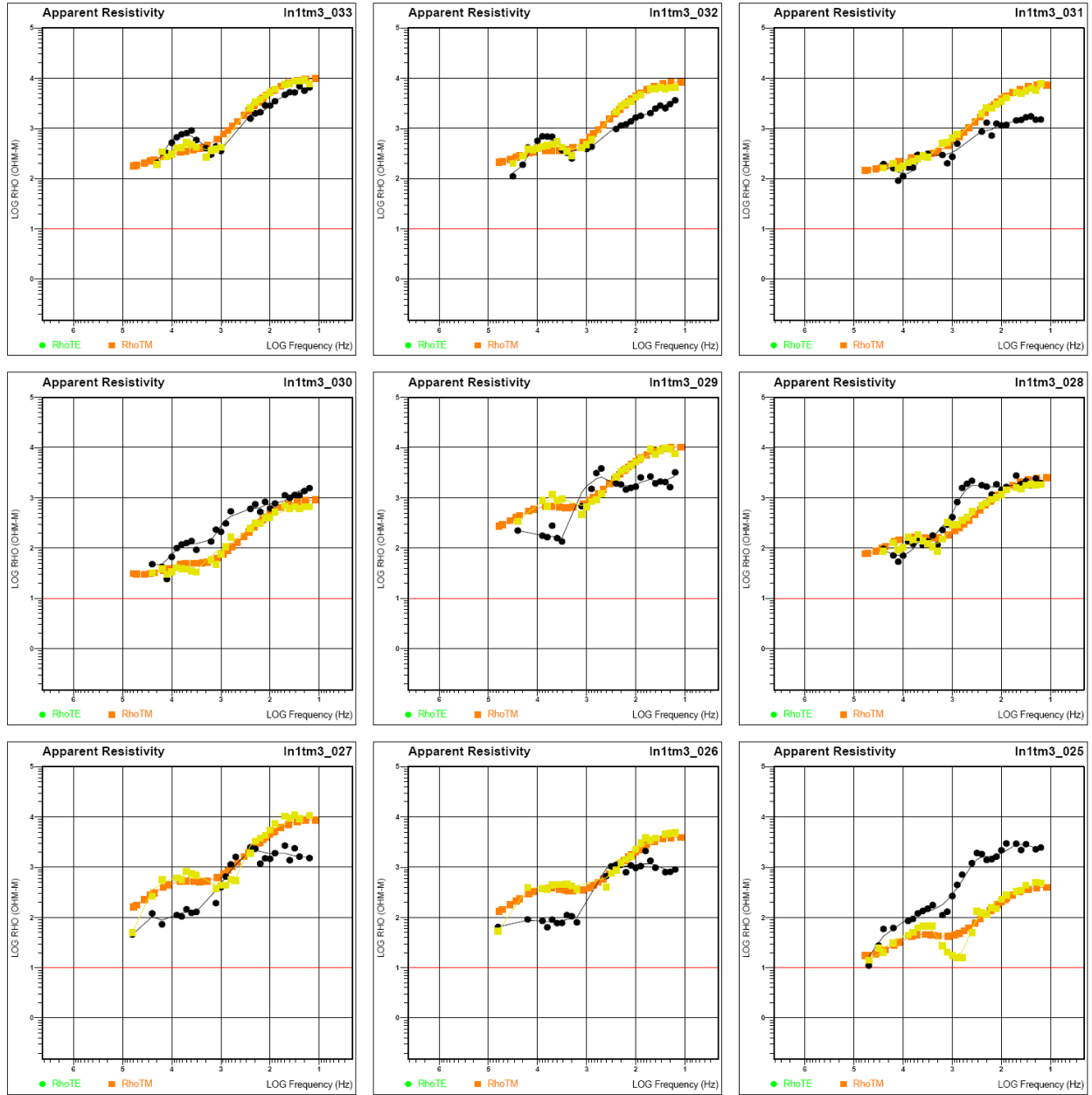


Figure A1-3. Line 1 impedance apparent resistivity data for TM mode inversion model, sites 25 - 33.



## Appendix 1 – Audio-Magnetotelluric Data and Models

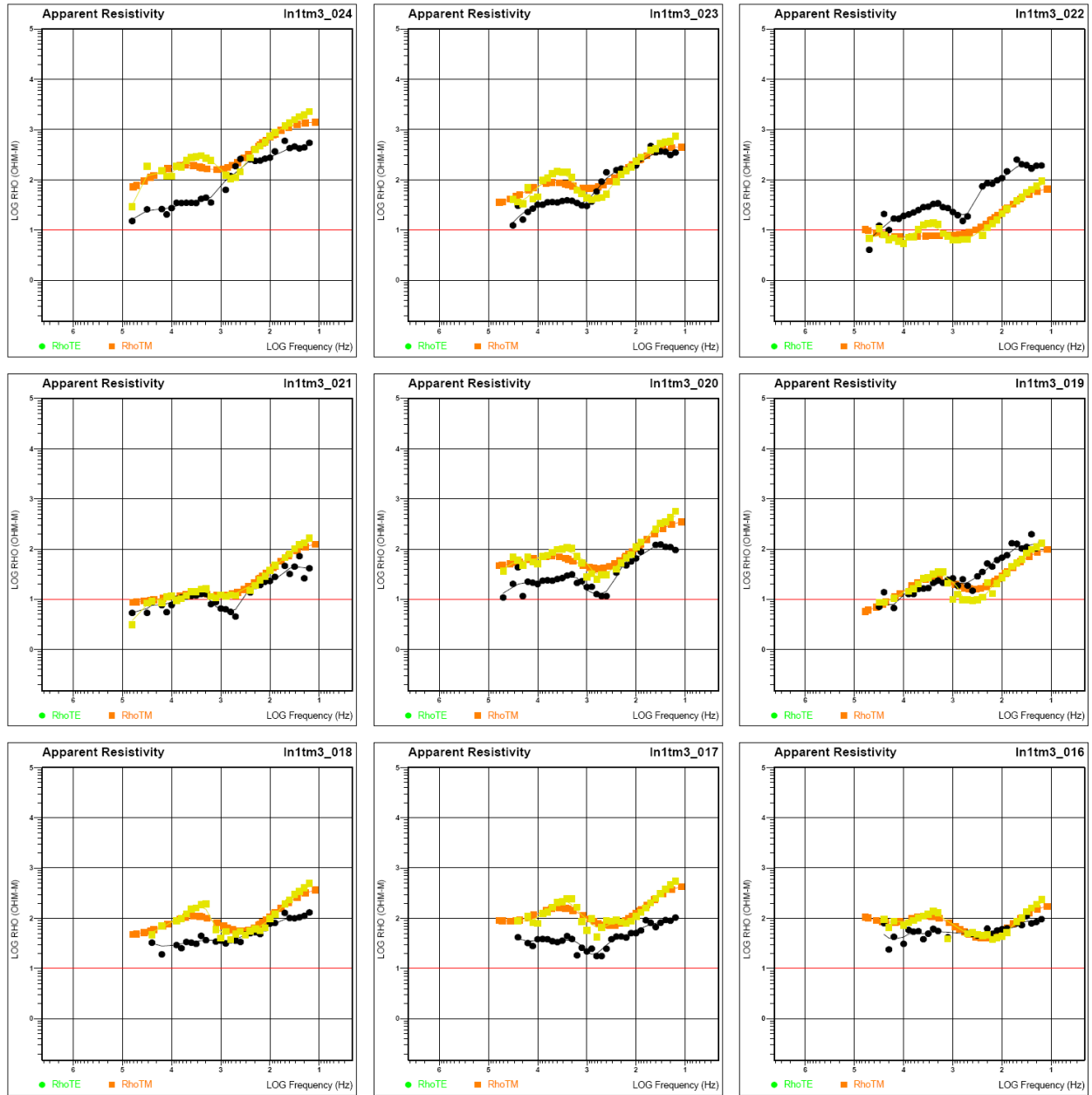
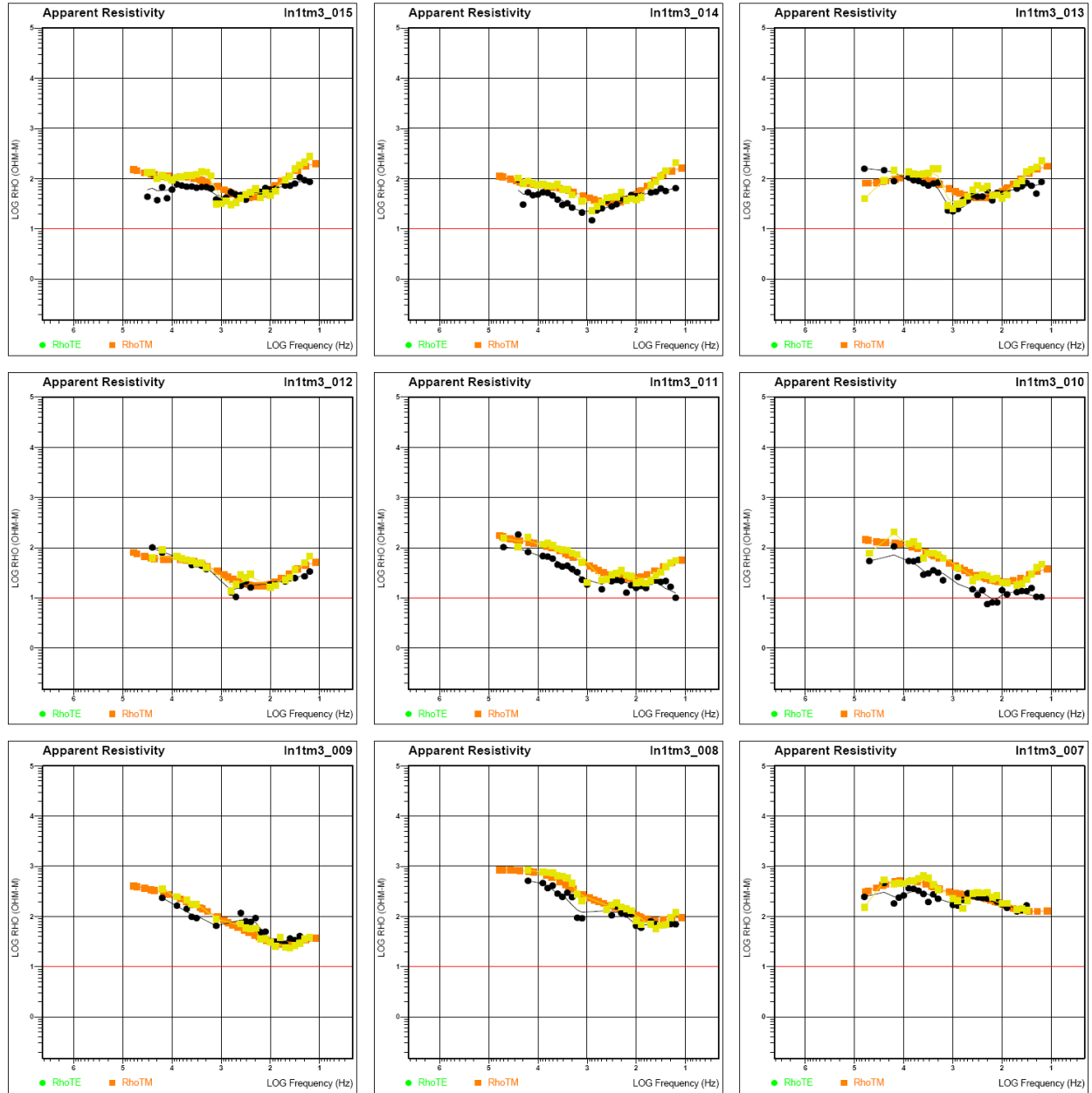


Figure A1-4. Line 1 impedance apparent resistivity data for TM mode inversion model, sites 16 – 24.

## Appendix 1 – Audio-Magnetotelluric Data and Models



**Figure A1-5.** Line 1 impedance apparent resistivity data for TM mode inversion model, sites 7 – 15.

## Appendix 1 – Audio-Magnetotelluric Data and Models

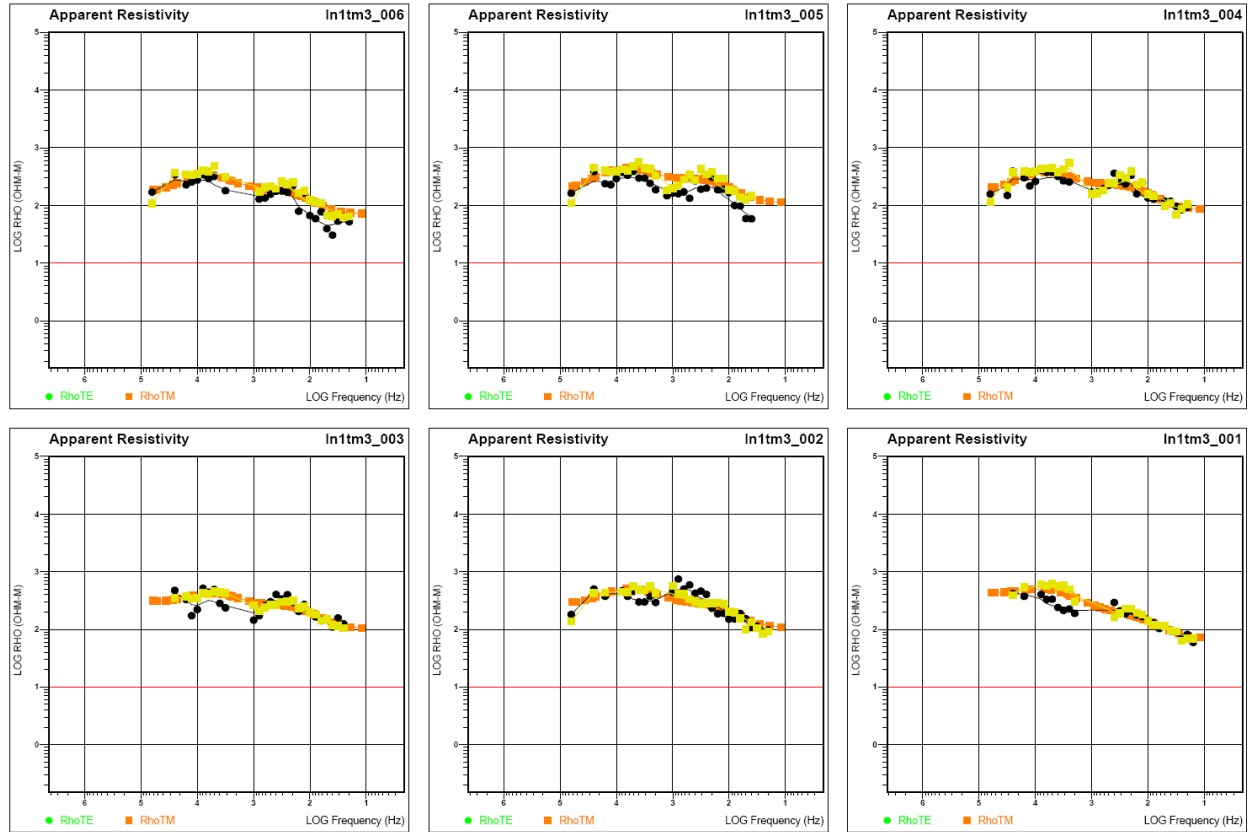
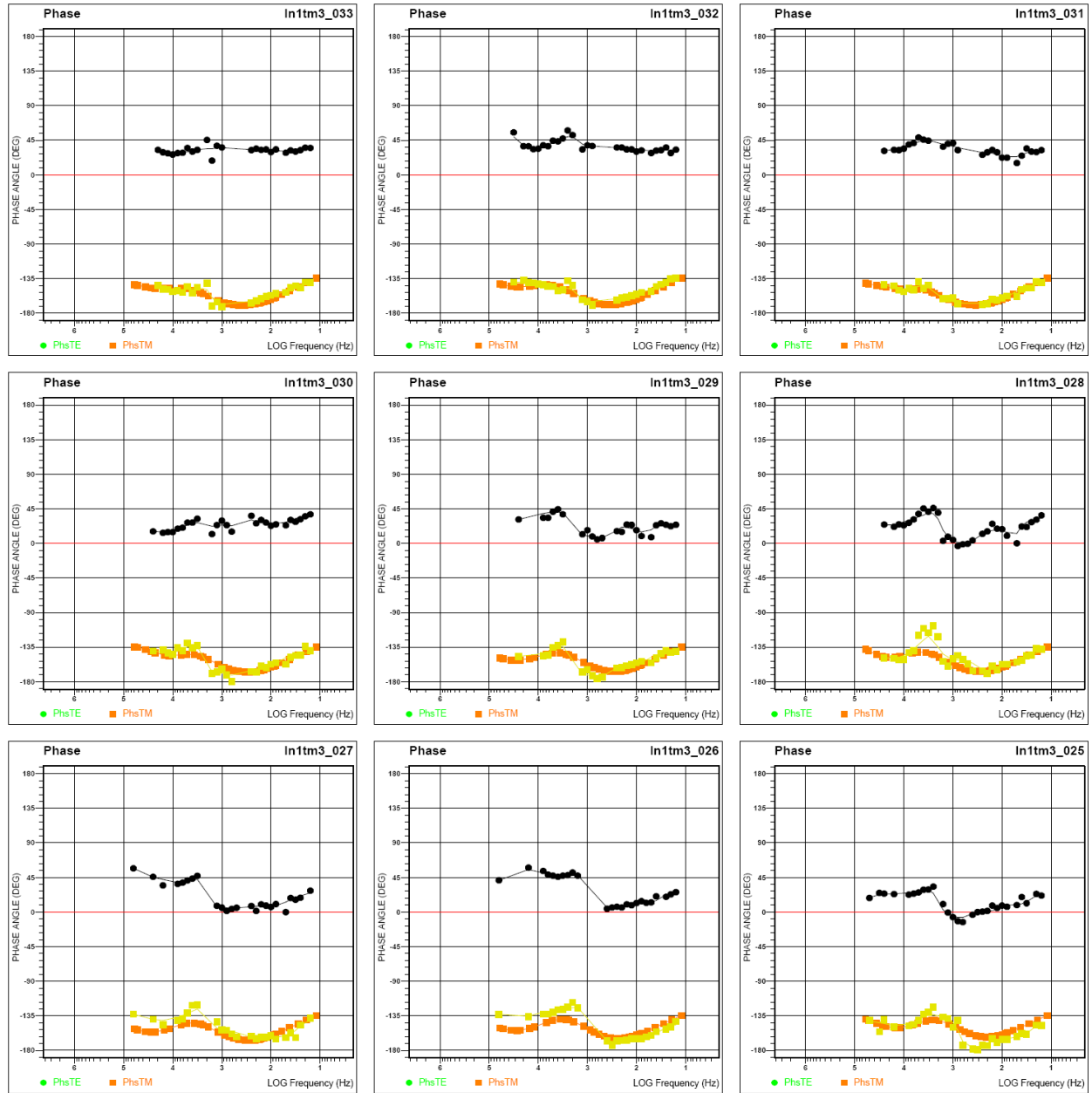


Figure A1-6. Line 1 impedance apparent resistivity data for TM mode inversion model, sites 1 – 6.

## Appendix 1 – Audio-Magnetotelluric Data and Models



**Figure A1-7.** Line 1 impedance phase data for TM mode inversion model, sites 25 – 33.

## Appendix 1 – Audio-Magnetotelluric Data and Models

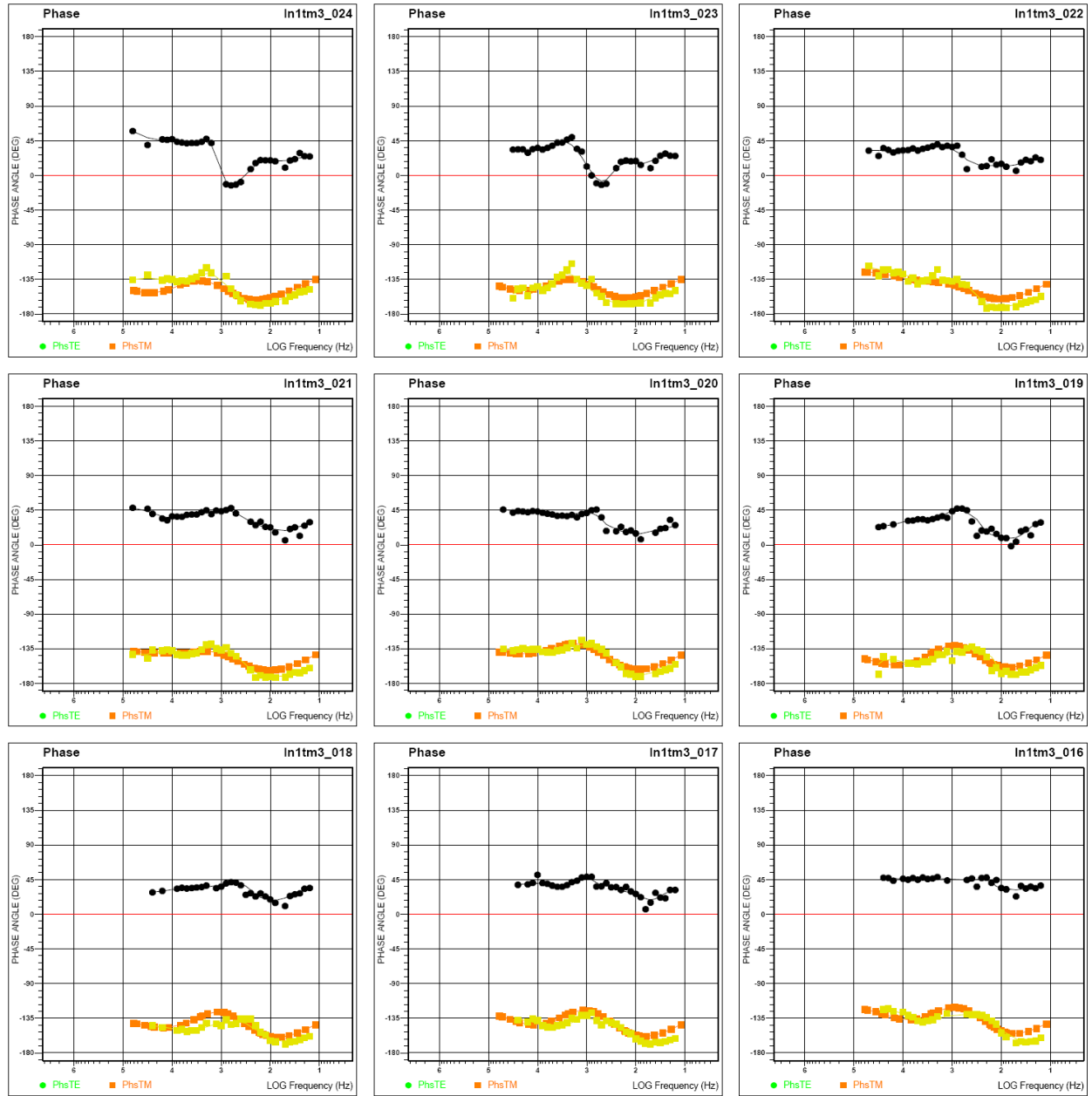
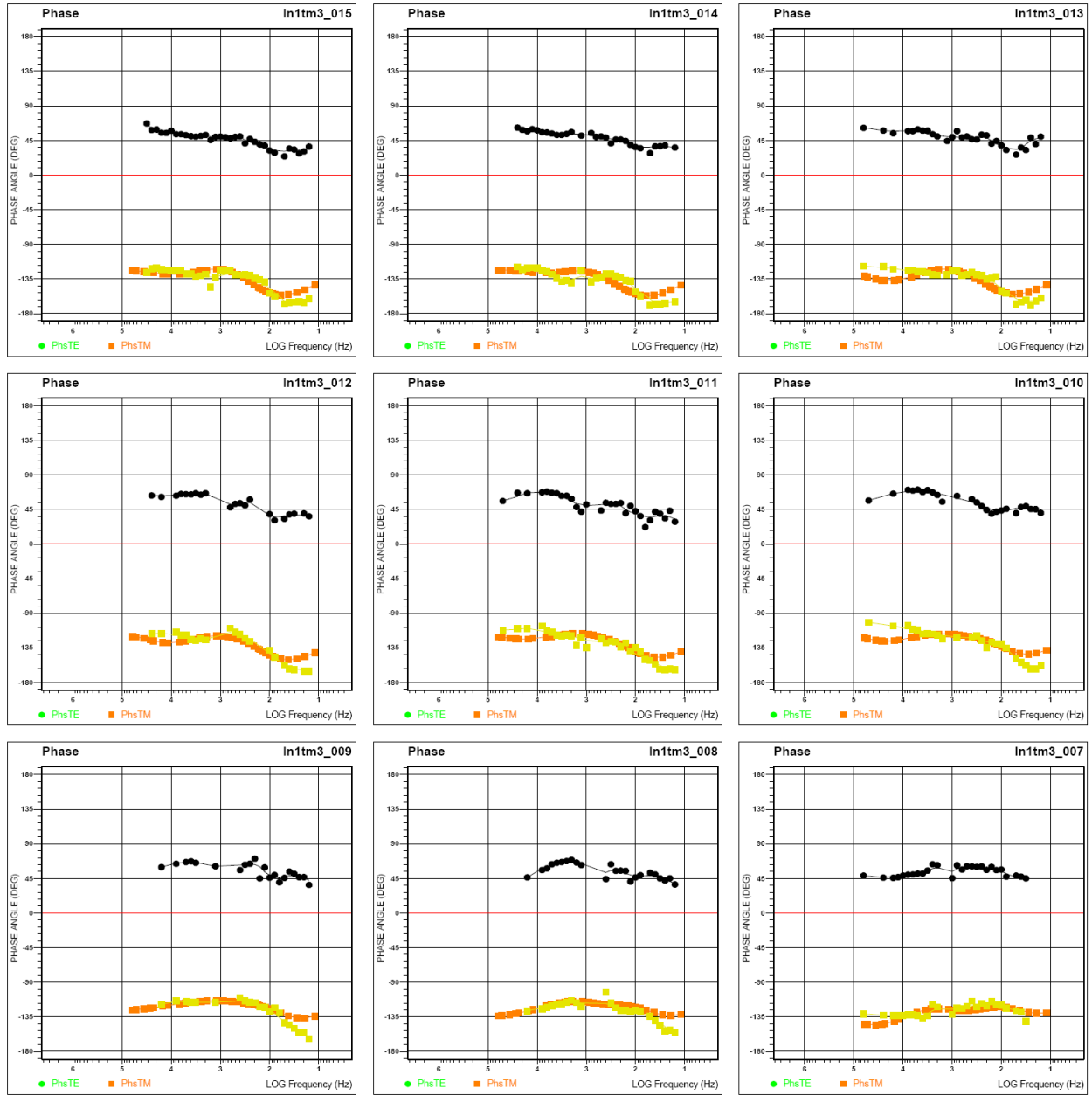


Figure A1-8. Line 1 impedance phase data for TM mode inversion model, sites 16 – 24.

## Appendix 1 – Audio-Magnetotelluric Data and Models



**Figure A1-9.** Line 1 impedance phase data for TM mode inversion model, sites 7 – 15.

## Appendix 1 – Audio-Magnetotelluric Data and Models

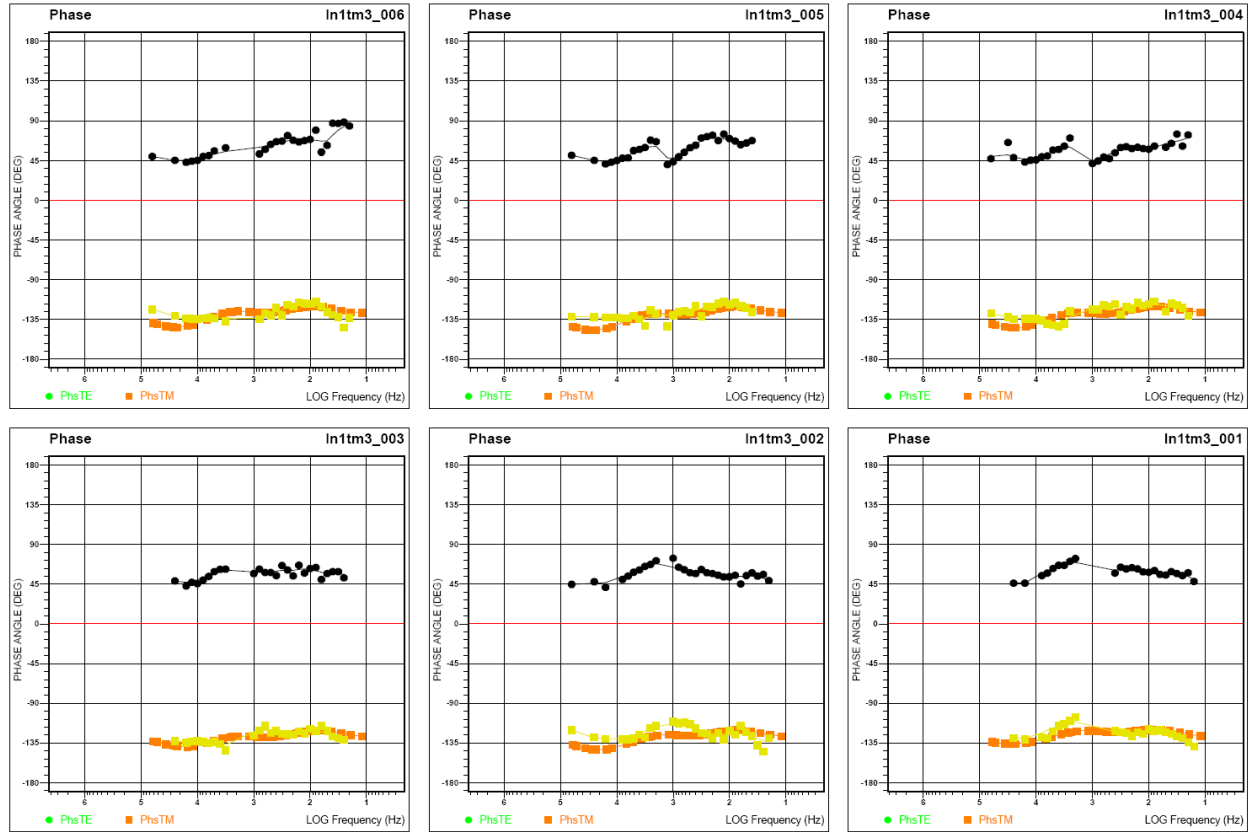


**Figure A1-10.** Line 1 impedance phase data for TM mode inversion model, sites 1 – 6.

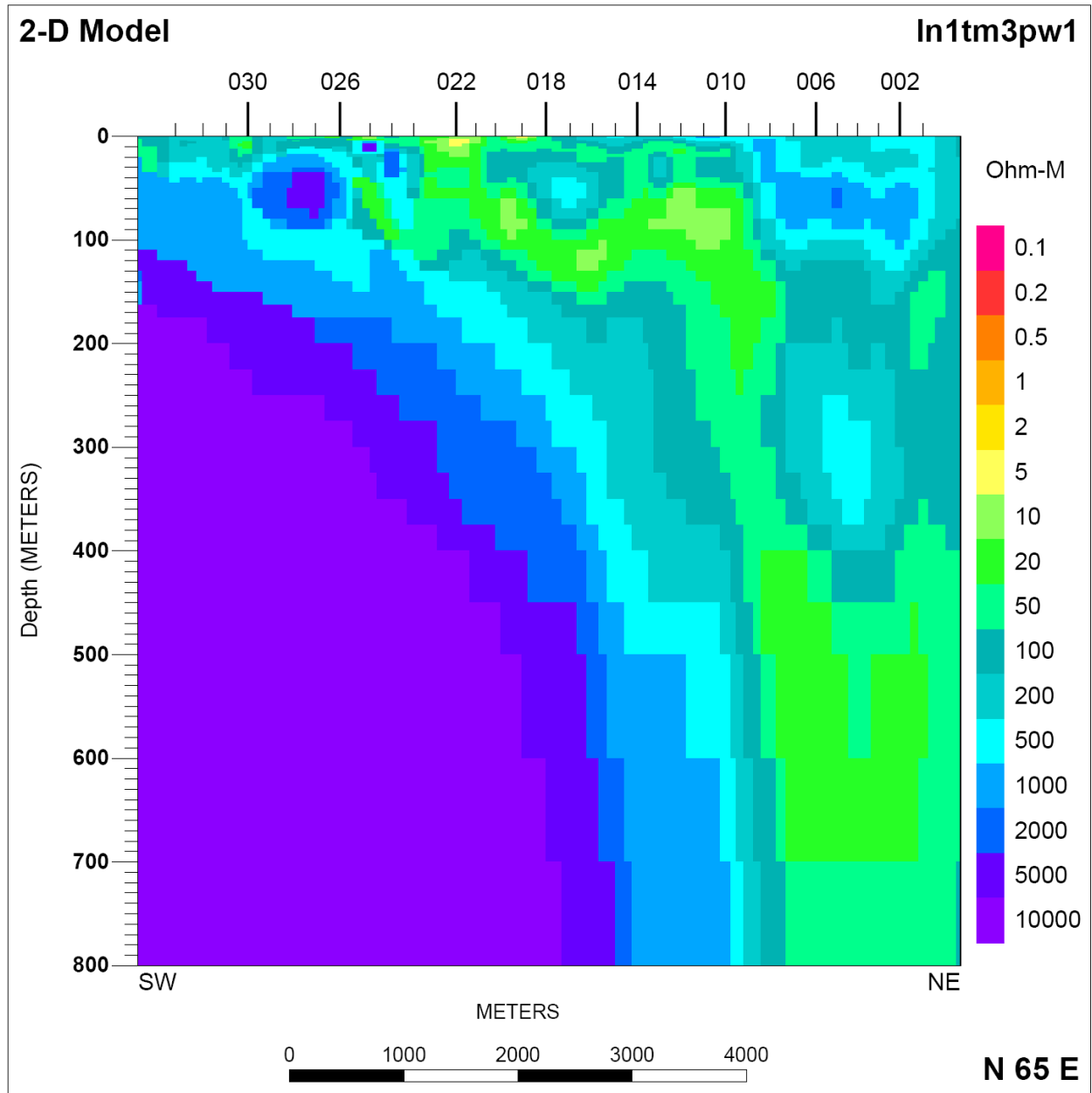


**Figure A1-11.** Line 1 2-D forward modeling result for TM mode inversion result without model mesh lines. This forward model is built from inversion model ln1tm3 in figures A1-1 and A1-2. Tic marks at top of model are projected AMT station locations. Vertical exaggeration is 8.3:1.



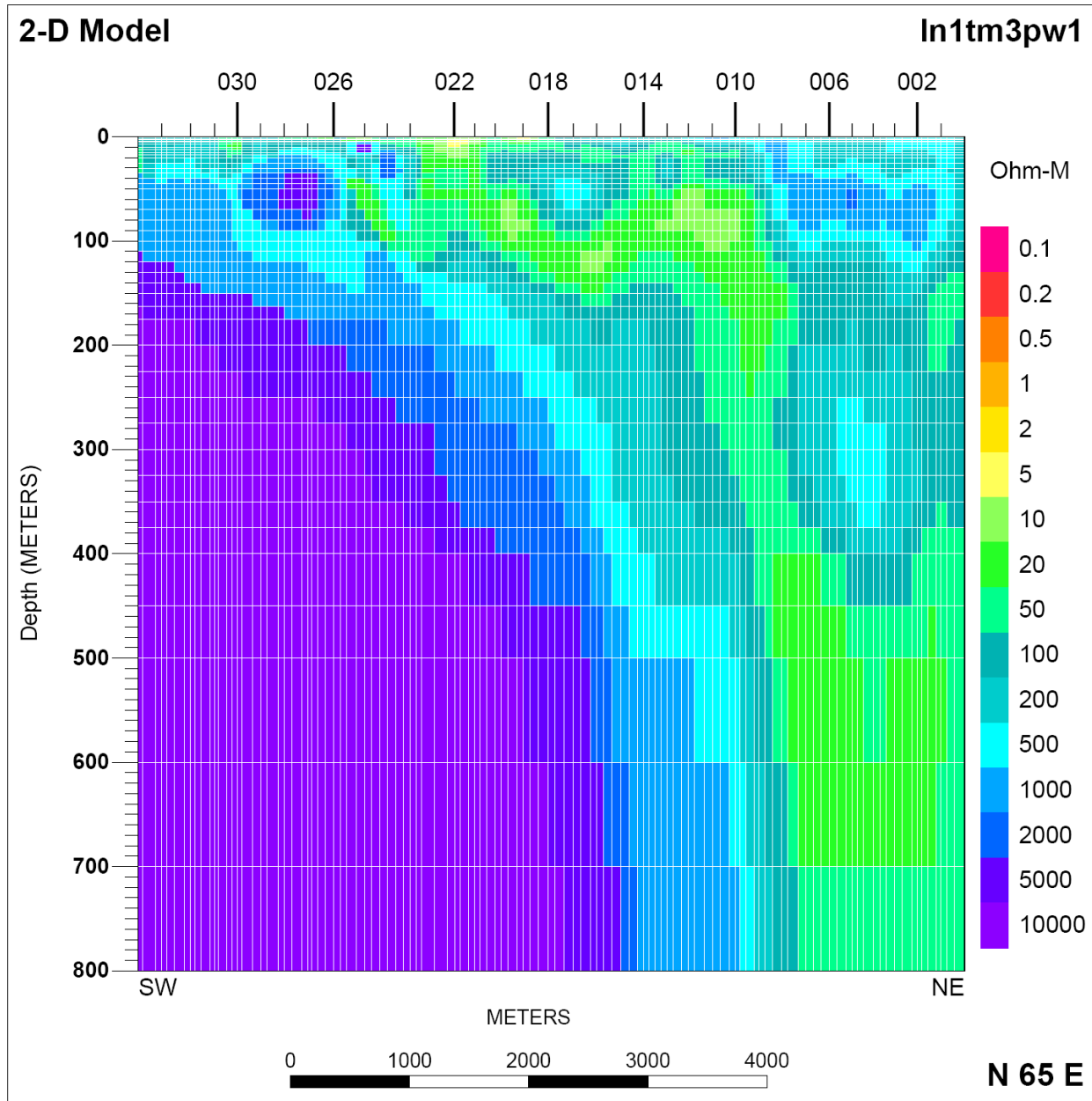


**Figure A1-12.** Line 1 2-D forward modeling result for TM mode with white model mesh lines. Tic marks at top of model are projected AMT station locations. Vertical exaggeration is 8.3:1.

## Appendix 1 – Audio-Magnetotelluric Data and Models

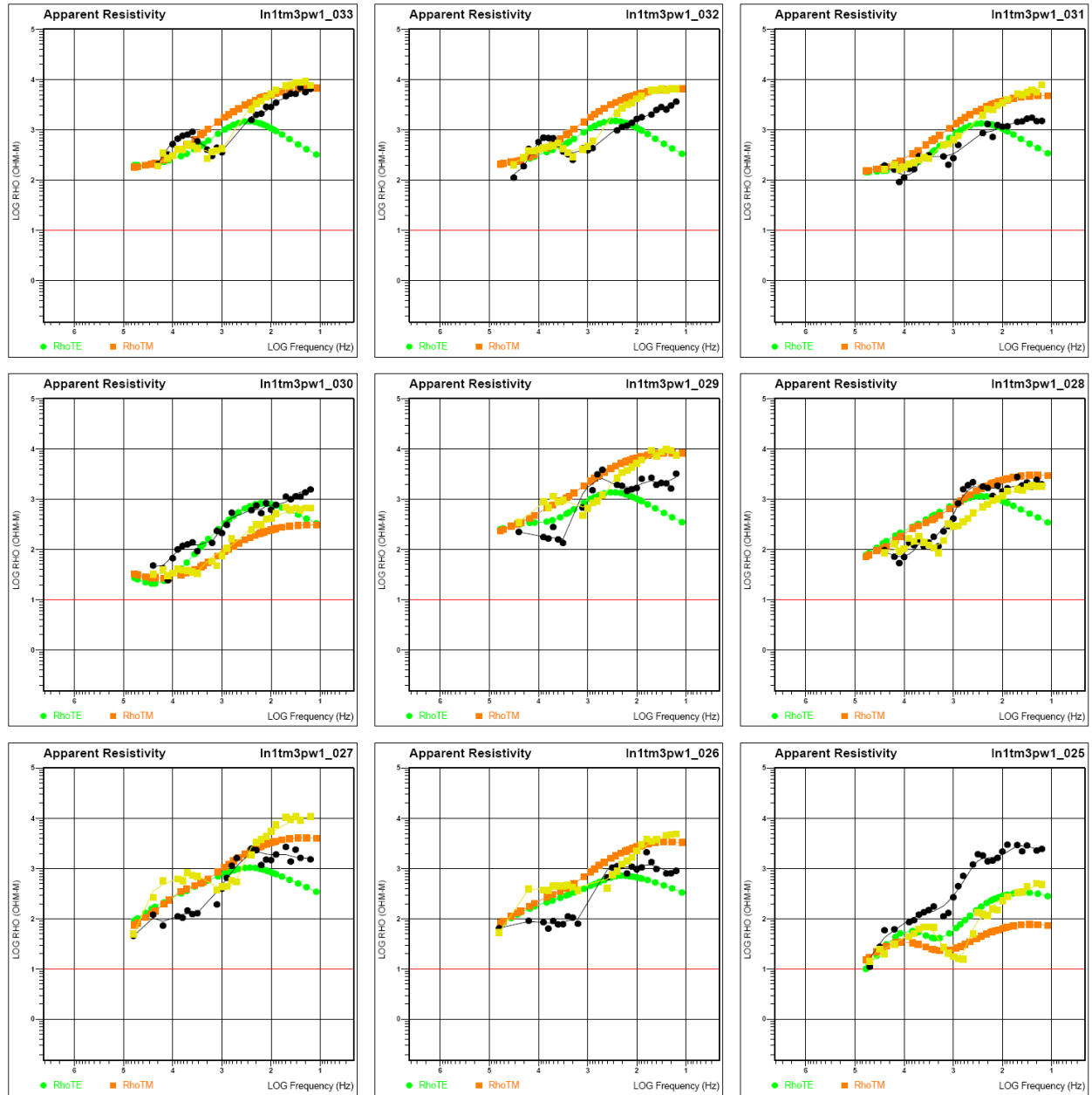


Figure A1-13. Line 1 impedance apparent resistivity data for TM mode forward model, sites 25 - 33.

## Appendix 1 – Audio-Magnetotelluric Data and Models

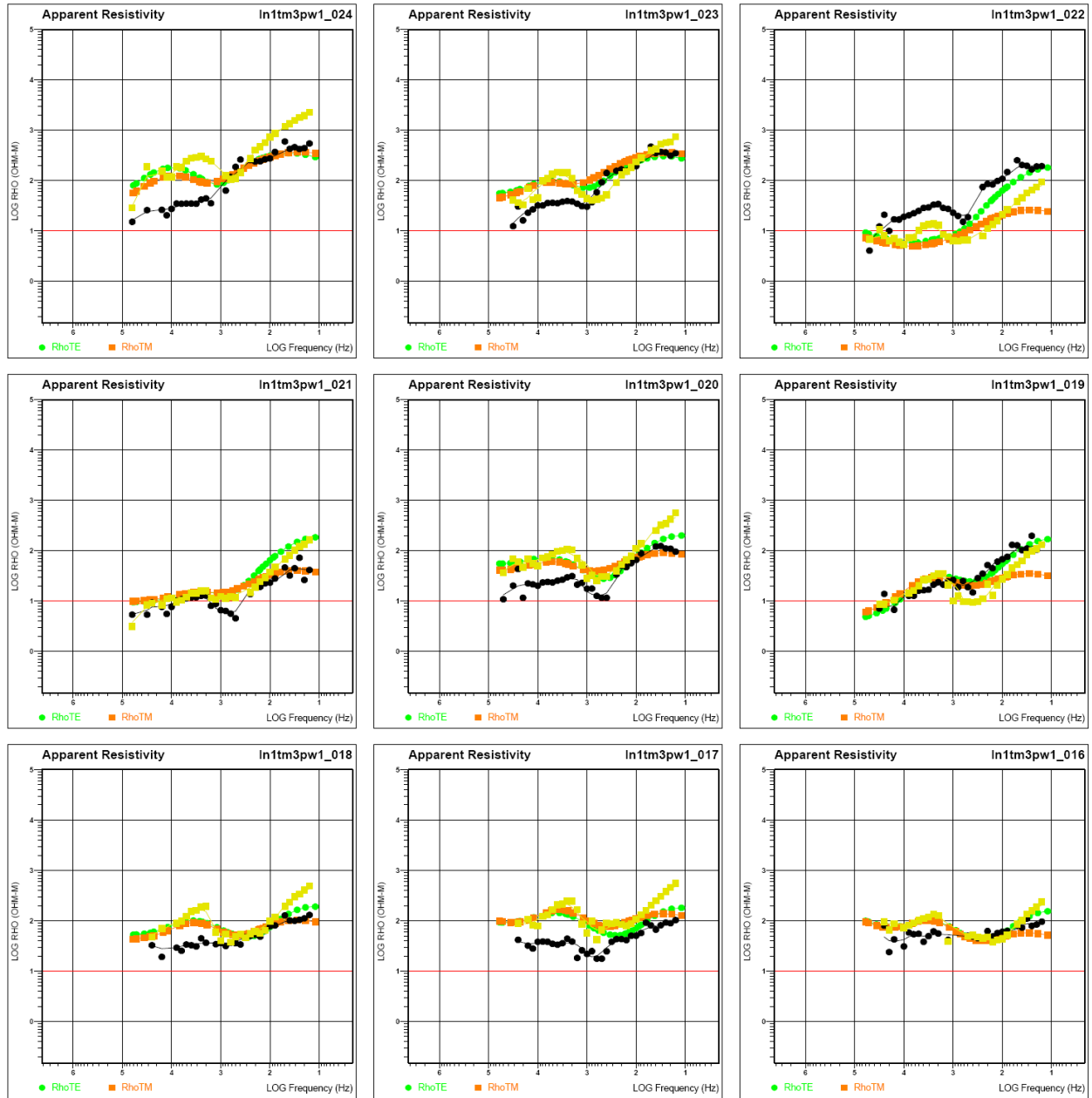


Figure A1-14. Line 1 impedance apparent resistivity data for TM mode forward model, sites 16 - 24.

## Appendix 1 – Audio-Magnetotelluric Data and Models

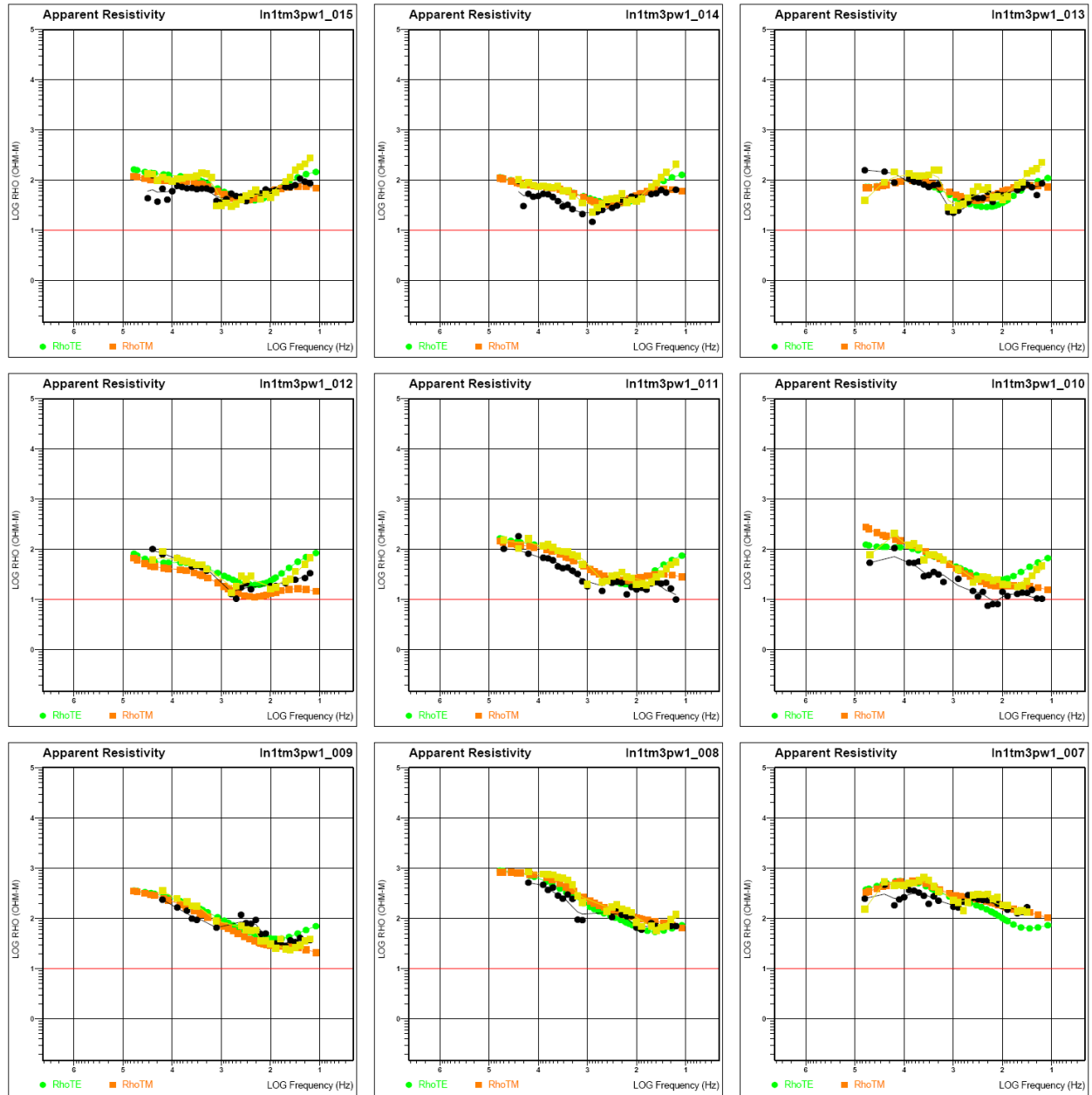
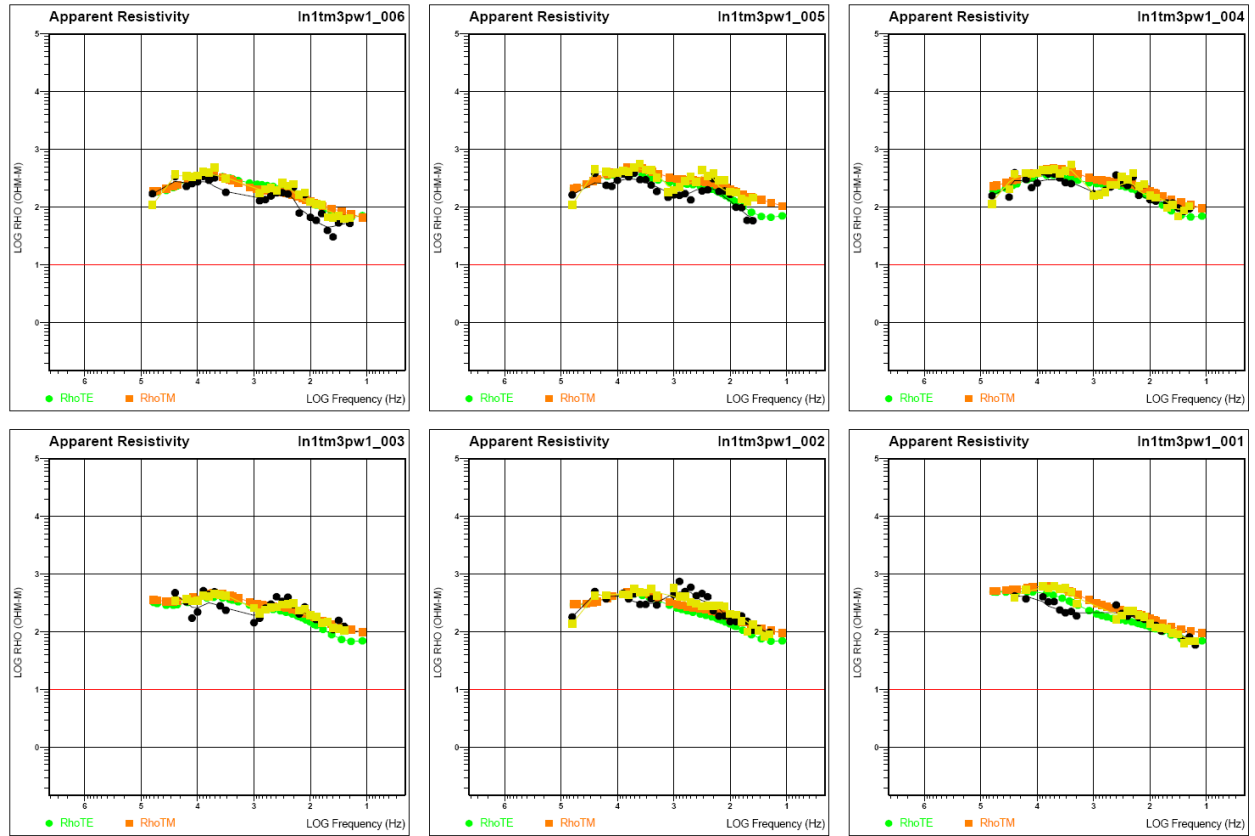


Figure A1-15. Line 1 impedance apparent resistivity data for TM mode forward model, sites 7 – 15.

## Appendix 1 – Audio-Magnetotelluric Data and Models



**Figure A1-16.** Line 1 impedance apparent resistivity data for TM mode forward model, sites 1 – 6.

## Appendix 1 – Audio-Magnetotelluric Data and Models

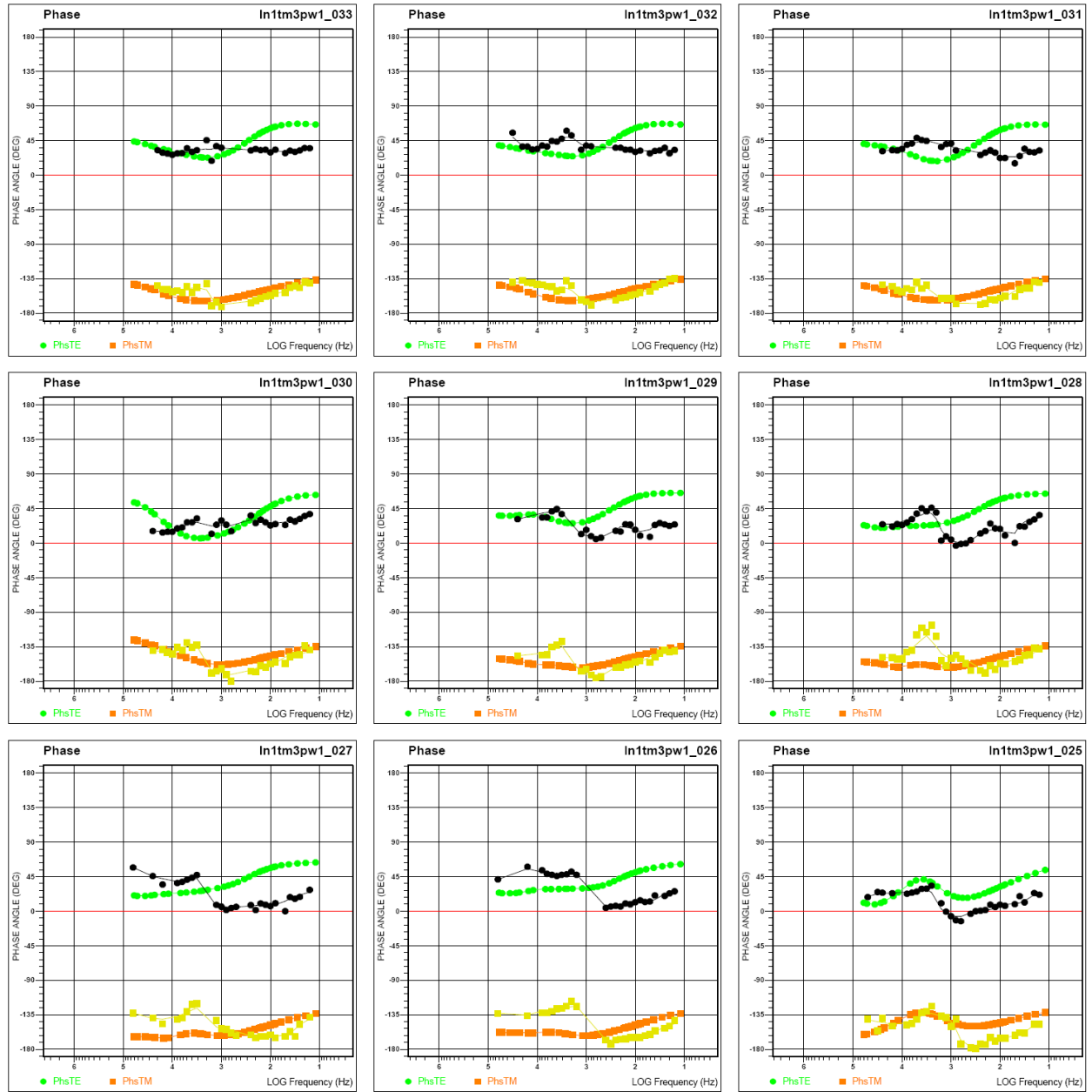


Figure A1-17. Line 1 impedance phase data for TM mode forward model, sites 25 – 33.

## Appendix 1 – Audio-Magnetotelluric Data and Models

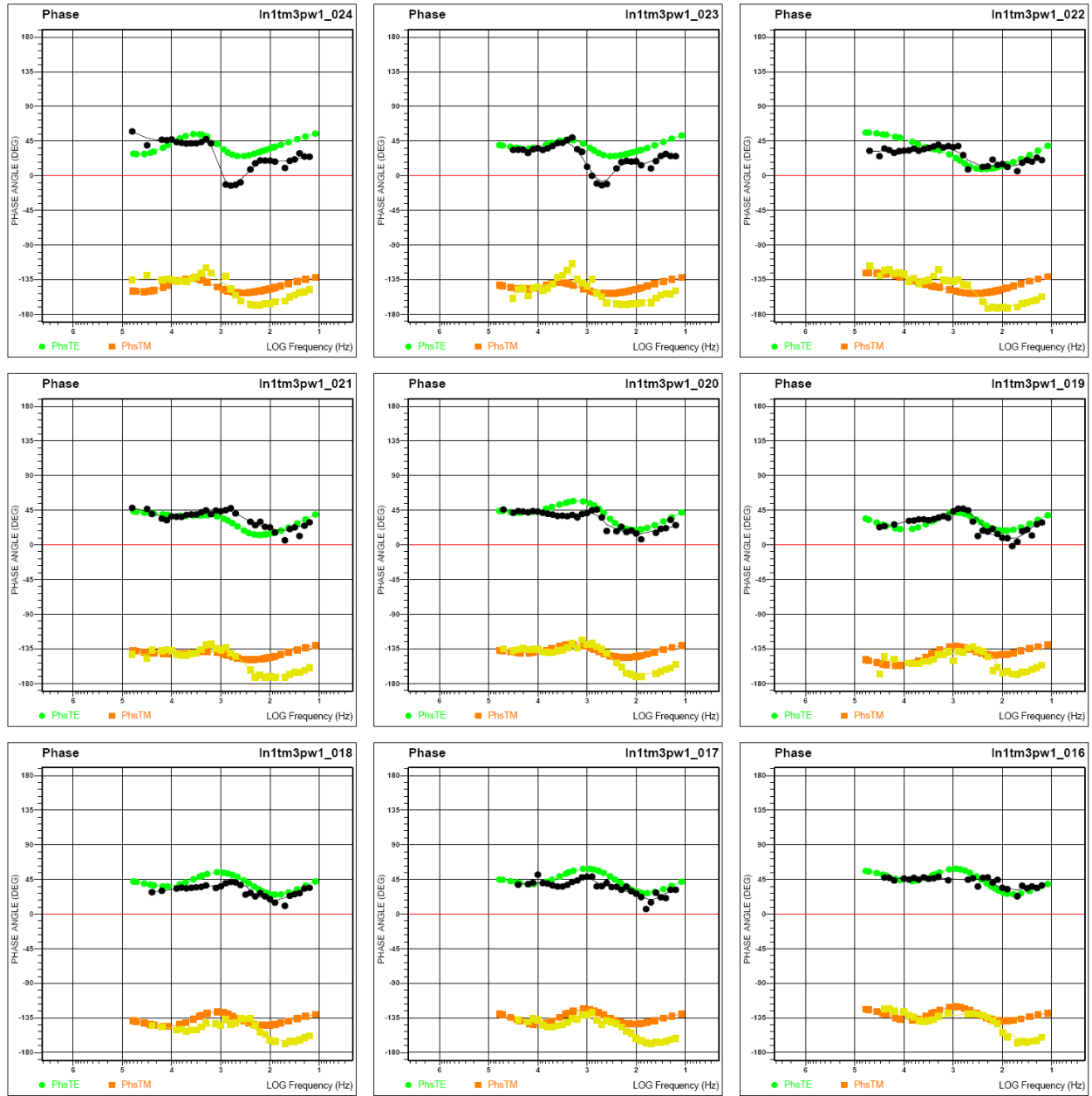


Figure A1-18. Line 1 impedance phase data for TM mode forward model, sites 16 – 24.

## Appendix 1 – Audio-Magnetotelluric Data and Models

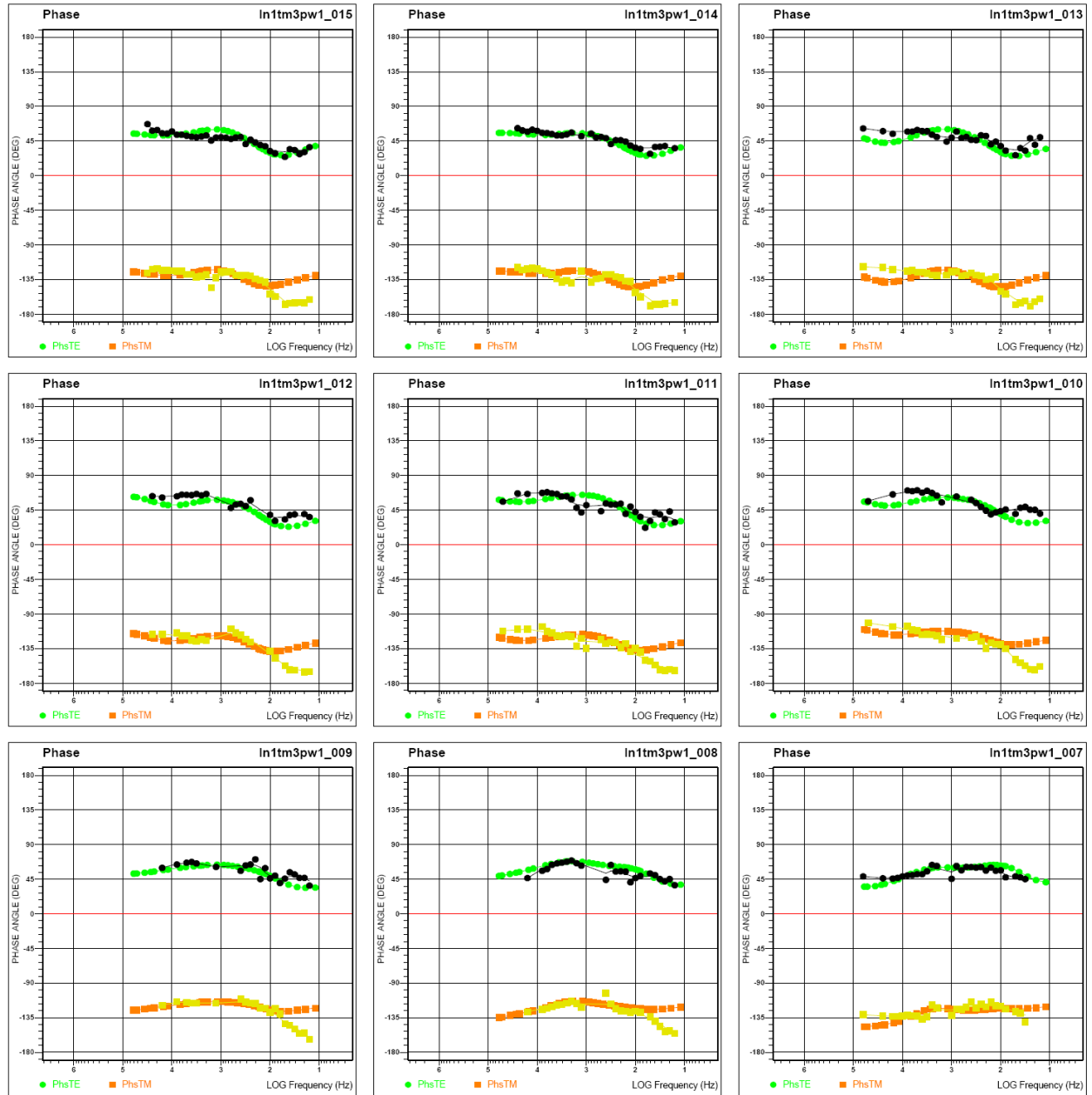


Figure A1-19. Line 1 impedance phase data for TM mode forward model, sites 7 – 15.



## Appendix 1 – Audio-Magnetotelluric Data and Models

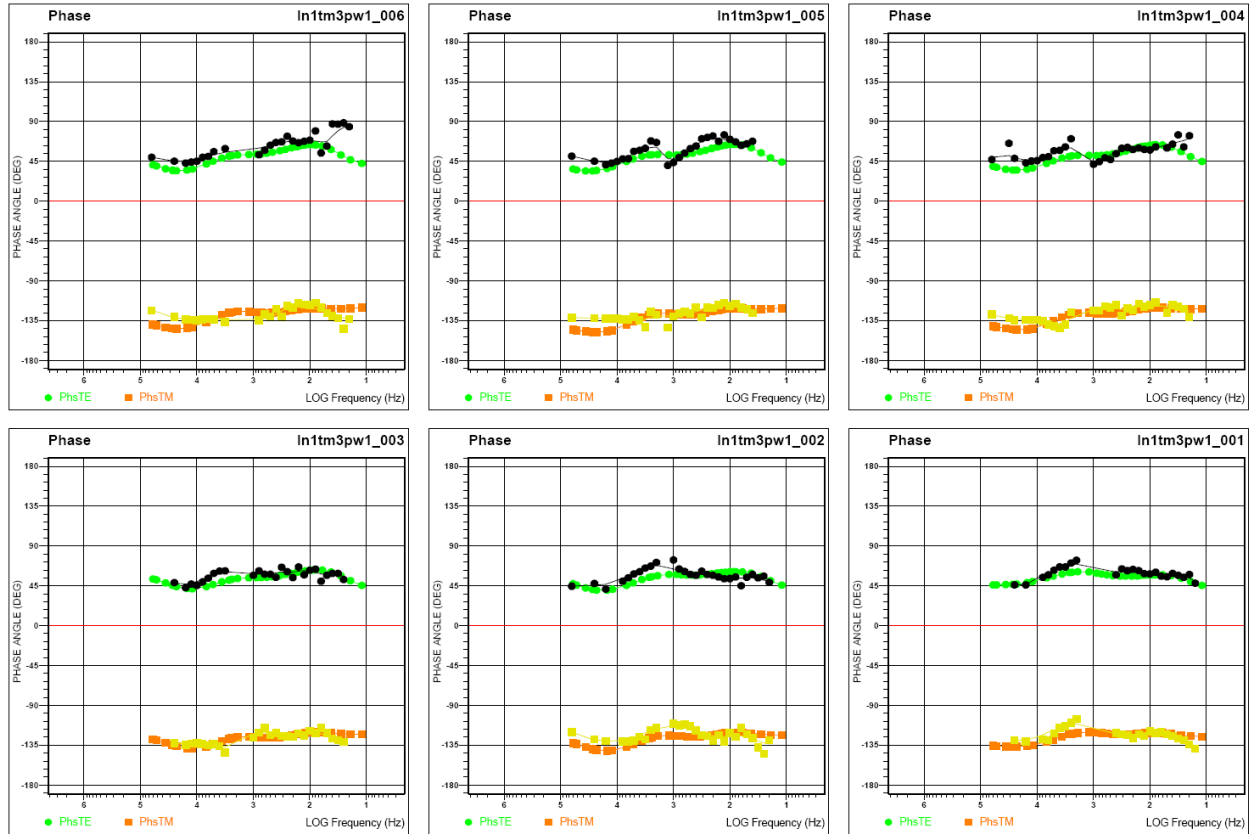
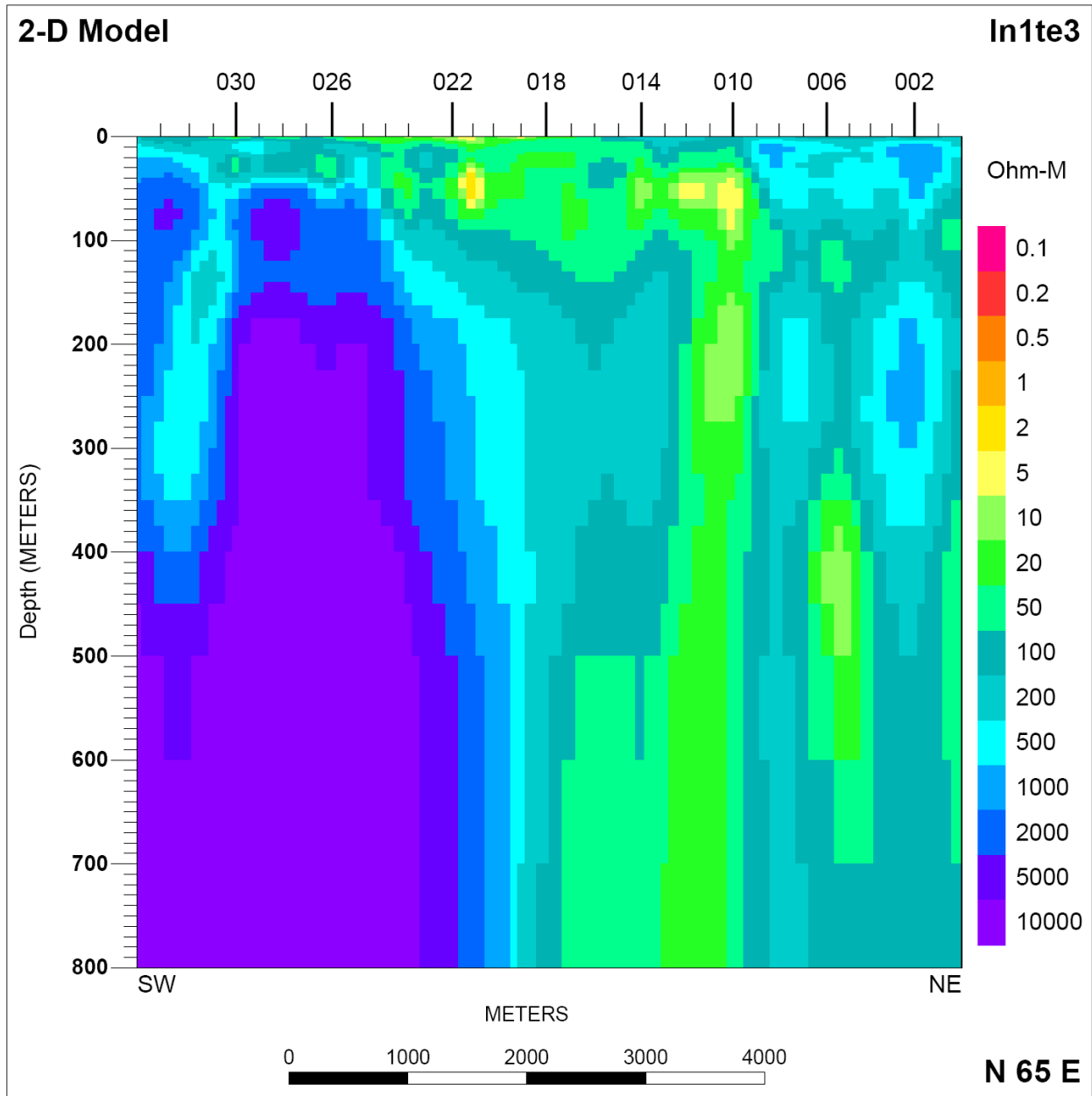
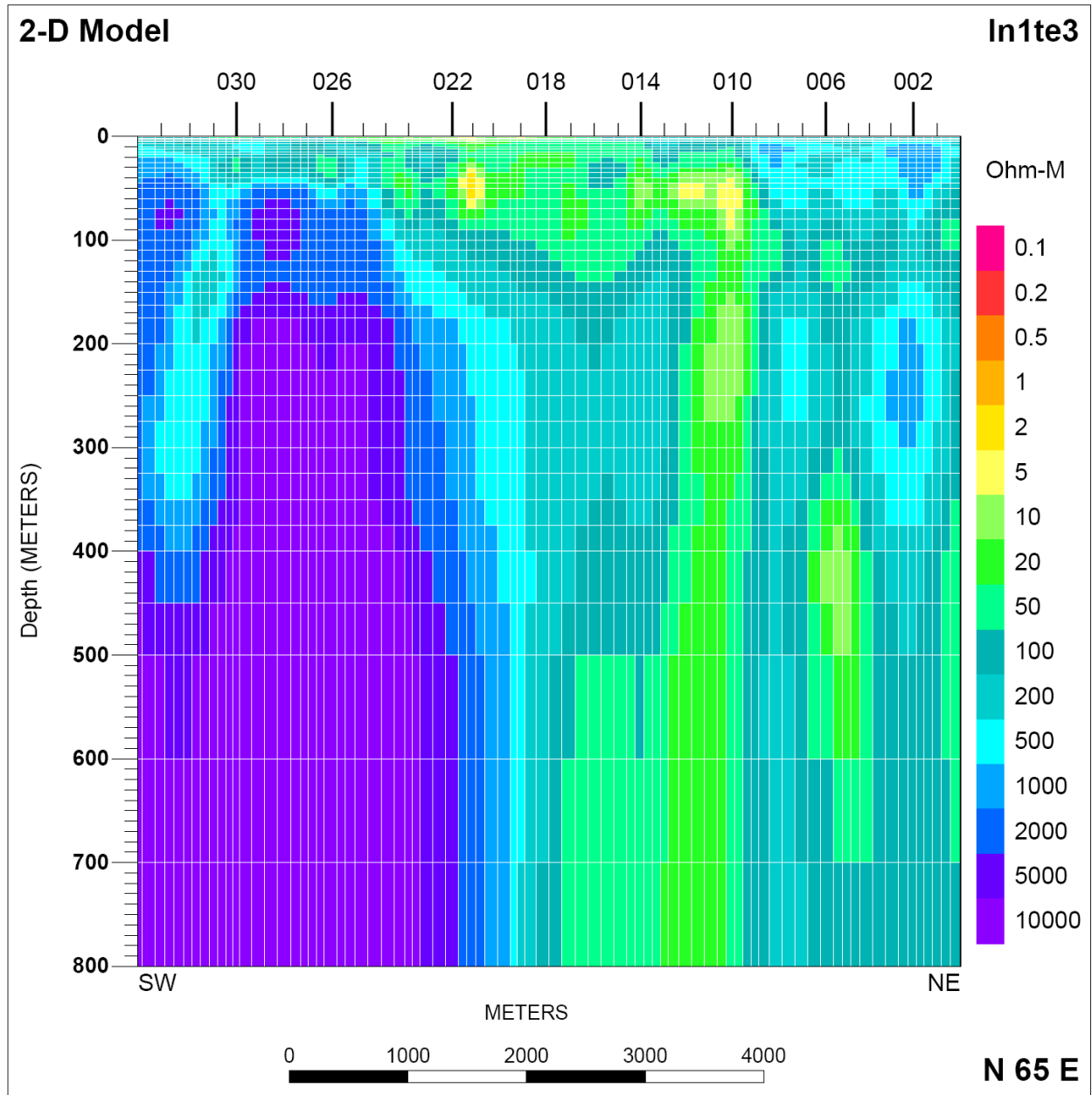


Figure A1-20. Line 1 impedance phase data for TM mode forward model, sites 1 – 6.



**Figure A1-21.** Line 1 2-D resistivity inversion modeling result for TE mode without model mesh lines. Tic marks at top of model are projected AMT station locations. Vertical exaggeration is 8.3:1.



**Figure A1-22.** Line 1 2-D inversion modeling result for TE mode with white model mesh lines. Tic marks at top of model are projected AMT station locations. Vertical exaggeration is 8.3:1.

## Appendix 1 – Audio-Magnetotelluric Data and Models

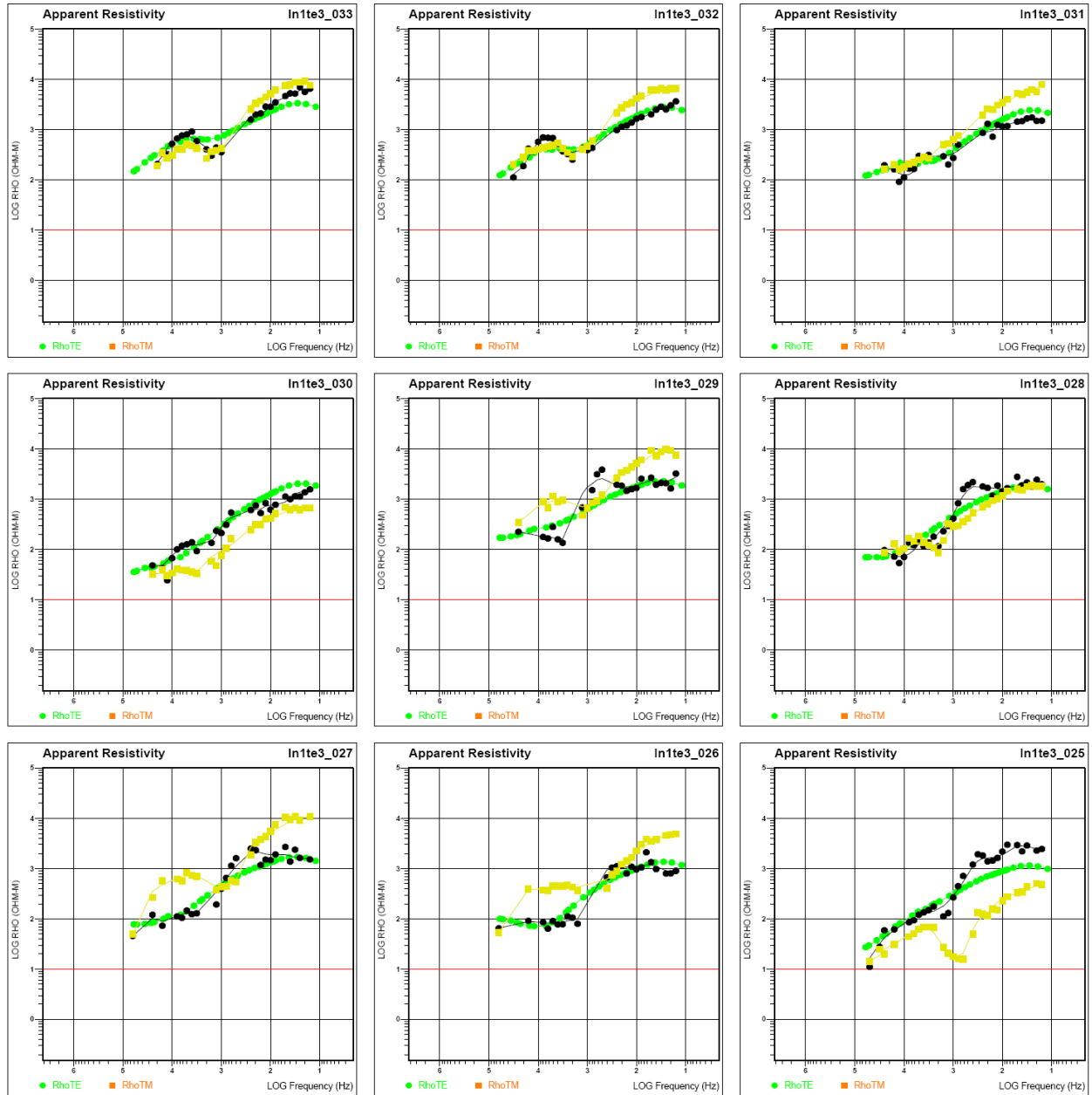


Figure A1-23. Line 1 impedance apparent resistivity data for TE mode inversion model, sites 25 – 33.

## Appendix 1 – Audio-Magnetotelluric Data and Models

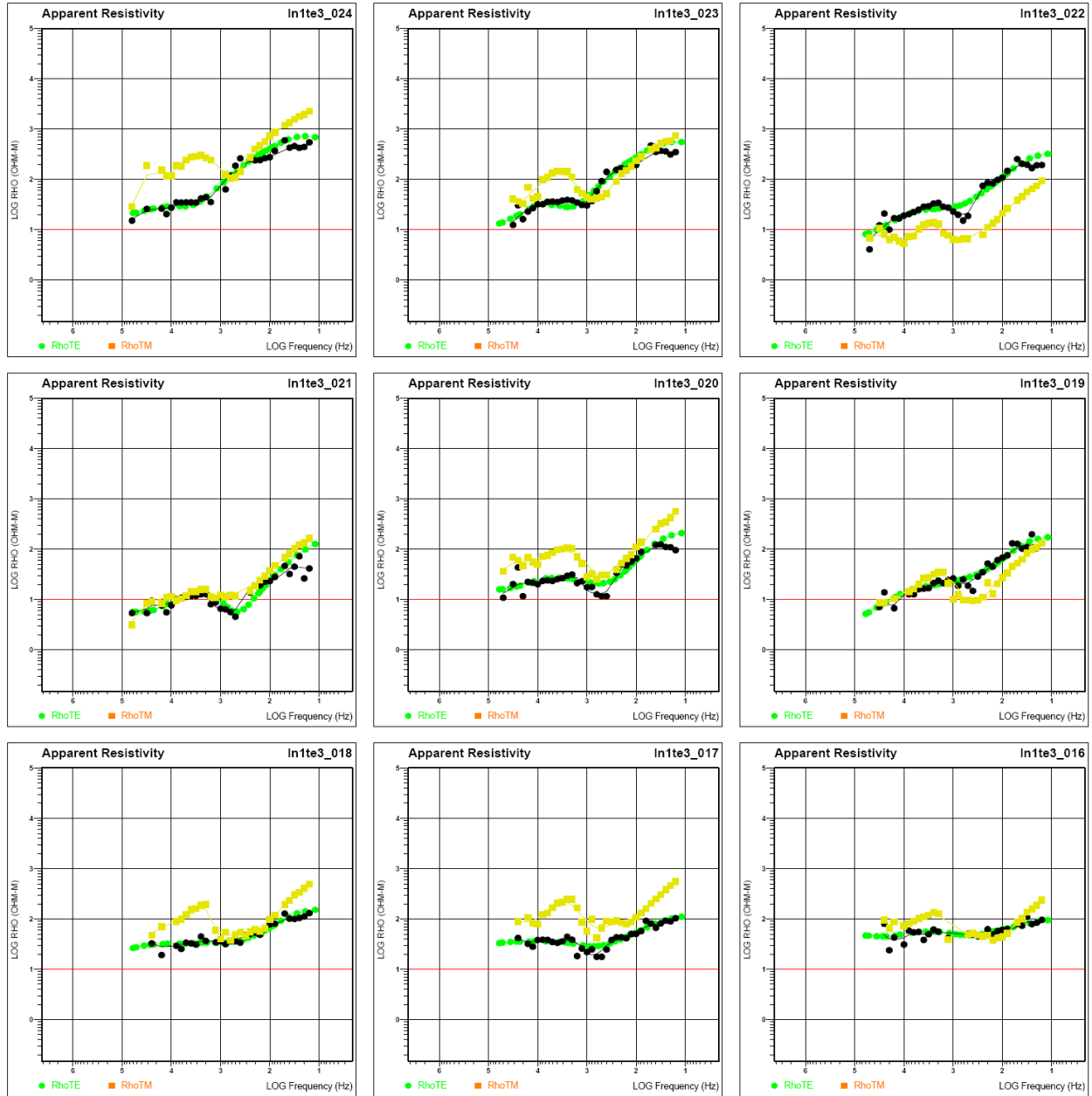


Figure A1-24. Line 1 impedance apparent resistivity data for TE mode inversion model, sites 16 – 24.

## Appendix 1 – Audio-Magnetotelluric Data and Models

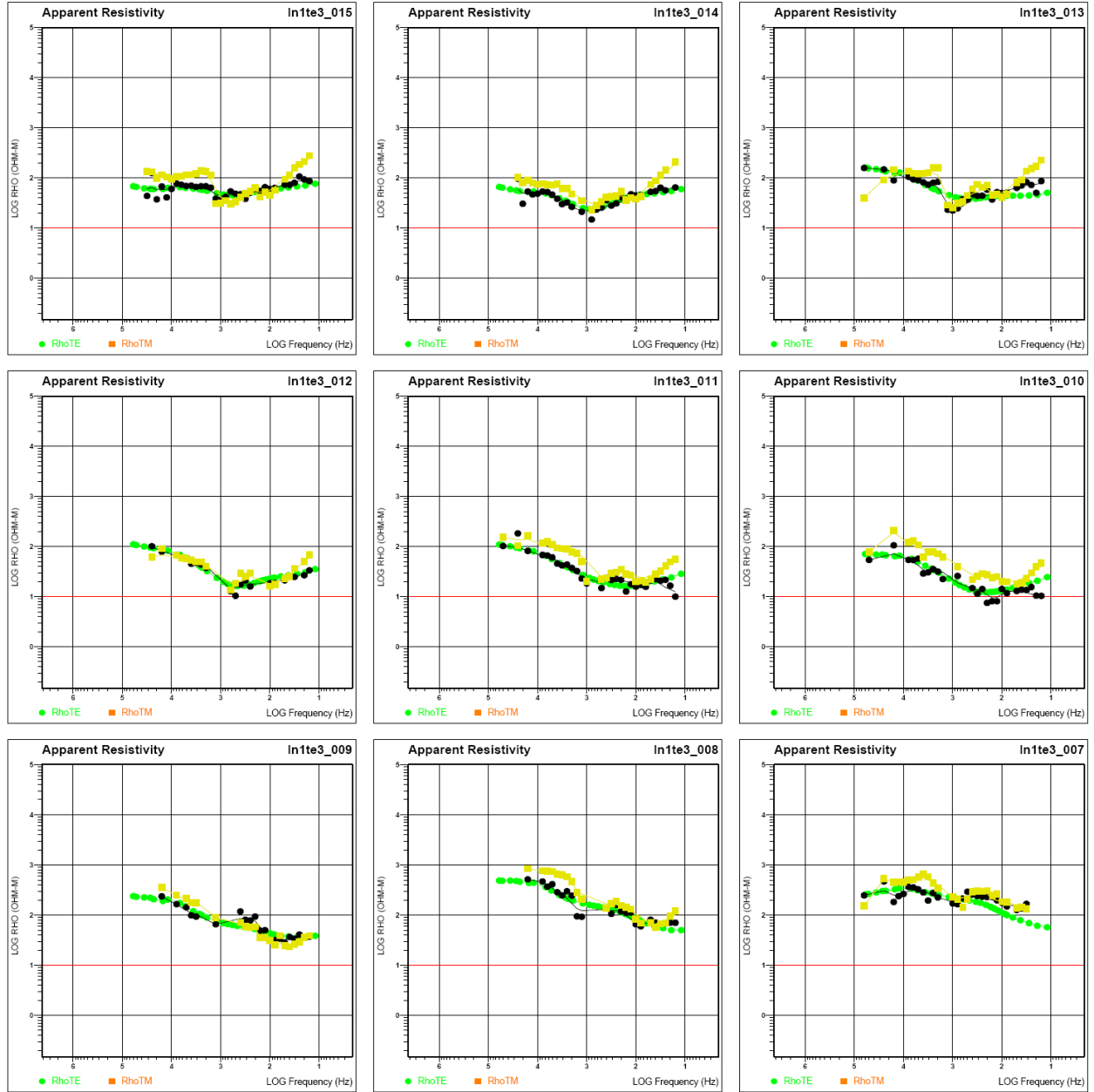
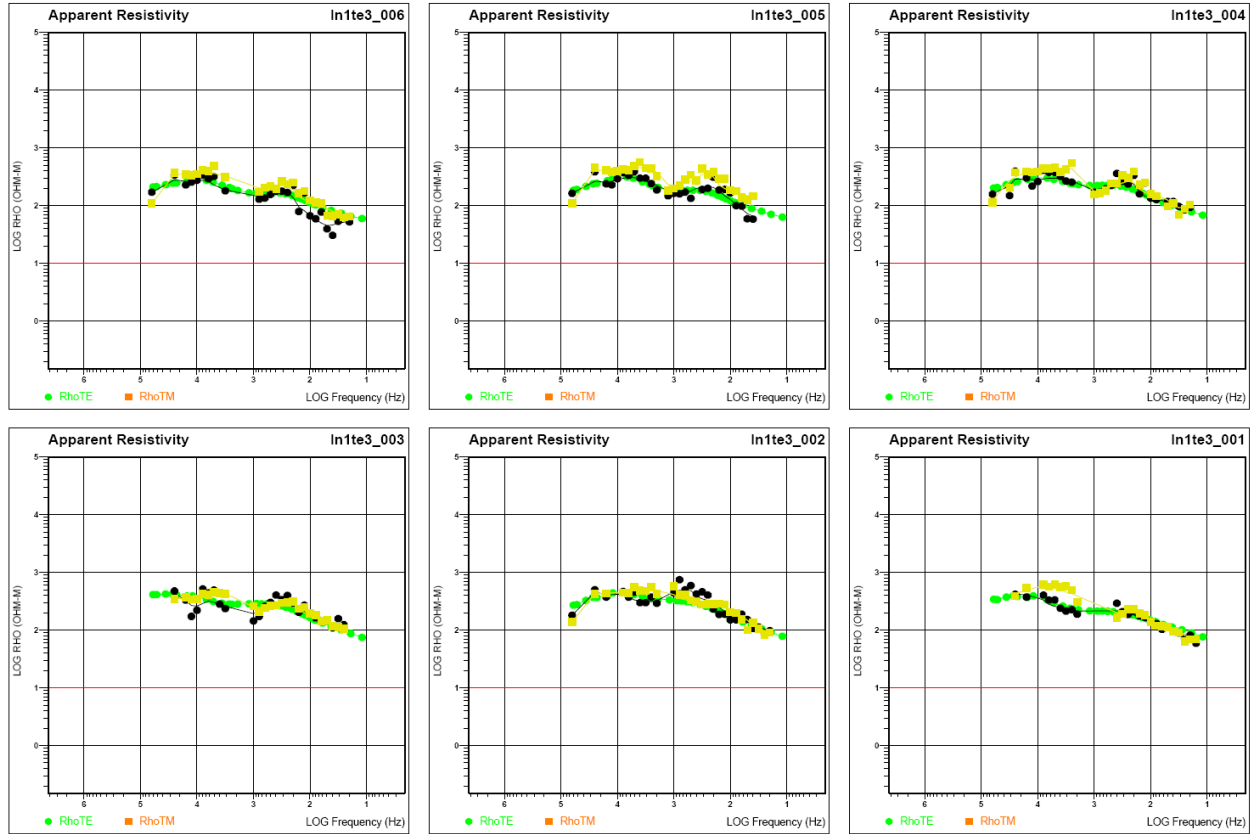


Figure A1-25. Line 1 impedance apparent resistivity data for TE mode inversion model, sites 7 – 15.

## Appendix 1 – Audio-Magnetotelluric Data and Models



**Figure A1-26.** Line 1 impedance apparent resistivity data for TE mode inversion model, sites 1 – 6.

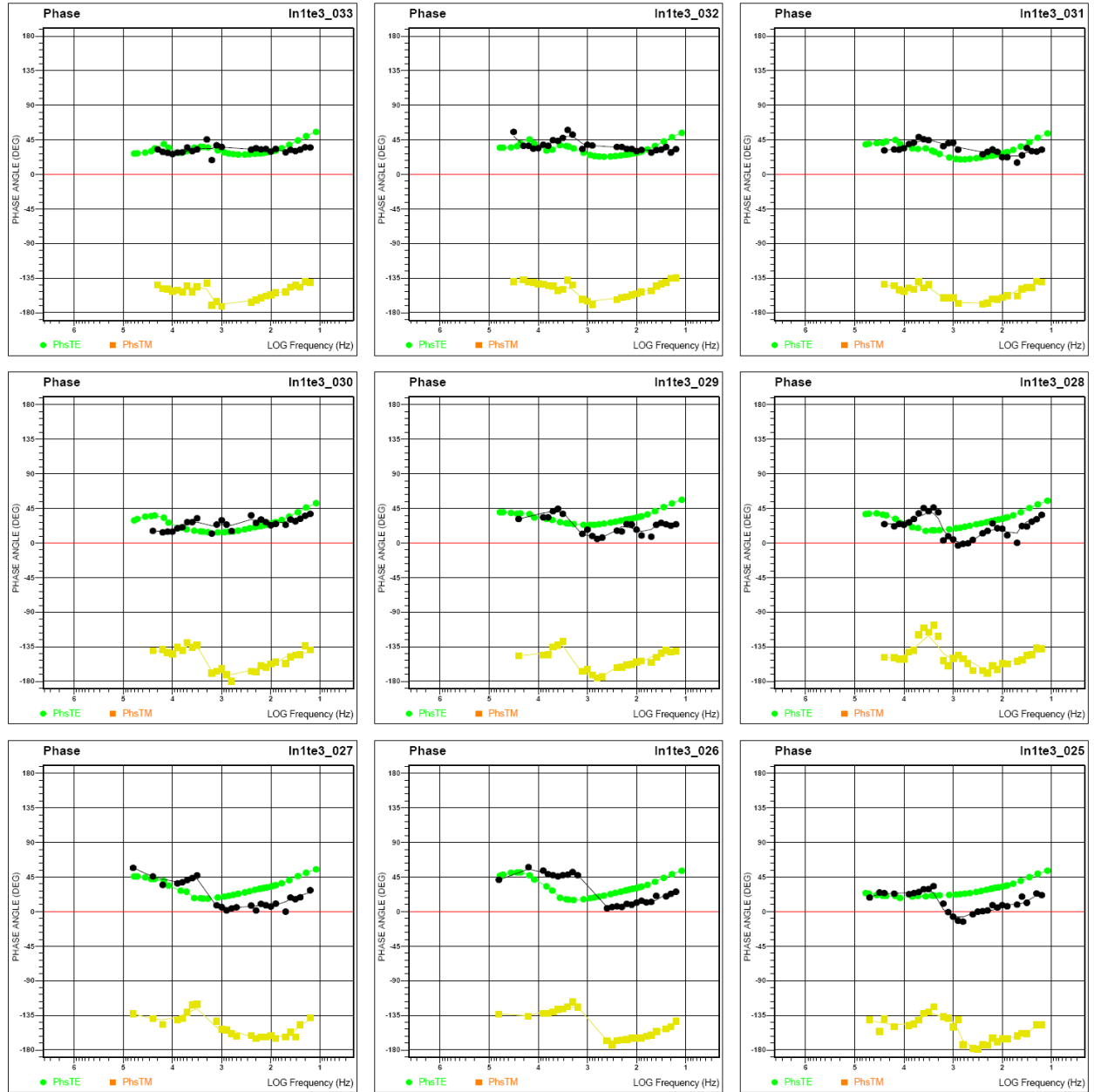


Figure A1-27. Line 1 impedance phase data for TE mode inversion model, sites 25 – 33.



## Appendix 1 – Audio-Magnetotelluric Data and Models

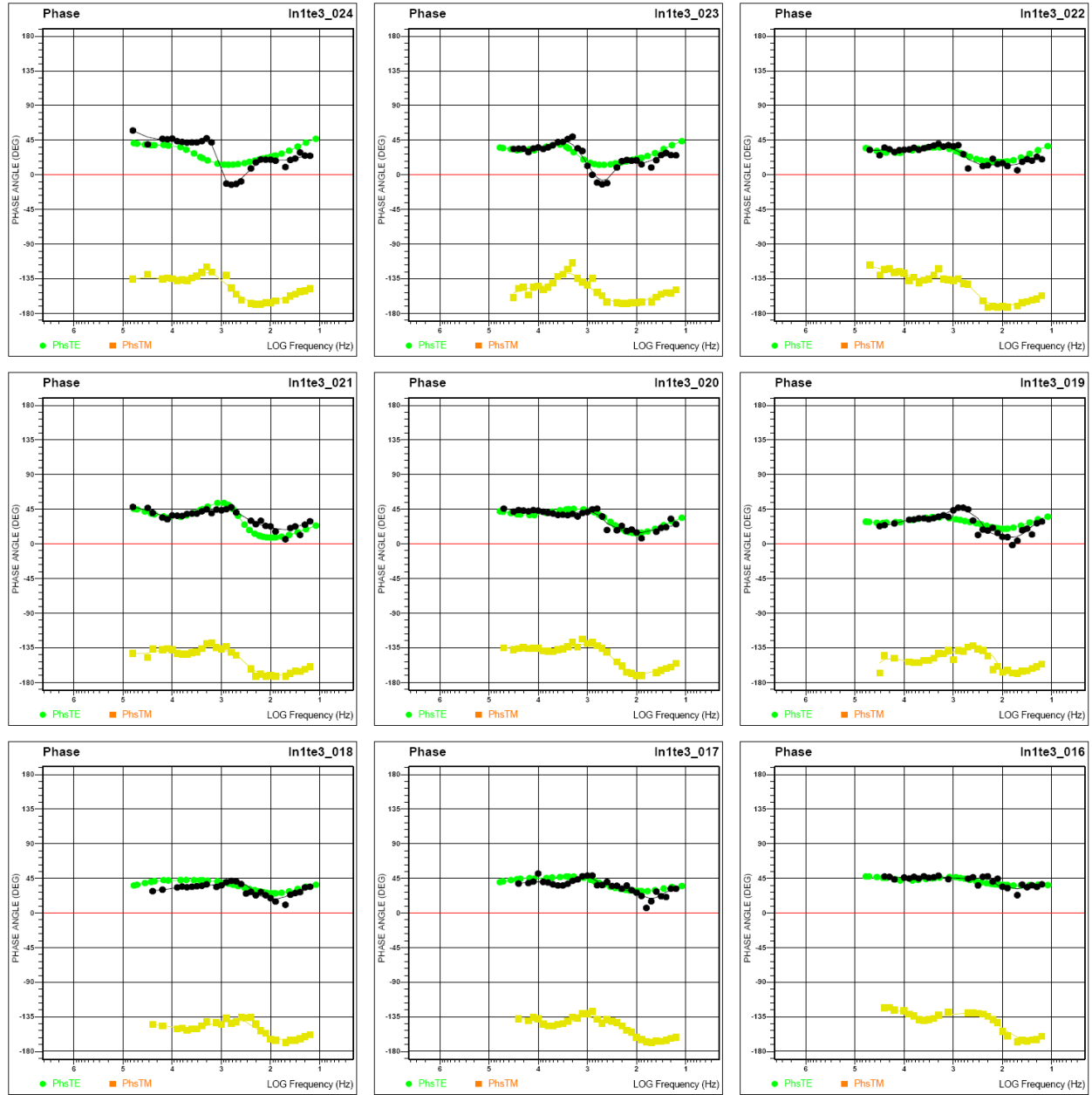


Figure A1-28. Line 1 impedance phase data for TE mode inversion model, sites 16 – 24.

## Appendix 1 – Audio-Magnetotelluric Data and Models

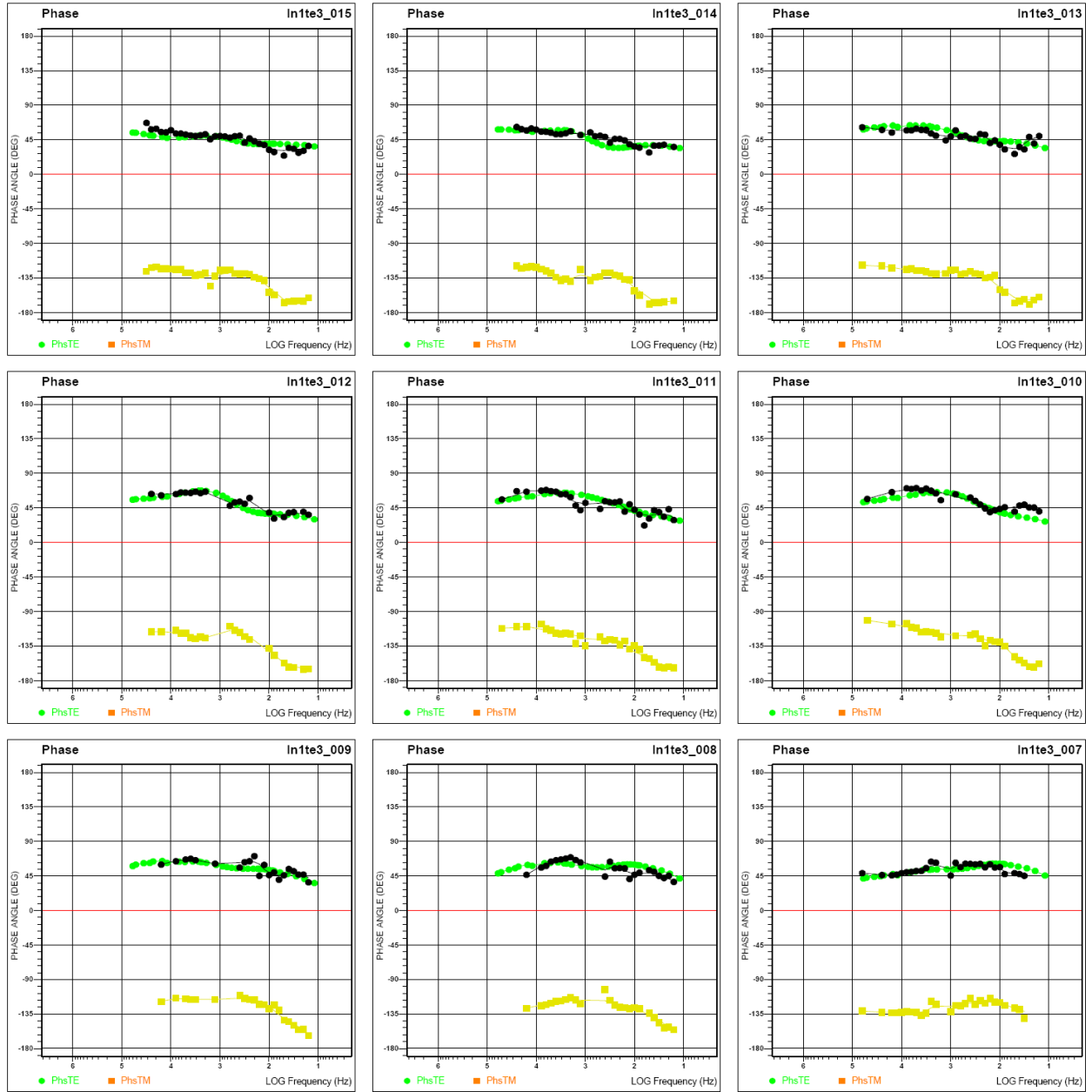
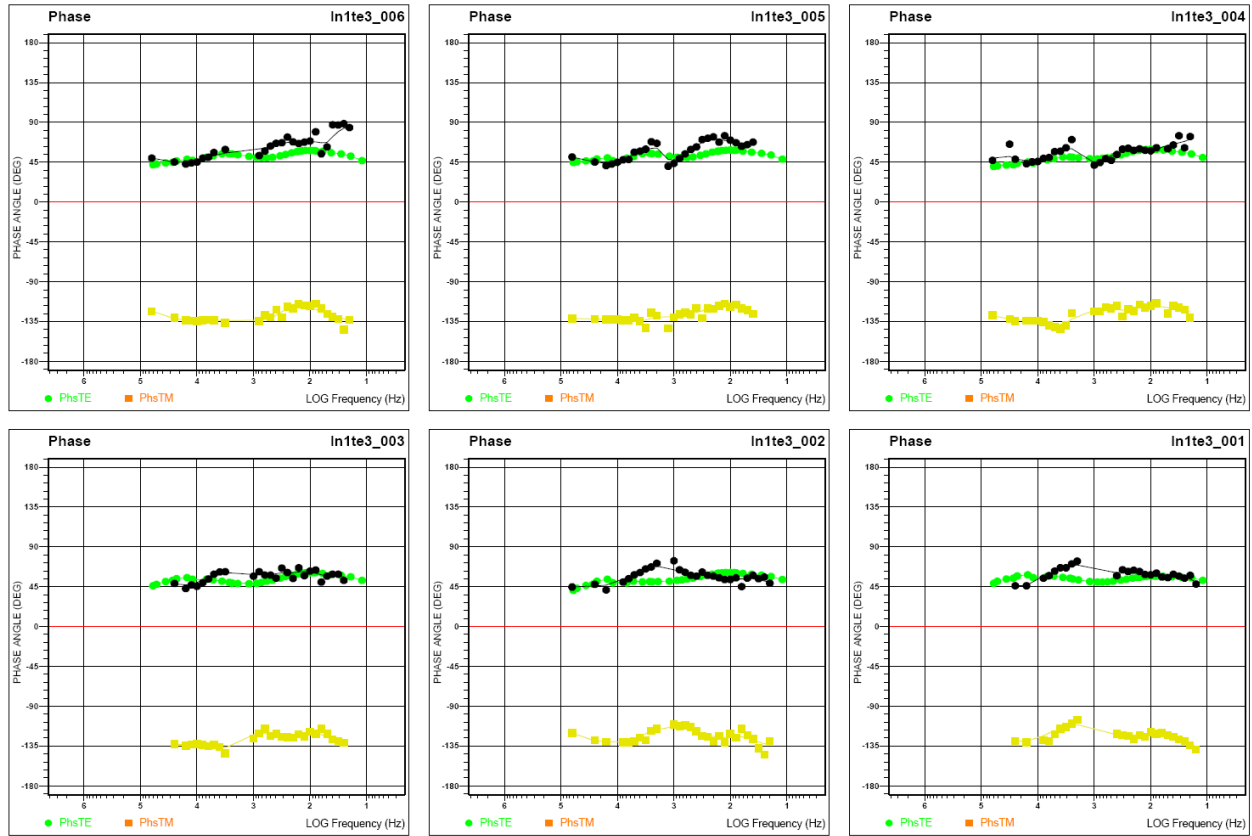
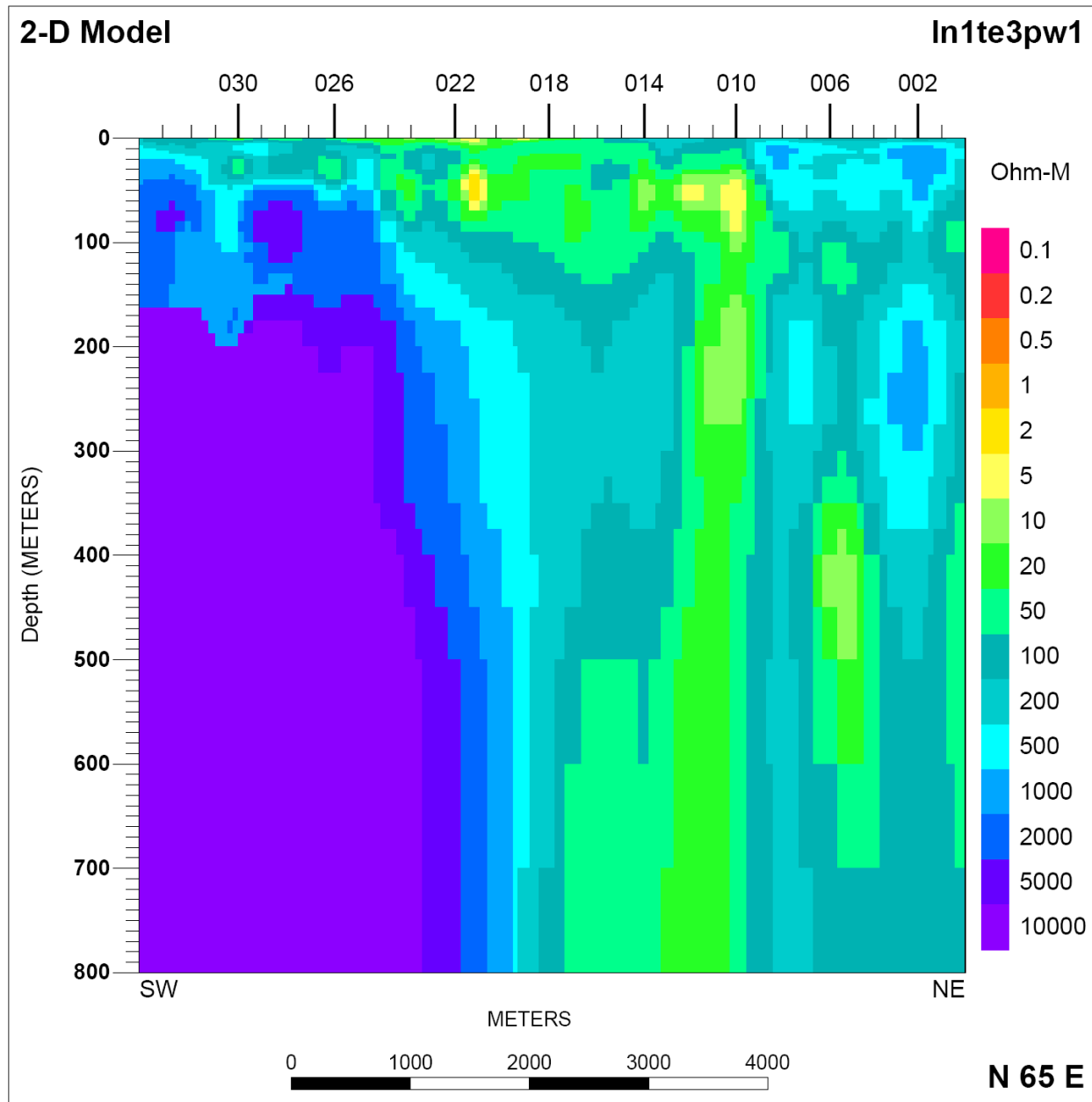


Figure A1-29. Line 1 impedance phase data for TE mode inversion model, sites 7 – 15.

## Appendix 1 – Audio-Magnetotelluric Data and Models



**Figure A1-30.** Line 1 impedance phase data for TE mode inversion model, sites 1 – 6.



**Figure A1-31.** Line 1 2-D forward modeling result for TE mode inversion result without model mesh lines. This forward model is built from inversion model In1te3 in figures A1-21 and A1-22. Tic marks at top of model are projected AMT station locations. Vertical exaggeration is 8.3:1.

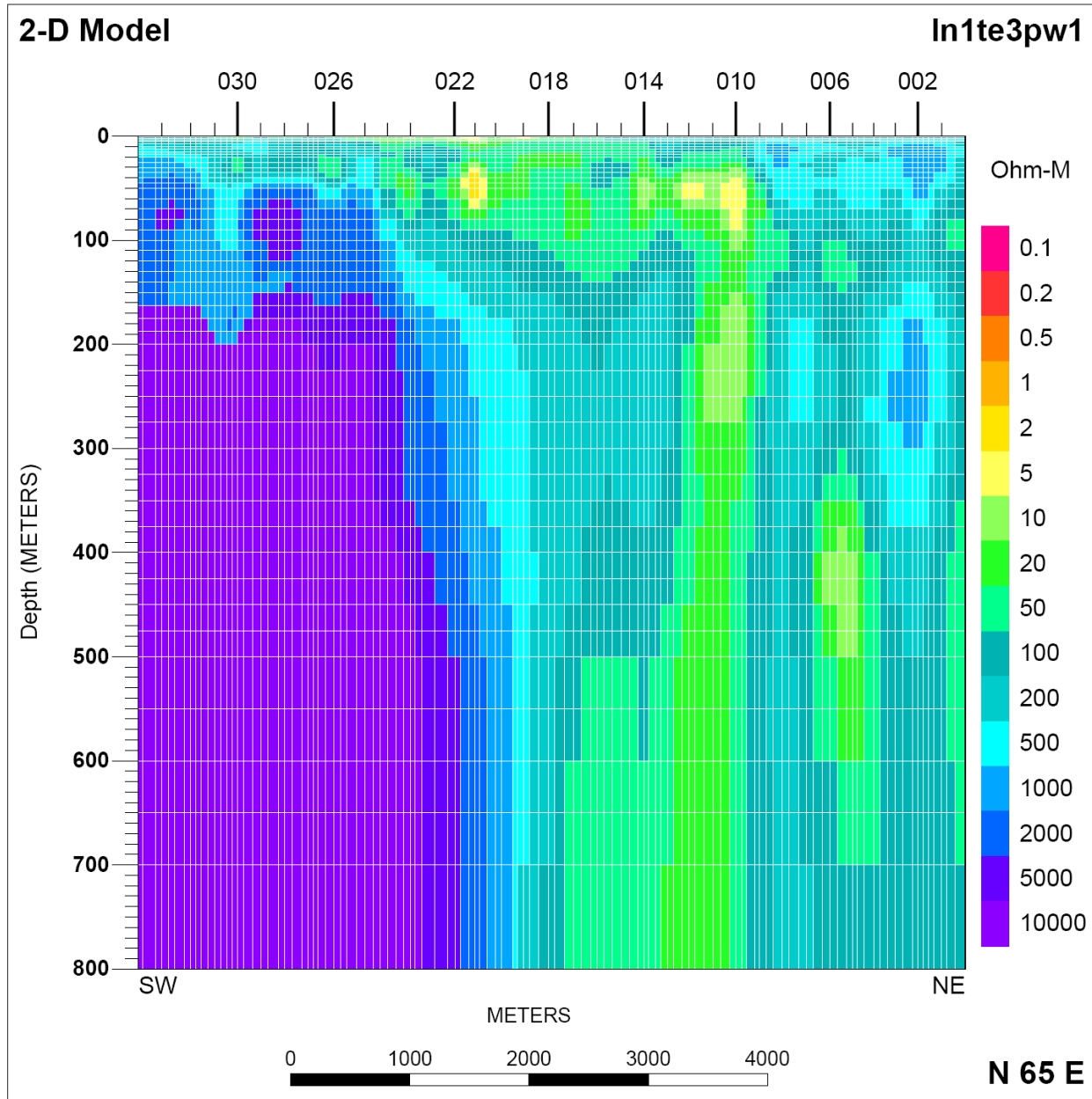


**Figure A1-32.** Line 1 2-D forward modeling result for TE mode inversion result with white model mesh lines. Tic marks at top of model are projected AMT station locations. Vertical exaggeration is 8.3:1.

## Appendix 1 – Audio-Magnetotelluric Data and Models

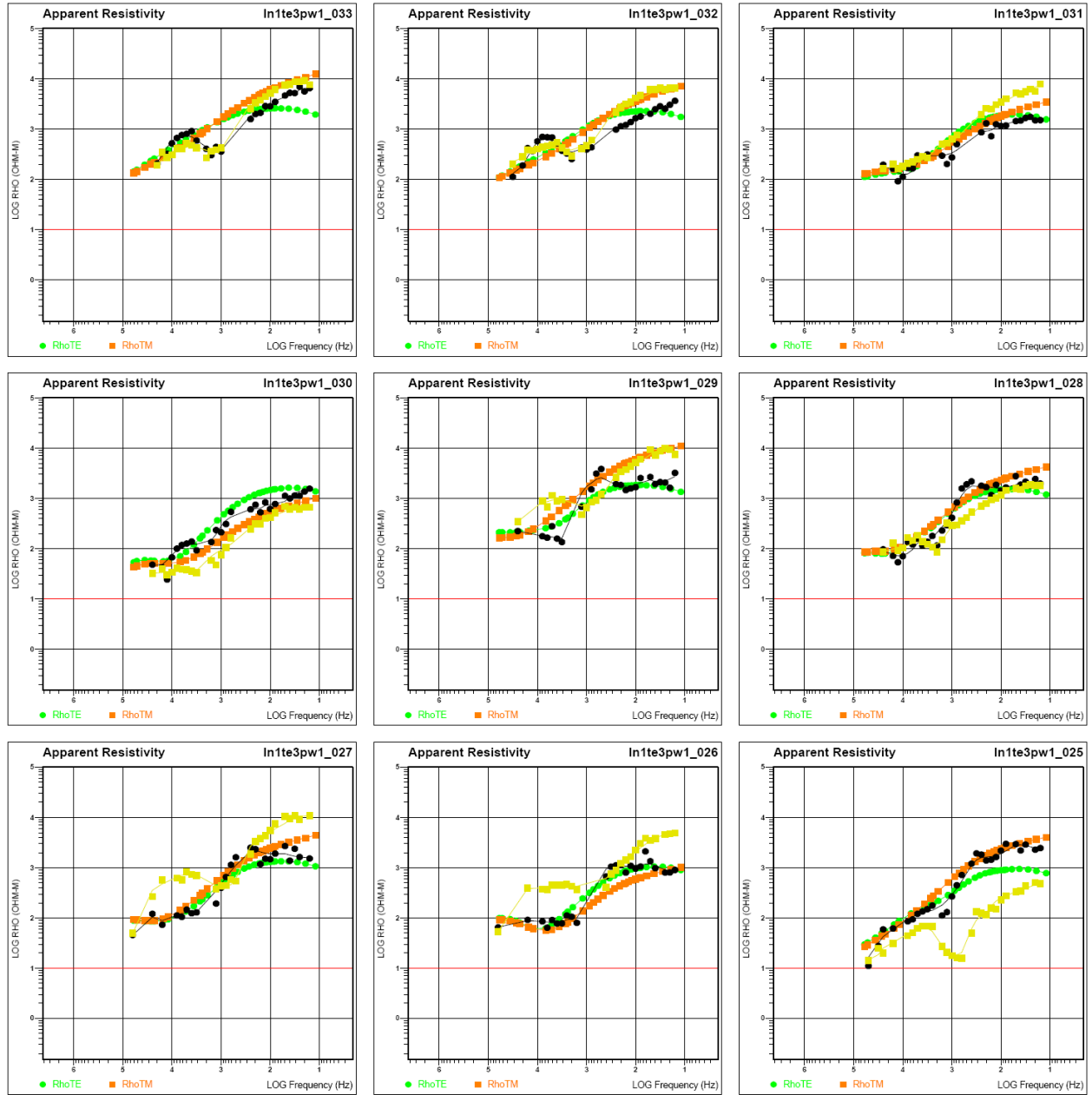


Figure A1-33. Line 1 impedance apparent resistivity data for TE mode forward model, sites 25 – 33.

## Appendix 1 – Audio-Magnetotelluric Data and Models

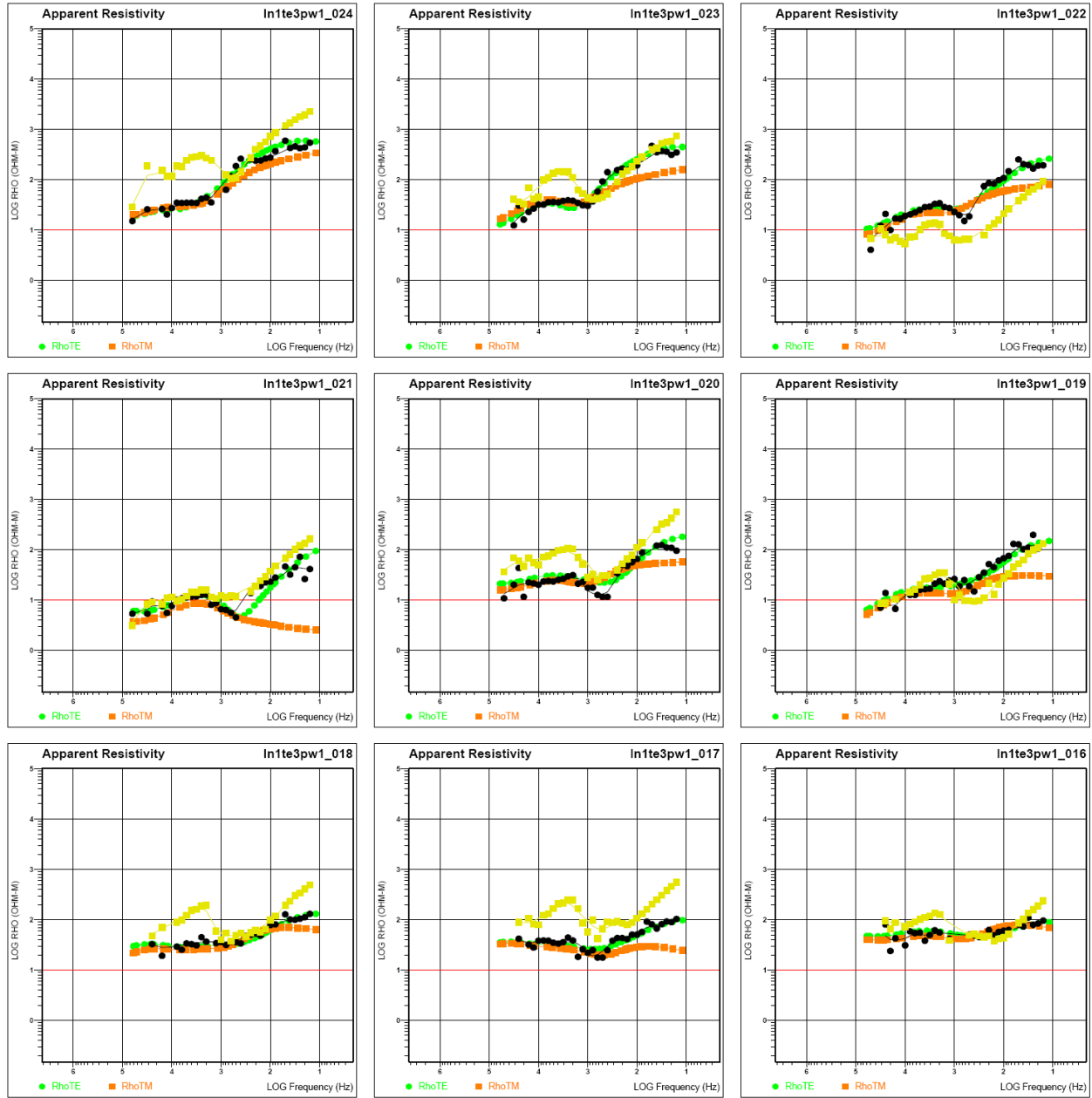


Figure A1-34. Line 1 impedance apparent resistivity data for TE mode forward model, sites 16 – 24.

## Appendix 1 – Audio-Magnetotelluric Data and Models

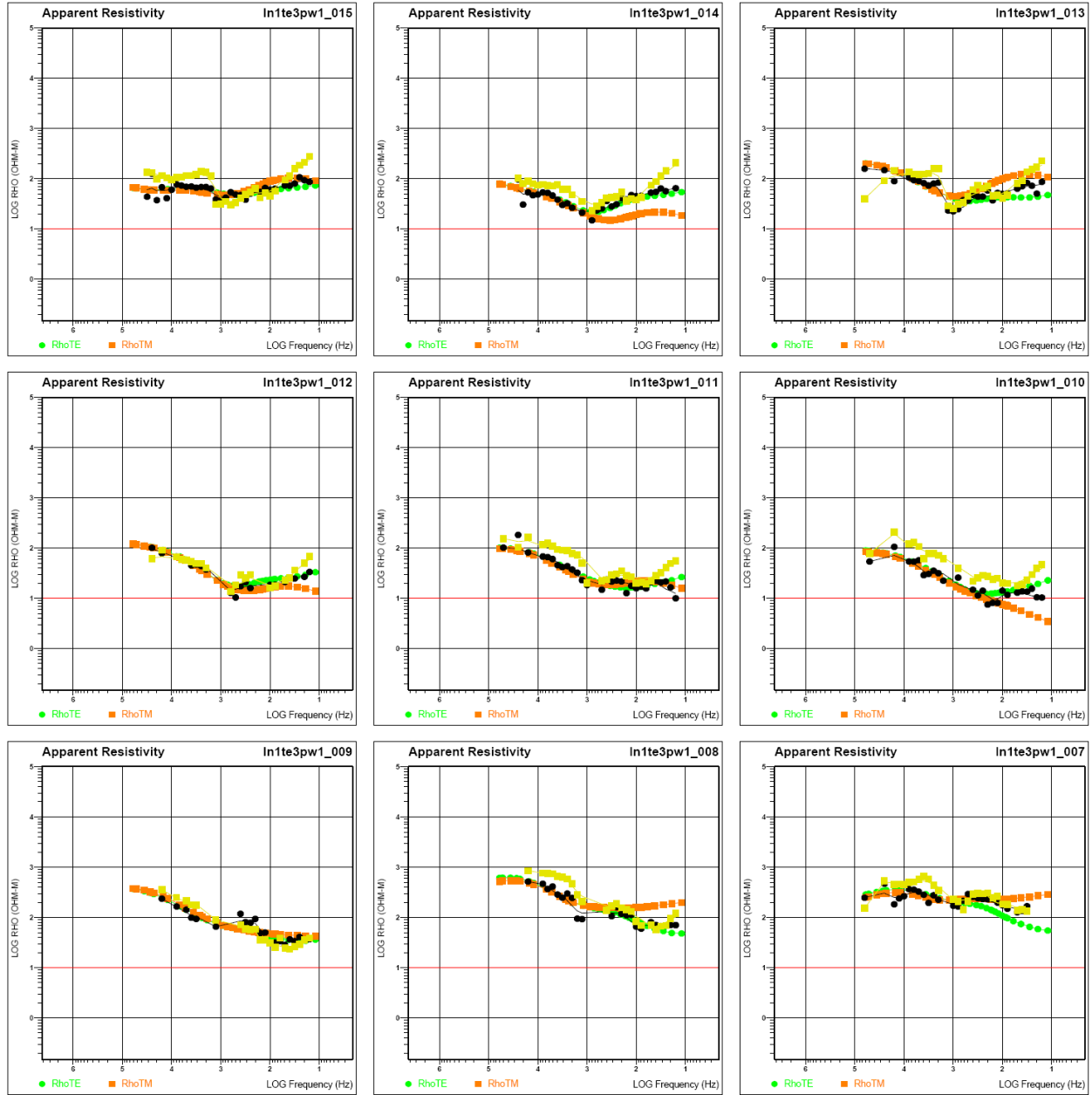
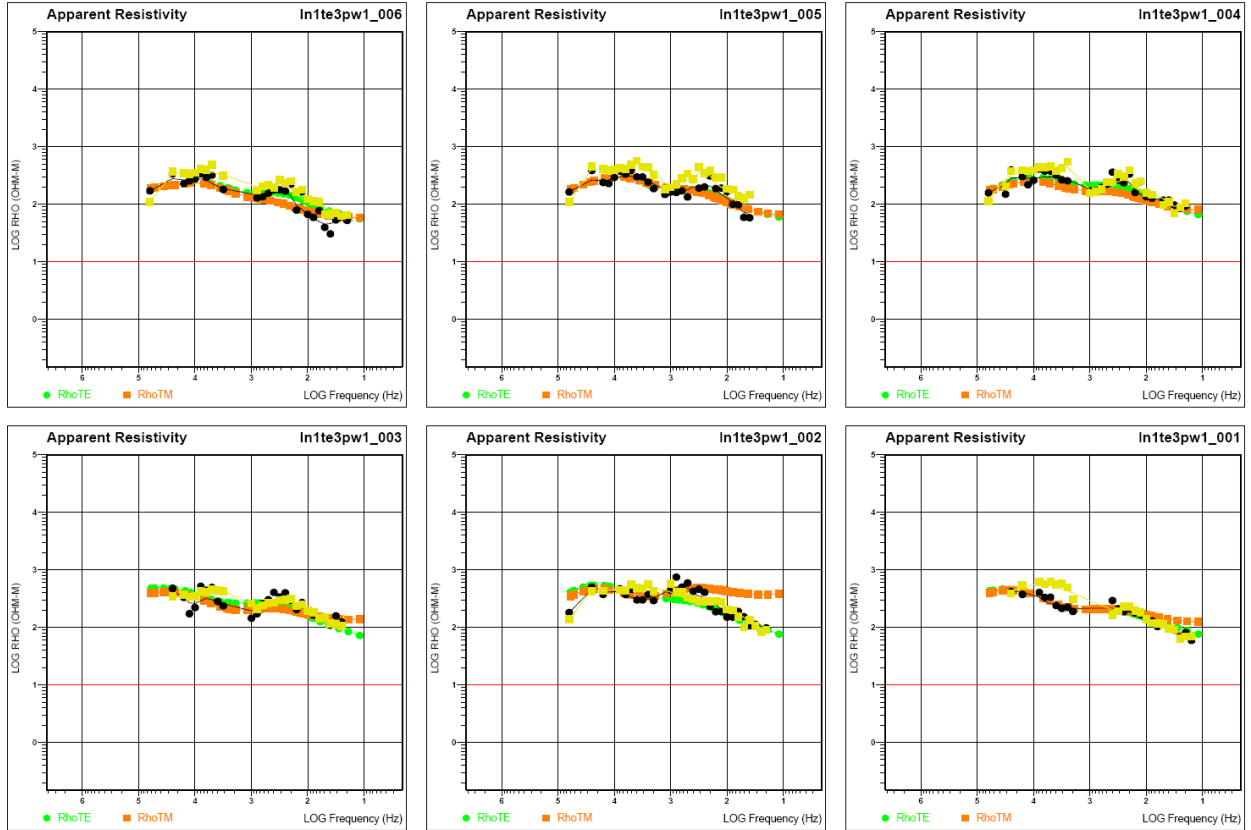


Figure A1-35. Line 1 impedance apparent resistivity data for TE mode forward model, sites 7 – 15.



## Appendix 1 – Audio-Magnetotelluric Data and Models



**Figure A1-36.** Line 1 impedance apparent resistivity data for TE mode forward model, sites 1 – 6.

## Appendix 1 – Audio-Magnetotelluric Data and Models

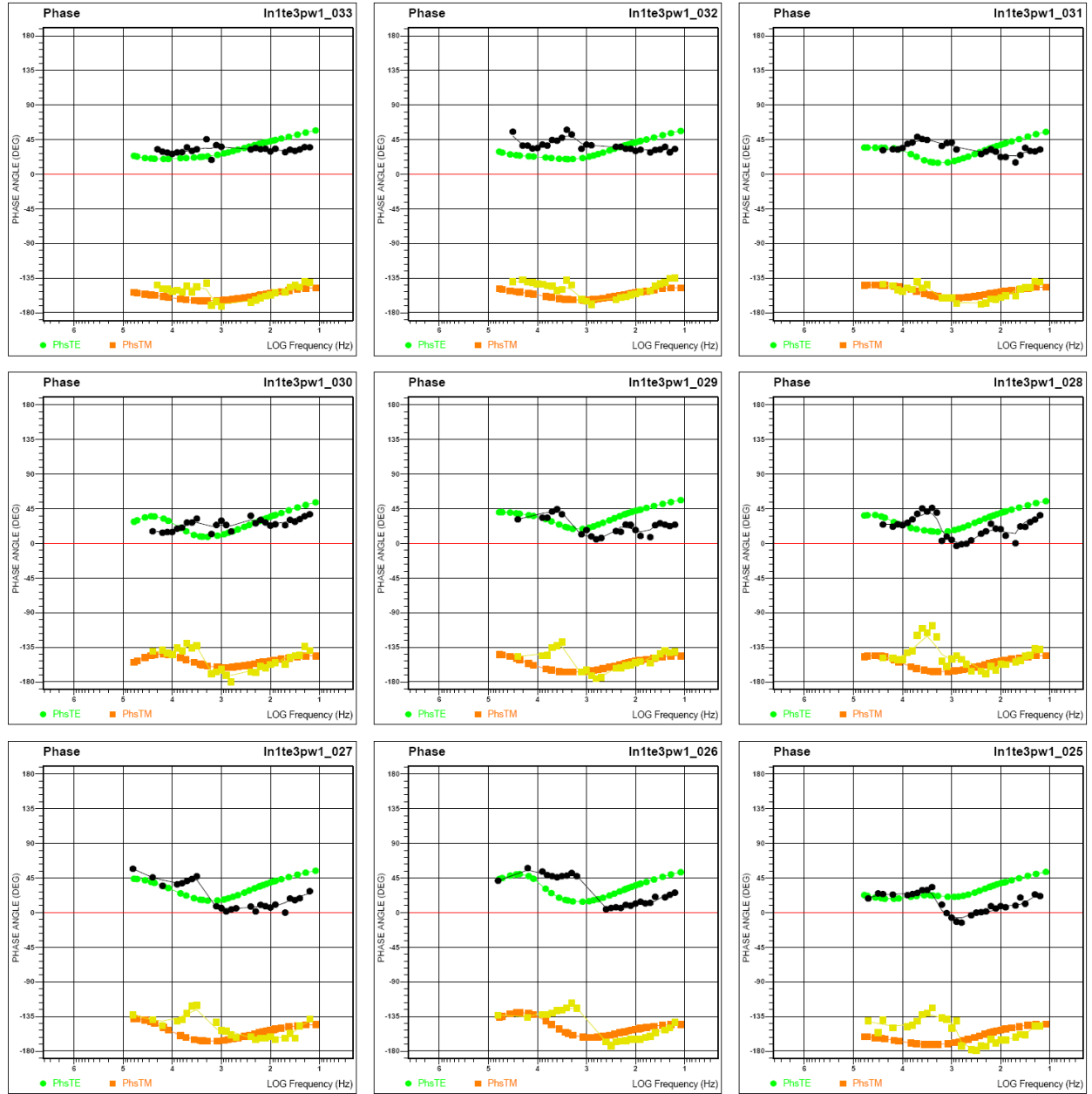


Figure A1-37. Line 1 impedance phase data for TE mode forward model, sites 25 – 33.

## Appendix 1 – Audio-Magnetotelluric Data and Models

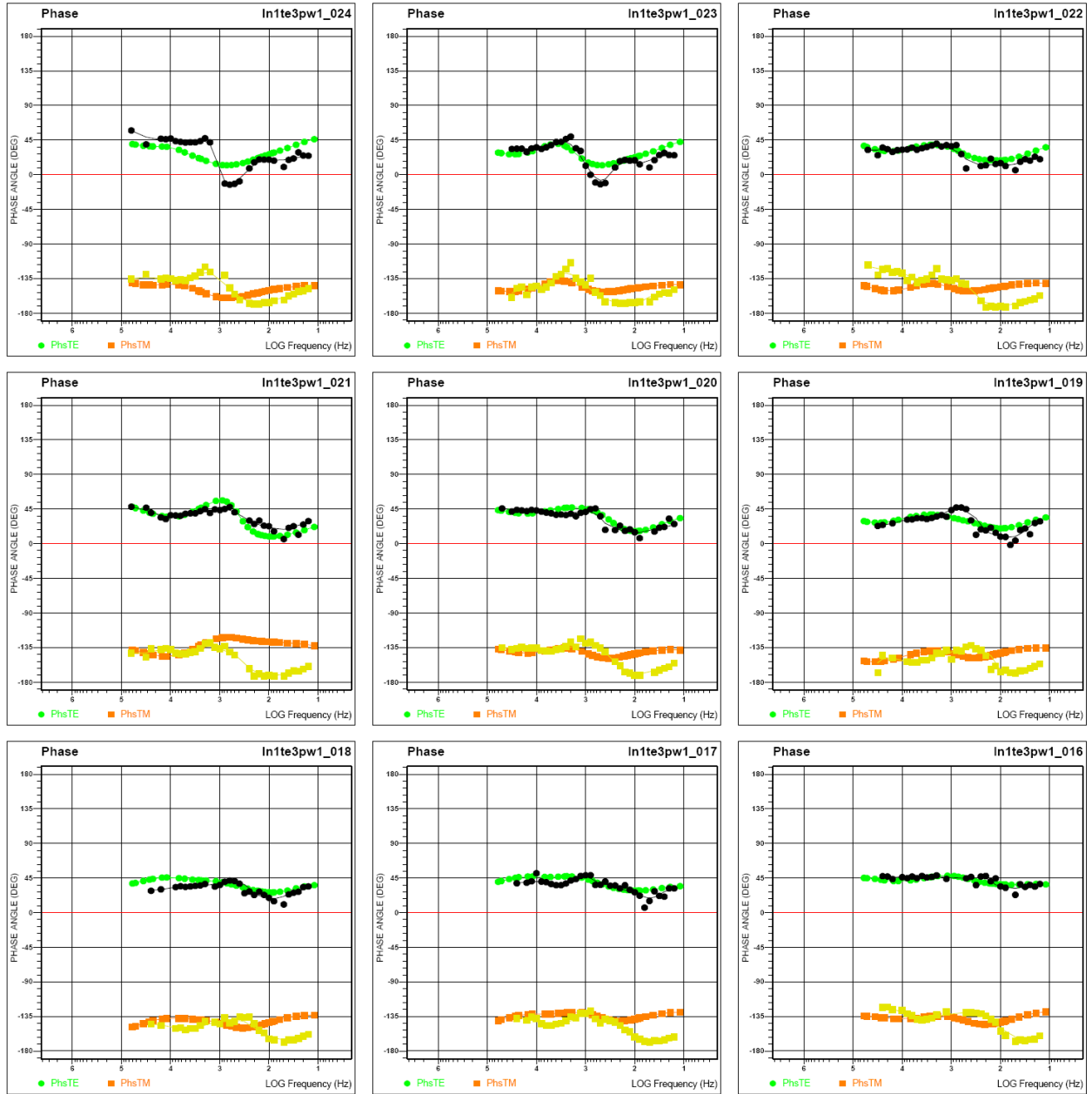


Figure A1-38. Line 1 impedance phase data for TE mode forward model, sites 16 – 24.

## Appendix 1 – Audio-Magnetotelluric Data and Models

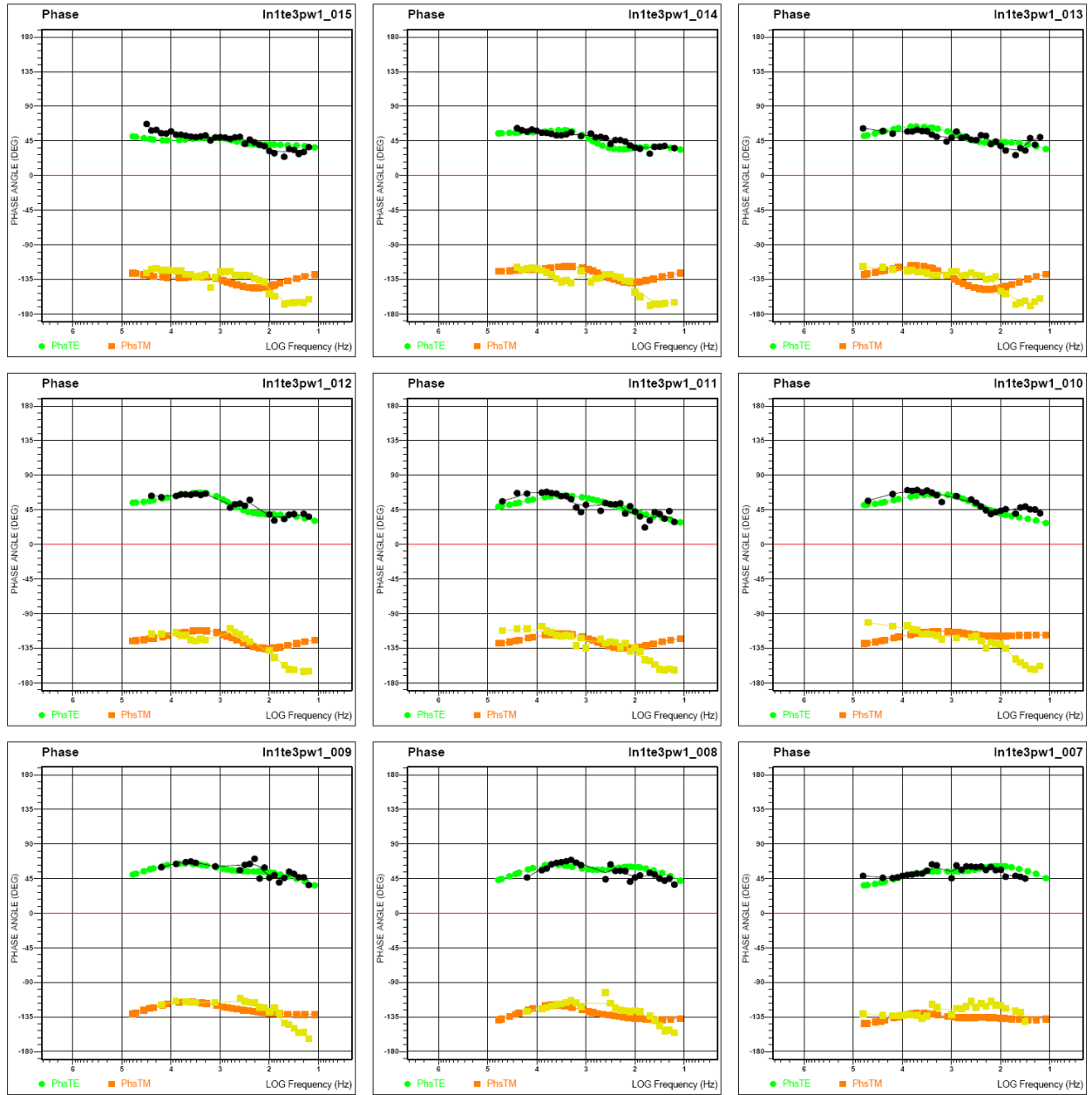


Figure A1-39. Line 1 impedance phase data for TE mode forward model, sites 7 – 15.

## Appendix 1 – Audio-Magnetotelluric Data and Models

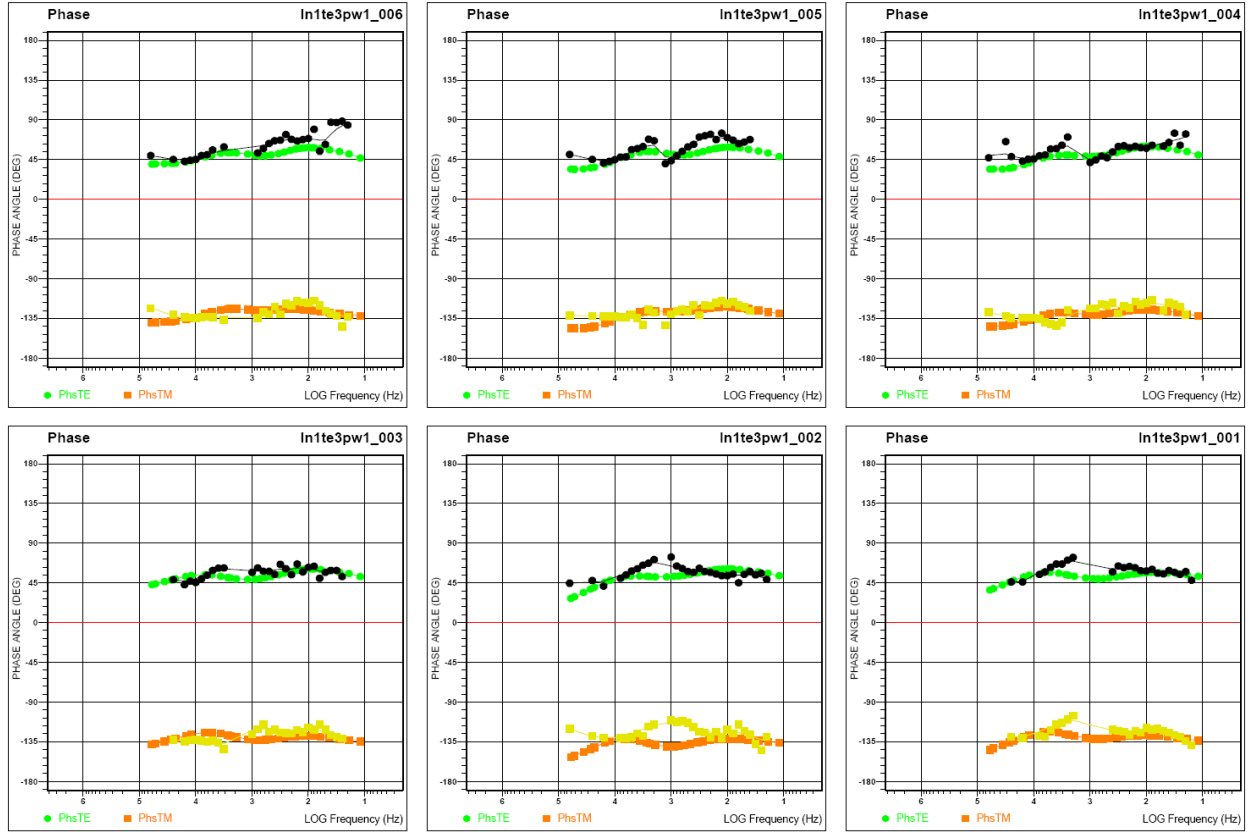
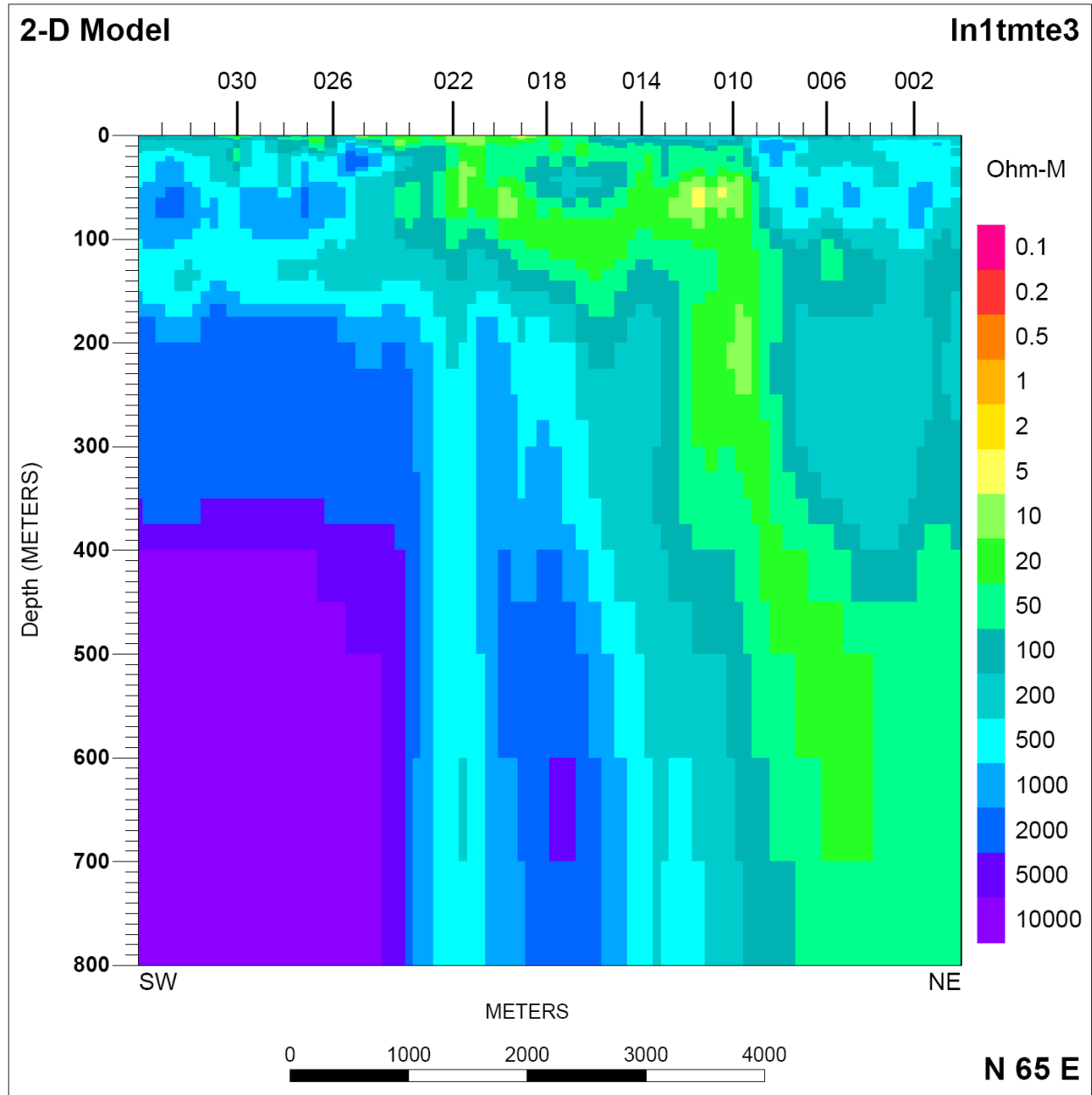
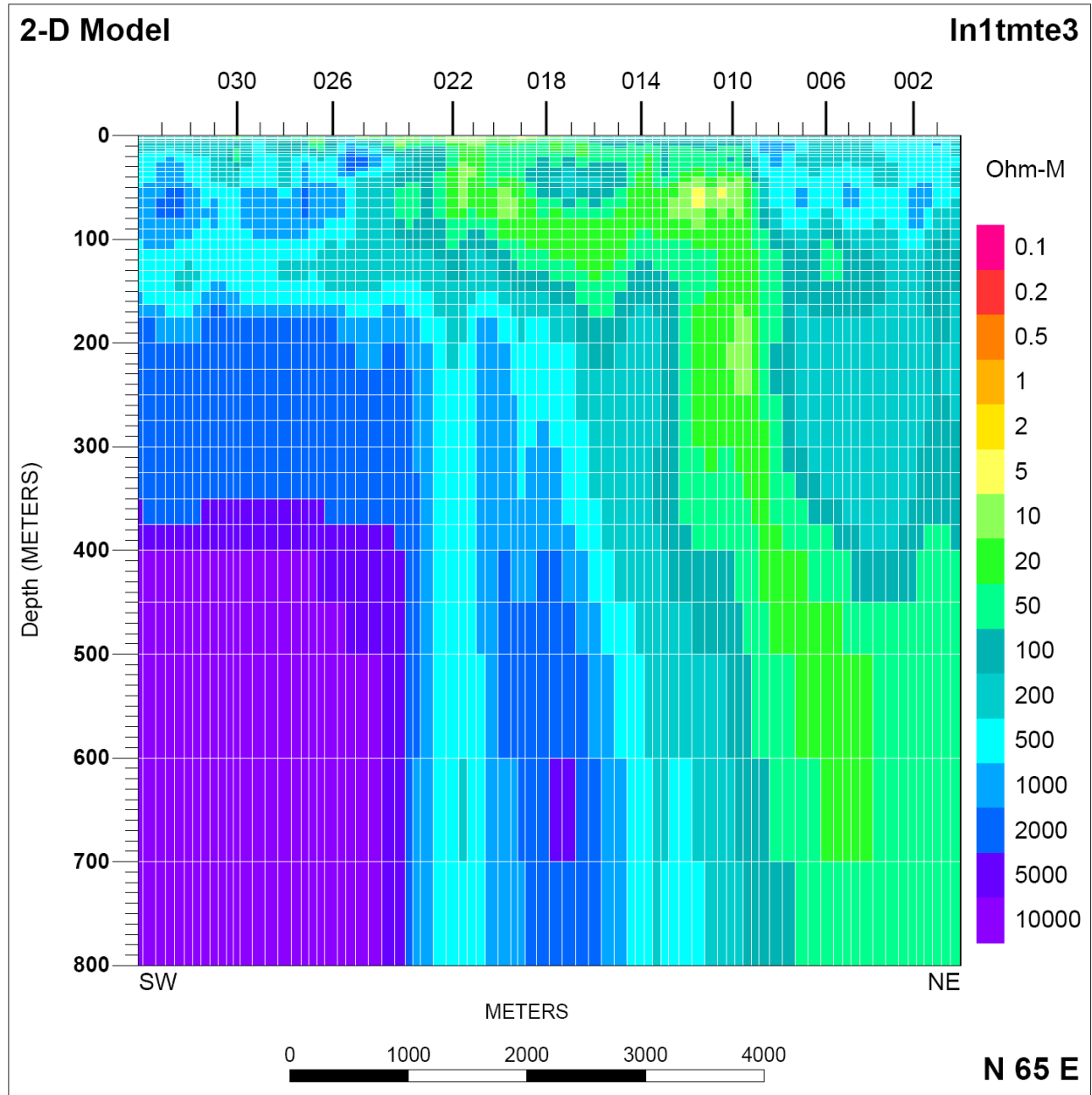


Figure A1-40. Line 1 impedance phase data for TE mode forward model, sites 1 – 6.



**Figure A1-41.** Line 1 2-D inversion modeling result for combined TM & TE modes without model mesh lines. Tic marks at top of model are projected AMT station locations. Vertical exaggeration is 8.3:1.



**Figure A1-42.** Line 1 2-D inversion modeling result for combined TM & TE modes with white model mesh lines. Tic marks at top of model are projected AMT station locations. Vertical exaggeration is 8.3:1.

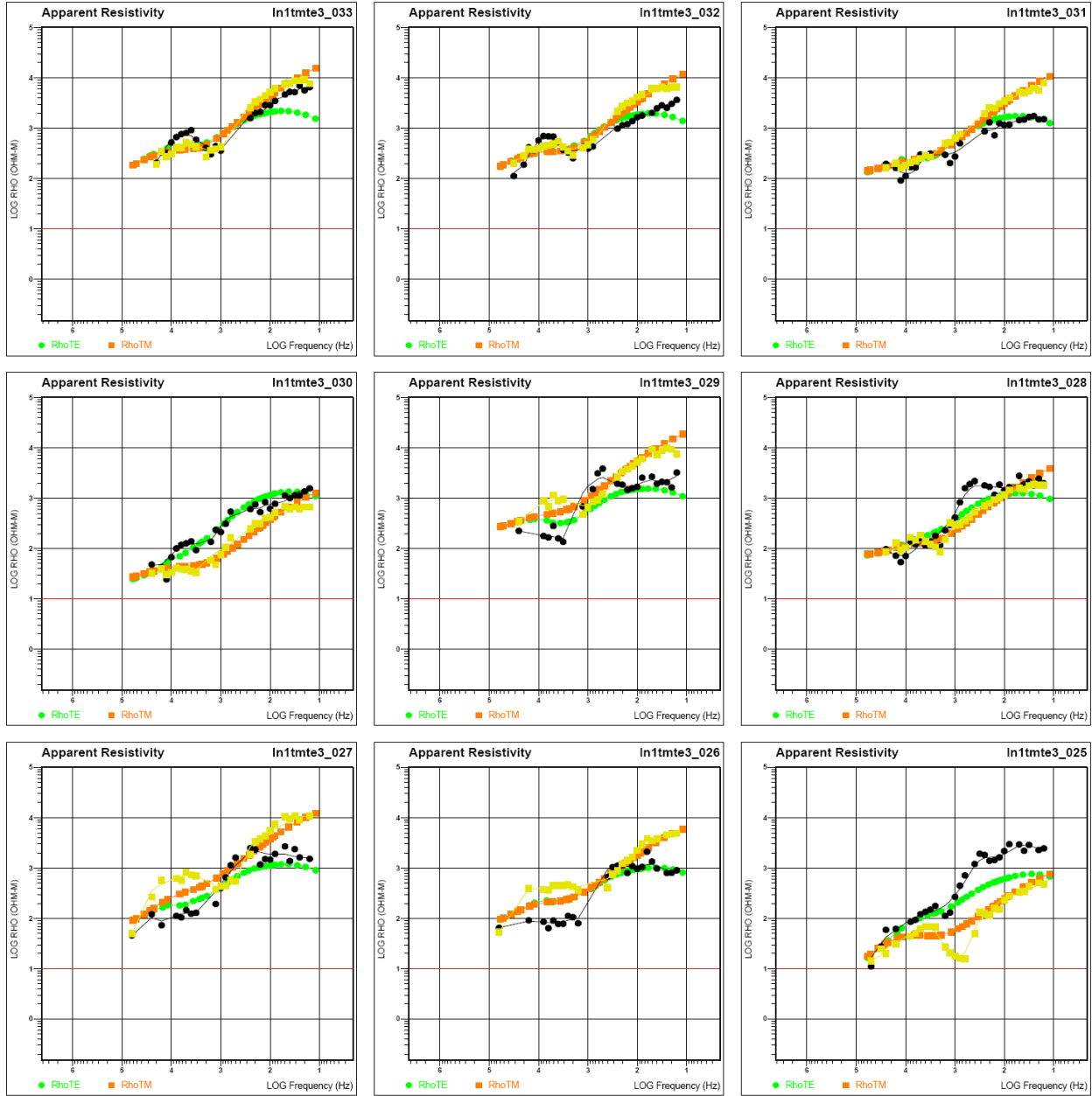
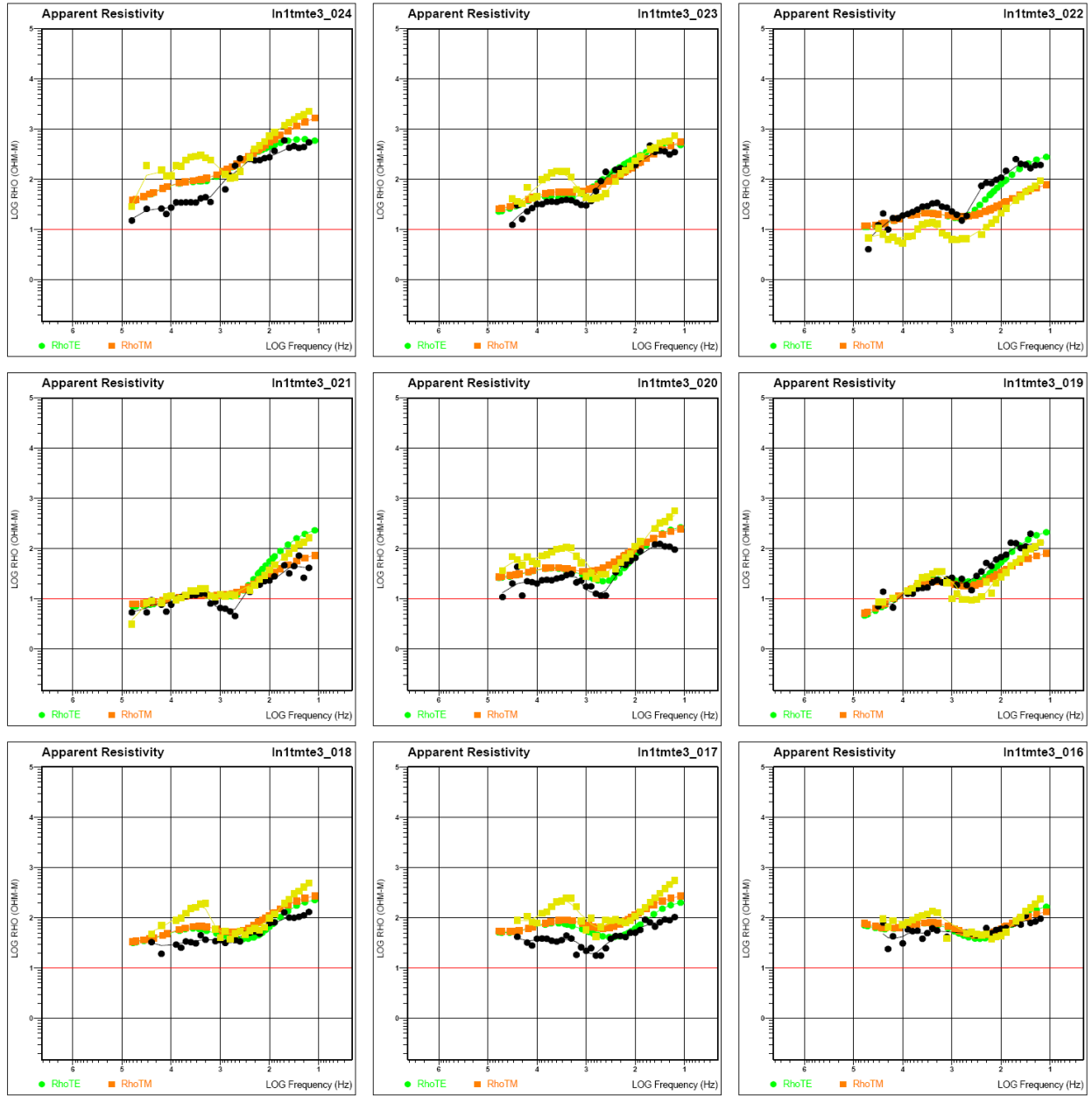


Figure A1-43. Line 1 impedance apparent resistivity data for mixed TMTE mode inversion model, sites 25



## Appendix 1 – Audio-Magnetotelluric Data and Models



**Figure A1-44.** Line 1 impedance apparent resistivity data for mixed TMTE mode inversion model, sites 16 – 24.

## Appendix 1 – Audio-Magnetotelluric Data and Models

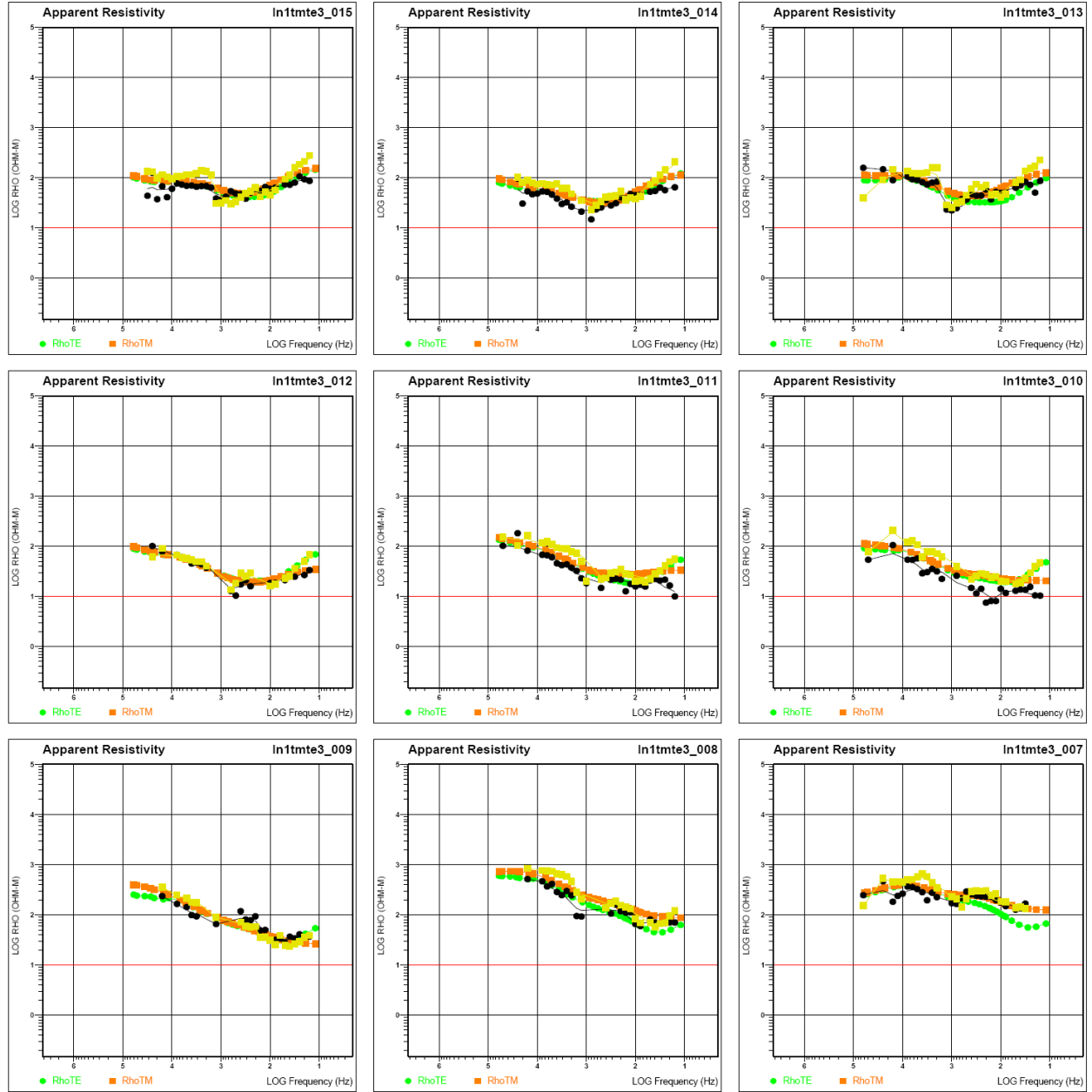
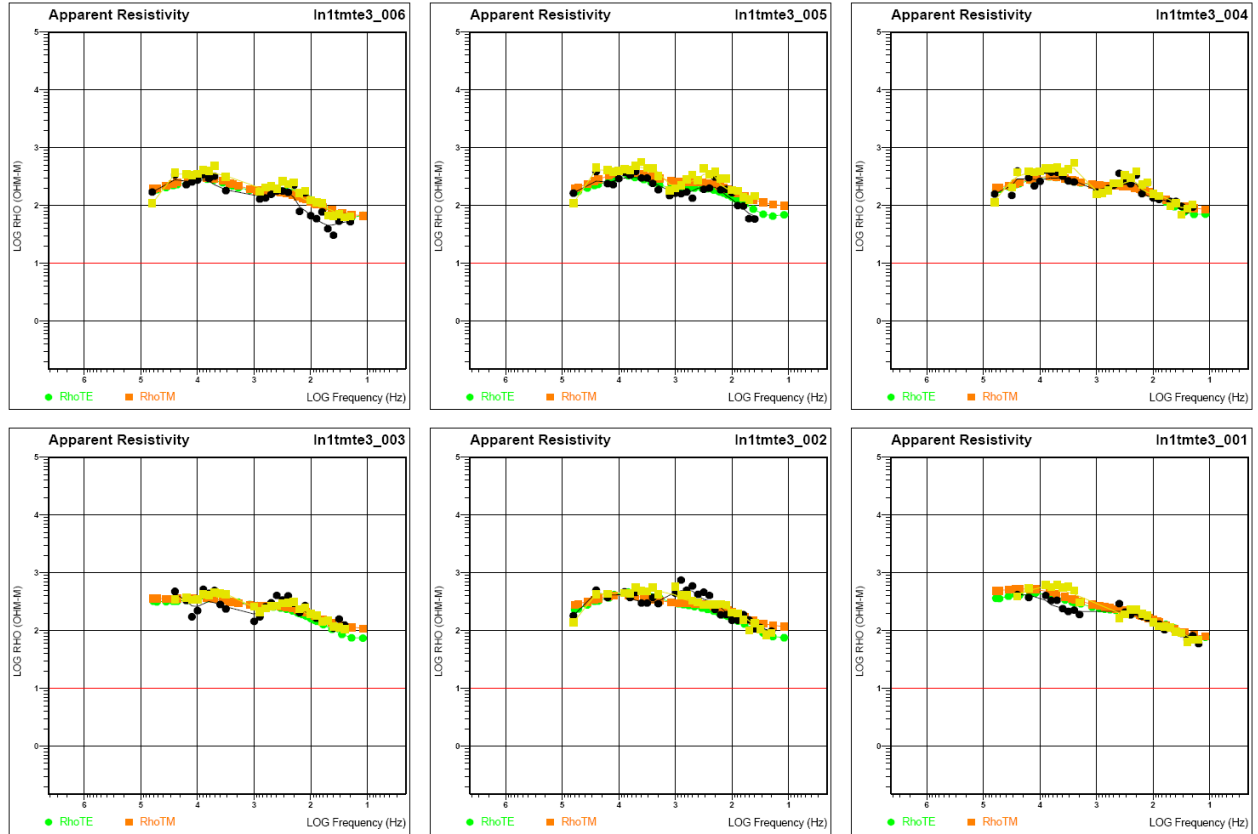


Figure A1-45. Line 1 impedance apparent resistivity data for mixed TMTE mode inversion model, sites 15 – 7.

## Appendix 1 – Audio-Magnetotelluric Data and Models



**Figure A1-46.** Line 1 impedance apparent resistivity data for mixed TMTE mode inversion model, sites 1 – 6.

## Appendix 1 – Audio-Magnetotelluric Data and Models

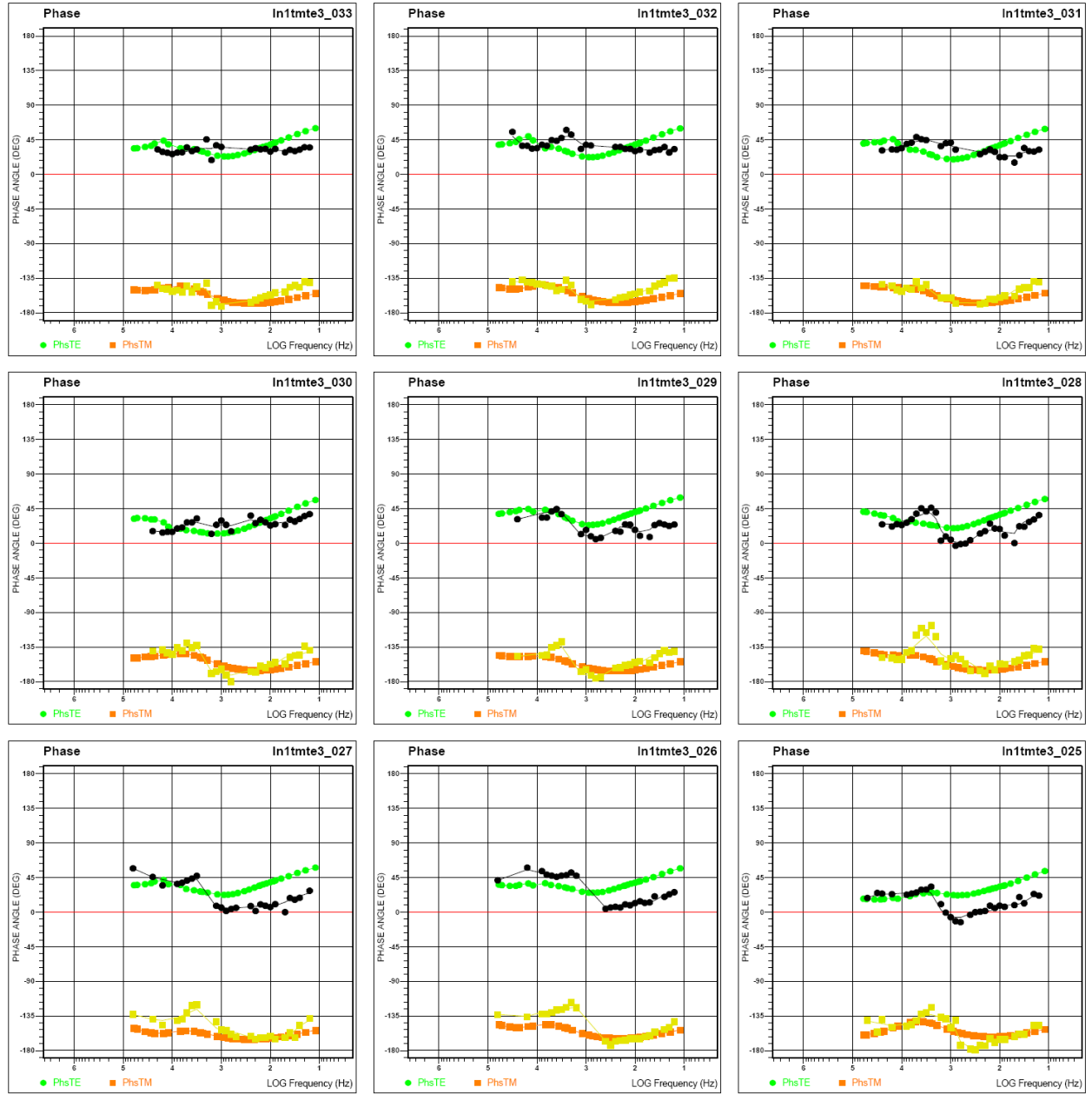


Figure A1-47. Line 1 impedance phase data for mixed TMTE mode inversion model, sites 25 – 33.

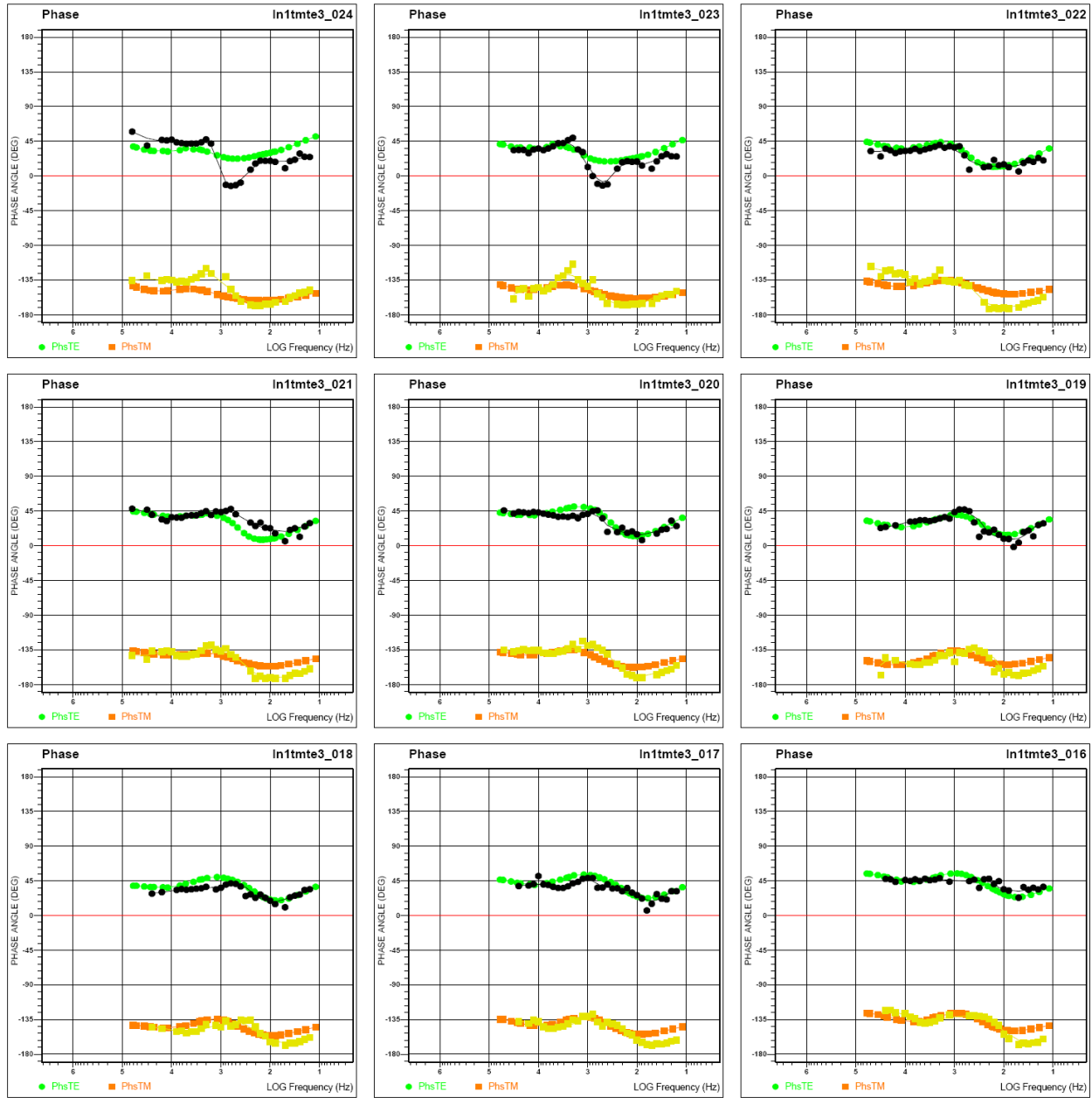


Figure A1-48. Line 1 impedance phase data for mixed TMTE mode inversion model, sites 16 – 24.

## Appendix 1 – Audio-Magnetotelluric Data and Models

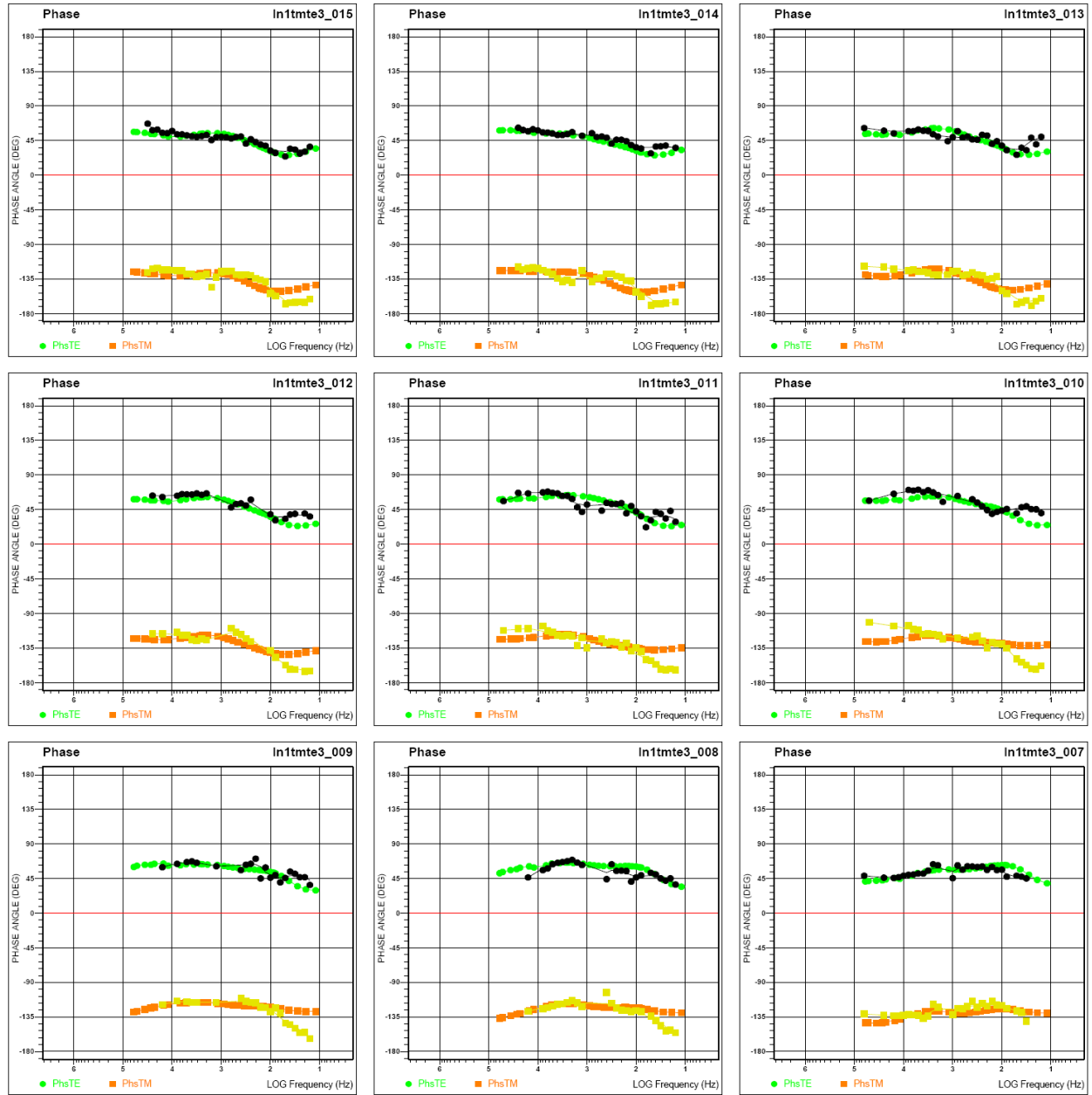


Figure A1-49. Line 1 impedance phase data for mixed TMTE mode inversion model, sites 7 – 15.

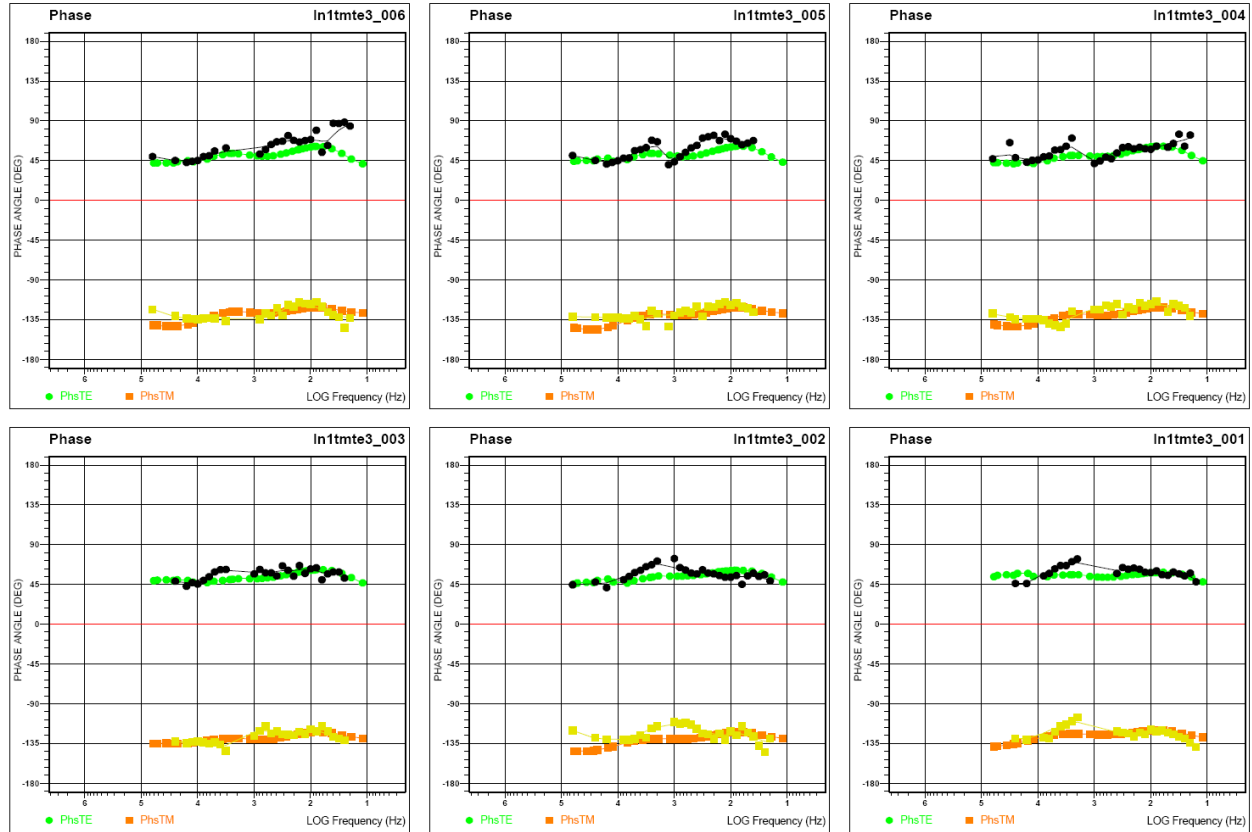


Figure A1-50. Line 1 impedance phase data for mixed TMTE mode inversion model, sites 1 – 6.

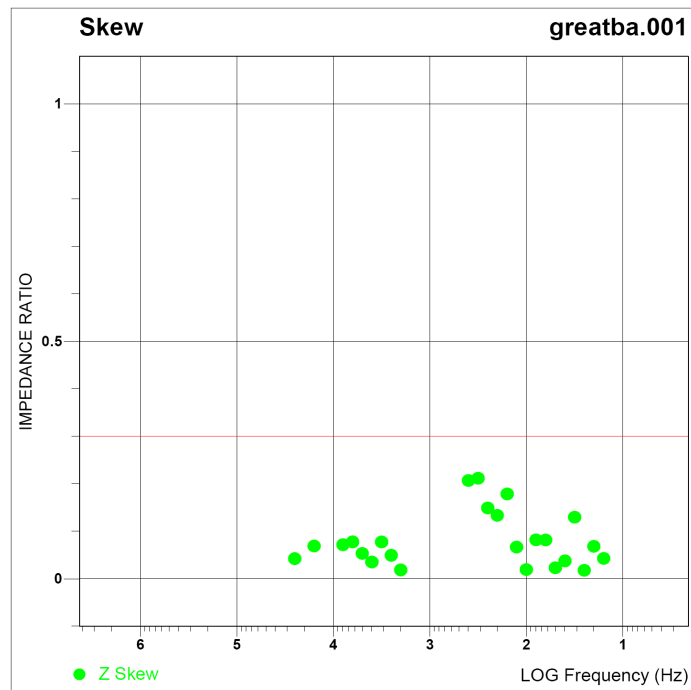


Figure A1-51. Line 1 impedance skew data for site 1.

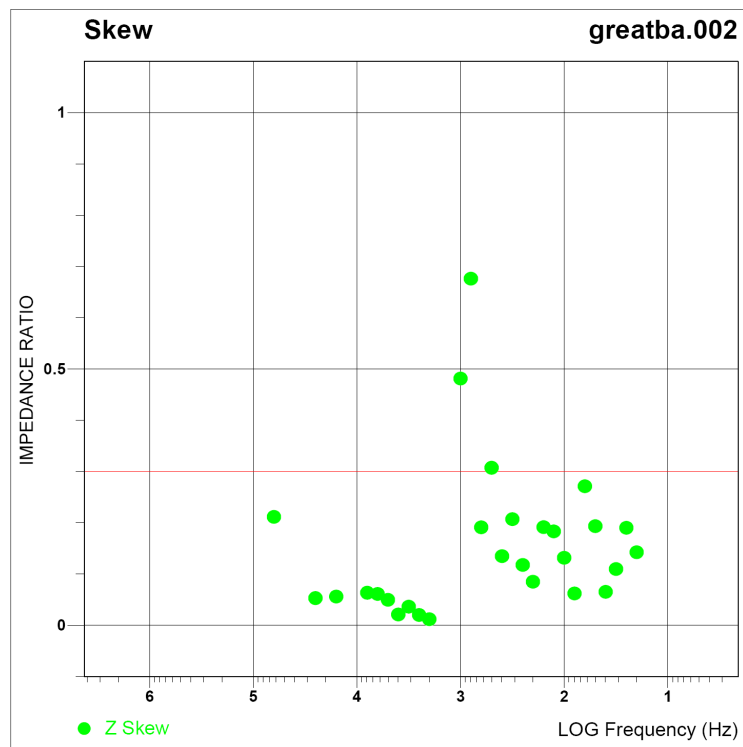


Figure A1-52. Line 1 impedance skew data for site 2.

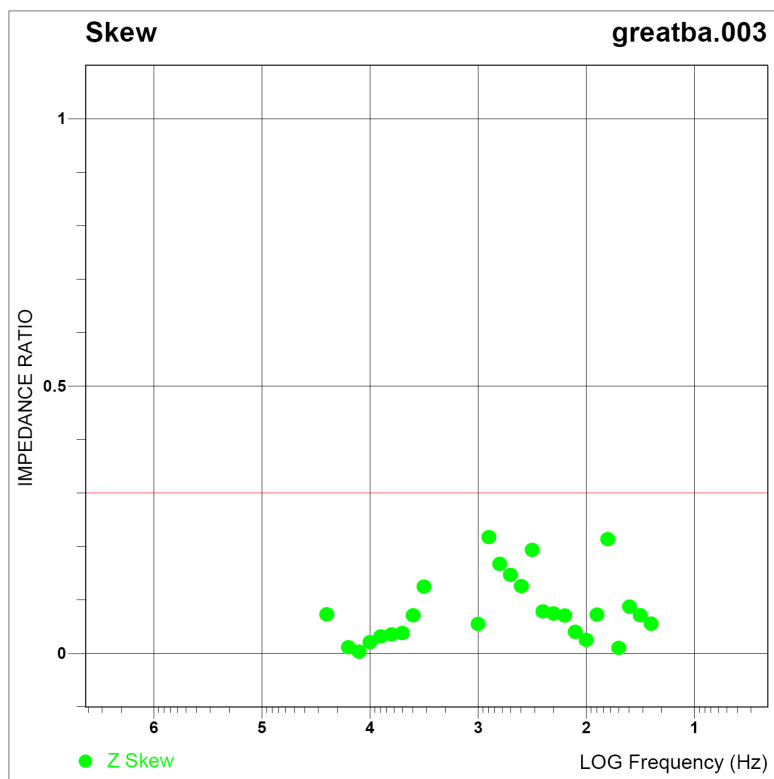


Figure A1-53. Line 1 impedance skew data for site 3.



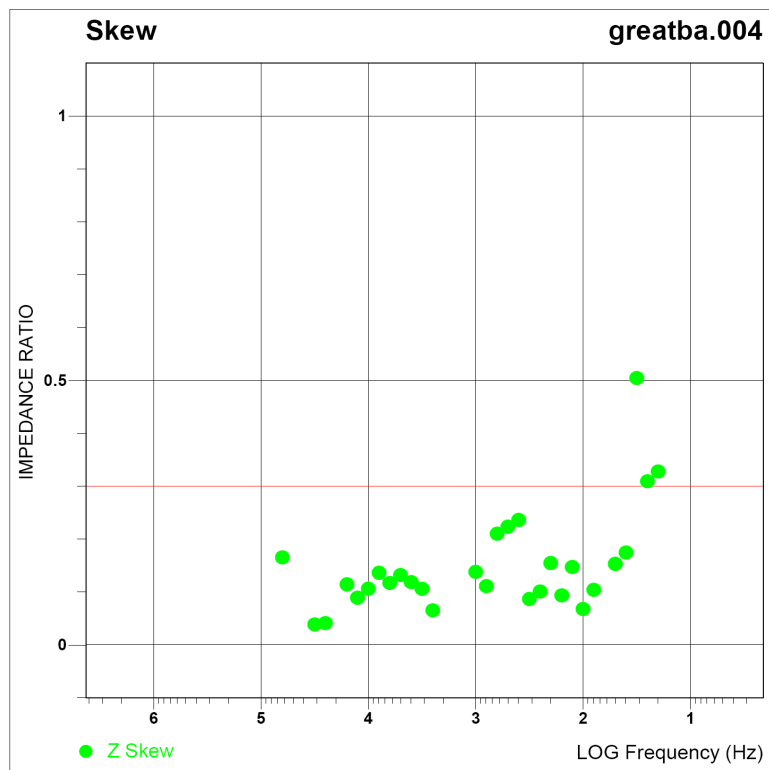


Figure A1-54. Line 1 impedance skew data for site 4.

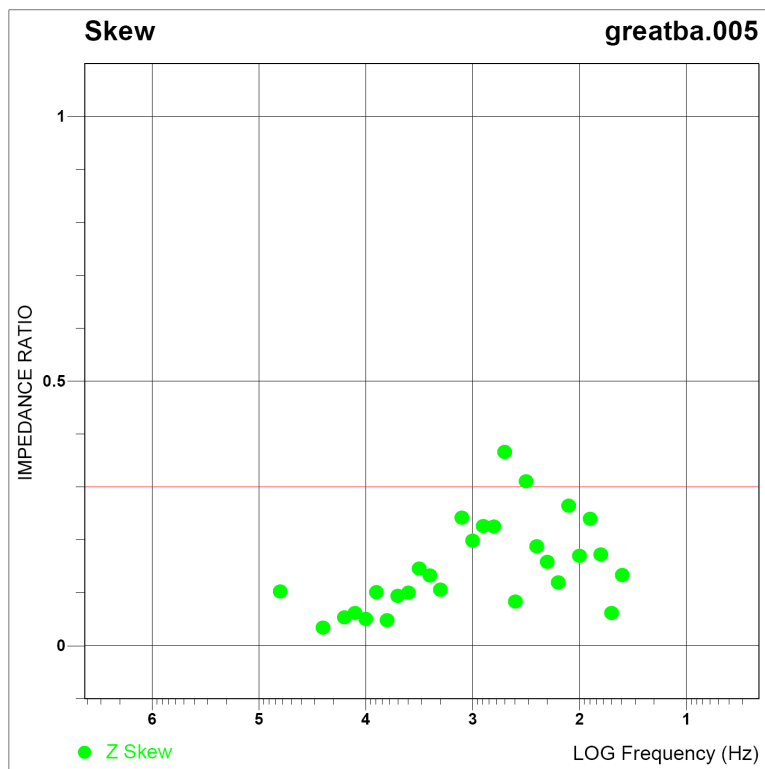


Figure A1-55. Line 1 impedance skew data for site 5.

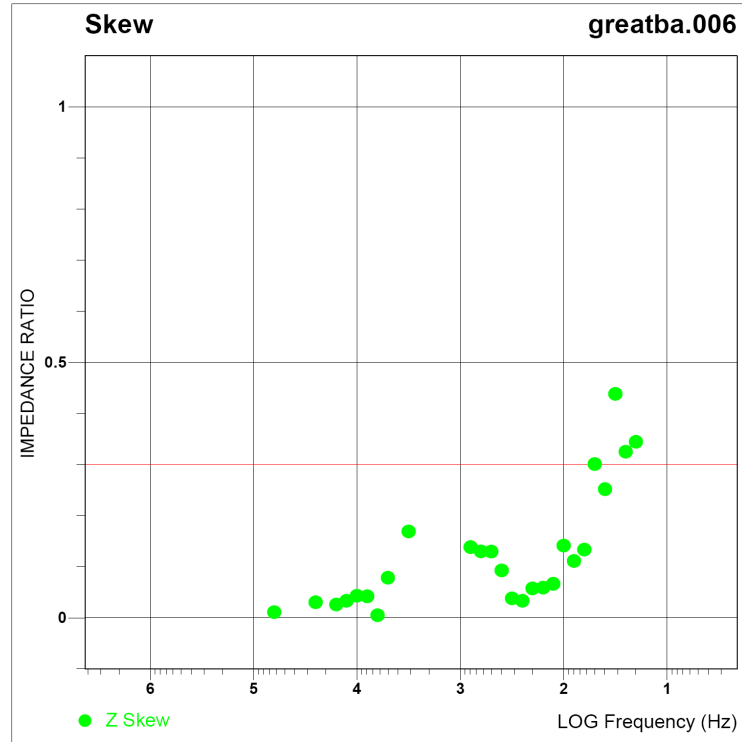


Figure A1-56. Line 1 impedance skew data for site 6.

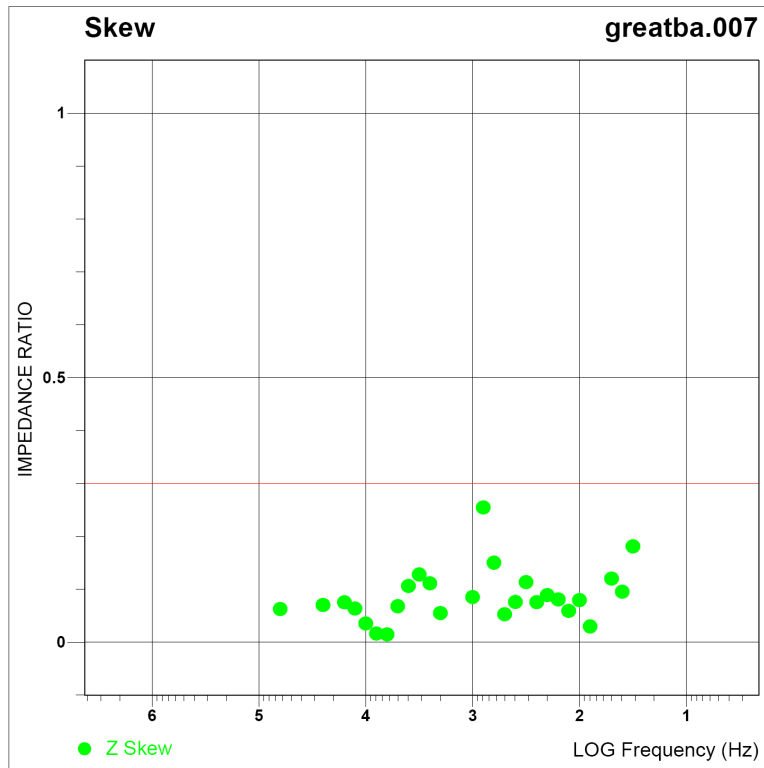


Figure A1-57. Line 1 impedance skew data for site 7.

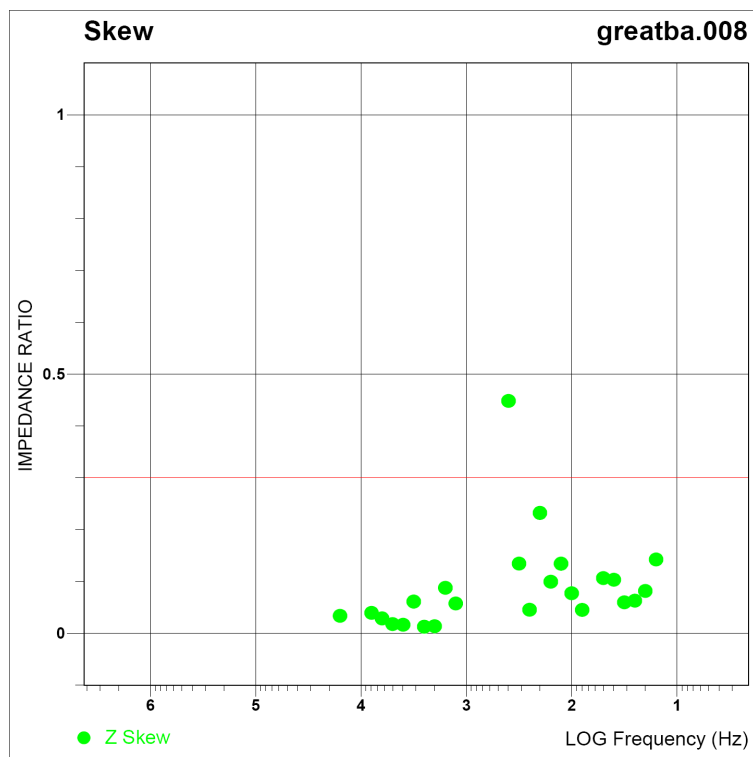


Figure A1-58. Line 1 impedance skew data for site 8.

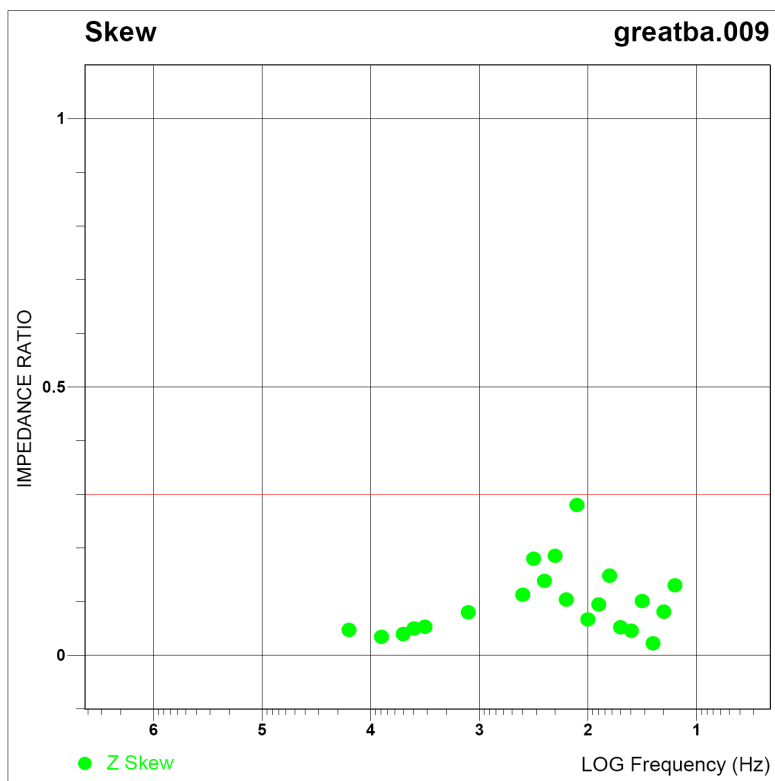


Figure A1-59. Line 1 impedance skew data for site 9.

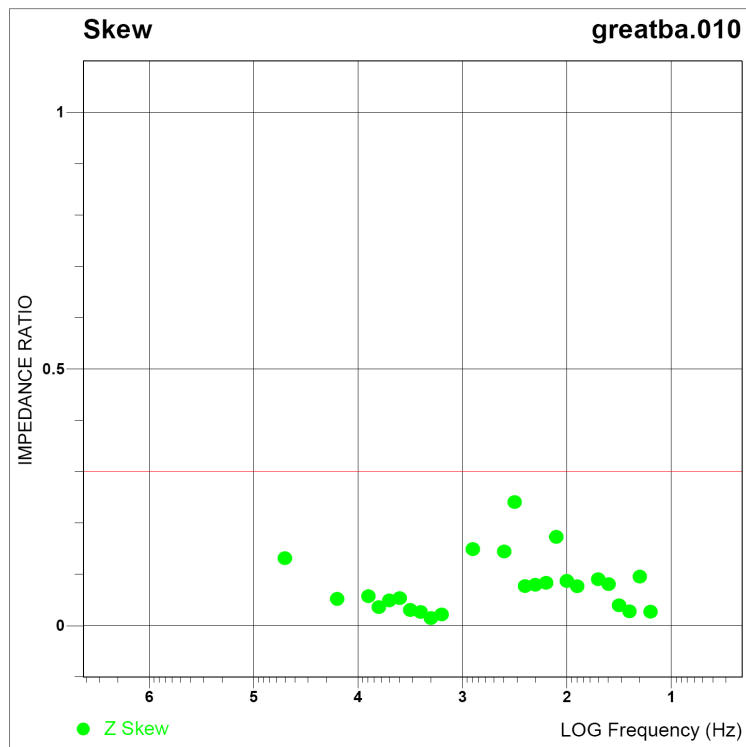


Figure A1-60. Line 1 impedance skew data for site 10.

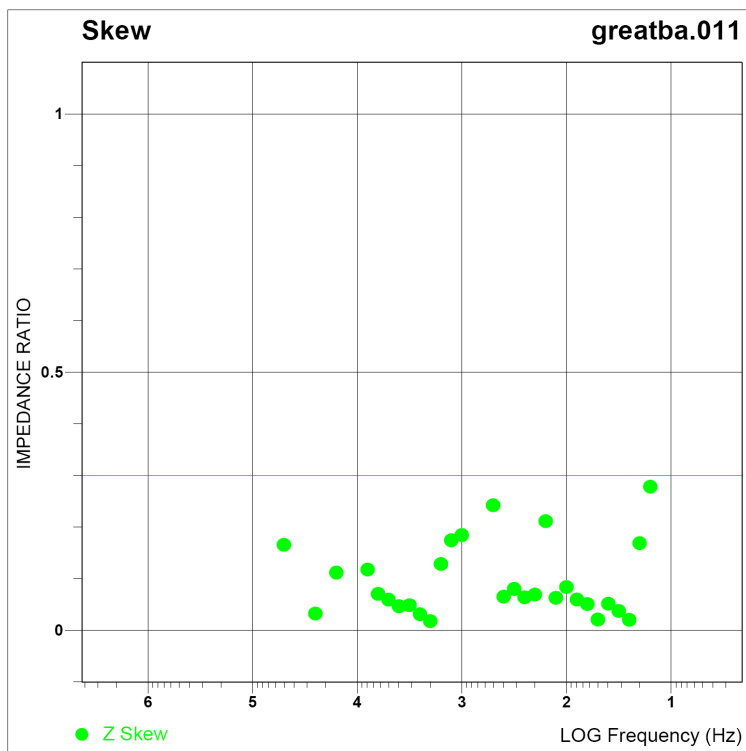


Figure A1-61. Line 1 impedance skew data for site 11.

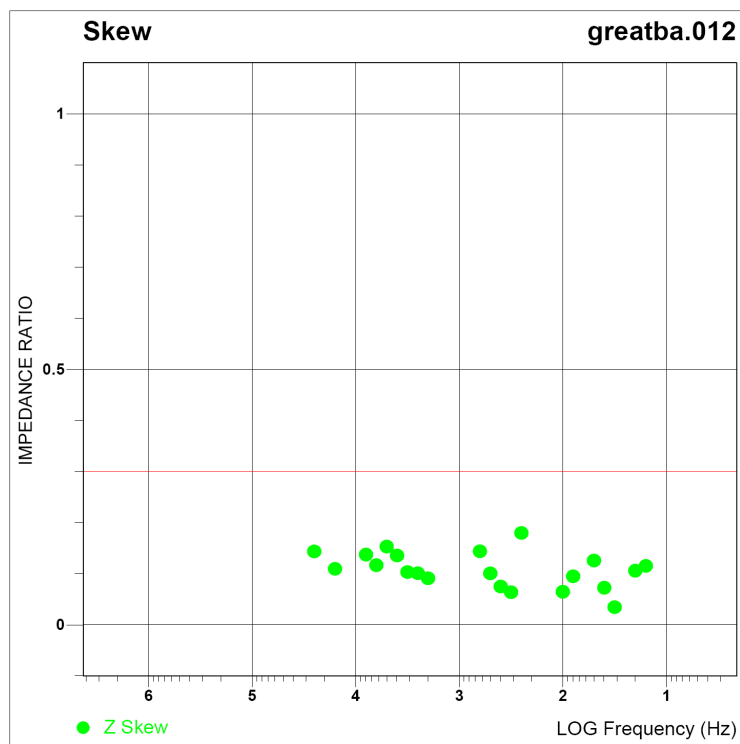


Figure A1-62. Line 1 impedance skew data for site 12.

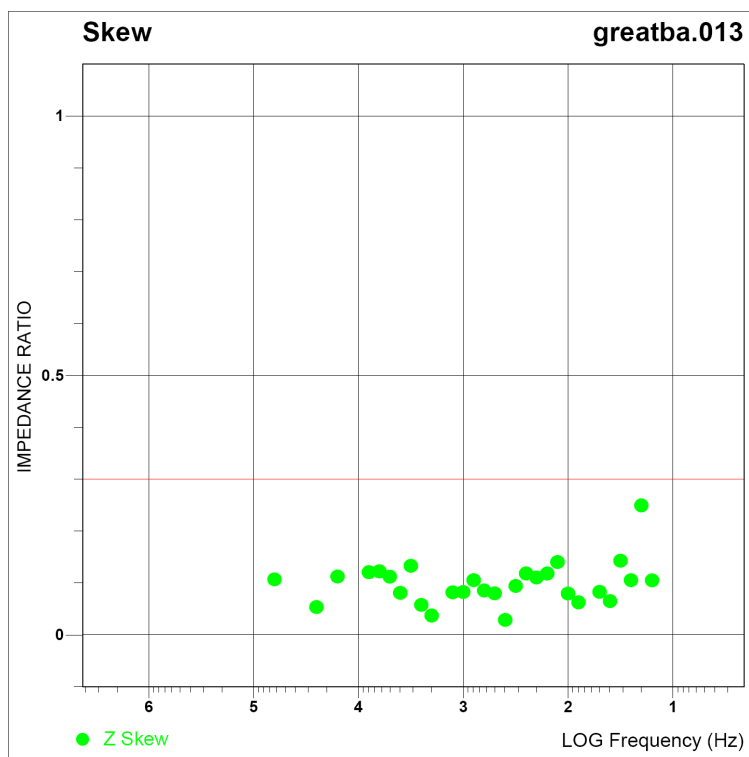


Figure A1-63. Line 1 impedance skew data for site 13.

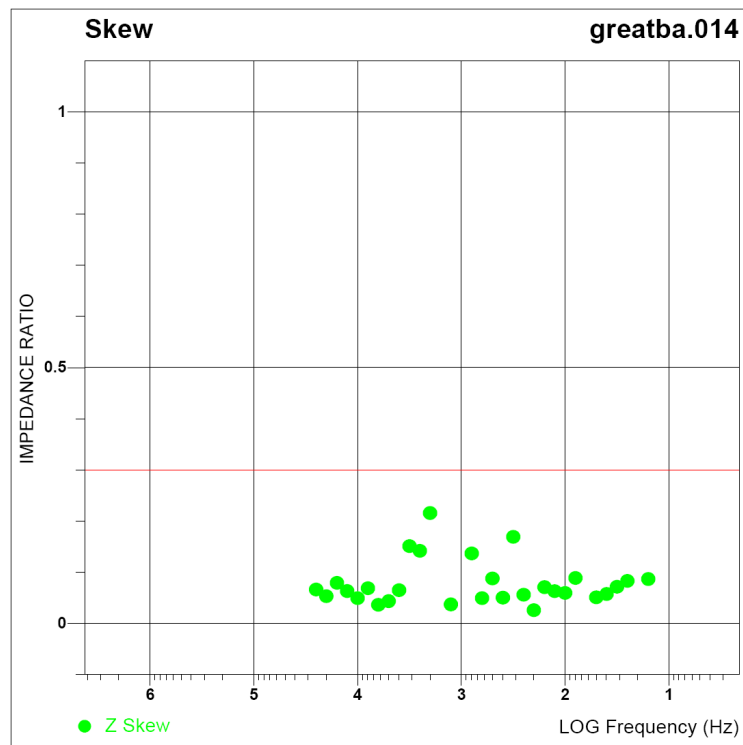


Figure A1-64. Line 1 impedance skew data for site 14.

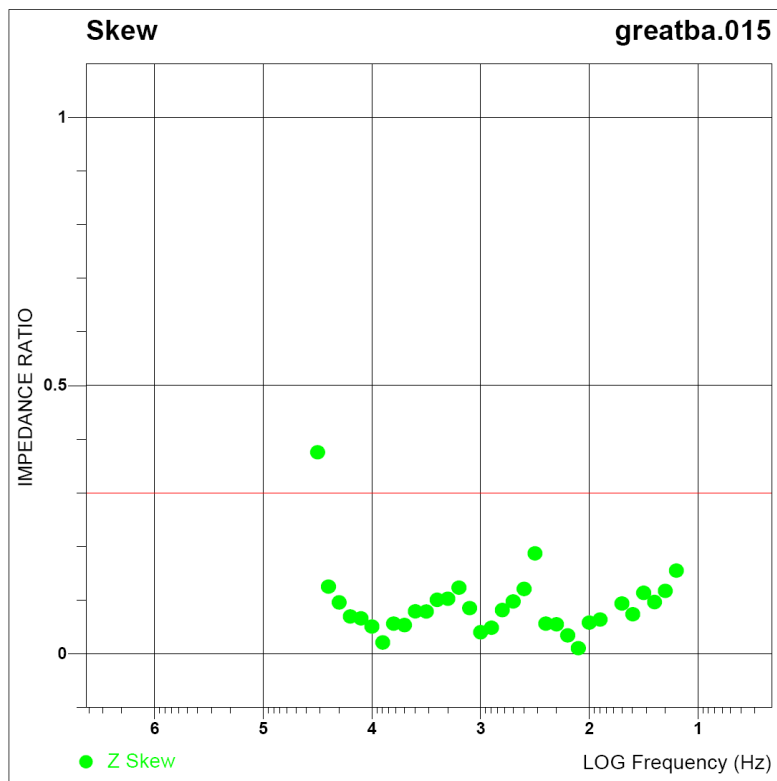


Figure A1-65. Line 1 impedance skew data for site 15.

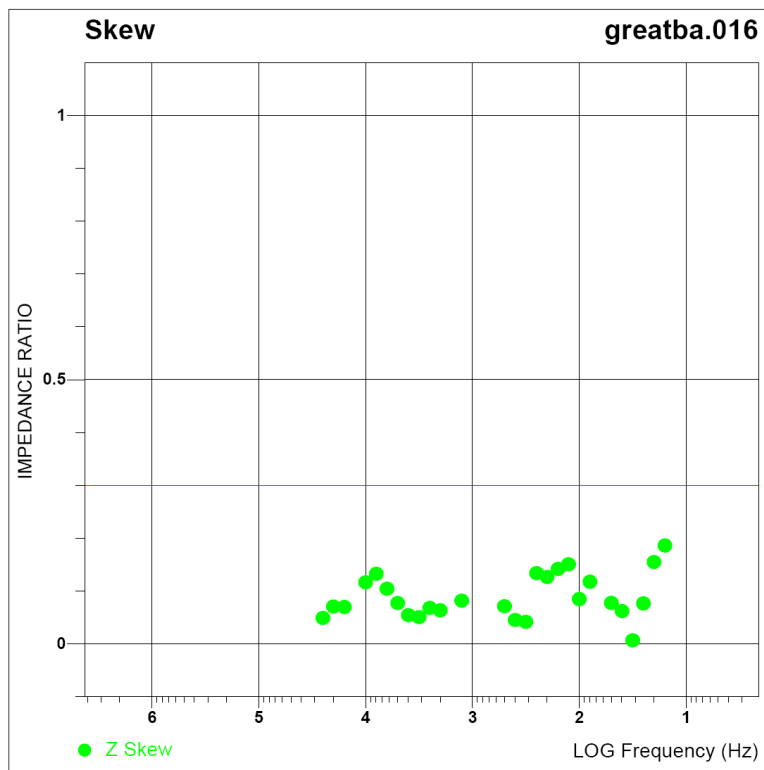


Figure A1-66. Line 1 impedance skew data for site 16.

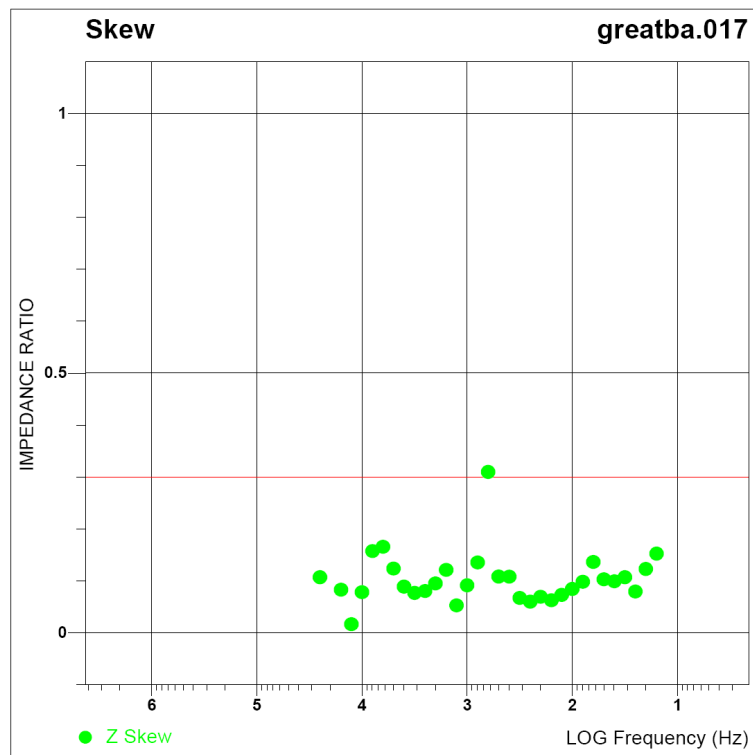


Figure A1-67. Line 1 impedance skew data for site 17.

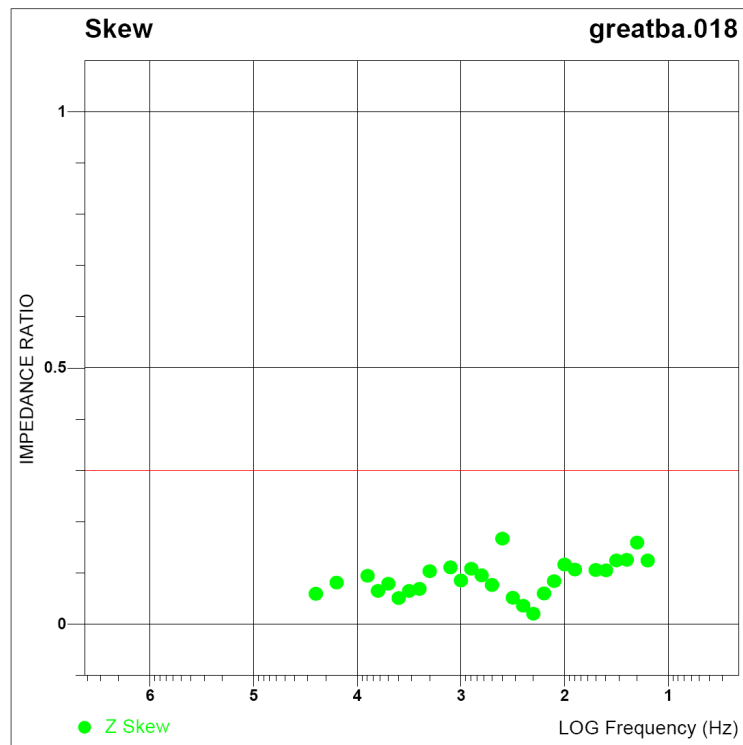


Figure A1-68. Line 1 impedance skew data for site 18.

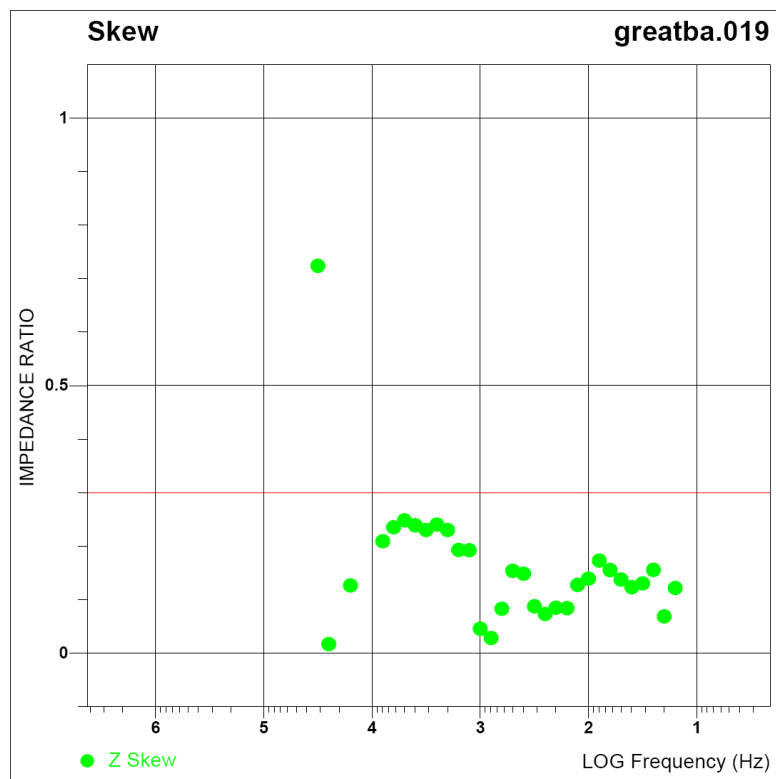


Figure A1-69. Line 1 impedance skew data for site 19.



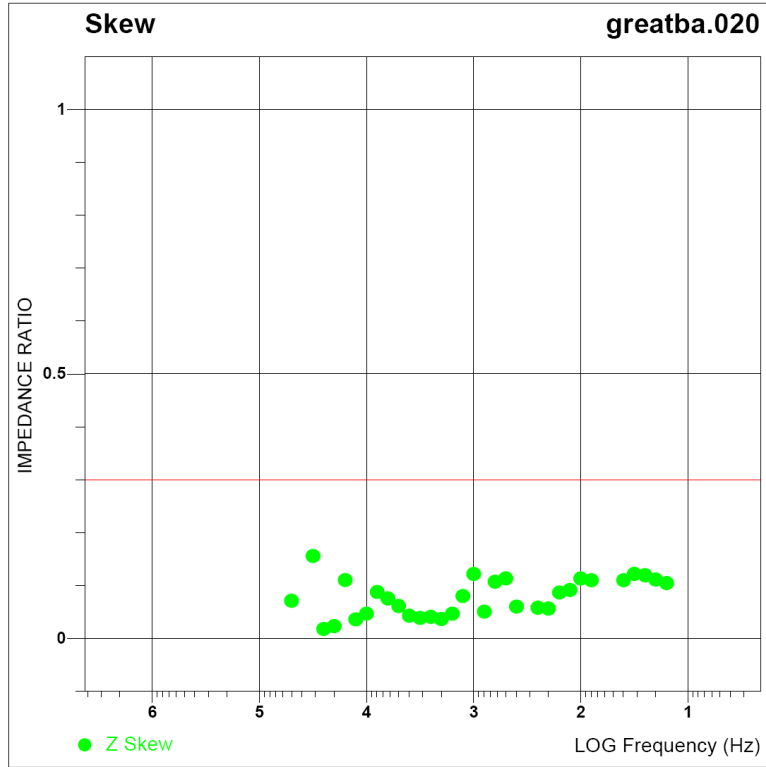


Figure A1-70. Line 1 impedance skew data for site 20.

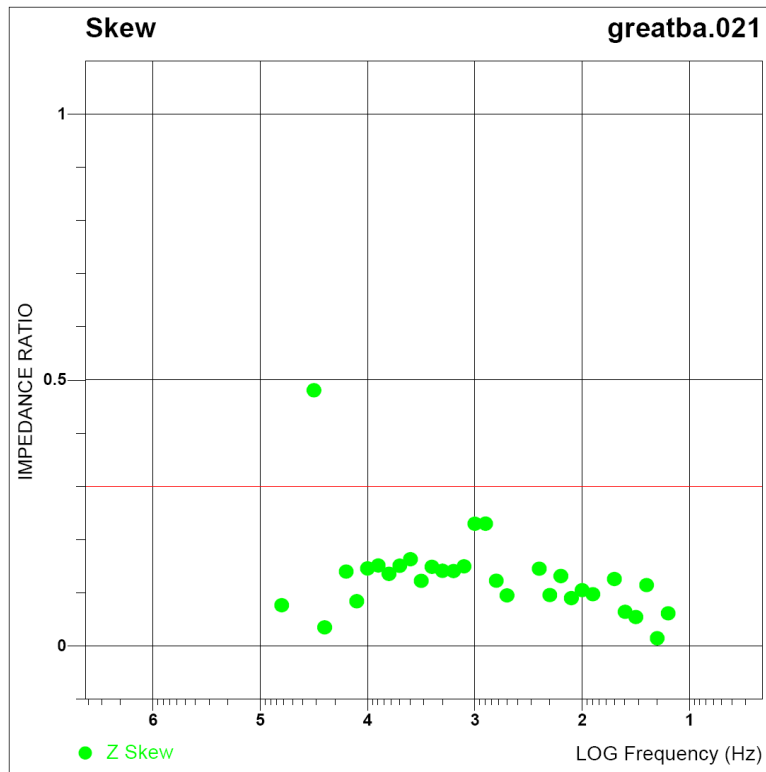
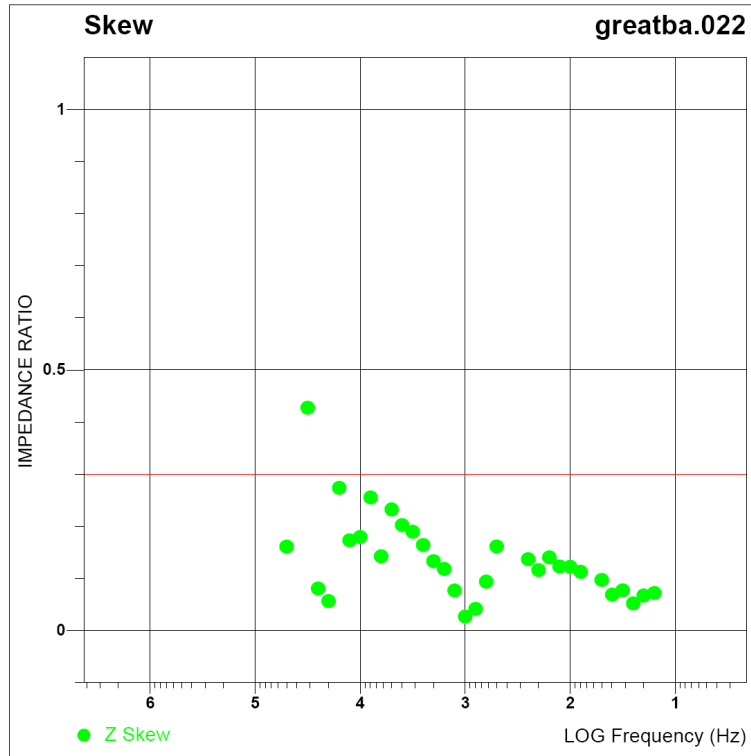
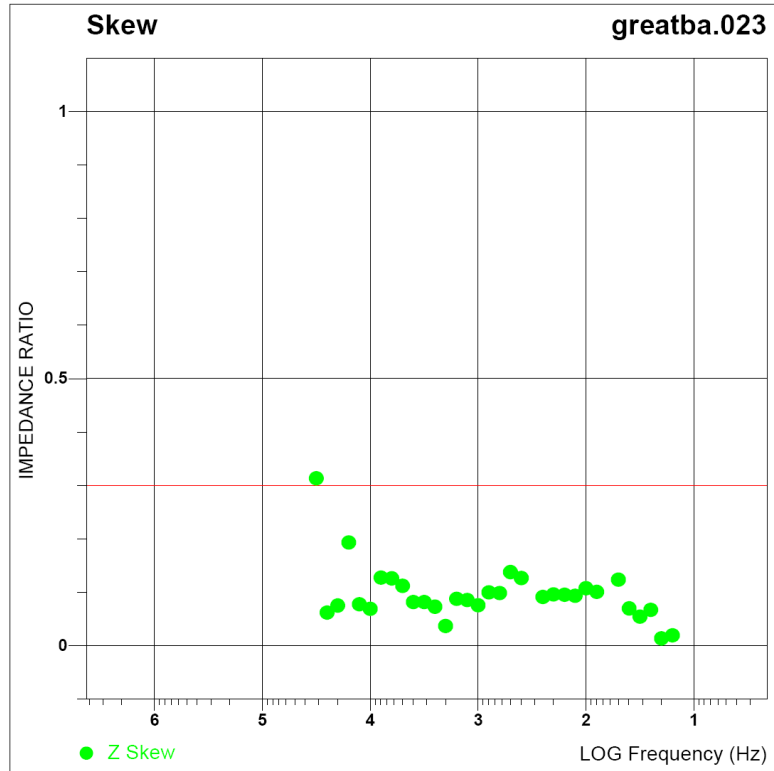


Figure A1-71. Line 1 impedance skew data for site 21.



**Figure A1-72.** Line 1 impedance skew data for site 22.



**Figure A1-73.** Line 1 impedance skew data for site 23.

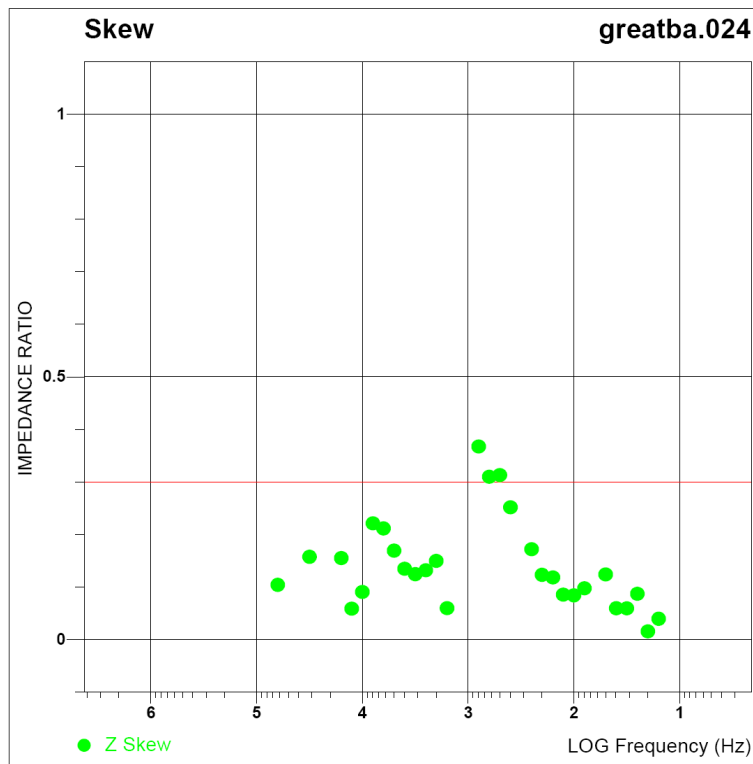


Figure A1-74. Line 1 impedance skew data for site 24.

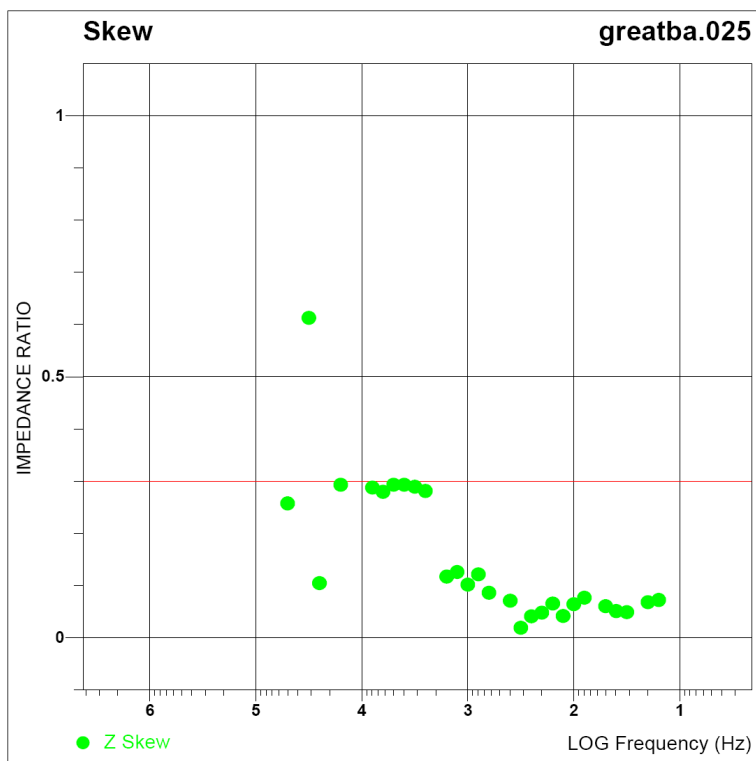


Figure A1-75. Line 1 impedance skew data for site 25.

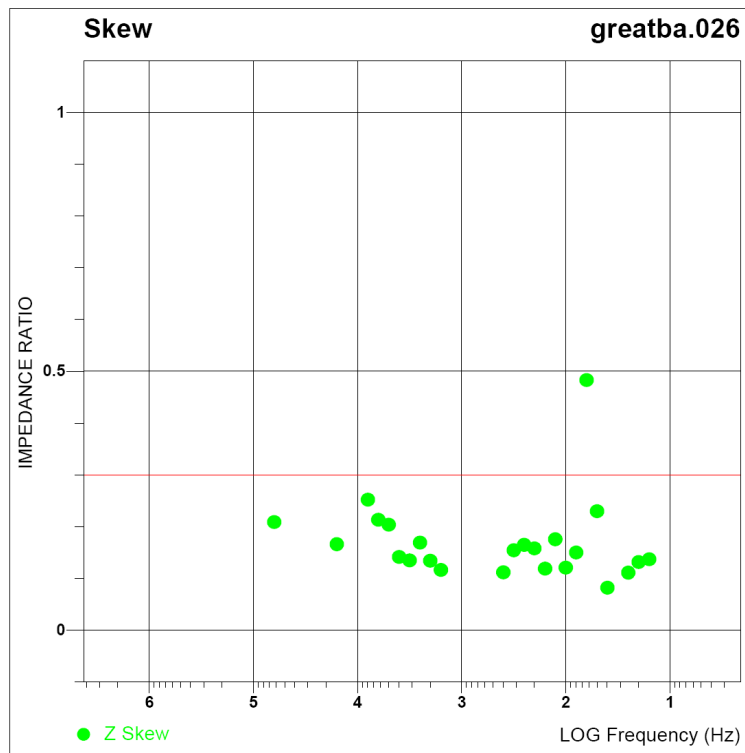


Figure A1-76. Line 1 impedance skew data for site 26.

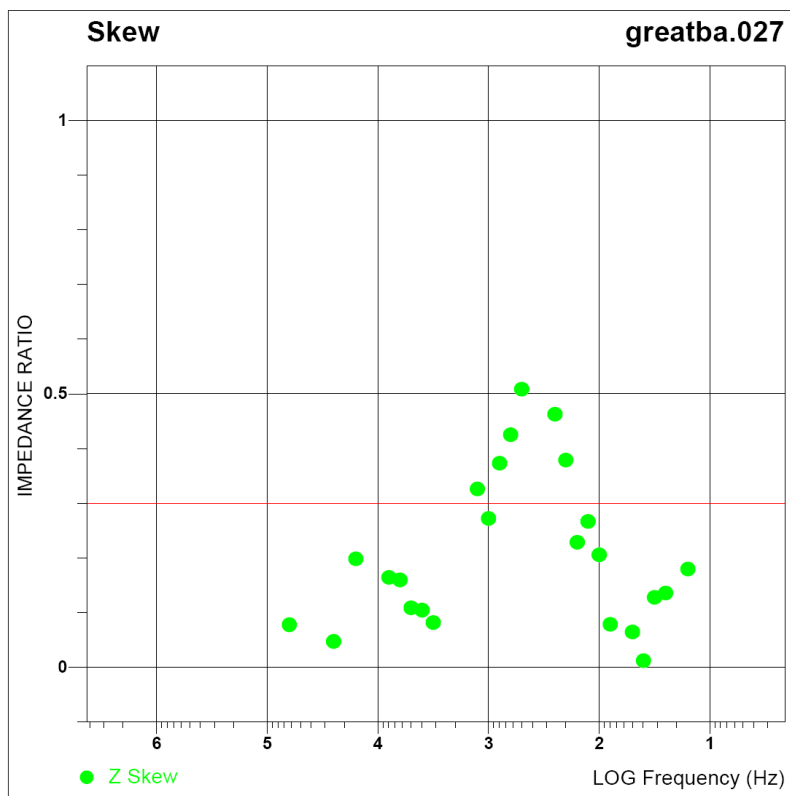


Figure A1-77. Line 1 impedance skew data for site 27.

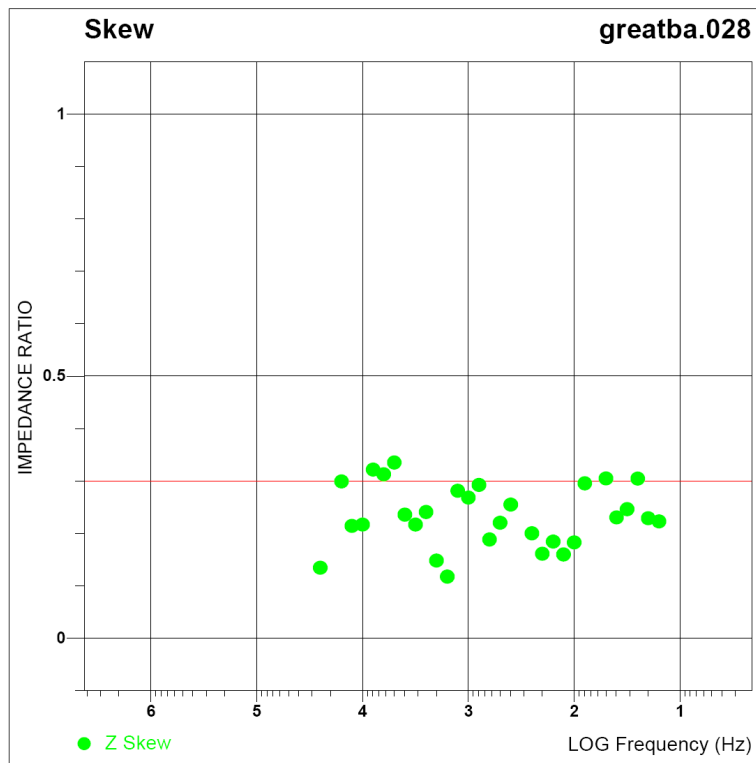


Figure A1-78. Line 1 impedance skew data for site 28.

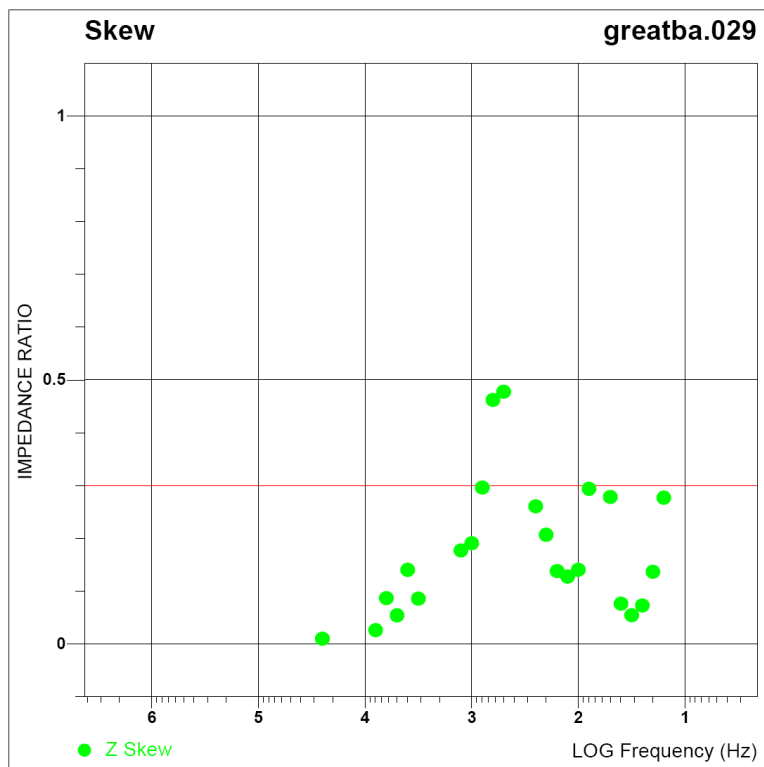


Figure A1-79. Line 1 impedance skew data for site 29.

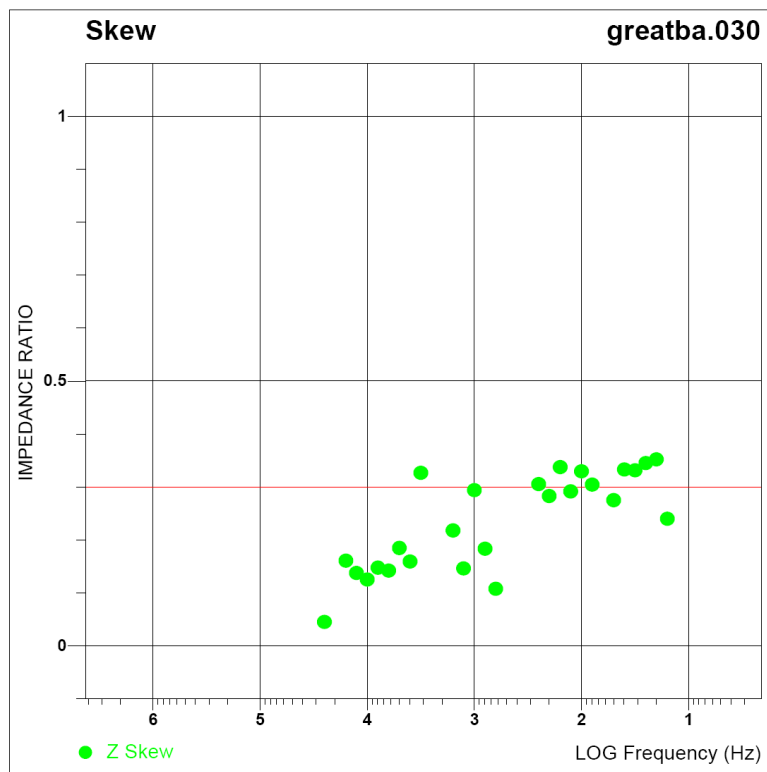


Figure A1-80. Line 1 impedance skew data for site 30.

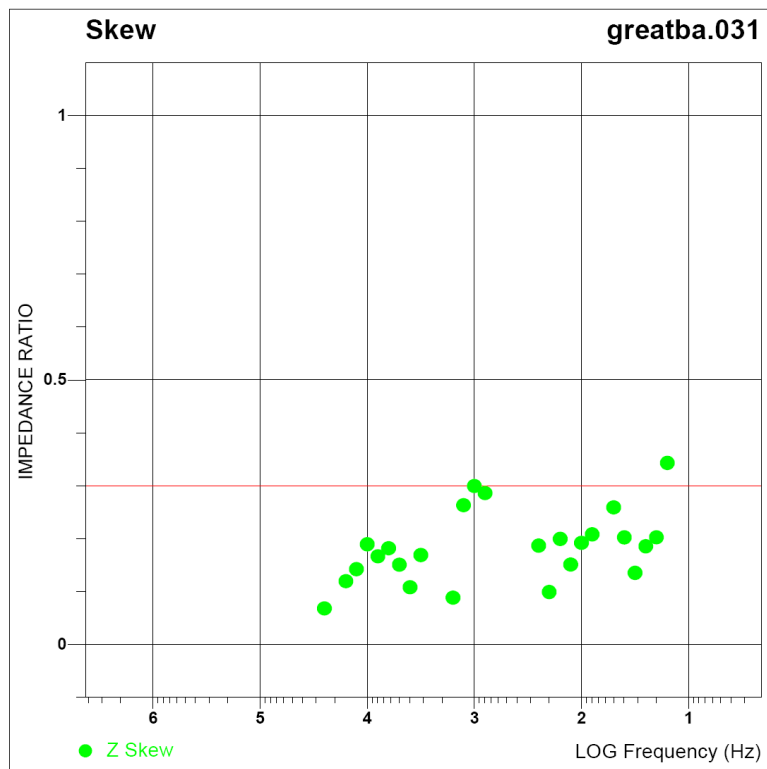


Figure A1-81. Line 1 impedance skew data for site 31.

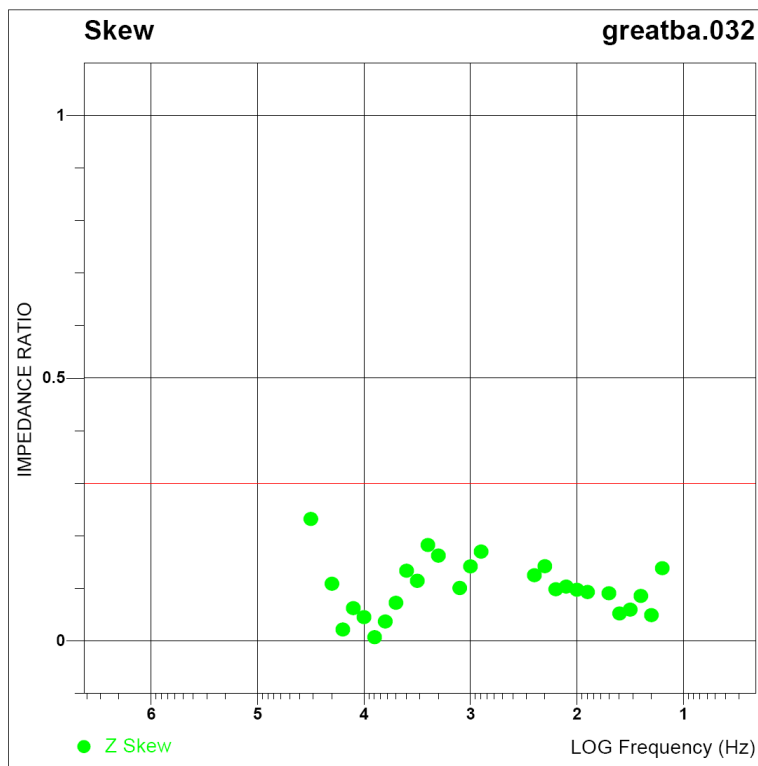


Figure A1-82. Line 1 impedance skew data for site 32.

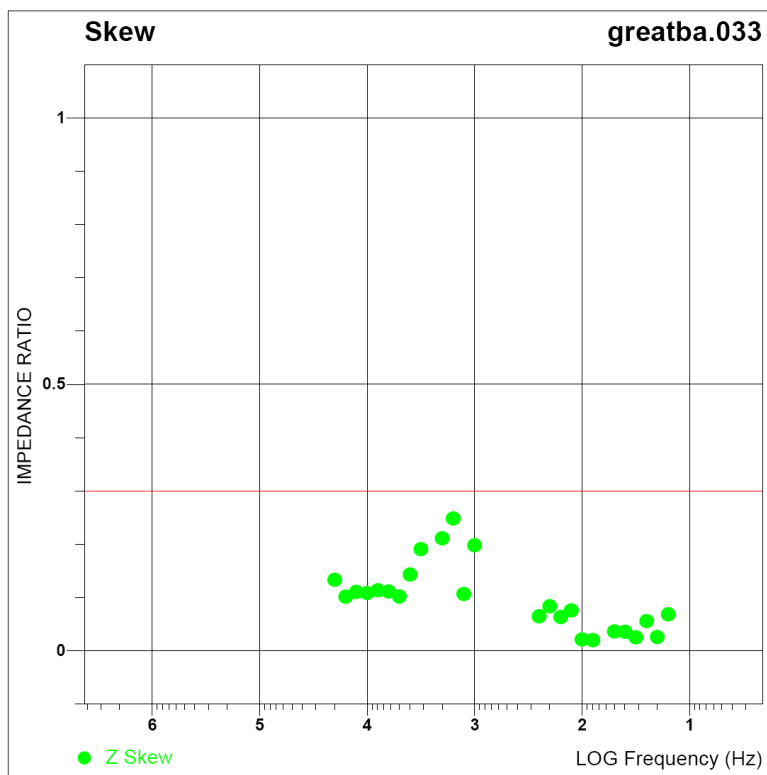


Figure A1-83. Line 1 impedance skew data for site 33.

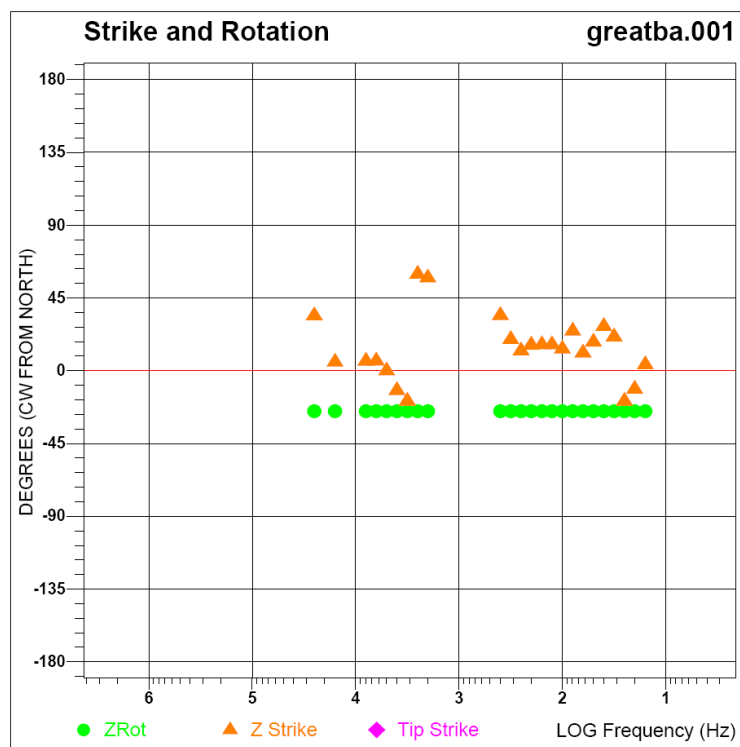


Figure A1-84. Line 1 impedance strike data for site 1.

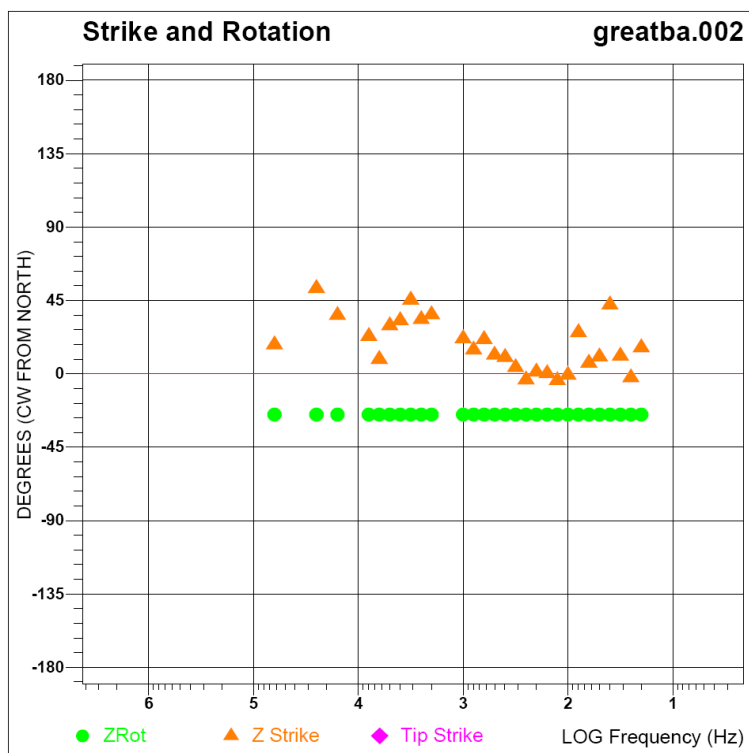


Figure A1-85. Line 1 impedance strike data for site 2.



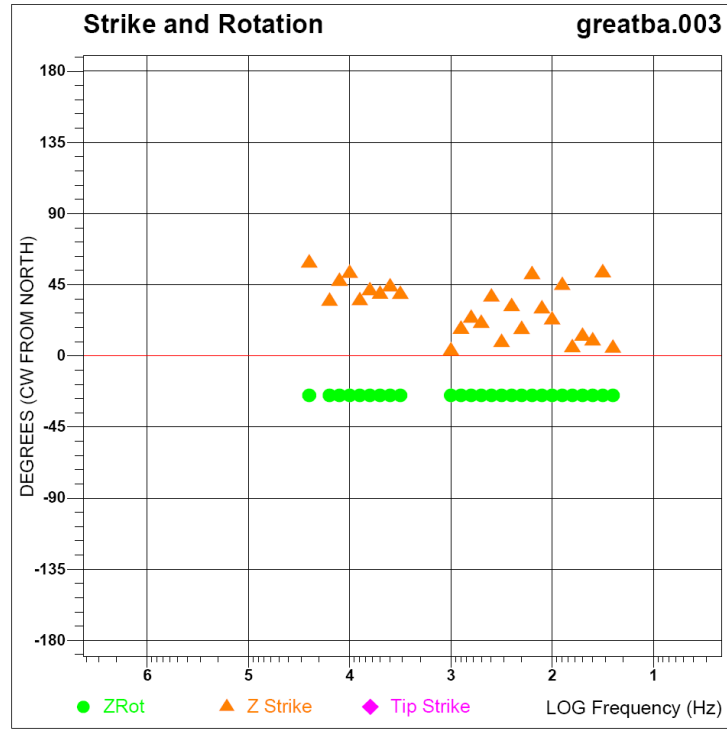


Figure A1-86. Line 1 impedance strike data for site 3.

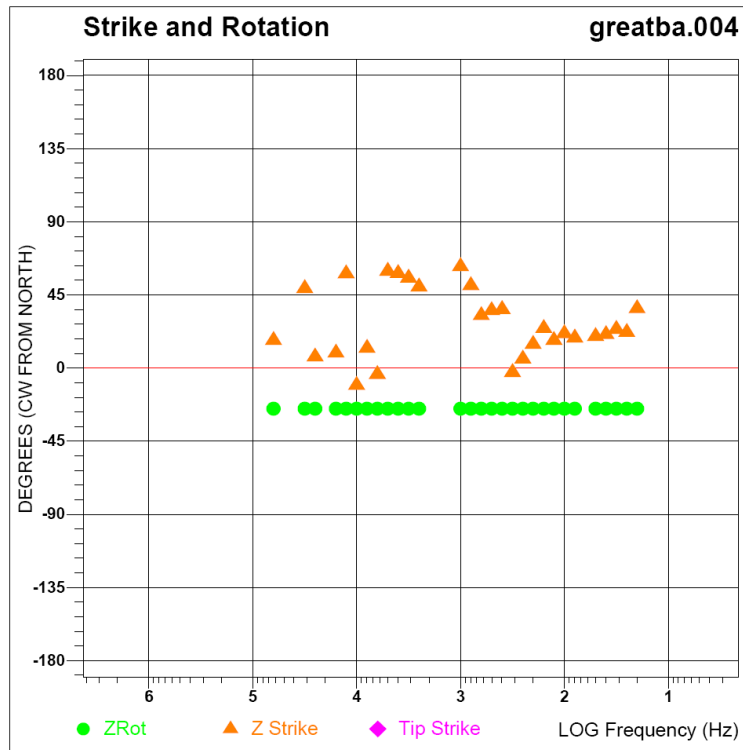


Figure A1-87. Line 1 impedance strike data for site 4.

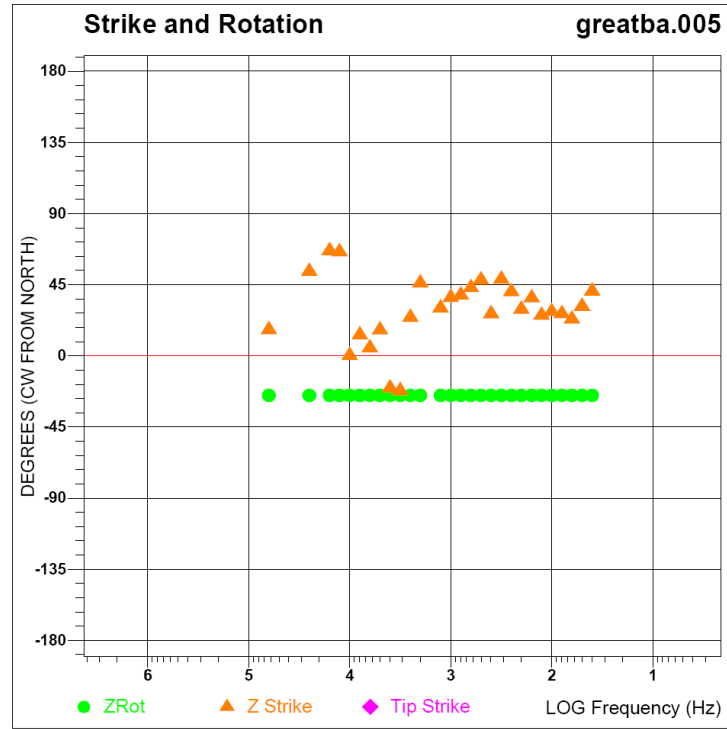


Figure A1-88. Line 1 impedance strike data for site 5.

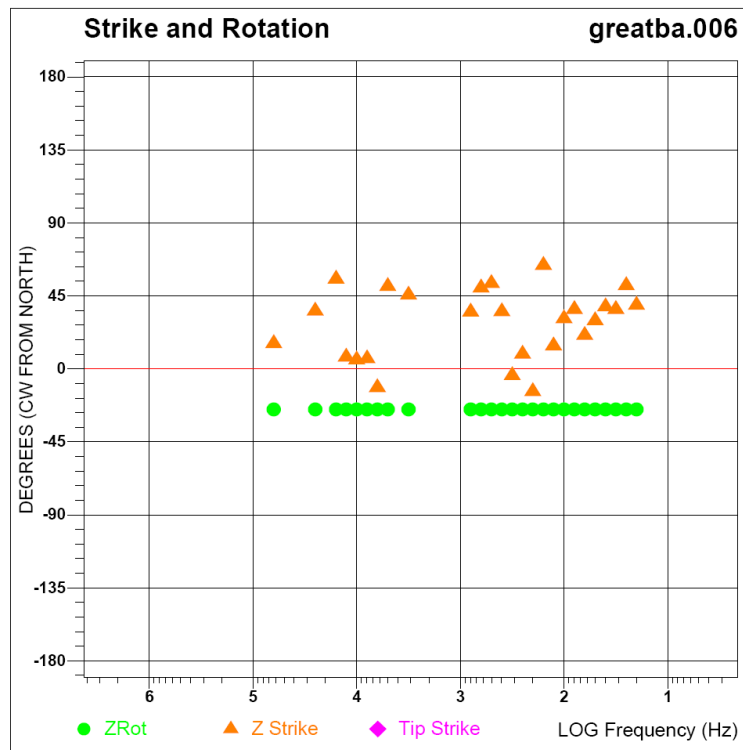


Figure A1-89. Line 1 impedance strike data for site 6.

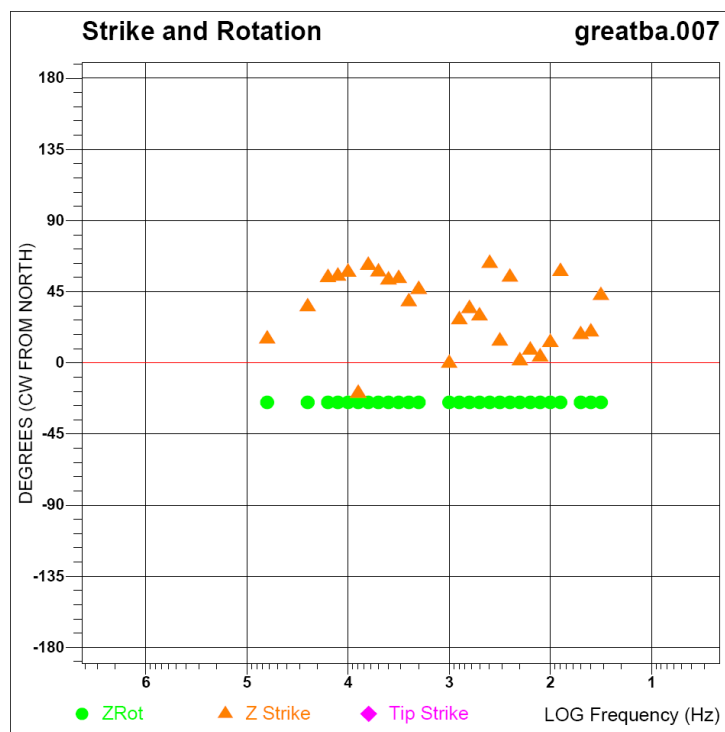


Figure A1-90. Line 1 impedance strike data for site 7.

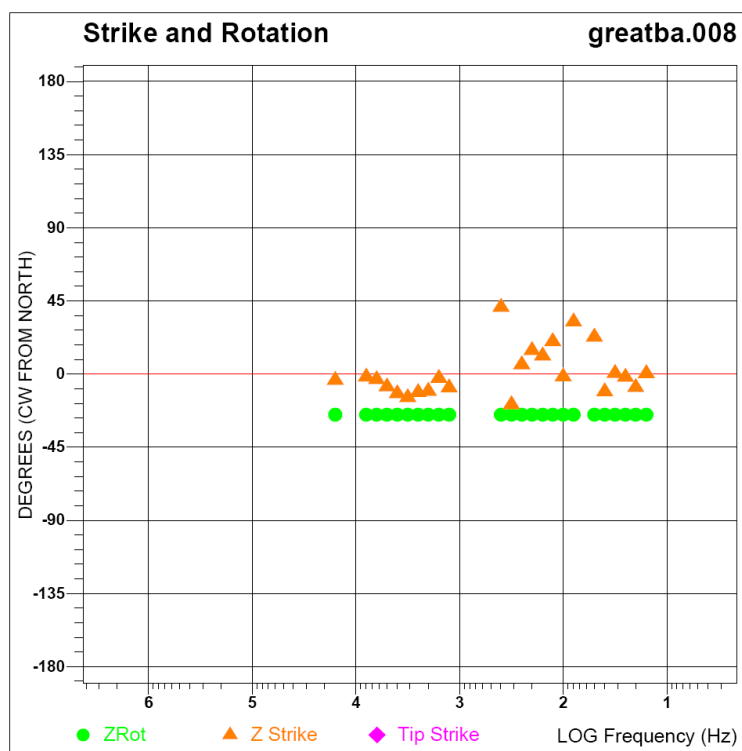


Figure A1-91. Line 1 impedance strike data for site 8.

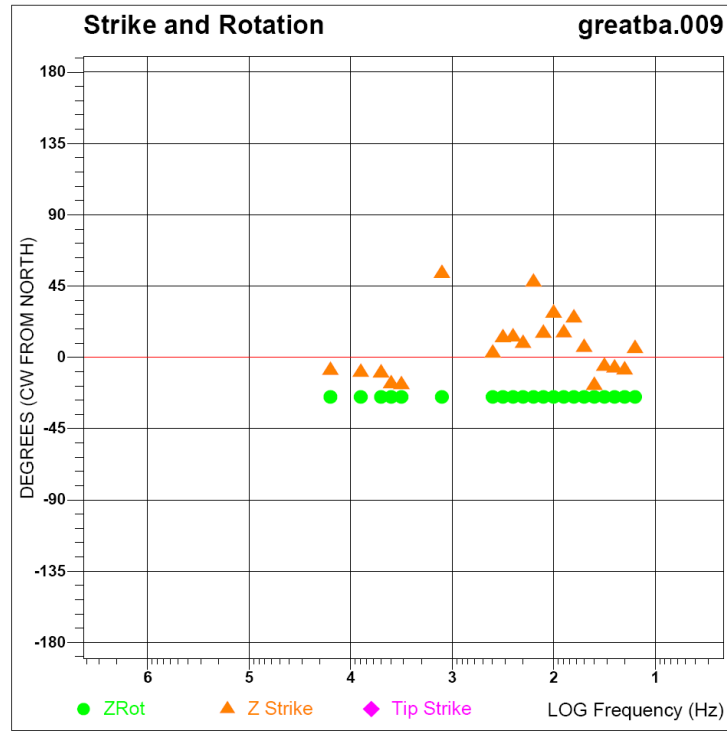


Figure A1-92. Line 1 impedance strike data for site 9.

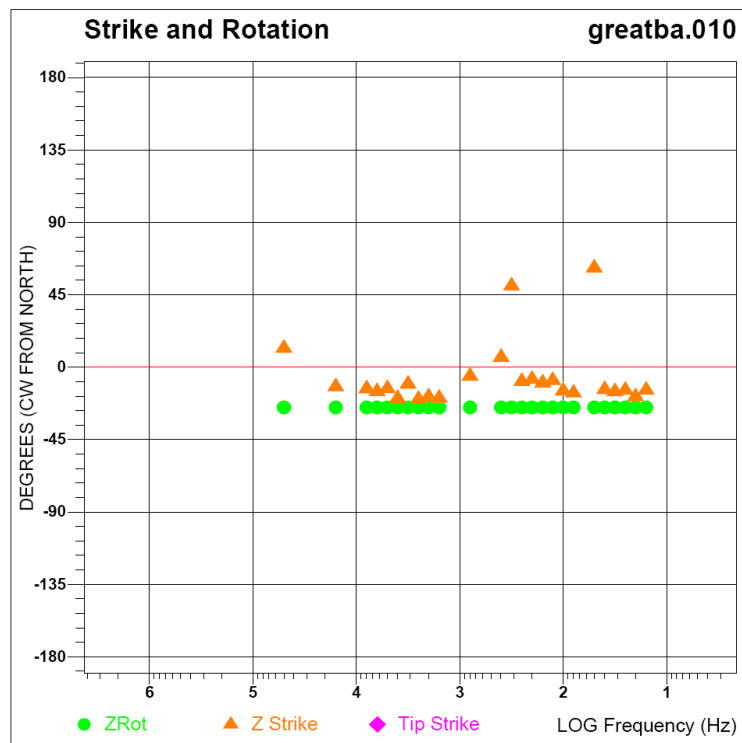


Figure A1-93. Line 1 impedance strike data for site 10.

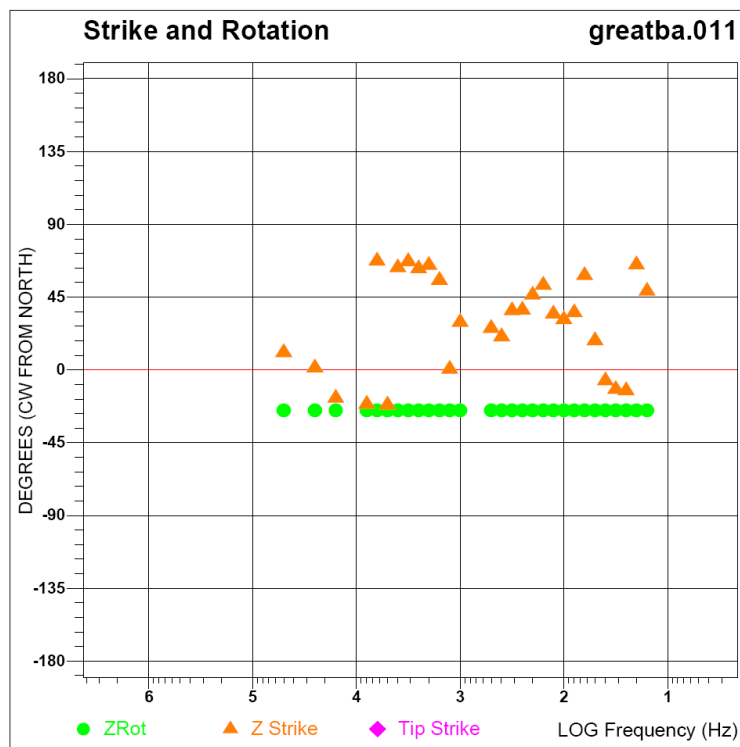


Figure A1-94. Line 1 impedance strike data for site 11.

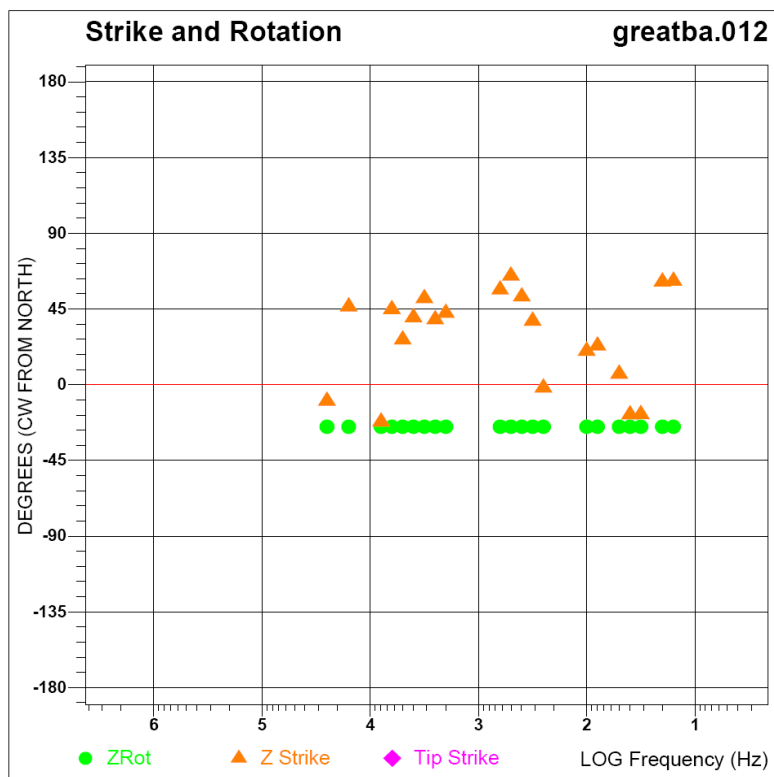


Figure A1-95. Line 1 impedance strike data for site 12.

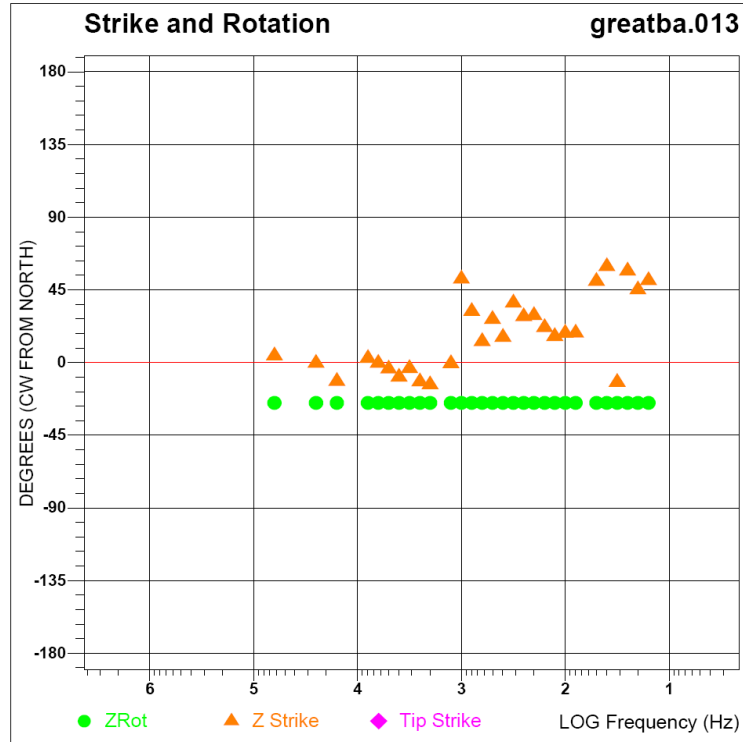


Figure A1-96. Line 1 impedance strike data for site 13.

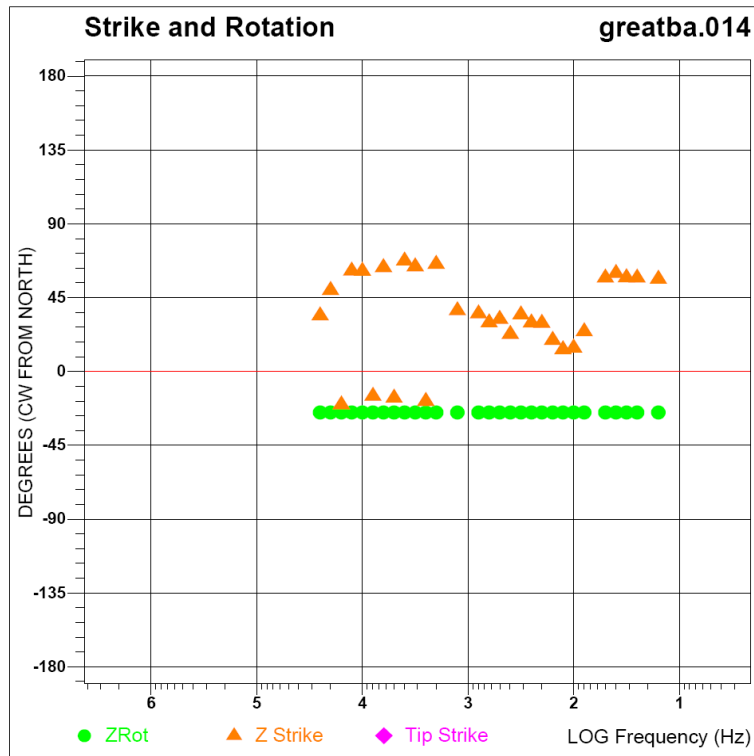


Figure A1-97. Line 1 impedance strike data for site 14.

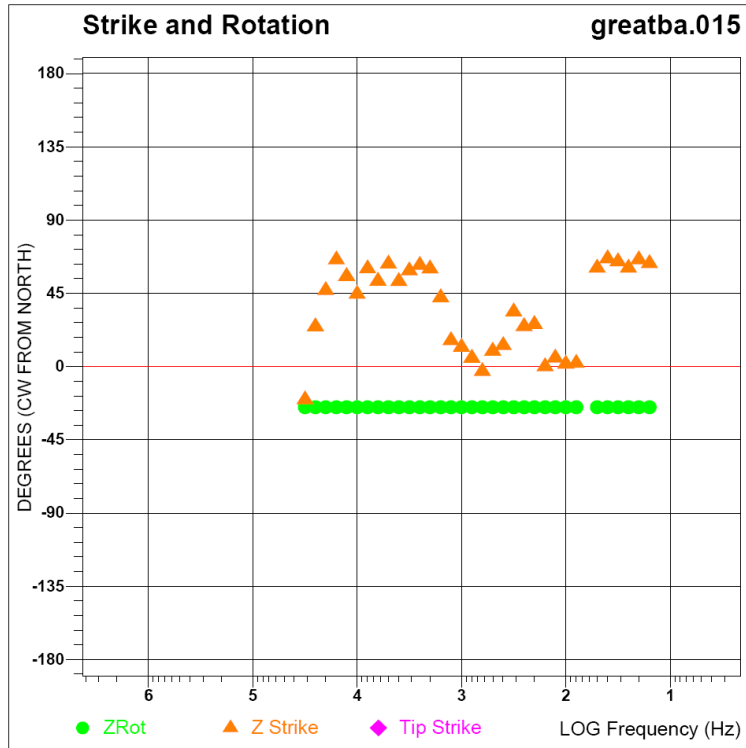


Figure A1-98. Line 1 impedance strike data for site 15.

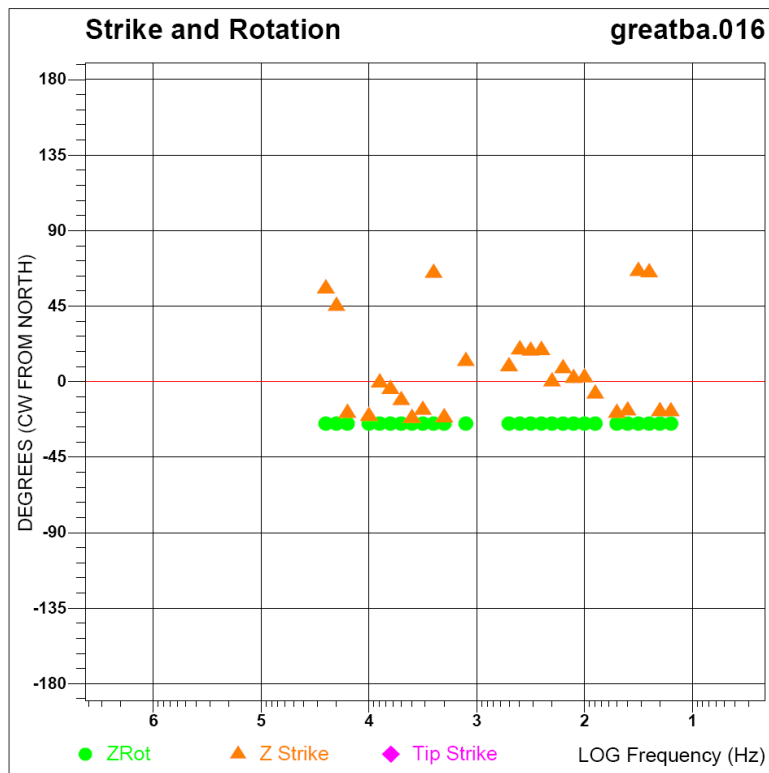


Figure A1-99. Line 1 impedance strike data for site 16.

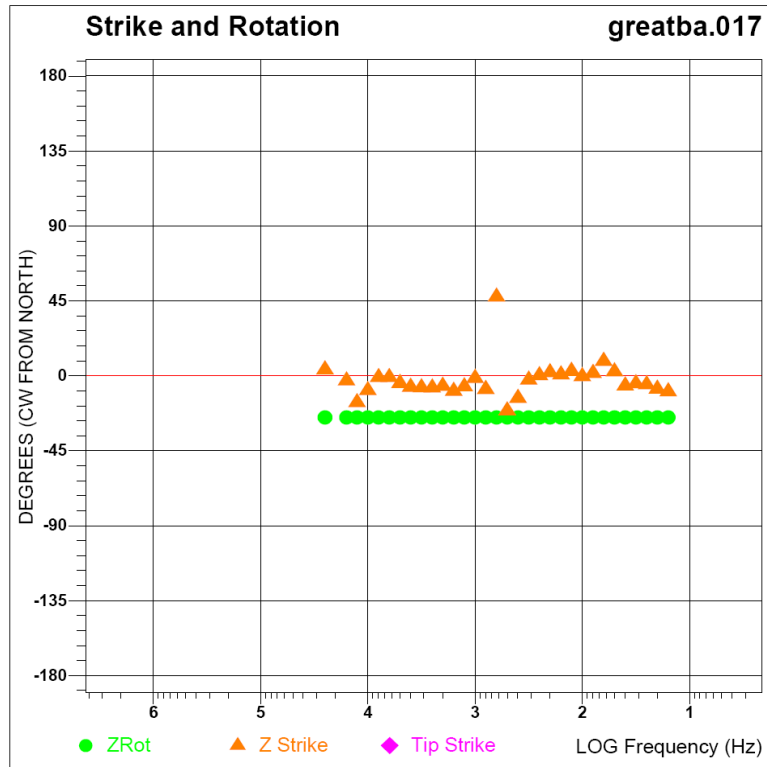


Figure A1-100. Line 1 impedance strike data for site 17.

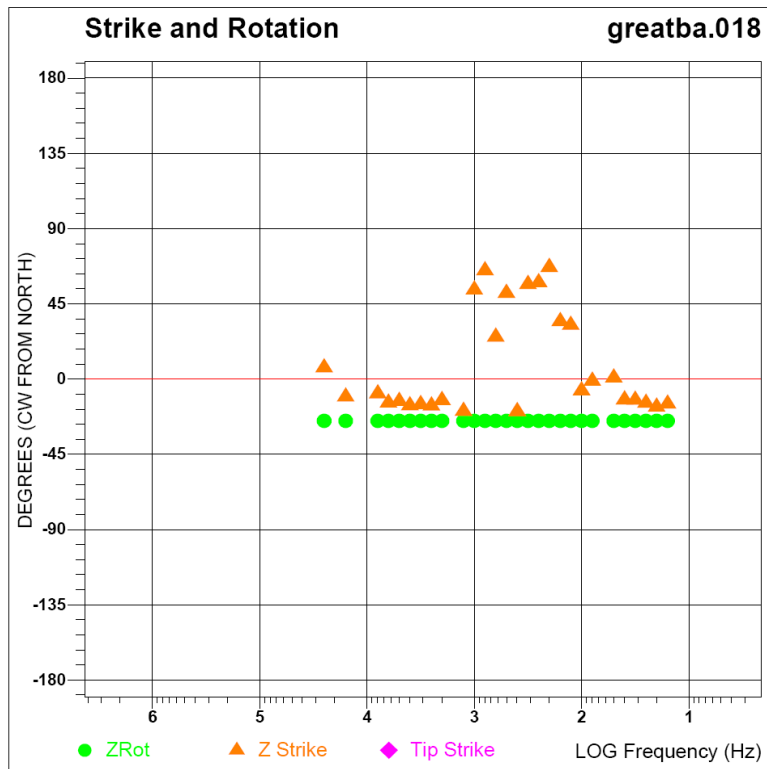


Figure A1-101. Line 1 impedance strike data for site 18.



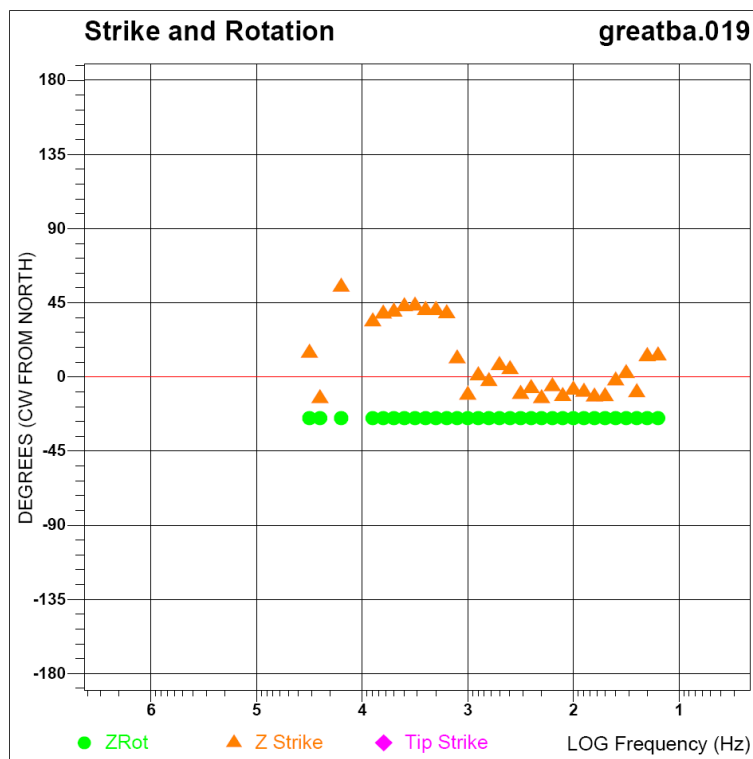


Figure A1-102. Line 1 impedance strike data for site 19.

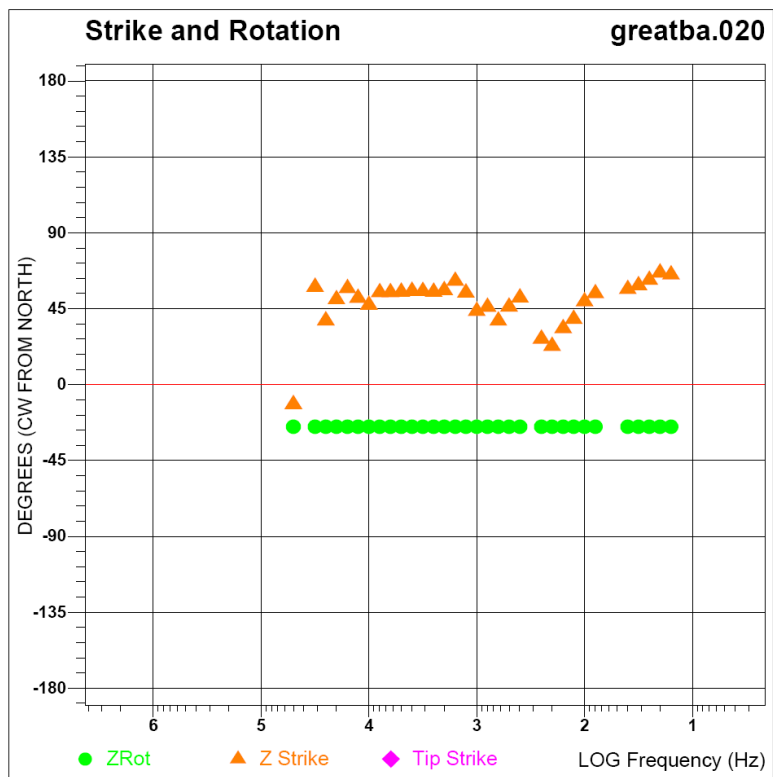


Figure A1-103. Line 1 impedance strike data for site 20.

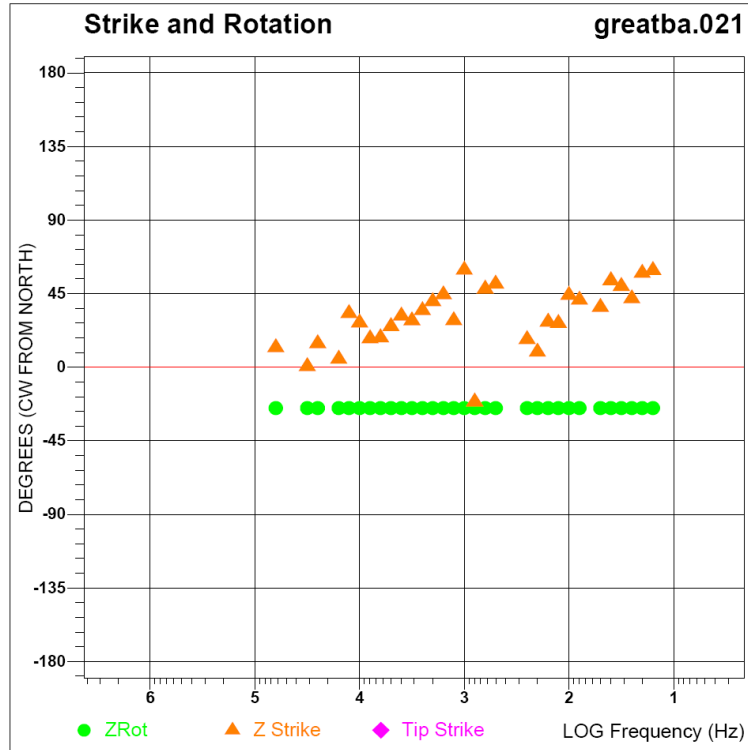


Figure A1-104. Line 1 impedance strike data for site 21.

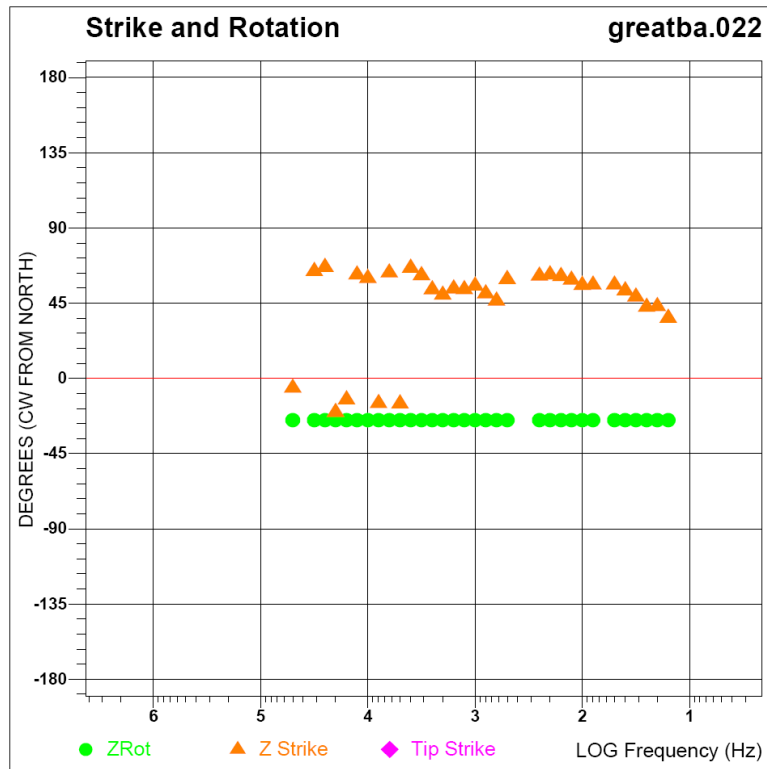


Figure A1-105. Line 1 impedance strike data for site 22.

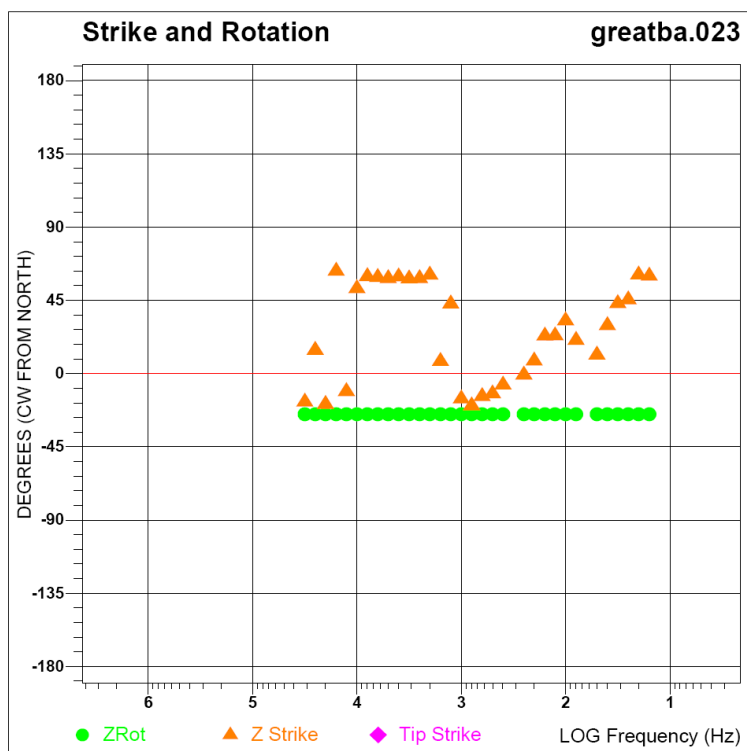


Figure A1-106. Line 1 impedance strike data for site 23.

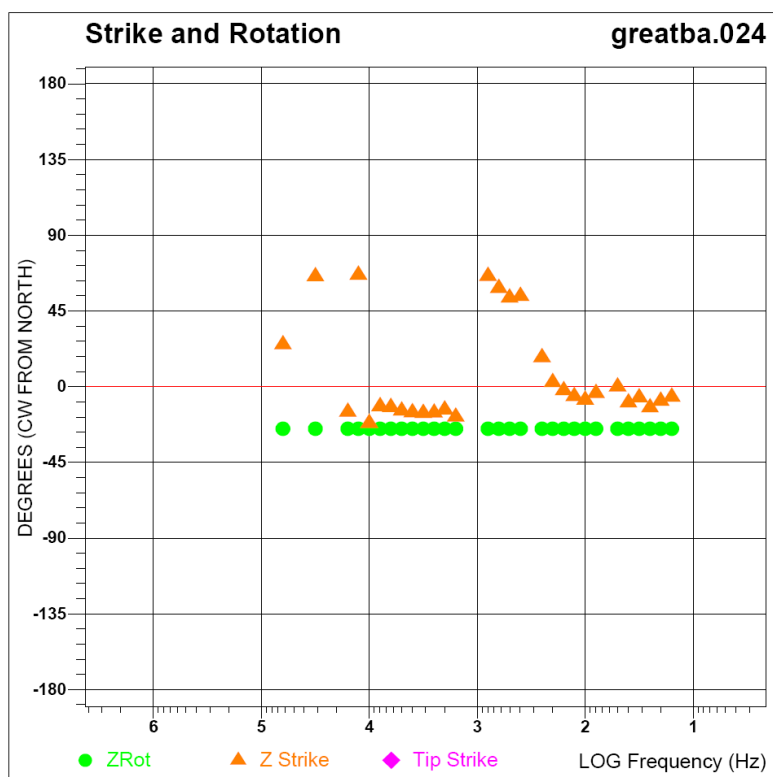


Figure A1-107. Line 1 impedance strike data for site 24.

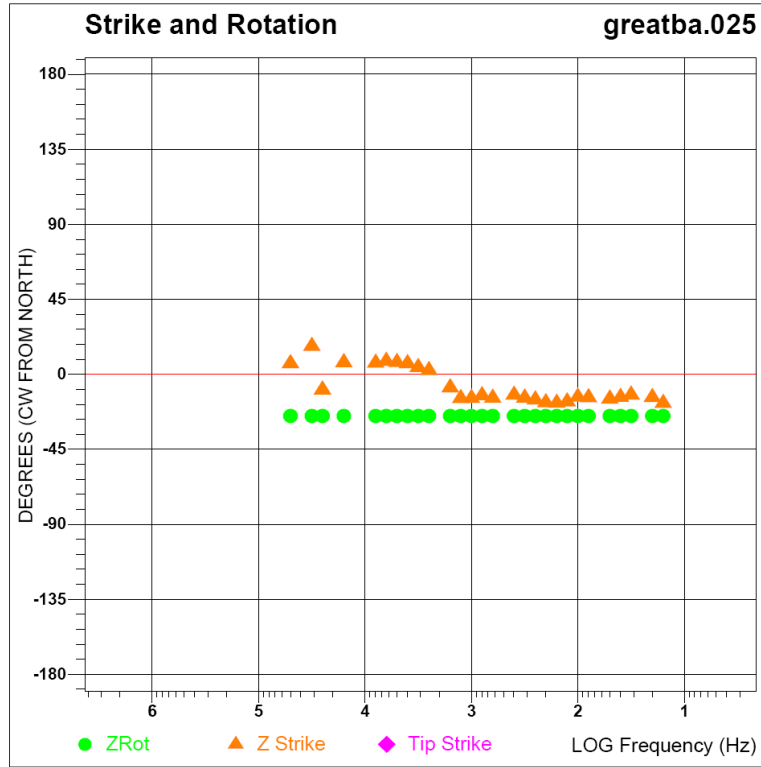


Figure A1-108. Line 1 impedance strike data for site 25.

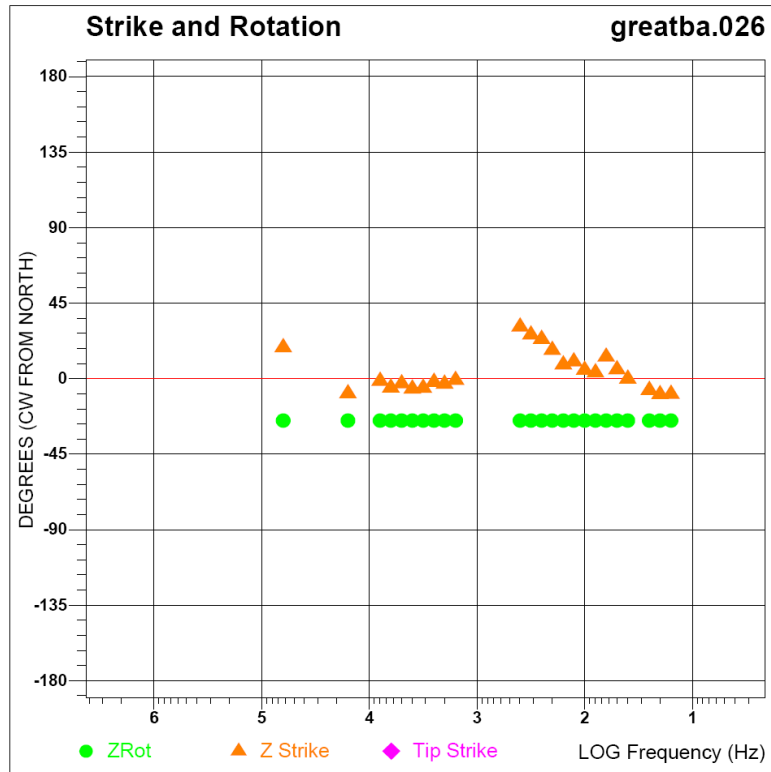


Figure A1-109. Line 1 impedance strike data for site 26.

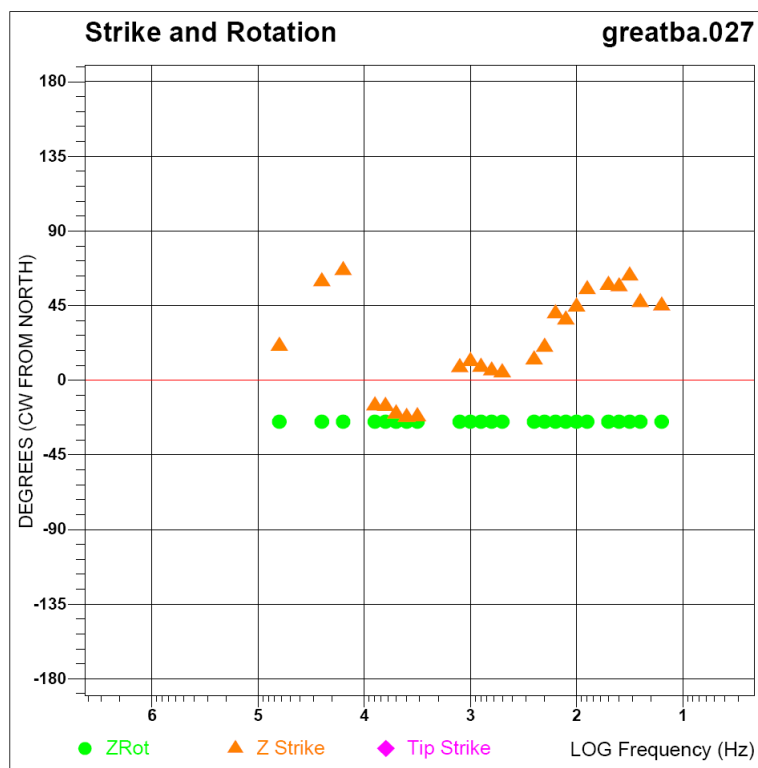


Figure A1-110. Line 1 impedance strike data for site 27.

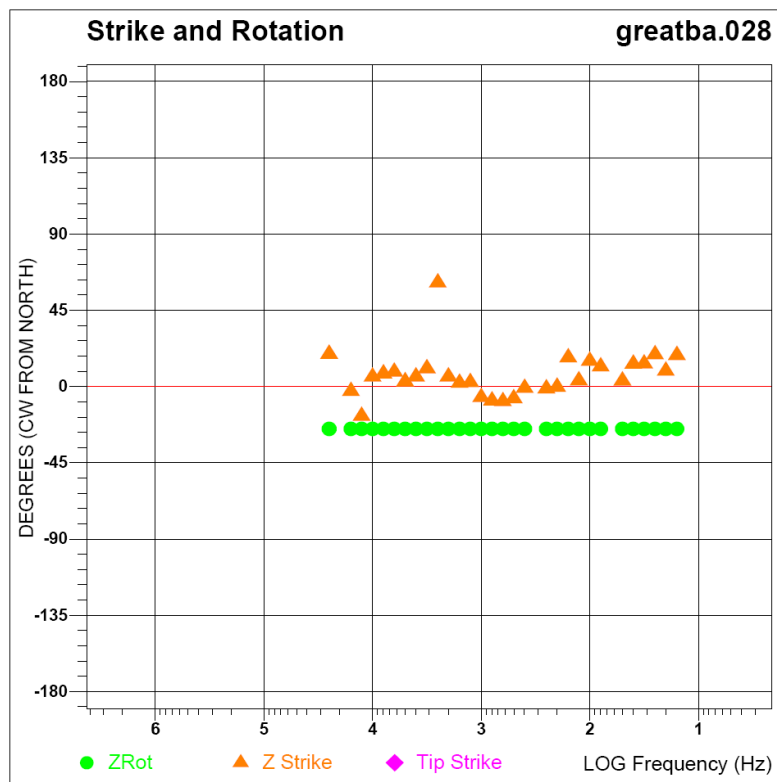


Figure A1-111. Line 1 impedance strike data for site 28.

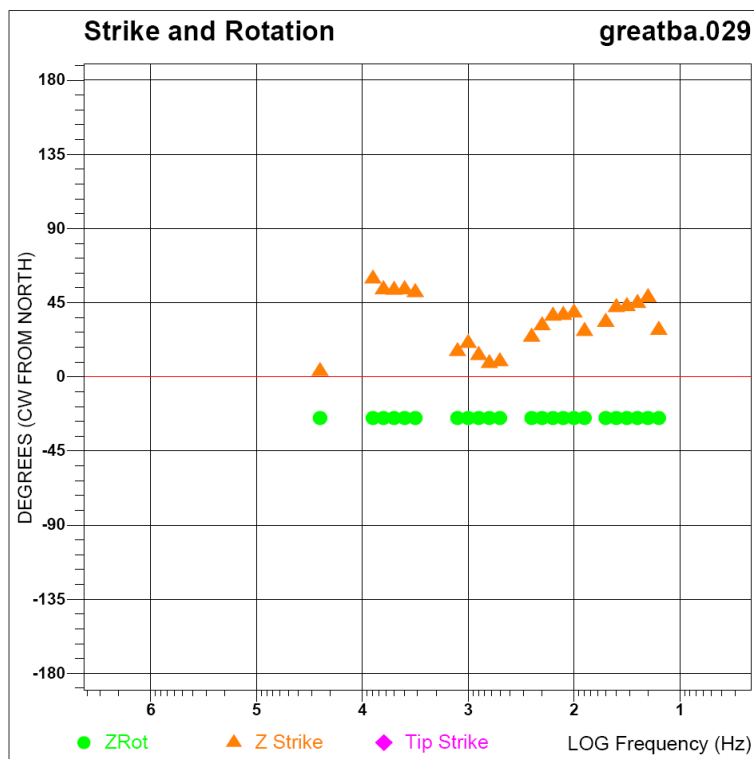


Figure A1-112. Line 1 impedance strike data for site 29.

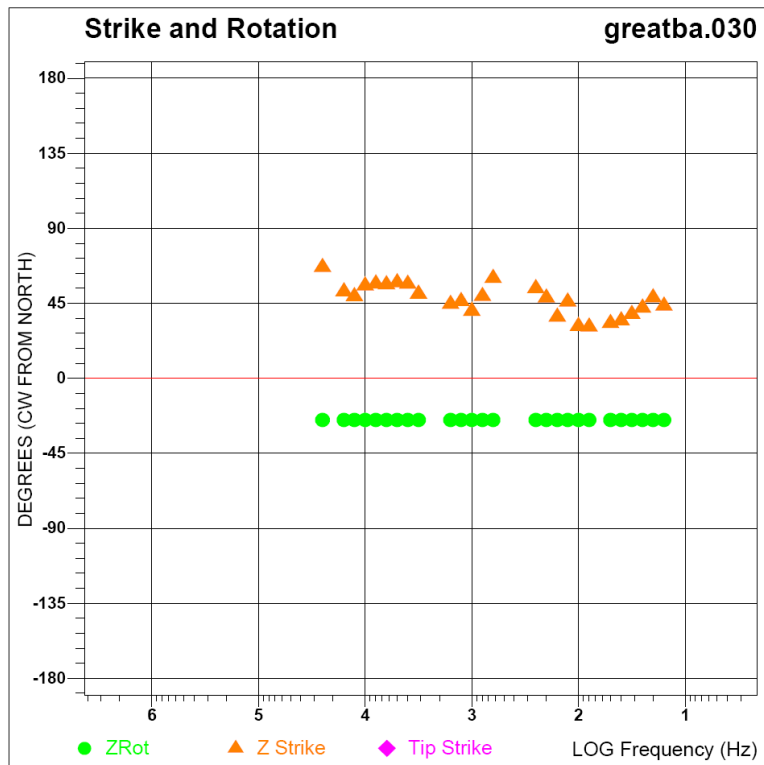


Figure A1-113. Line 1 impedance strike data for site 30.

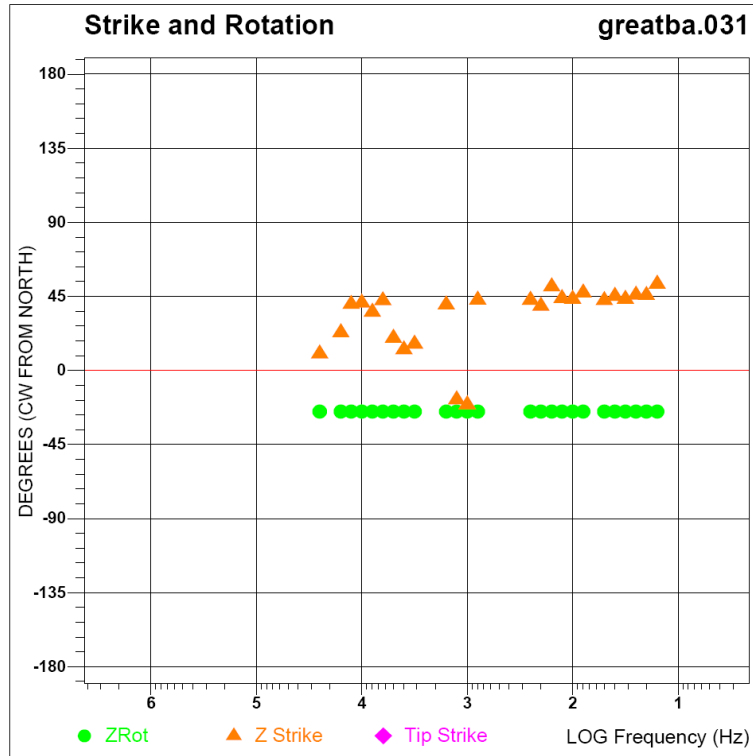


Figure A1-114. Line 1 impedance strike data for site 31.

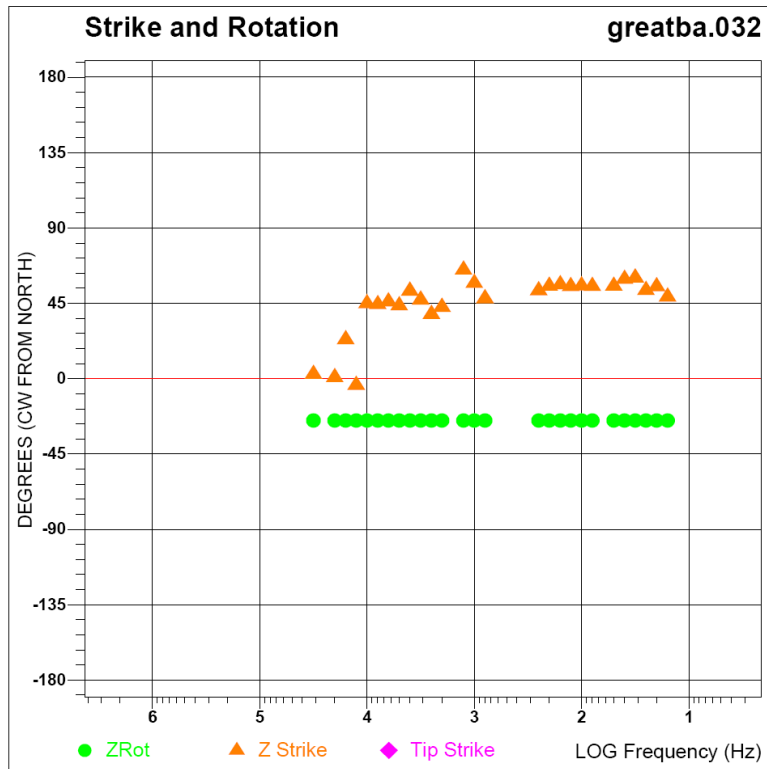


Figure A1-115. Line 1 impedance strike data for site 32.

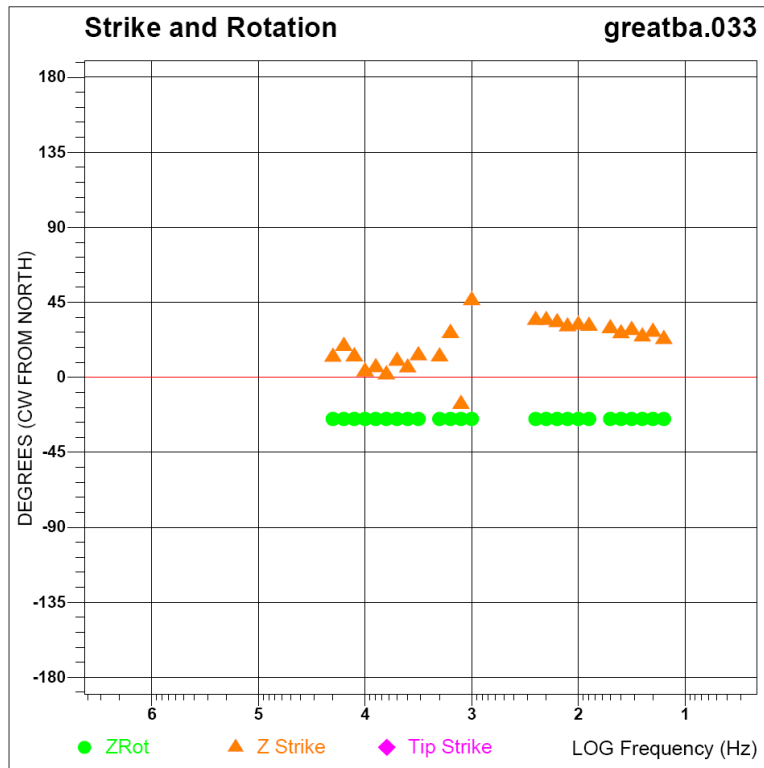


Figure A1-116. Line 1 impedance strike data for site 33.



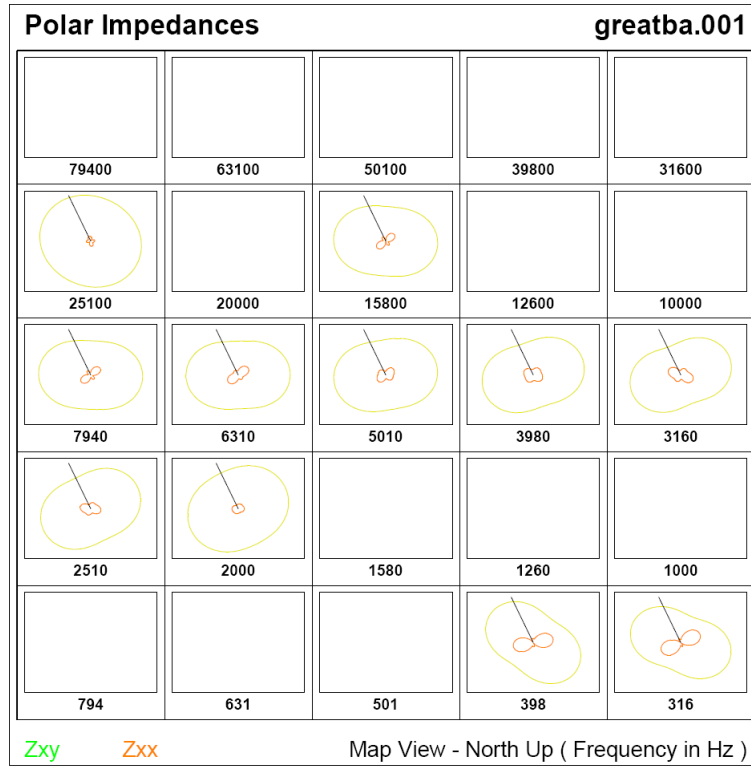


Figure A1-117. Line 1 polar impedance data for site 1 for frequencies 316 Hz – 79 kHz.

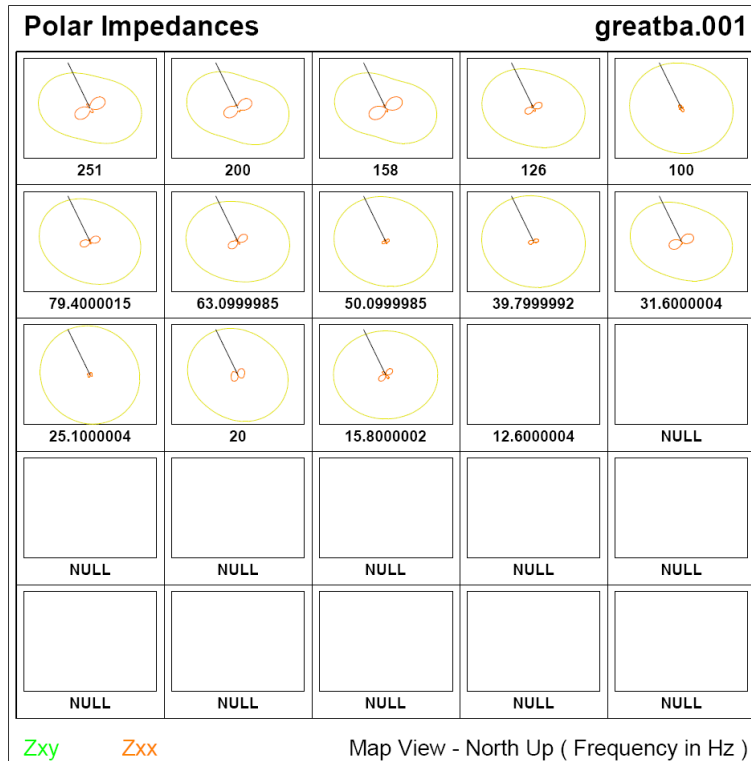


Figure A1-118. Line 1 polar impedance data for site 1 for frequencies 12 Hz – 251 Hz.

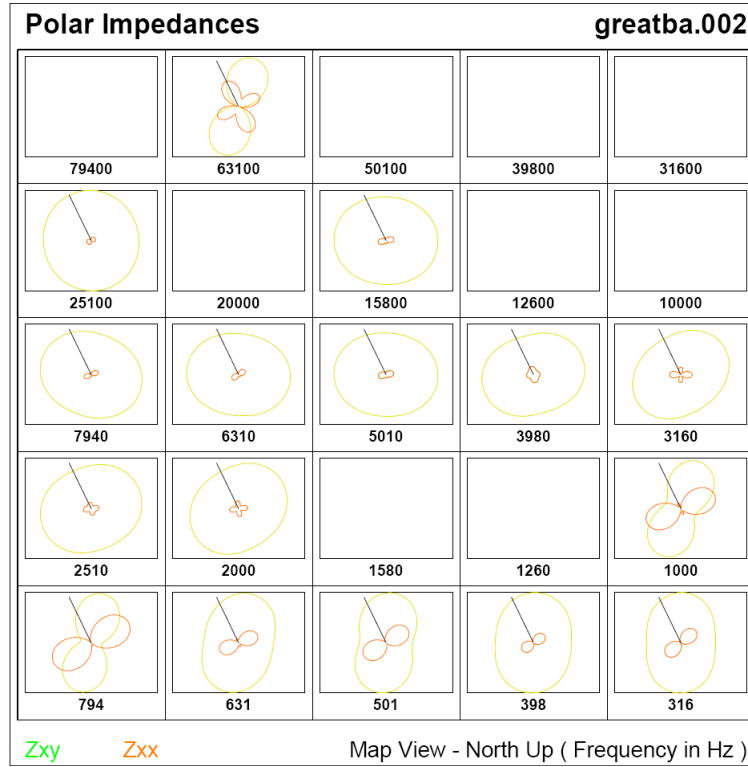


Figure A1-119. Line 1 polar impedance data for site 2 for frequencies 316 Hz – 79 kHz.

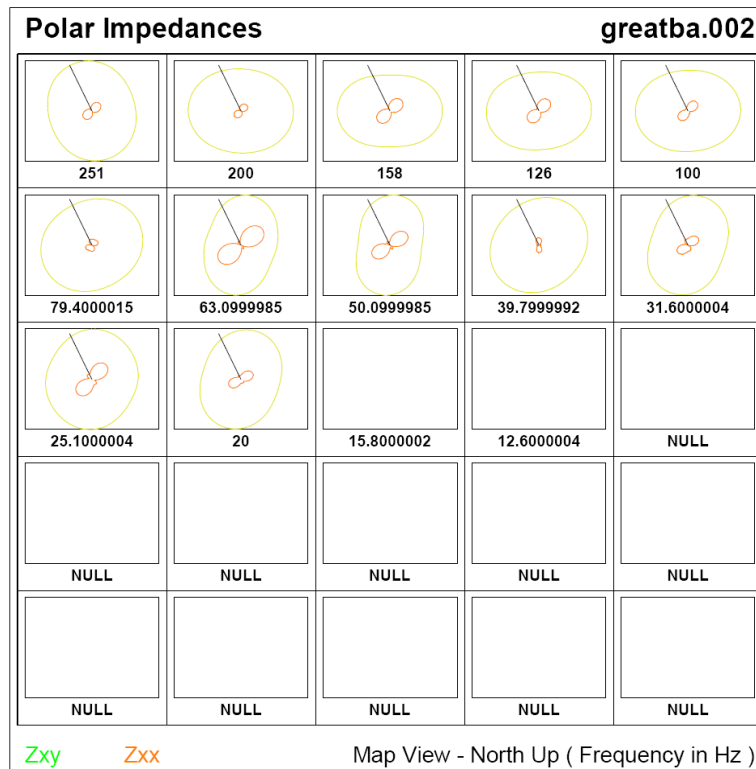


Figure A1-120. Line 1 polar impedance data for site 2 for frequencies 12 Hz – 251 Hz.

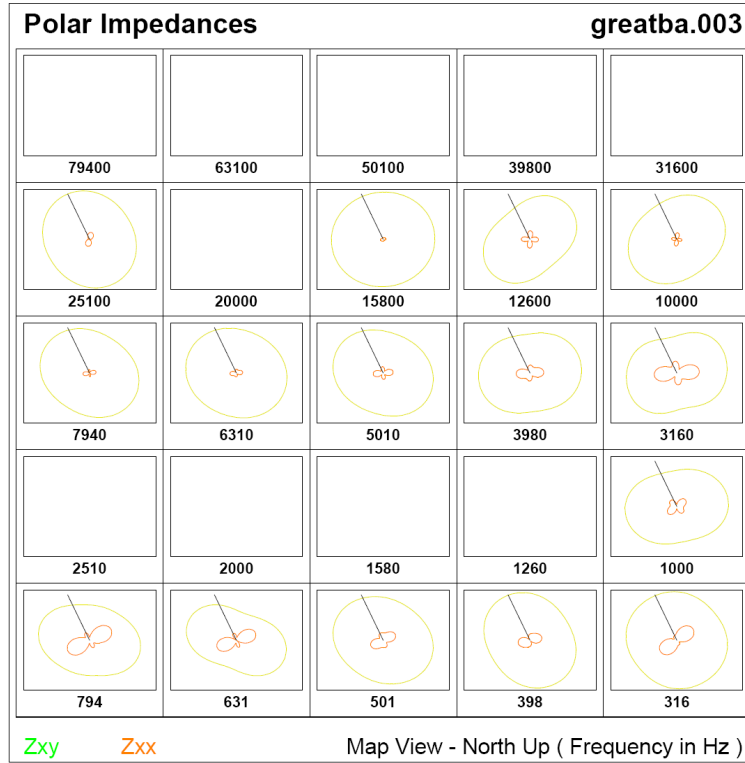


Figure A1-121. Line 1 polar impedance data for site 3 for frequencies 316 Hz – 79 kHz.

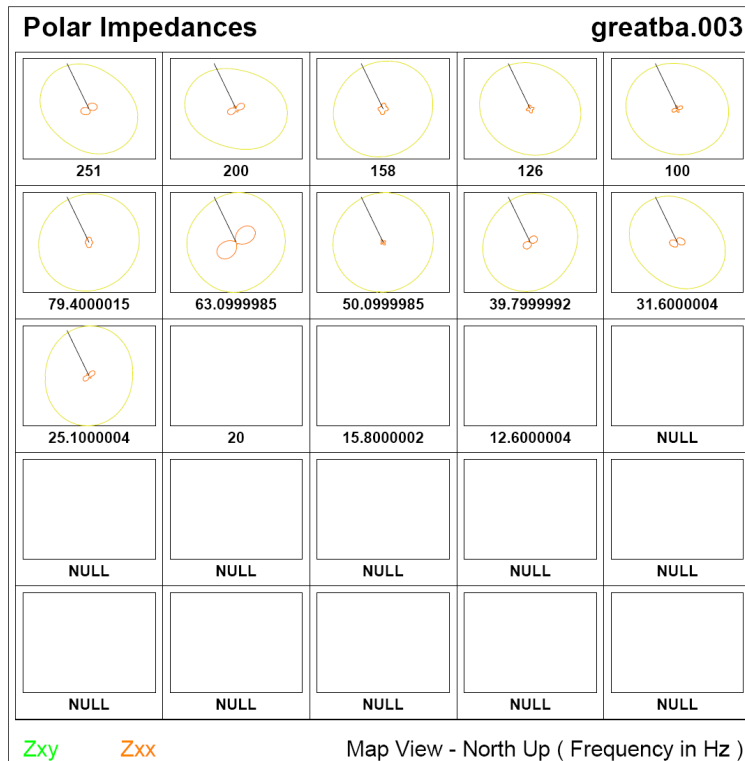


Figure A1-122. Line 1 polar impedance data for site 3 for frequencies 12 Hz – 251 Hz.

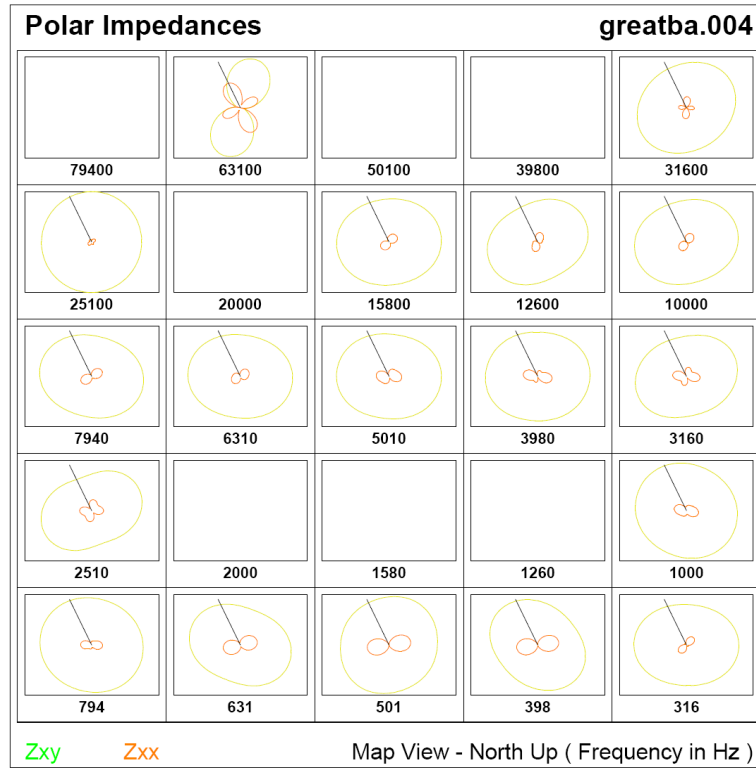


Figure A1-123. Line 1 polar impedance data for site 4 for frequencies 316 Hz – 79 kHz.

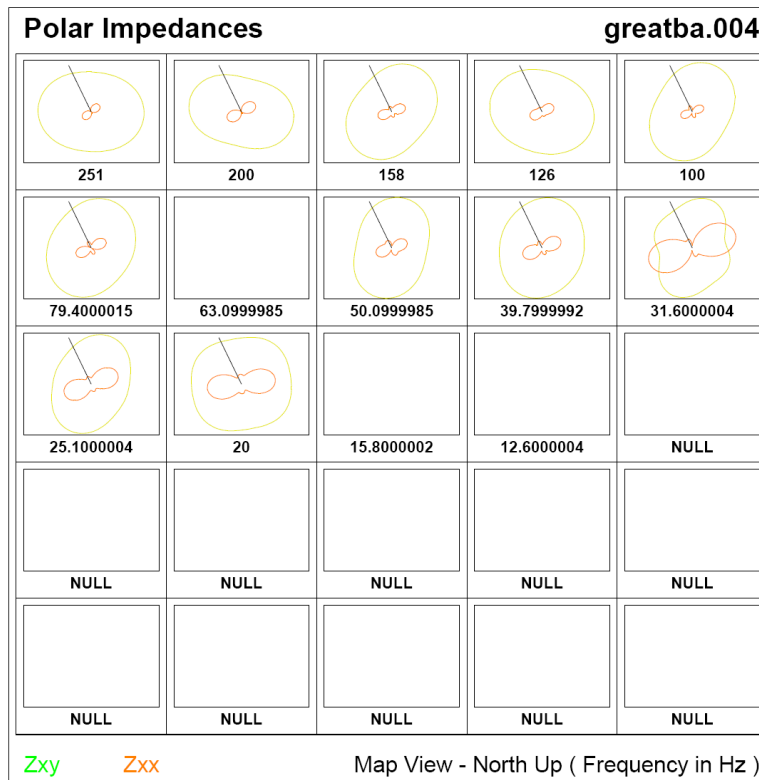
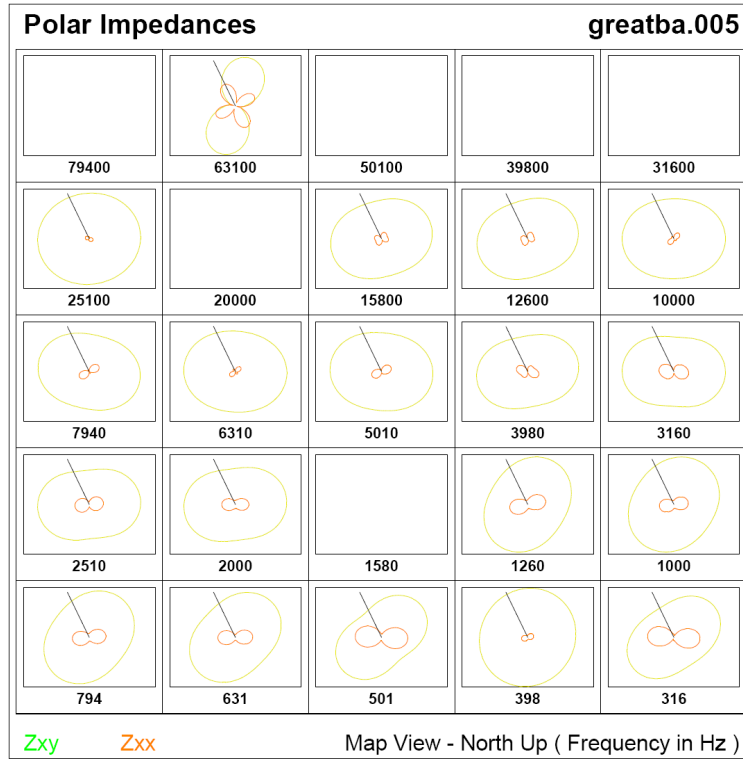
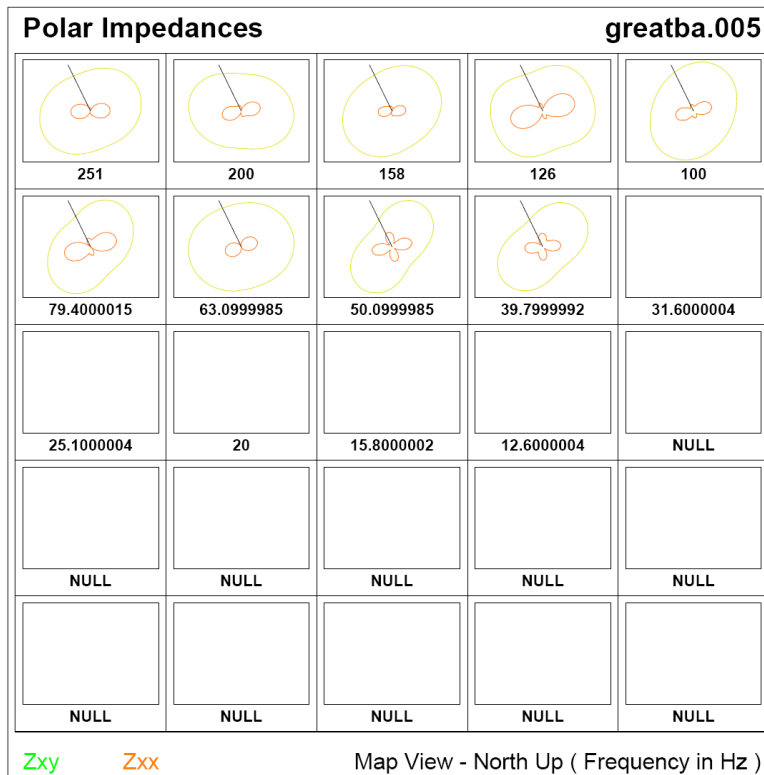


Figure A1-124. Line 1 polar impedance data for site 4 for frequencies 12 Hz – 251 Hz.



**Figure A1-125.** Line 1 polar impedance data for site 5 for frequencies 316 Hz – 79 kHz.



**Figure A1-126.** Line 1 polar impedance data for site 5 for frequencies 12 Hz – 251 Hz.

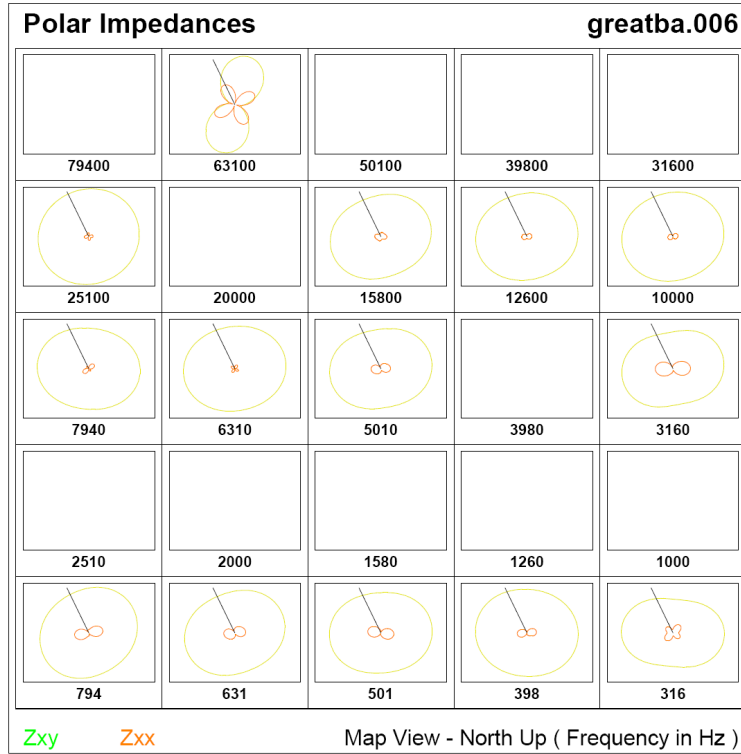


Figure A1-127. Line 1 polar impedance data for site 6 for frequencies 316 Hz – 79 kHz.

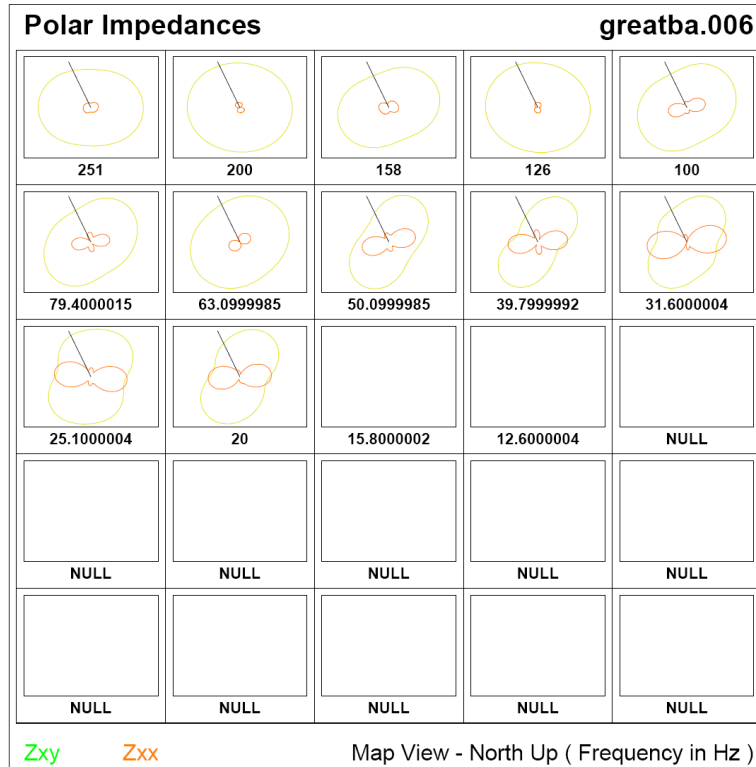


Figure A1-128. Line 1 polar impedance data for site 6 for frequencies 12 Hz – 251 Hz.

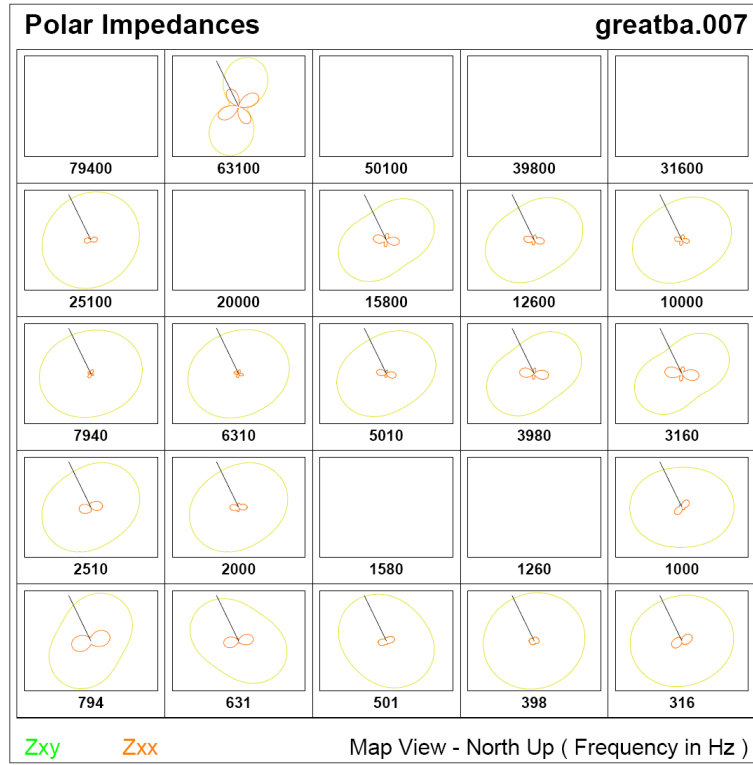


Figure A1-129. Line 1 polar impedance data for site 7 for frequencies 316 Hz – 79 kHz.

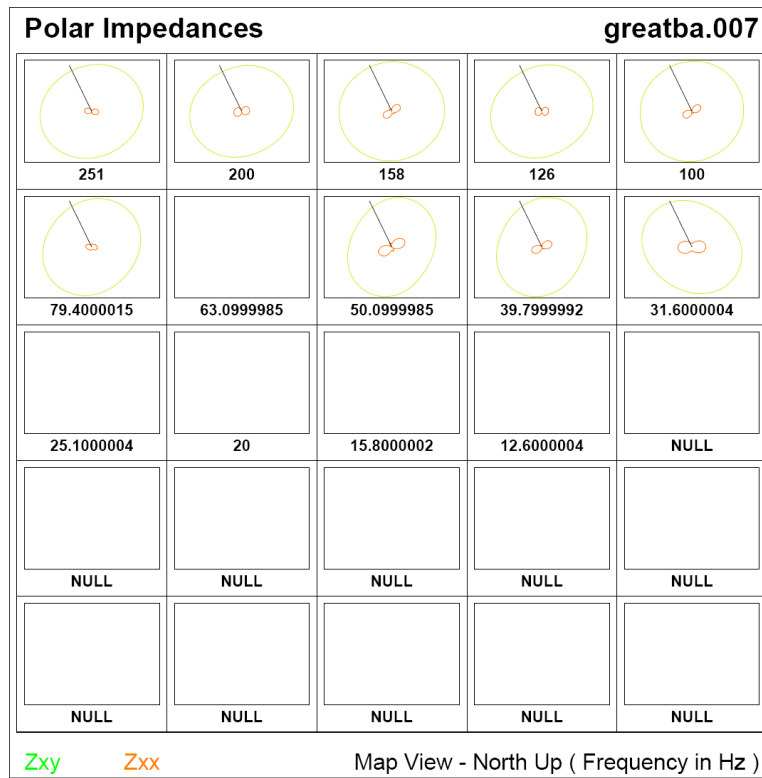


Figure A1-130. Line 1 polar impedance data for site 7 for frequencies 12 Hz – 251 Hz.

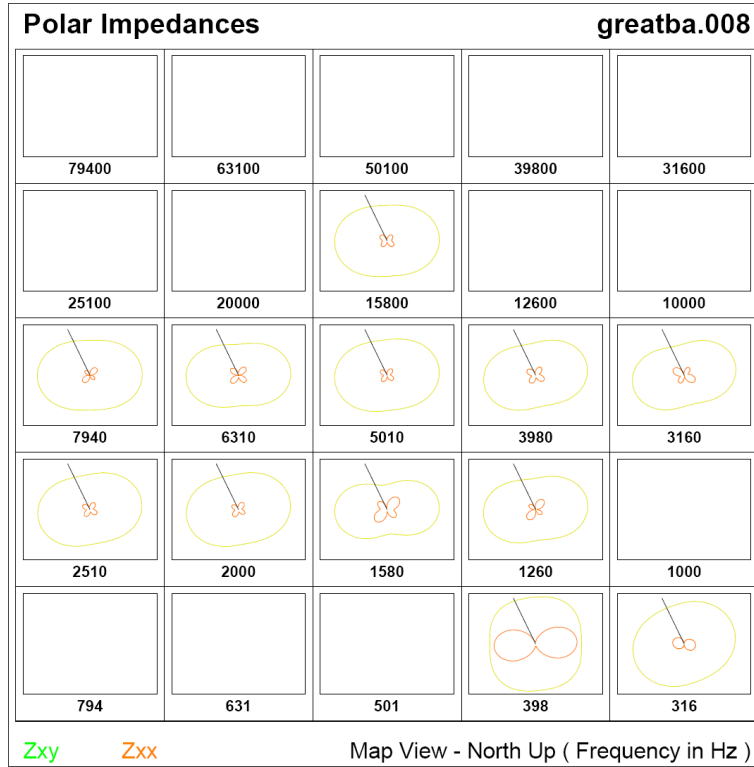


Figure A1-131. Line 1 polar impedance data for site 8 for frequencies 316 Hz – 79 kHz.

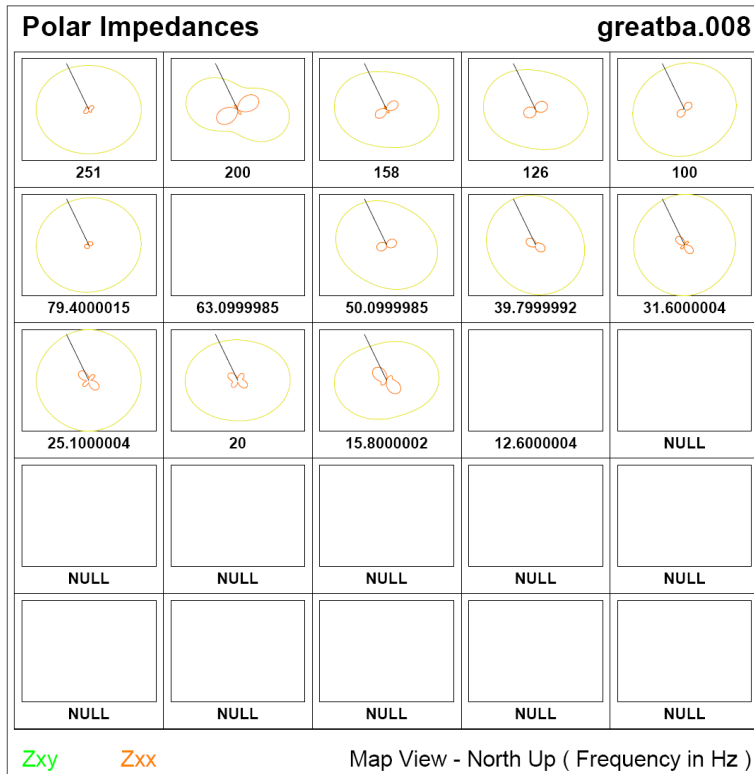
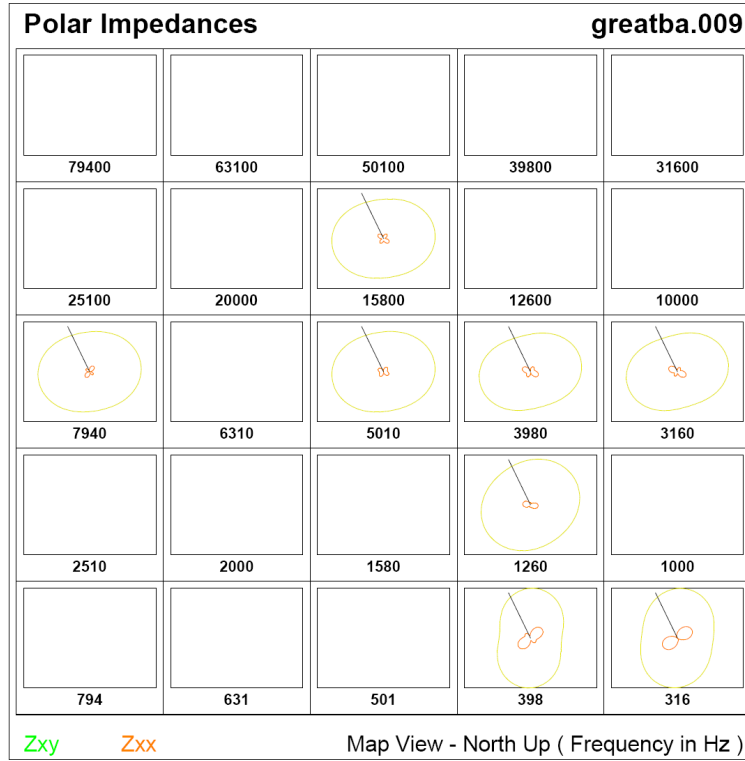
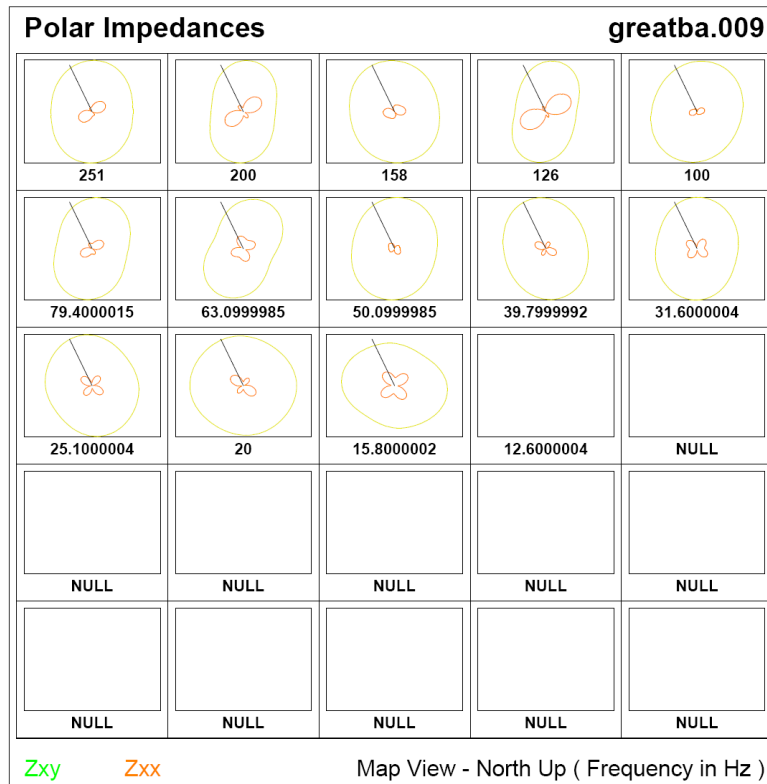


Figure A1-132. Line 1 polar impedance data for site 8 for frequencies 12 Hz – 251 Hz.





**Figure A1-133.** Line 1 polar impedance data for site 9 for frequencies 316 Hz – 79 kHz.



**Figure A1-134.** Line 1 polar impedance data for site 9 for frequencies 12 Hz – 251 Hz.

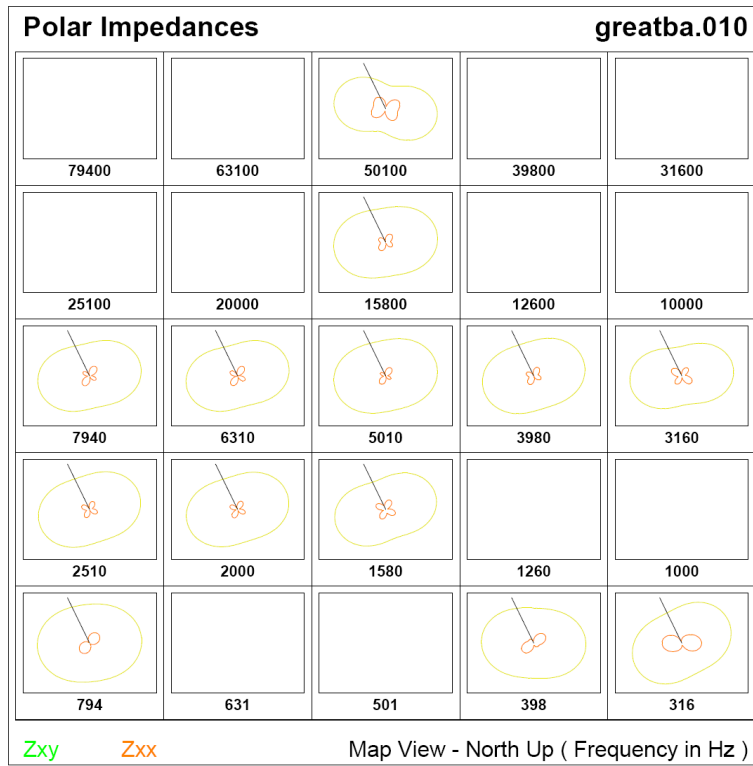


**Figure A1-135.** Line 1 polar impedance data for site 10 for frequencies 316 Hz – 79 kHz.

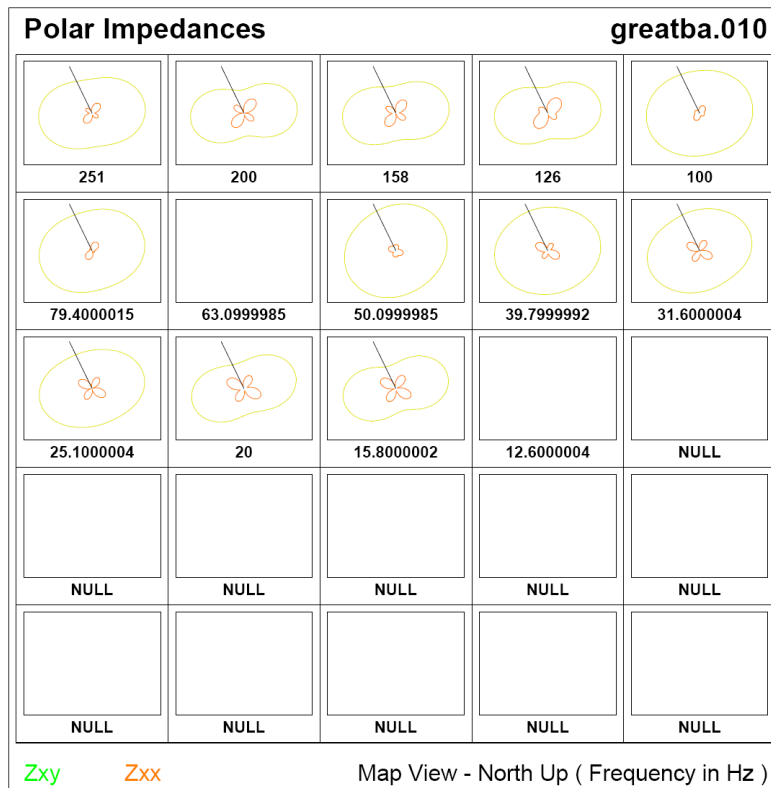


**Figure A1-136.** Line 1 polar impedance data for site 10 for frequencies 12 Hz – 251 Hz.

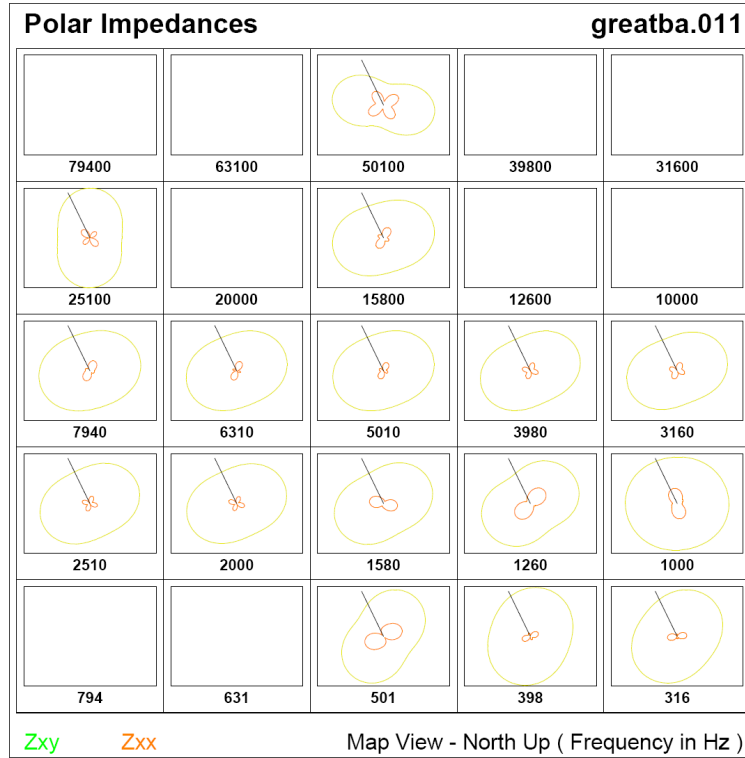


**Figure A1-137.** Line 1 polar impedance data for site 11 for frequencies 316 Hz – 79 kHz.

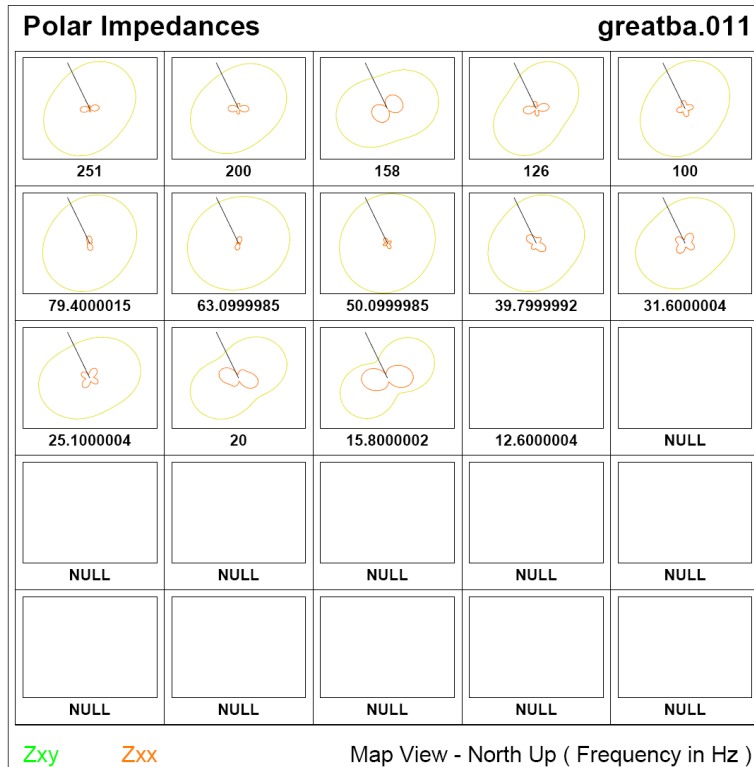


**Figure A1-138.** Line 1 polar impedance data for site 11 for frequencies 12 Hz – 251 Hz.

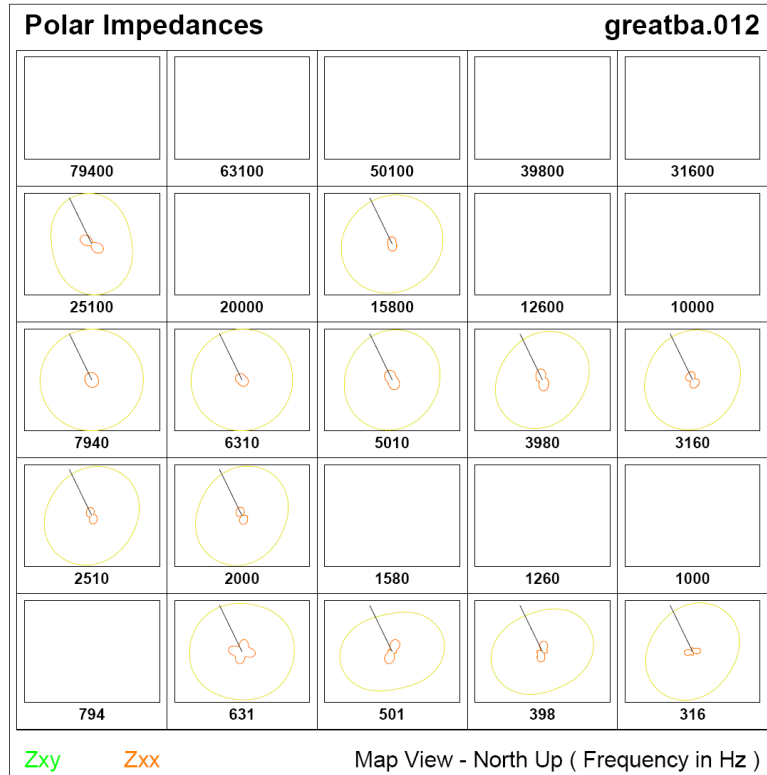


Figure A1-139. Line 1 polar impedance data for site 12 for frequencies 316 Hz – 79 kHz.

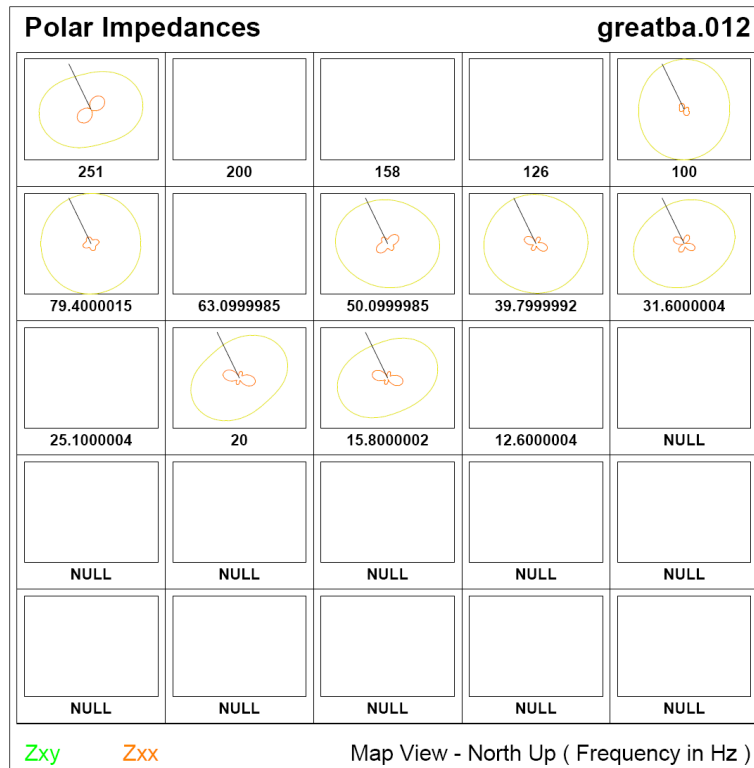


Figure A1-140. Line 1 polar impedance data for site 12 for frequencies 12 Hz – 251 Hz.

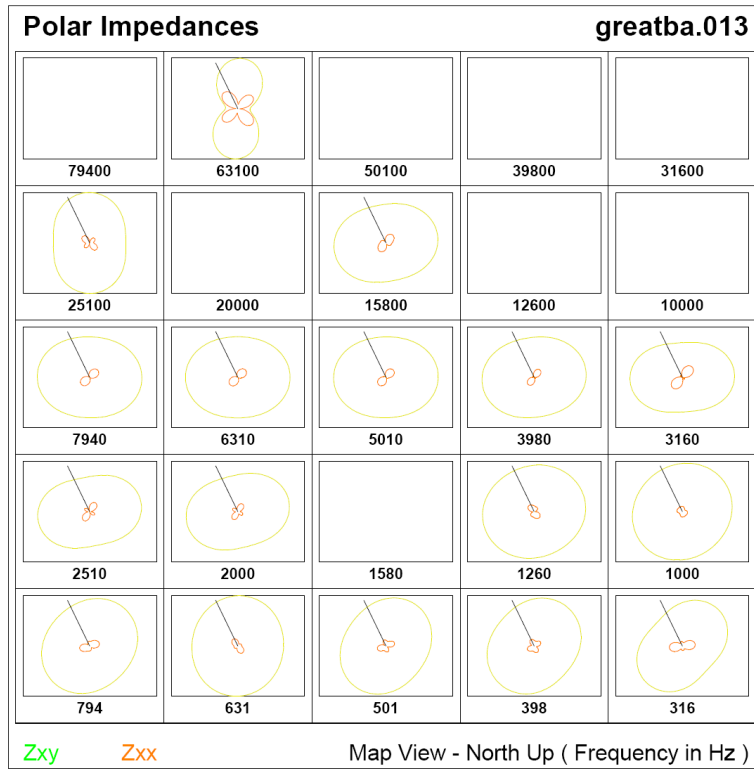


Figure A1-141. Line 1 polar impedance data for site 13 for frequencies 316 Hz – 79 kHz.

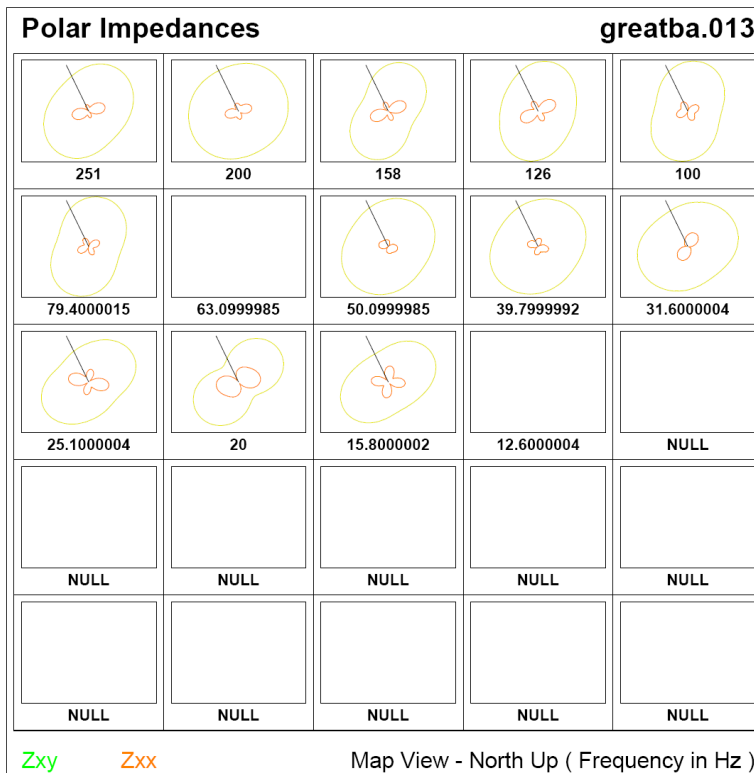
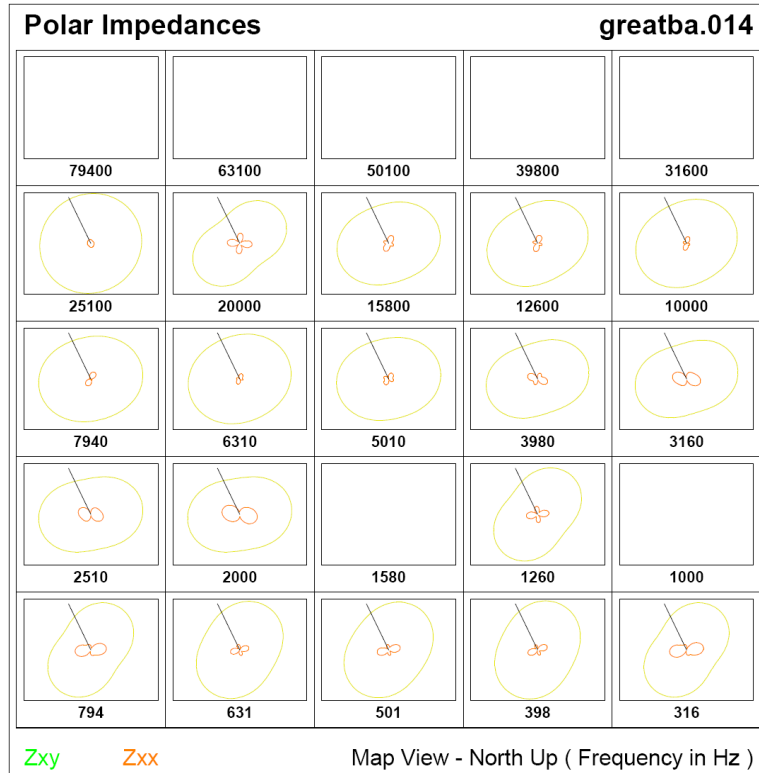
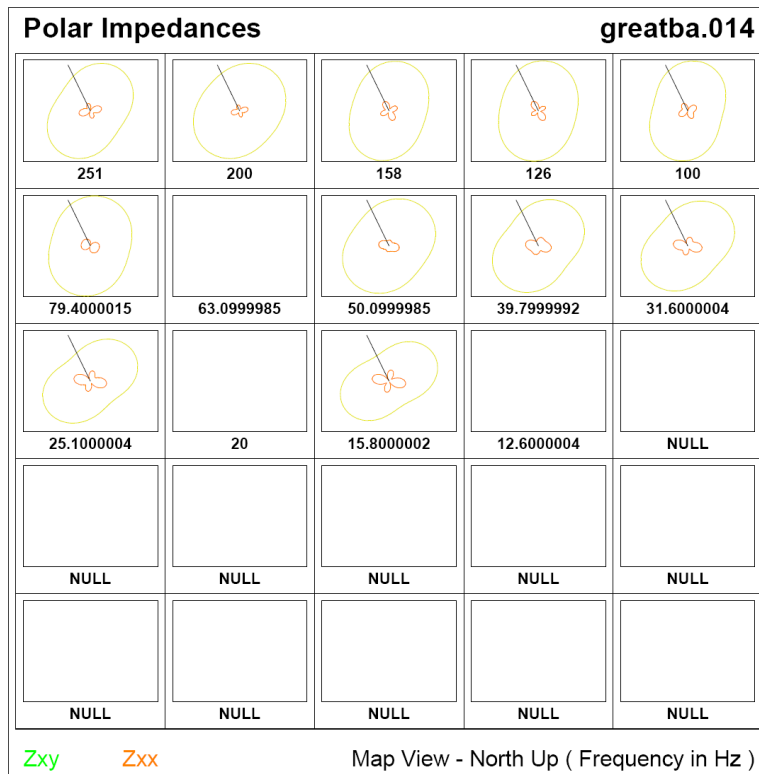


Figure A1-142. Line 1 polar impedance data for site 13 for frequencies 12 Hz – 251 Hz.



**Figure A1-143.** Line 1 polar impedance data for site 14 for frequencies 316 Hz – 79 kHz.



**Figure A1-144.** Line 1 polar impedance data for site 14 for frequencies 12 Hz – 251 Hz.

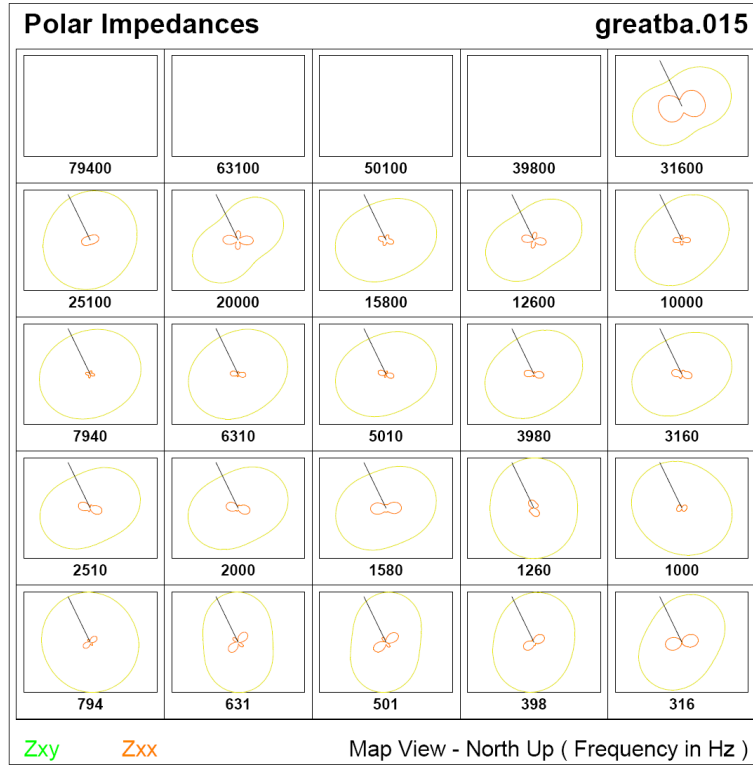


Figure A1-145. Line 1 polar impedance data for site 15 for frequencies 316 Hz – 79 kHz.

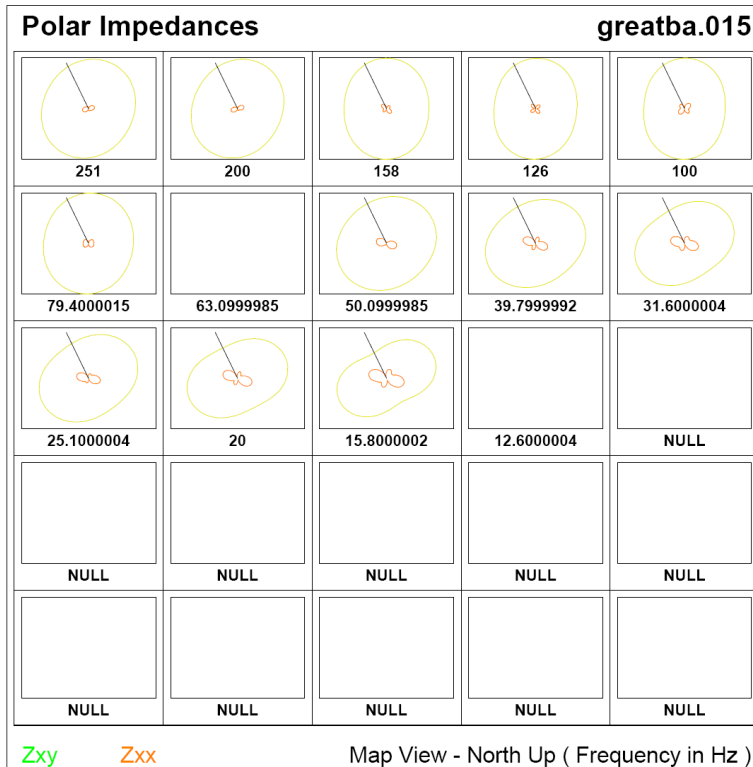


Figure A1-146. Line 1 polar impedance data for site 15 for frequencies 12 Hz – 251 Hz.

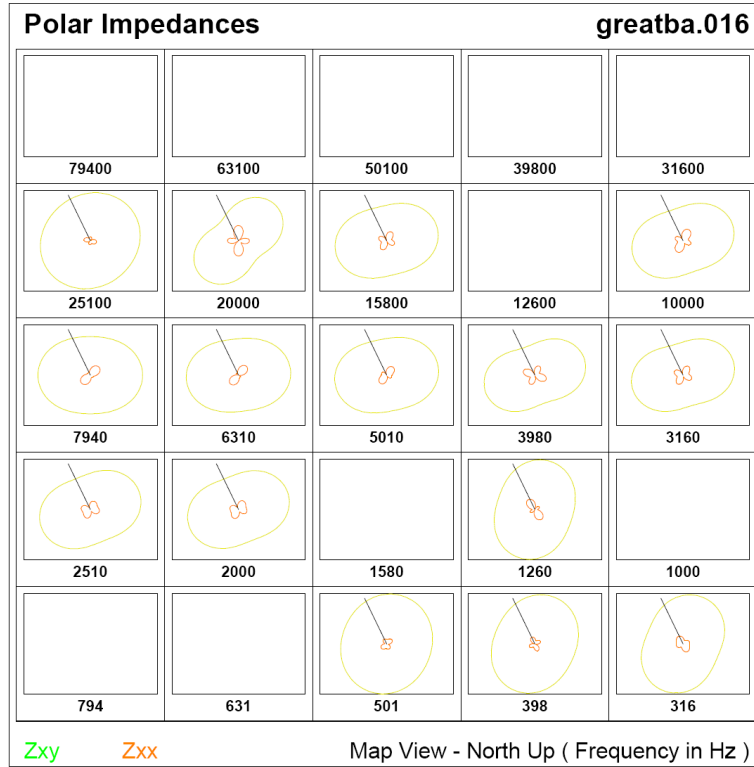


Figure A1-147. Line 1 polar impedance data for site 16 for frequencies 316 Hz – 79 kHz.

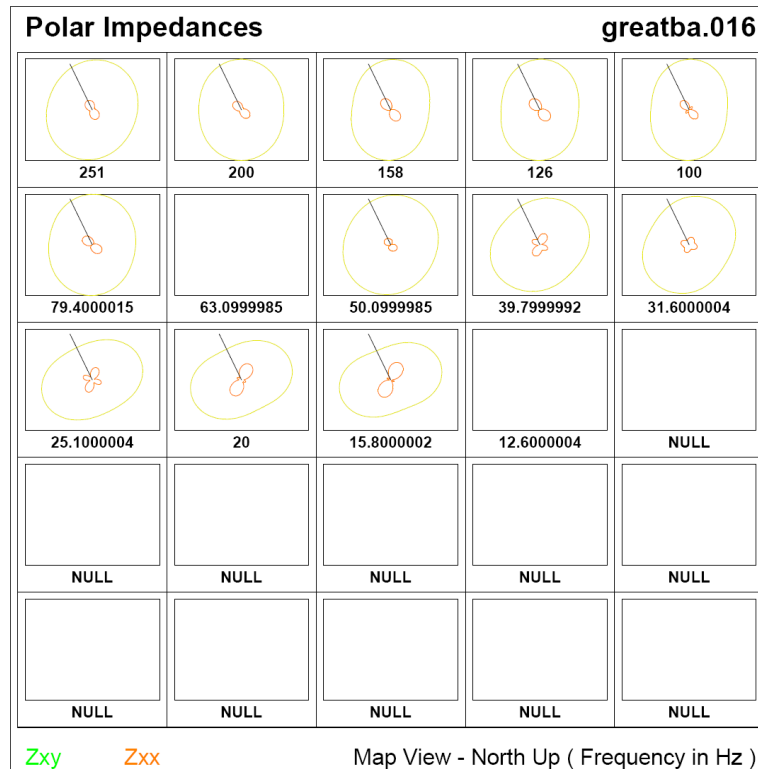
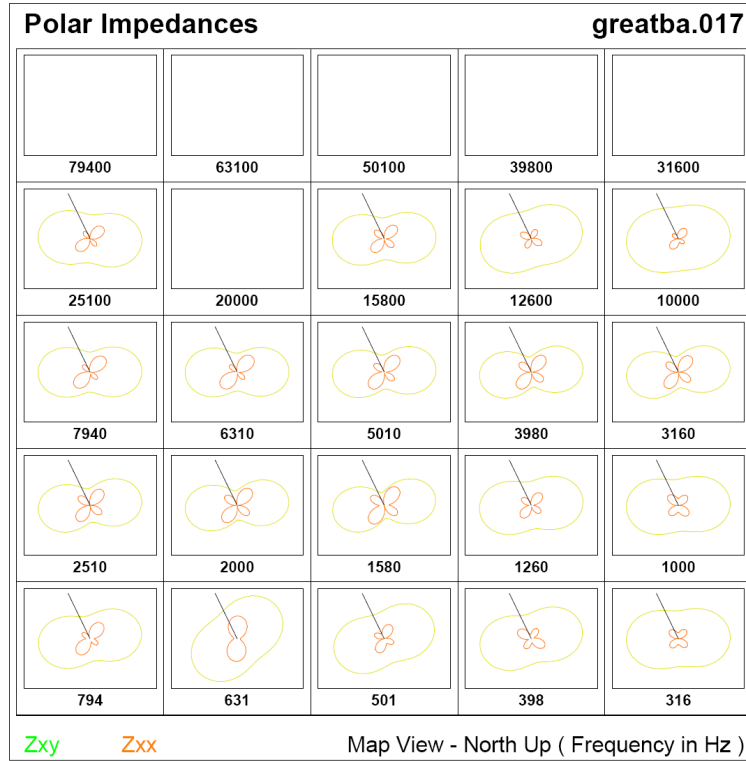
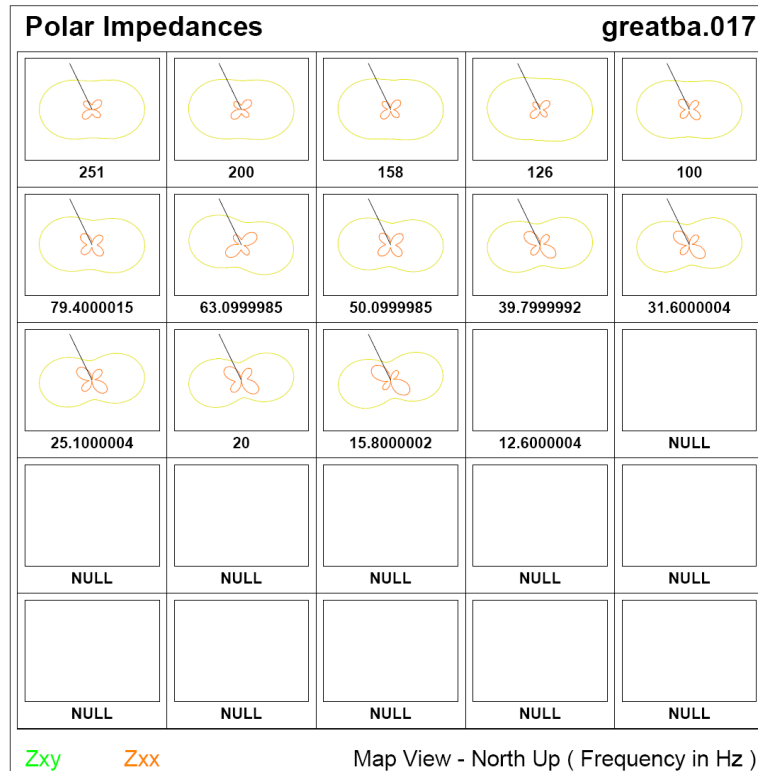


Figure A1-148. Line 1 polar impedance data for site 16 for frequencies 12 Hz – 251 Hz.





**Figure A1-149.** Line 1 polar impedance data for site 17 for frequencies 316 Hz – 79 kHz.



**Figure A1-150.** Line 1 polar impedance data for site 17 for frequencies 12 Hz – 251 Hz.

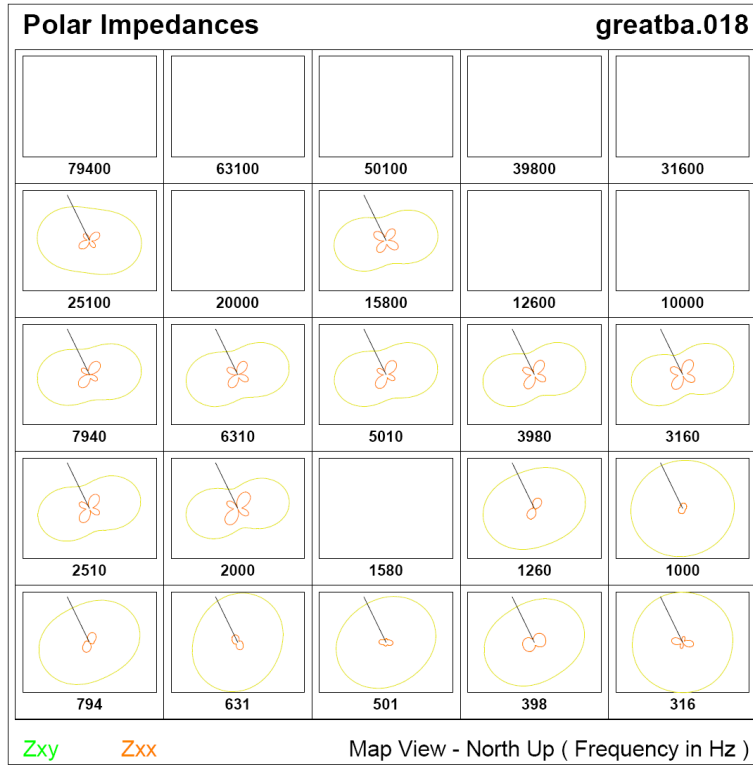


Figure A1-151. Line 1 polar impedance data for site 18 for frequencies 316 Hz – 79 kHz.

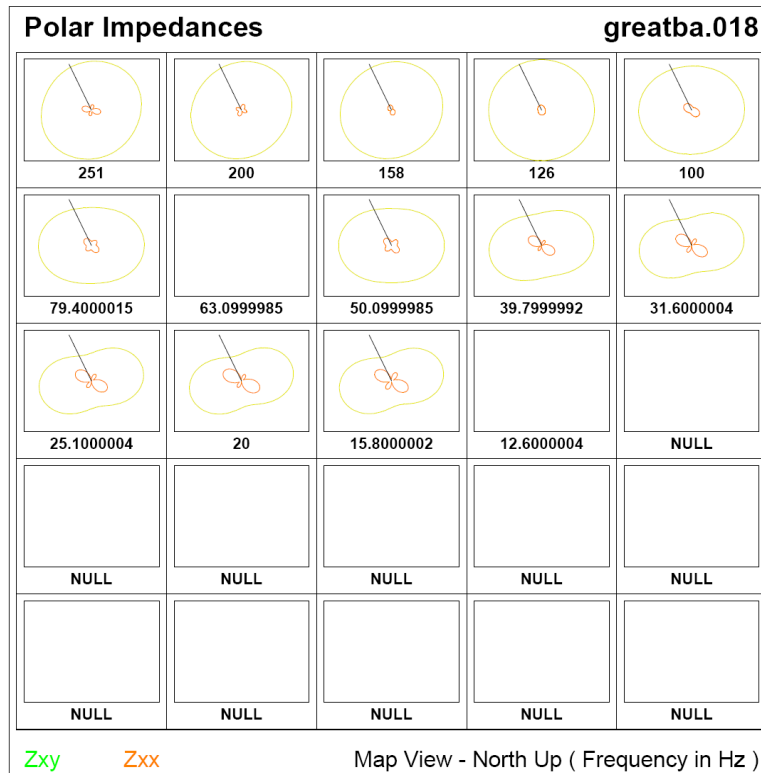


Figure A1-152. Line 1 polar impedance data for site 18 for frequencies 12 Hz – 251 Hz.

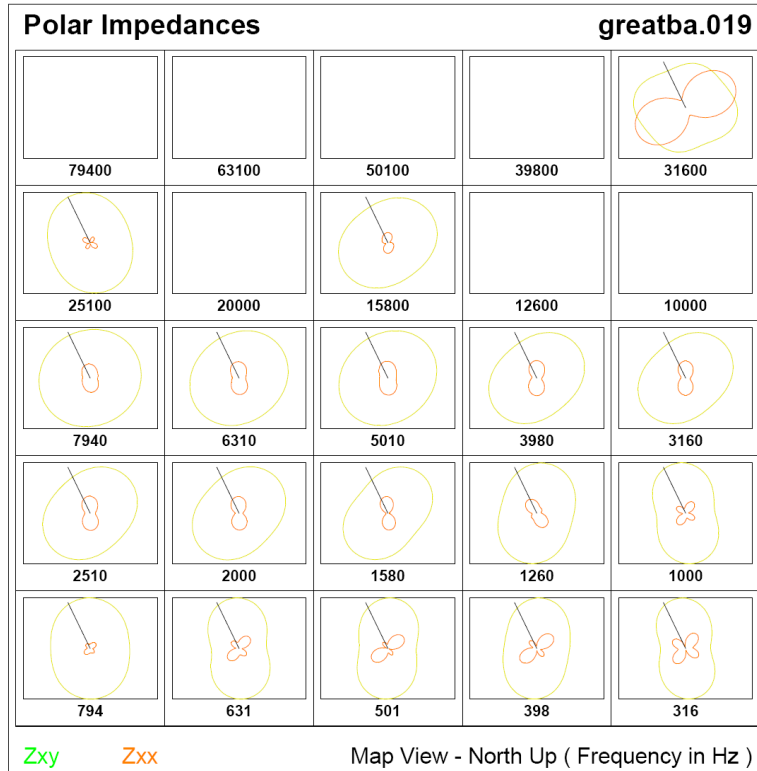


Figure A1-153. Line 1 polar impedance data for site 19 for frequencies 316 Hz – 79 kHz.

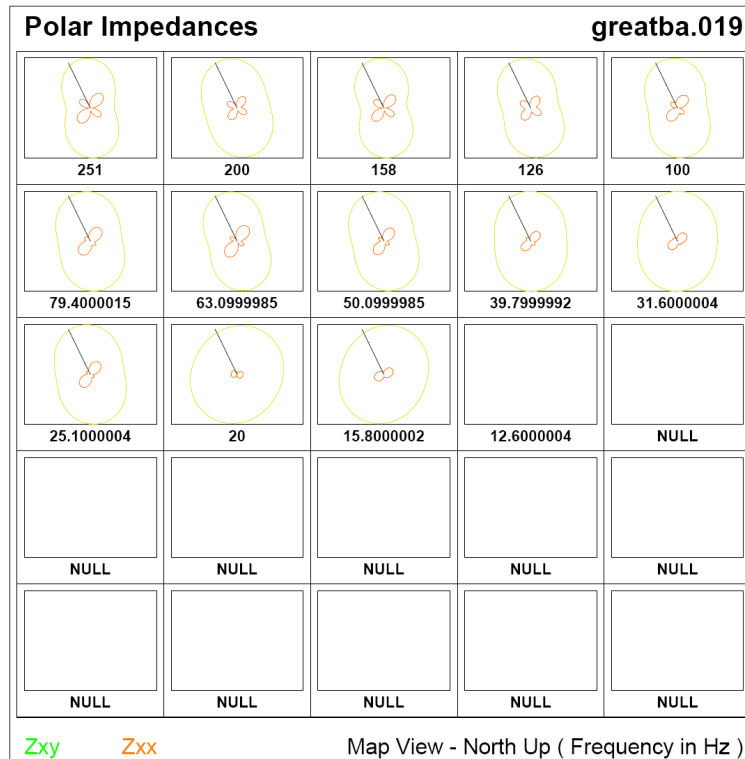


Figure A1-154. Line 1 polar impedance data for site 19 for frequencies 12 Hz – 251 Hz.

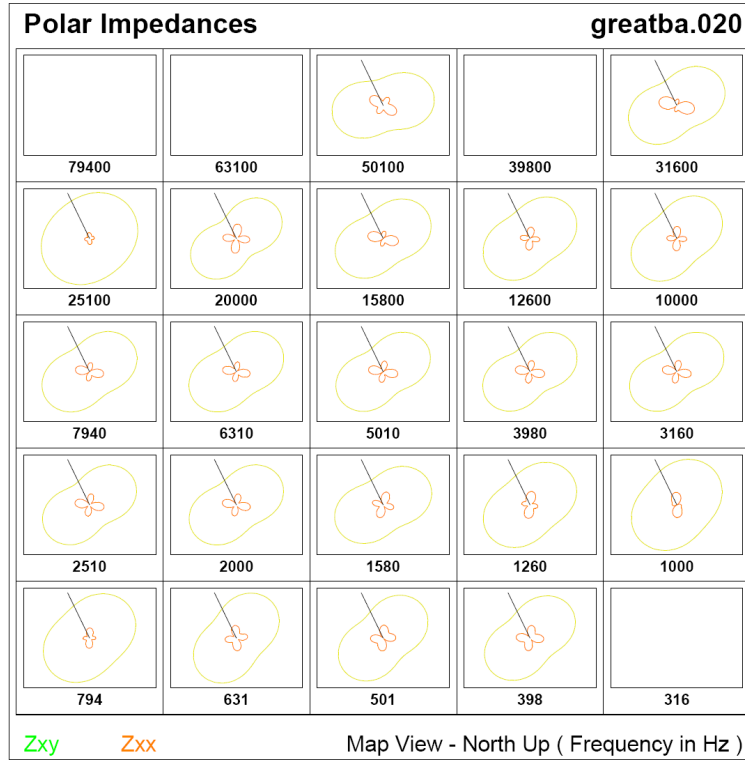


Figure A1-155. Line 1 polar impedance data for site 20 for frequencies 316 Hz – 79 kHz.

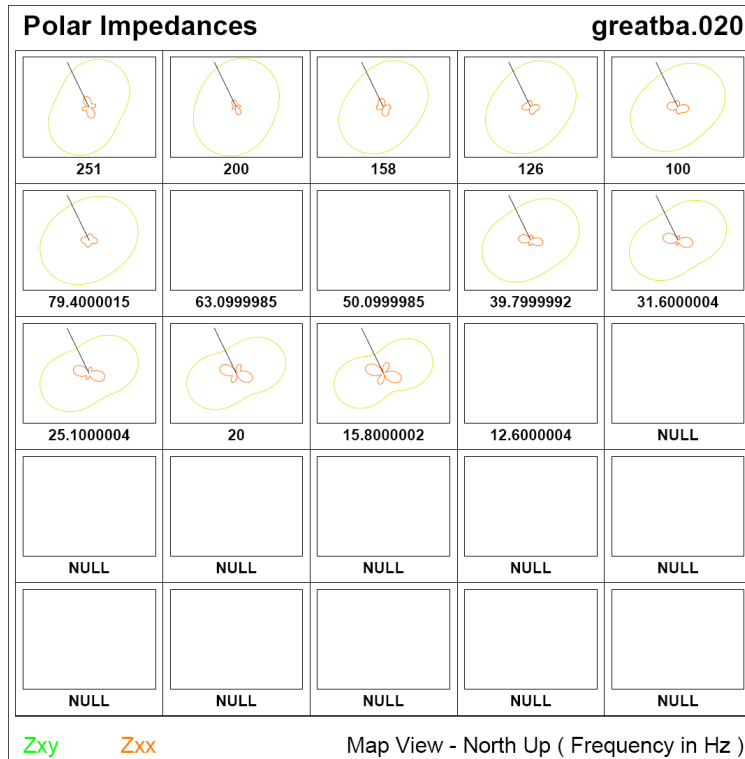


Figure A1-156. Line 1 polar impedance data for site 20 for frequencies 12 Hz – 251 Hz.

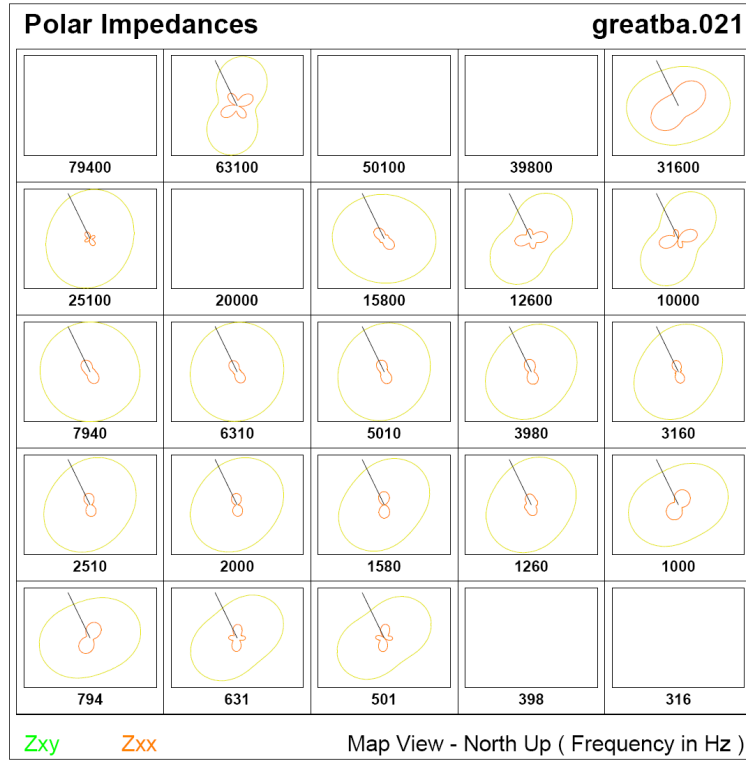


Figure A1-157. Line 1 polar impedance data for site 21 for frequencies 316 Hz – 79 kHz.

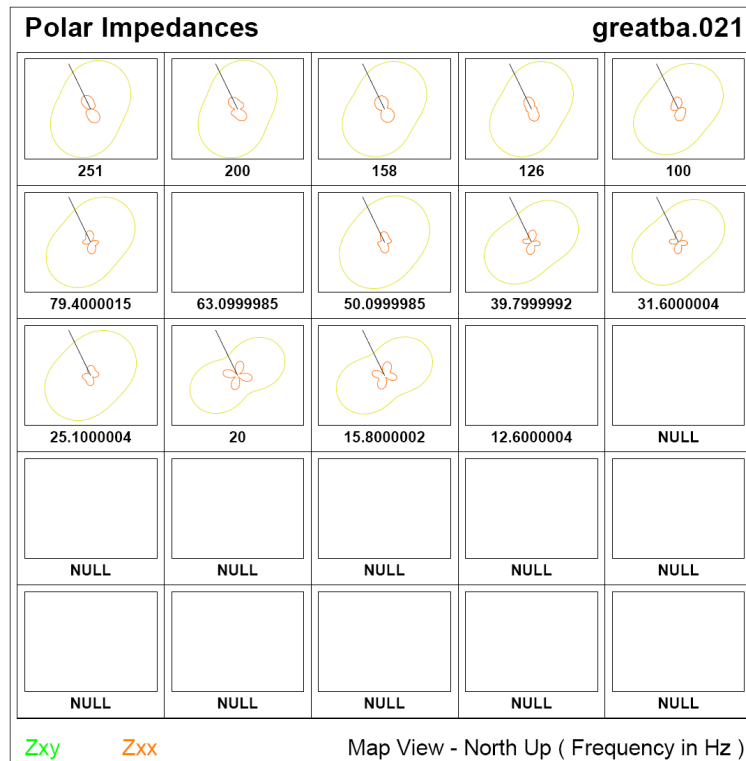
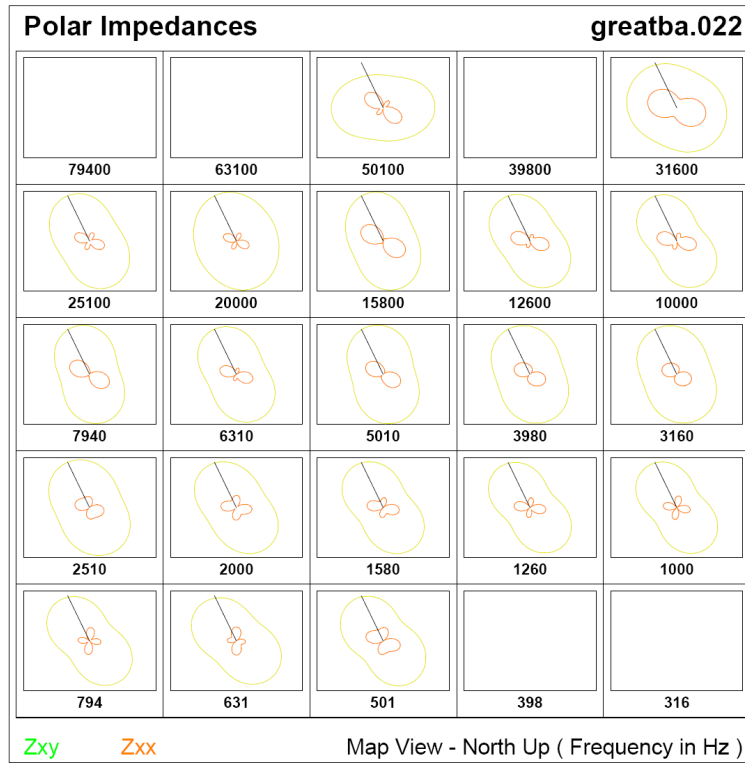
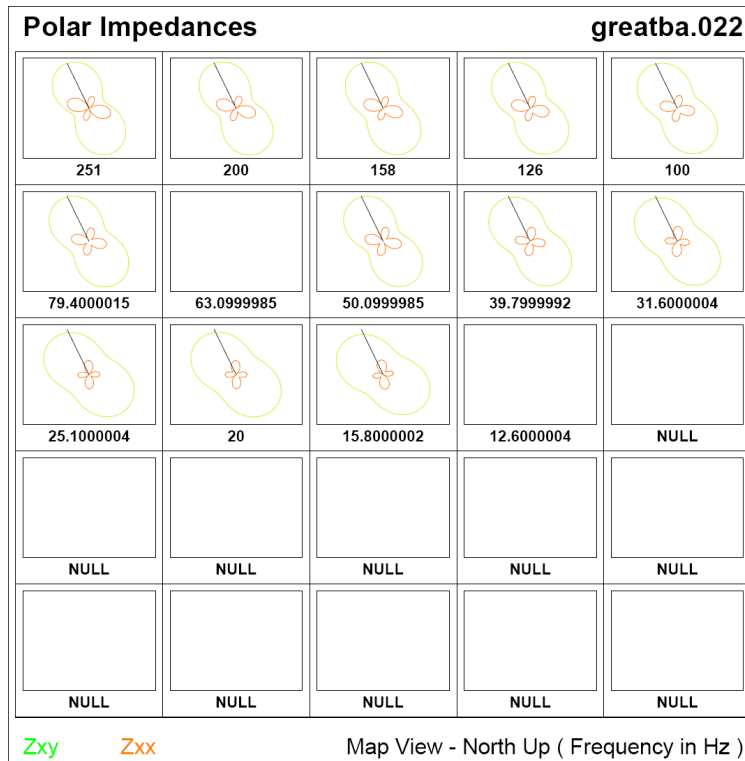


Figure A1-158. Line 1 polar impedance data for site 21 for frequencies 12 Hz – 251 Hz.



**Figure A1-159.** Line 1 polar impedance data for site 22 for frequencies 316 Hz – 79 kHz.



**Figure A1-160.** Line 1 polar impedance data for site 22 for frequencies 12 Hz – 251 Hz.

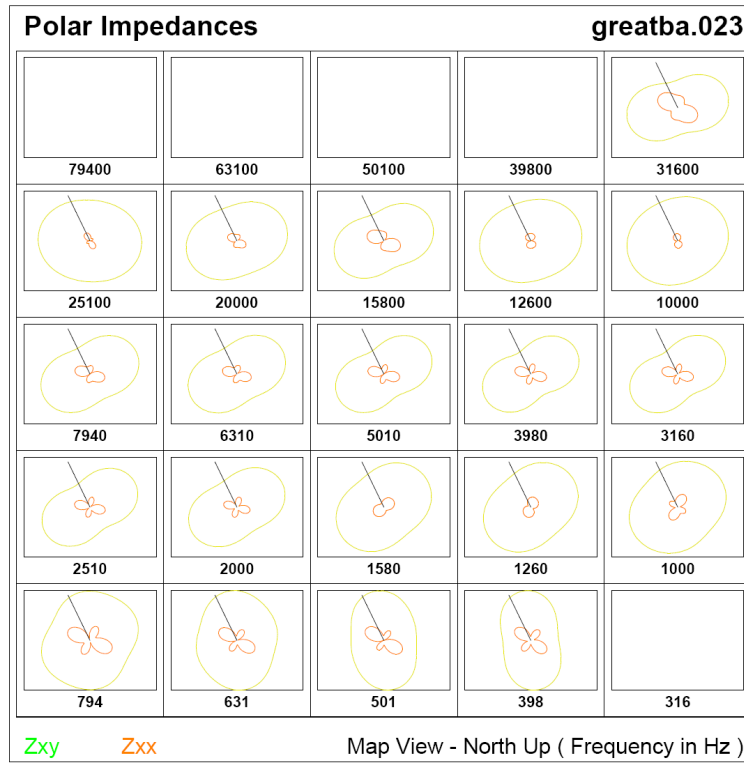


Figure A1-161. Line 1 polar impedance data for site 23 for frequencies 316 Hz – 79 kHz.

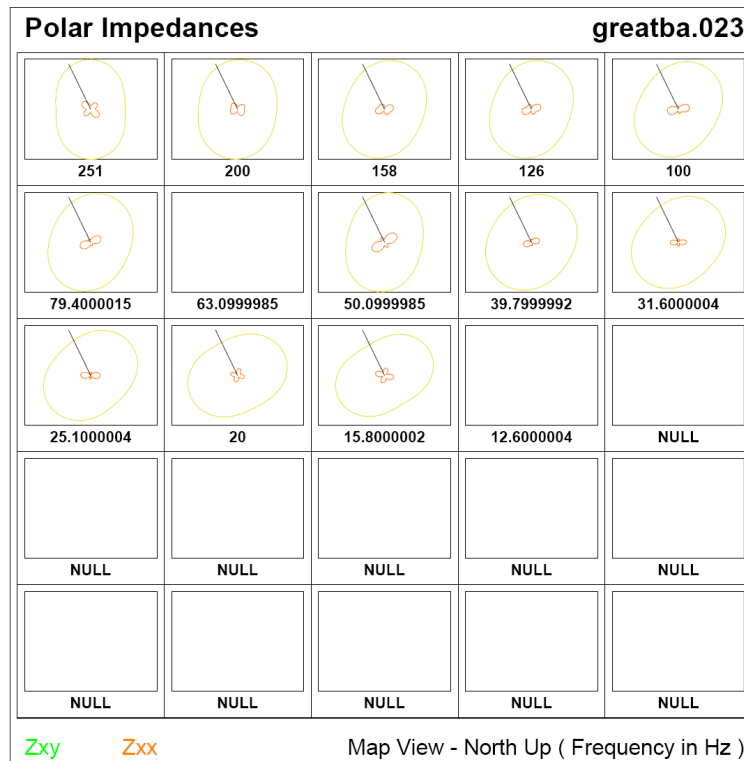


Figure A1-162. Line 1 polar impedance data for site 23 for frequencies 12 Hz – 251 Hz.

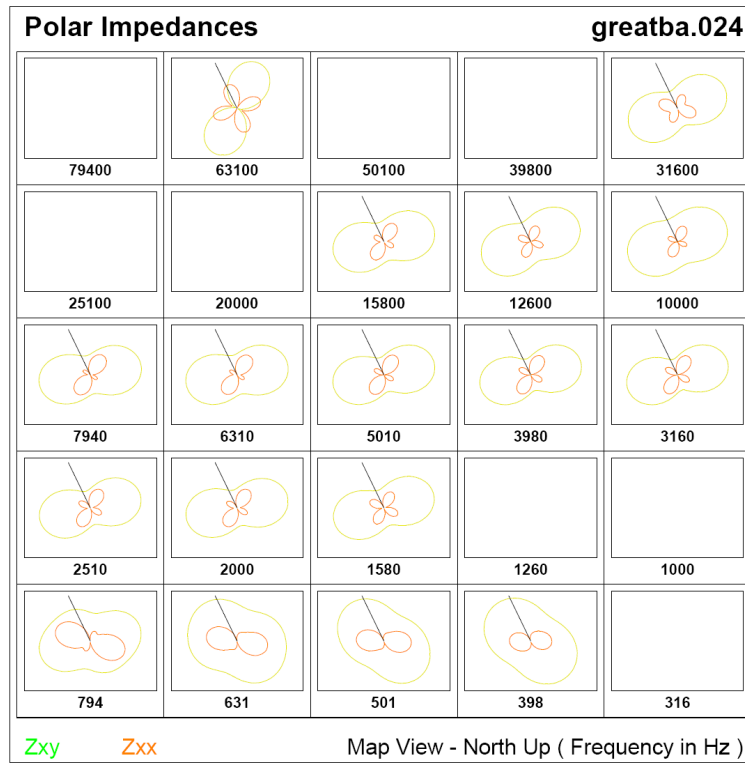


Figure A1-163. Line 1 polar impedance data for site 24 for frequencies 316 Hz – 79 kHz.

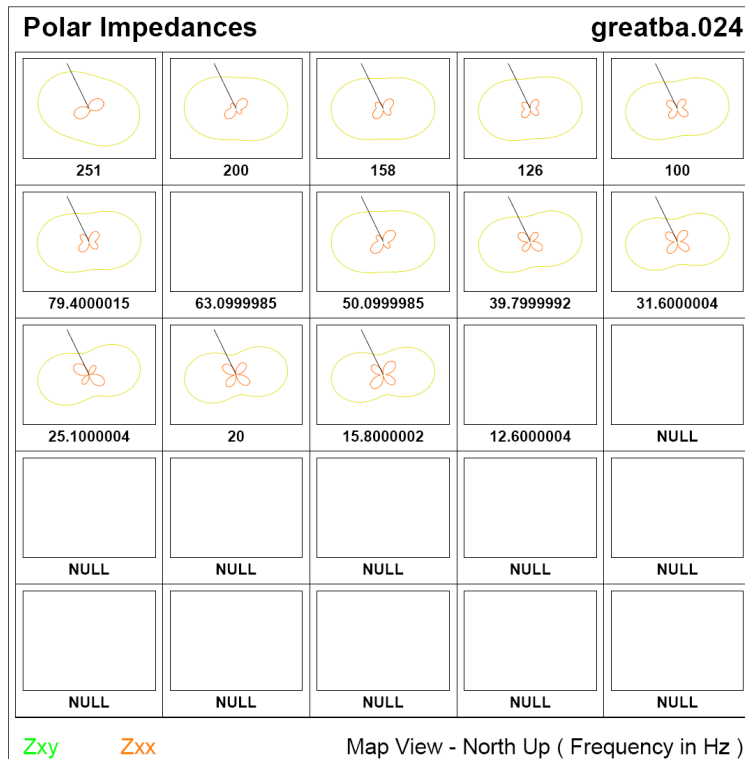


Figure A1-164. Line 1 polar impedance data for site 24 for frequencies 12 Hz – 251 Hz.



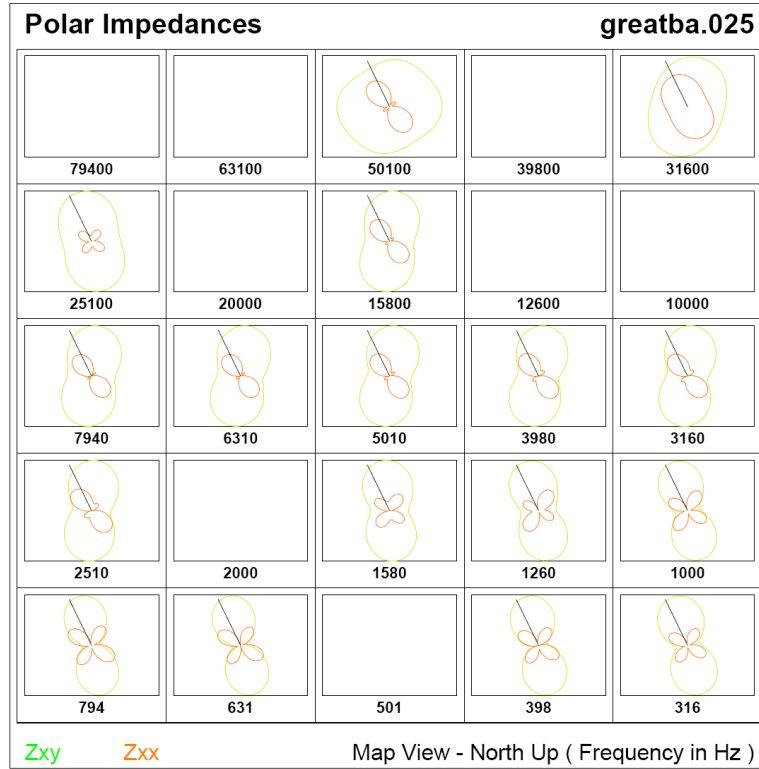


Figure A1-165. Line 1 polar impedance data for site 25 for frequencies 316 Hz – 79 kHz.

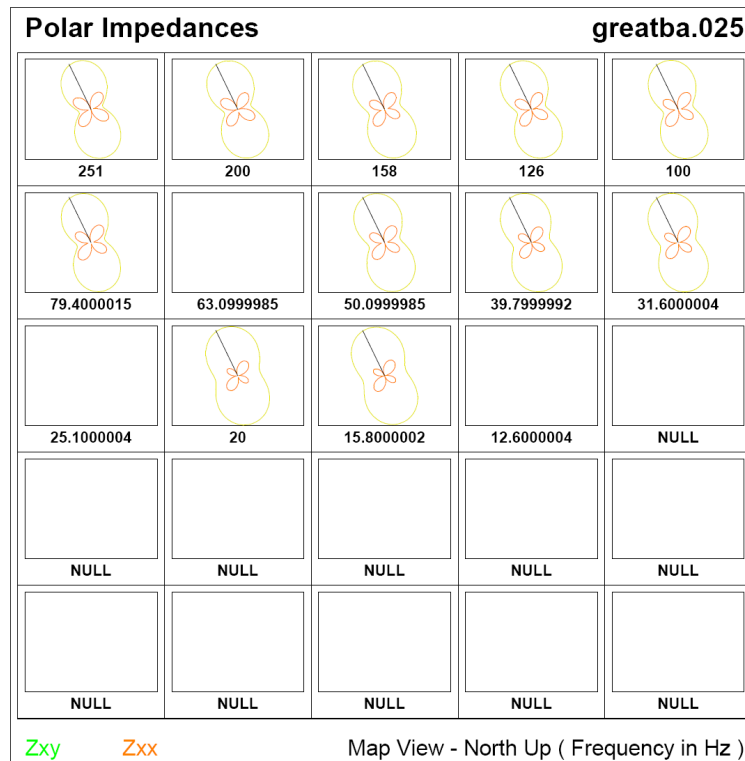


Figure A1-166. Line 1 polar impedance data for site 25 for frequencies 12 Hz – 251 Hz.

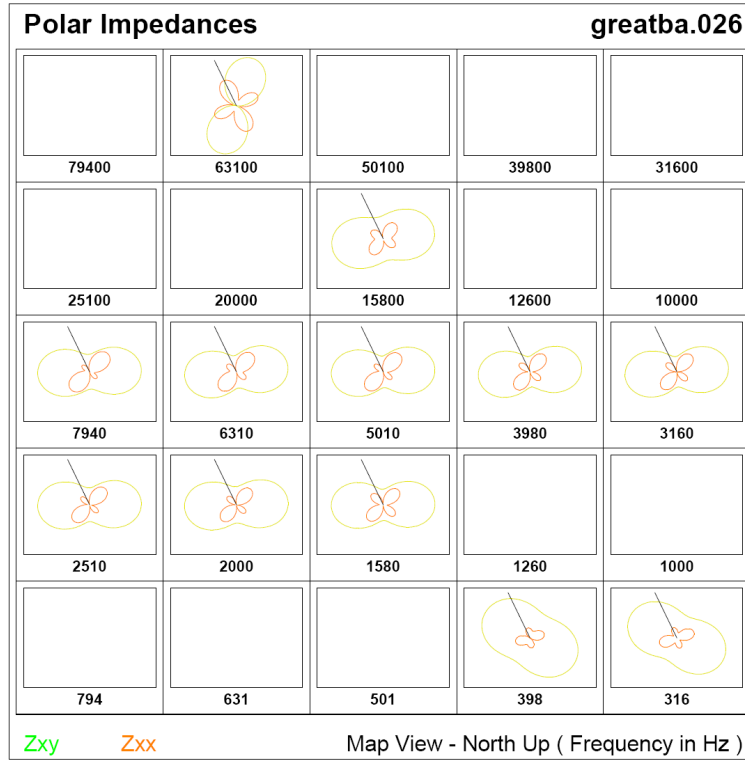


Figure A1-167. Line 1 polar impedance data for site 26 for frequencies 316 Hz – 79 kHz.

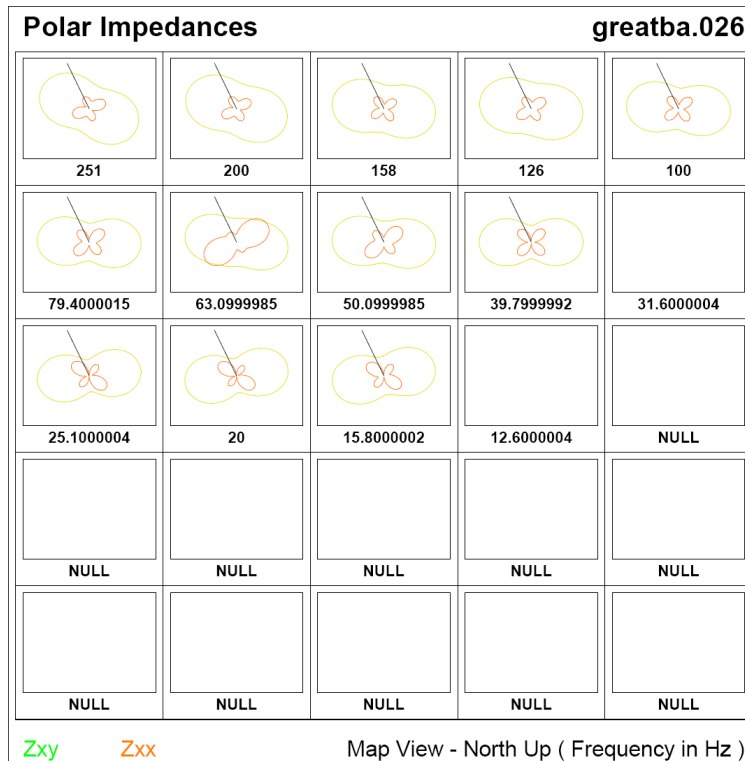


Figure A1-168. Line 1 polar impedance data for site 26 for frequencies 12 Hz – 251 Hz.

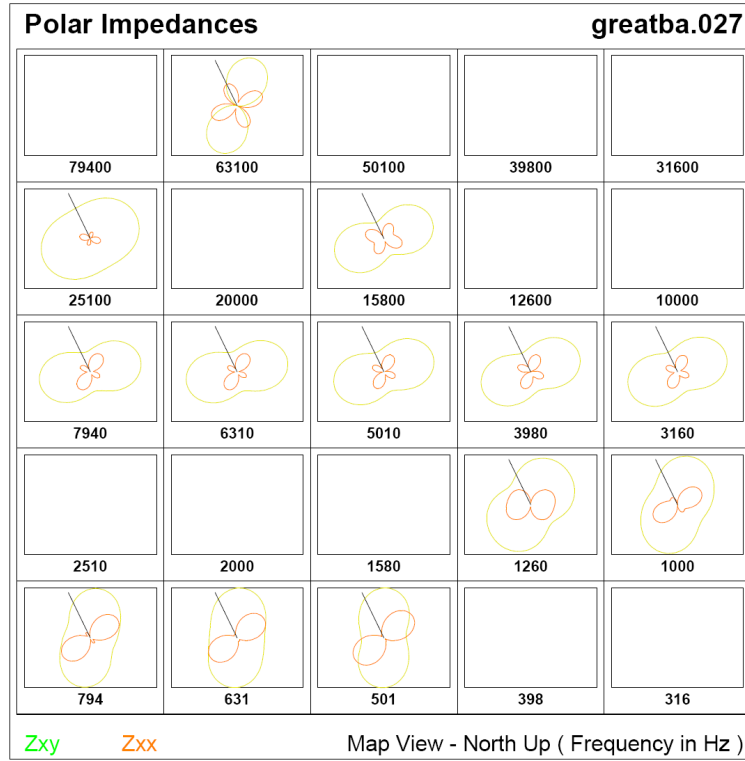


Figure A1-169. Line 1 polar impedance data for site 27 for frequencies 316 Hz – 79 kHz.

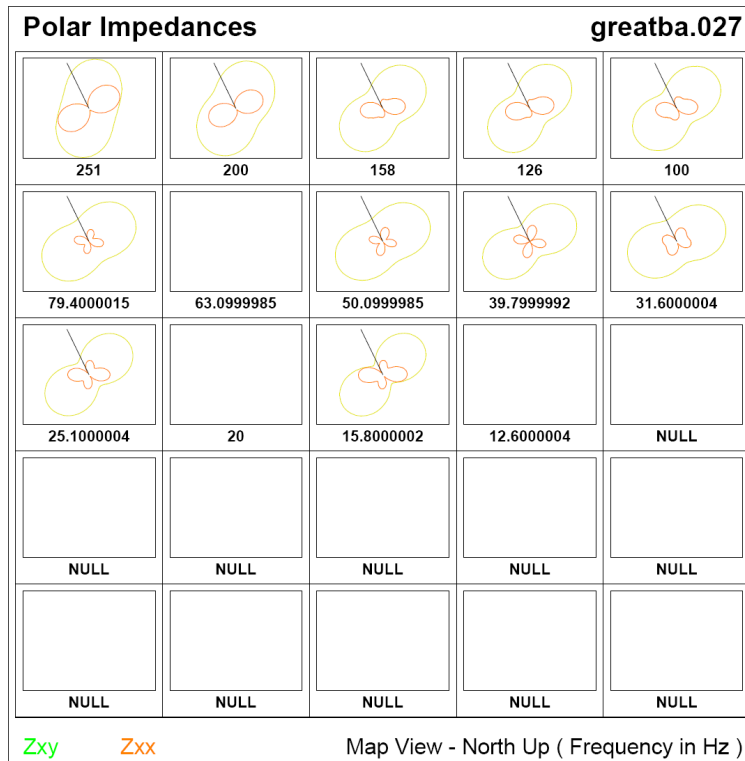


Figure A1-170. Line 1 polar impedance data for site 27 for frequencies 12 Hz – 251 Hz.

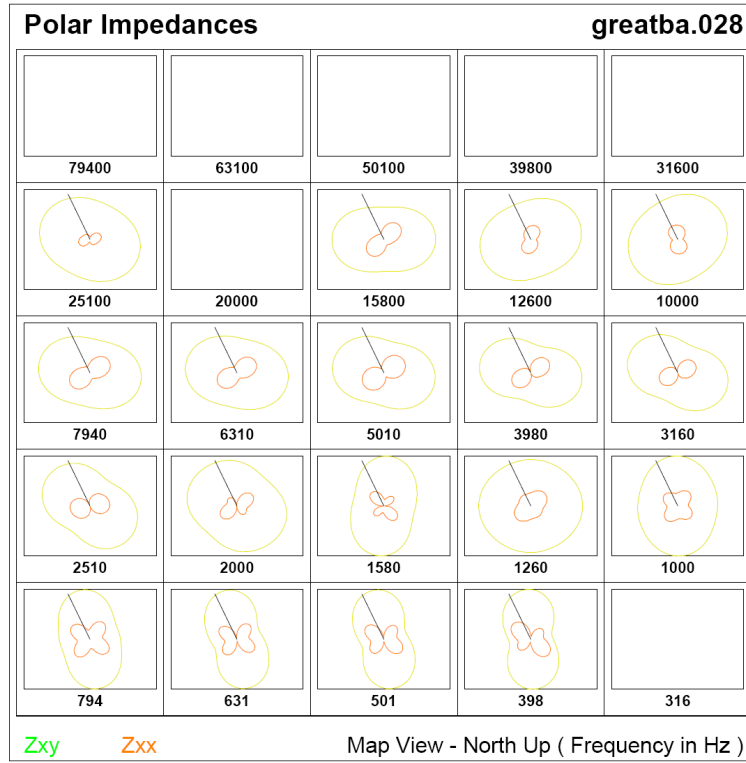


Figure A1-171. Line 1 polar impedance data for site 28 for frequencies 316 Hz – 79 kHz.

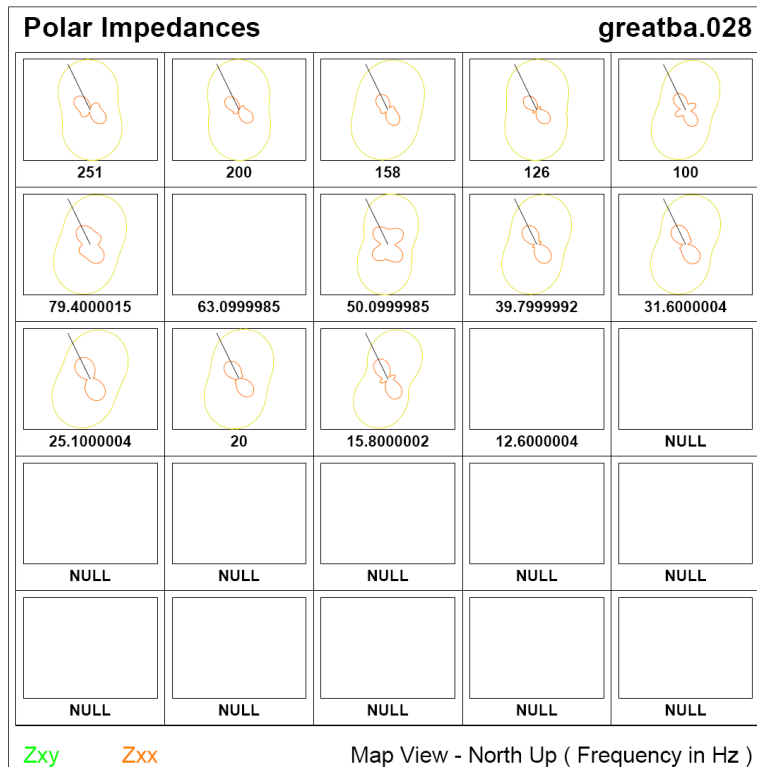


Figure A1-172. Line 1 polar impedance data for site 28 for frequencies 12 Hz – 251 Hz.

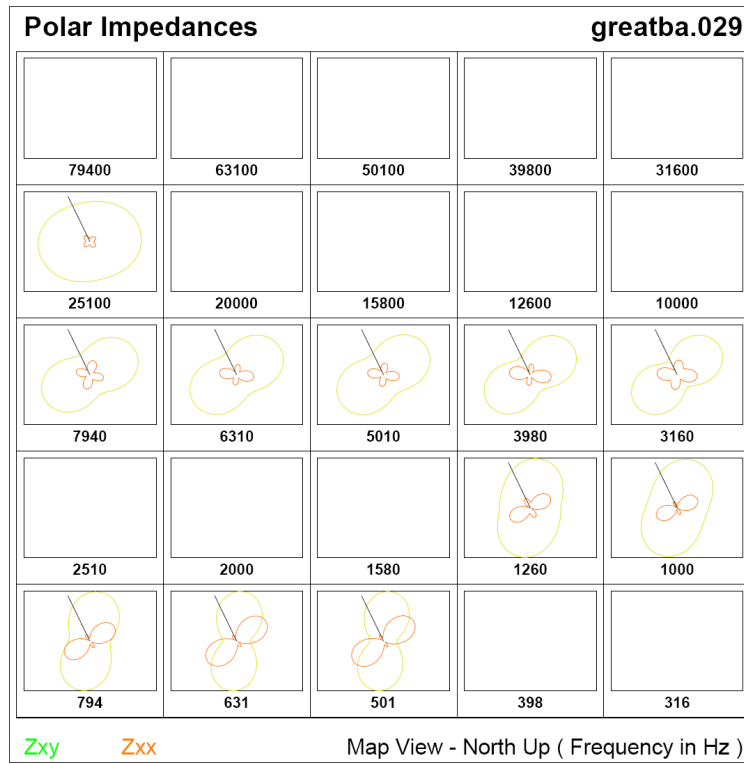


Figure A1-173. Line 1 polar impedance data for site 29 for frequencies 316 Hz – 79 kHz.

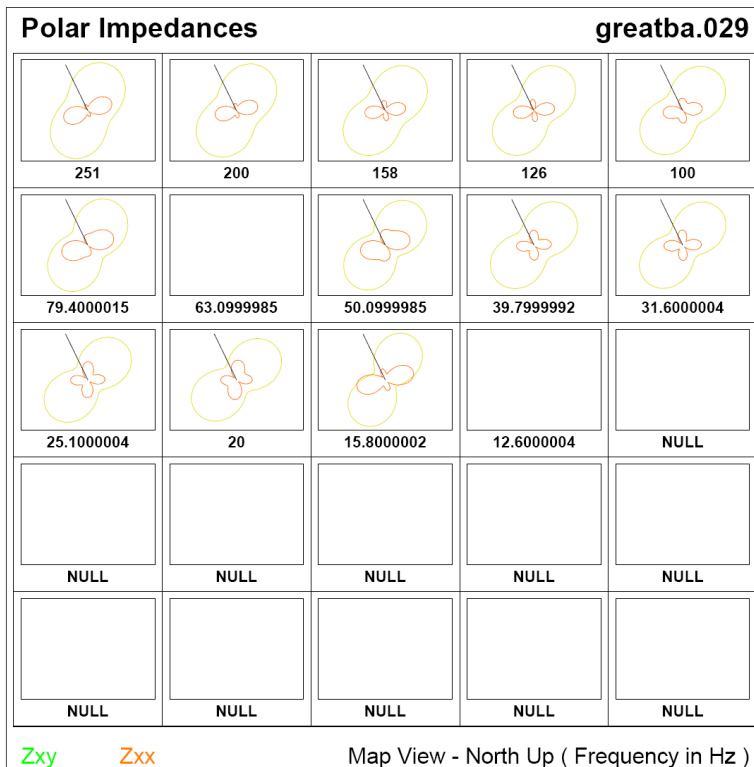
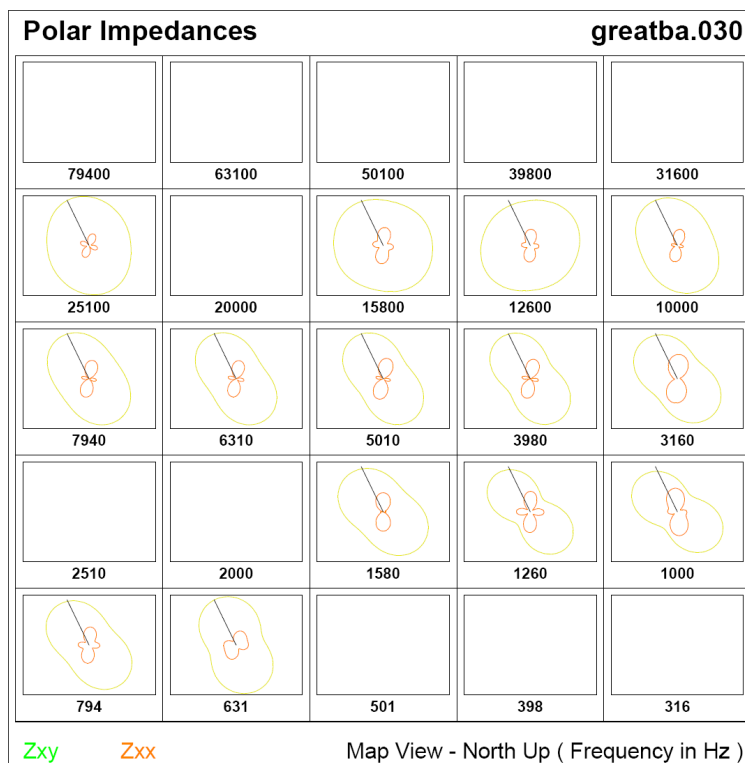
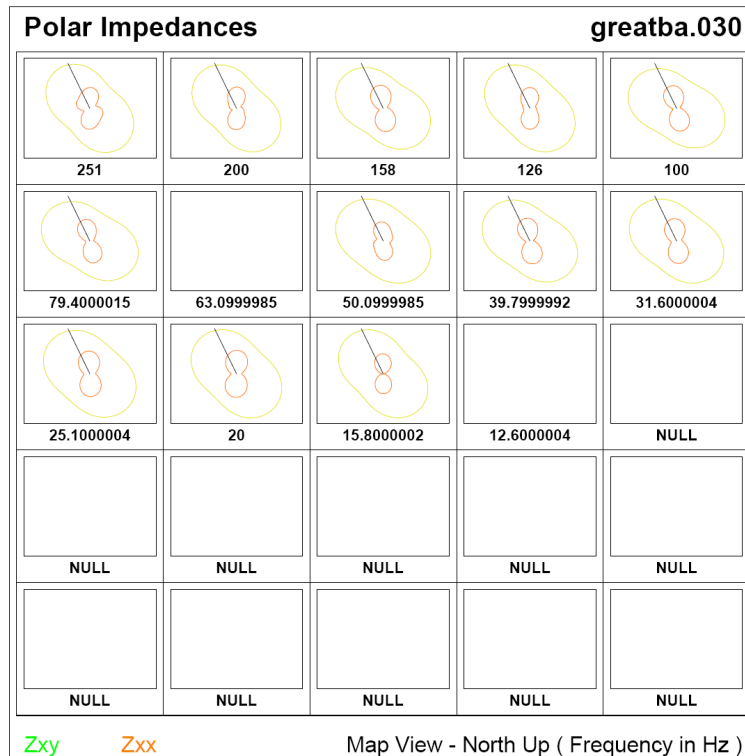


Figure A1-174. Line 1 polar impedance data for site 29 for frequencies 12 Hz – 251 Hz.



**Figure A1-175.** Line 1 polar impedance data for site 30 for frequencies 316 Hz – 79 kHz.



**Figure A1-176.** Line 1 polar impedance data for site 30 for frequencies 12 Hz – 251 Hz.

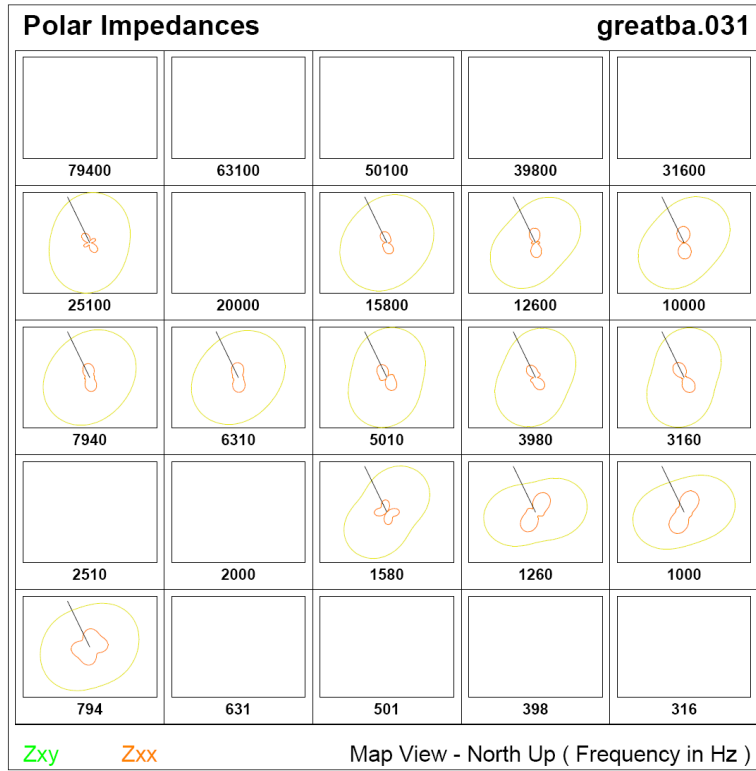


Figure A1-177. Line 1 polar impedance data for site 31 for frequencies 316 Hz – 79 kHz.

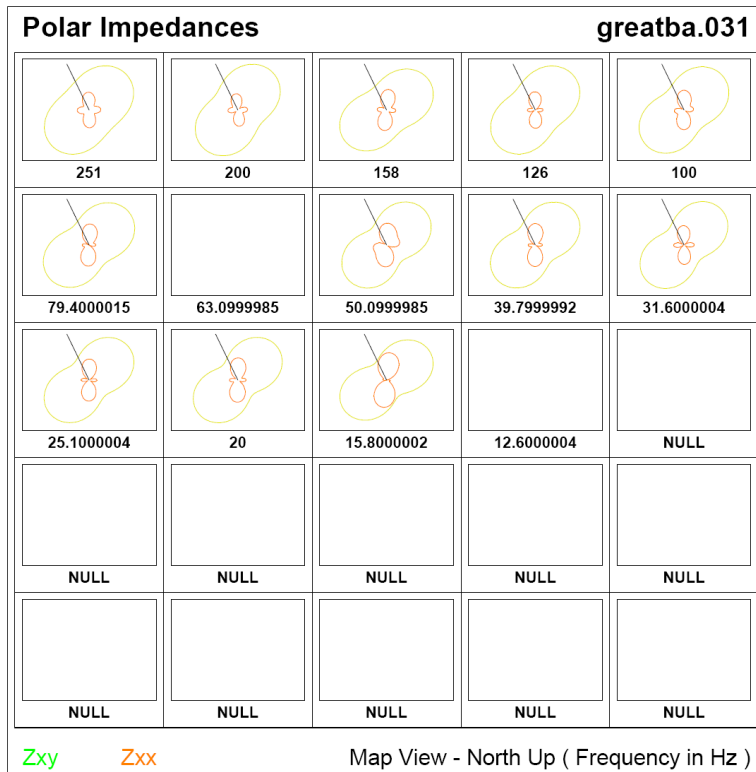


Figure A1-178. Line 1 polar impedance data for site 31 for frequencies 12 Hz – 251 Hz.

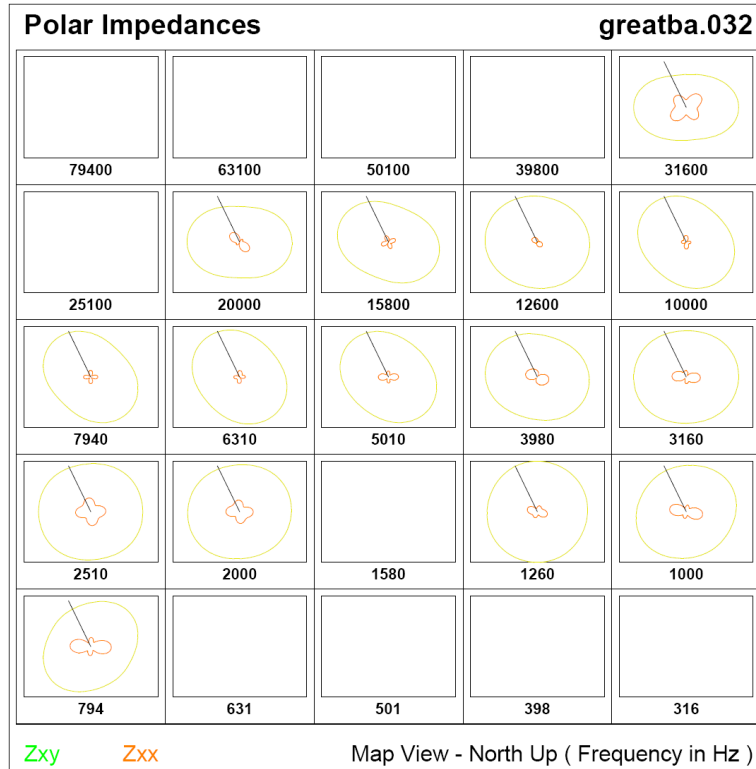


Figure A1-179. Line 1 polar impedance data for site 32 for frequencies 316 Hz – 79 kHz.

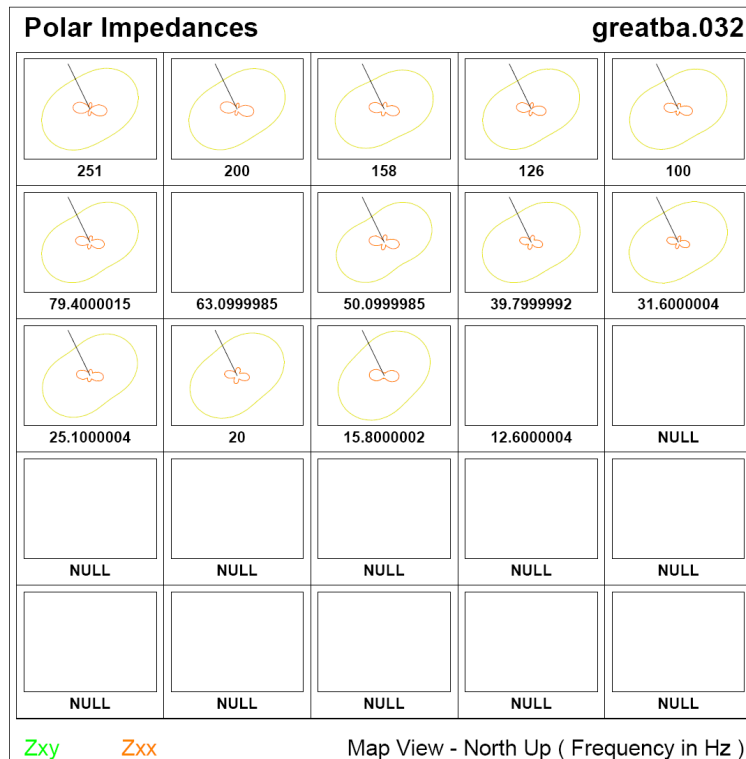
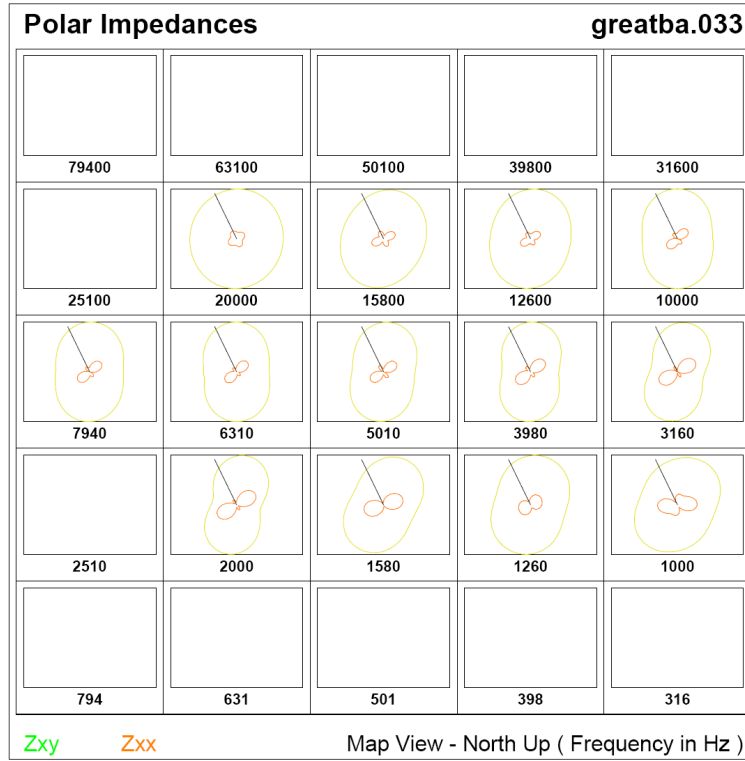
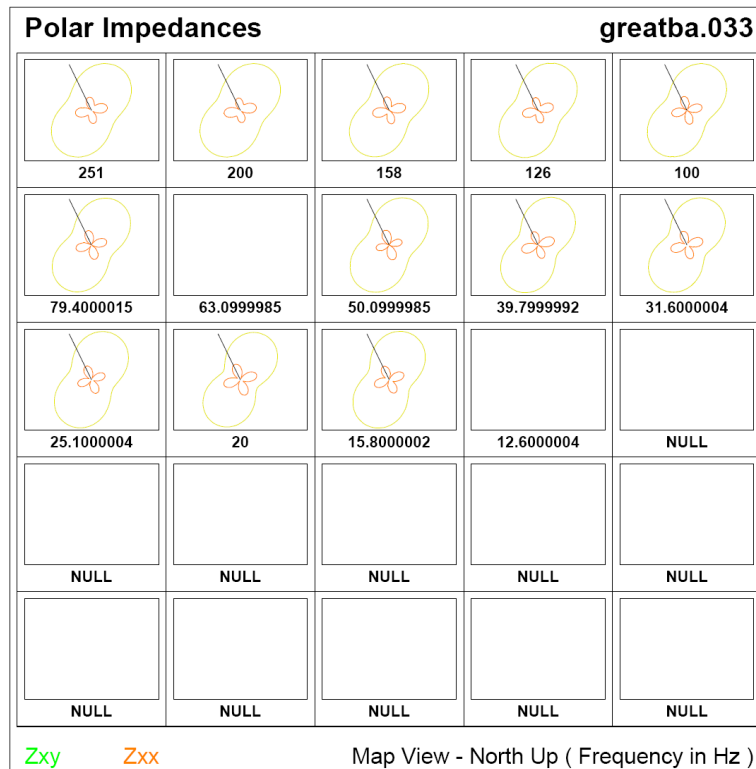


Figure A1-180. Line 1 polar impedance data for site 32 for frequencies 12 Hz – 251 Hz.





**Figure A1-181.** Line 1 polar impedance data for site 33 for frequencies 316 Hz – 79 kHz.



**Figure A1-181.** Line 1 polar impedance data for site 33 for frequencies 12 Hz – 251 Hz.

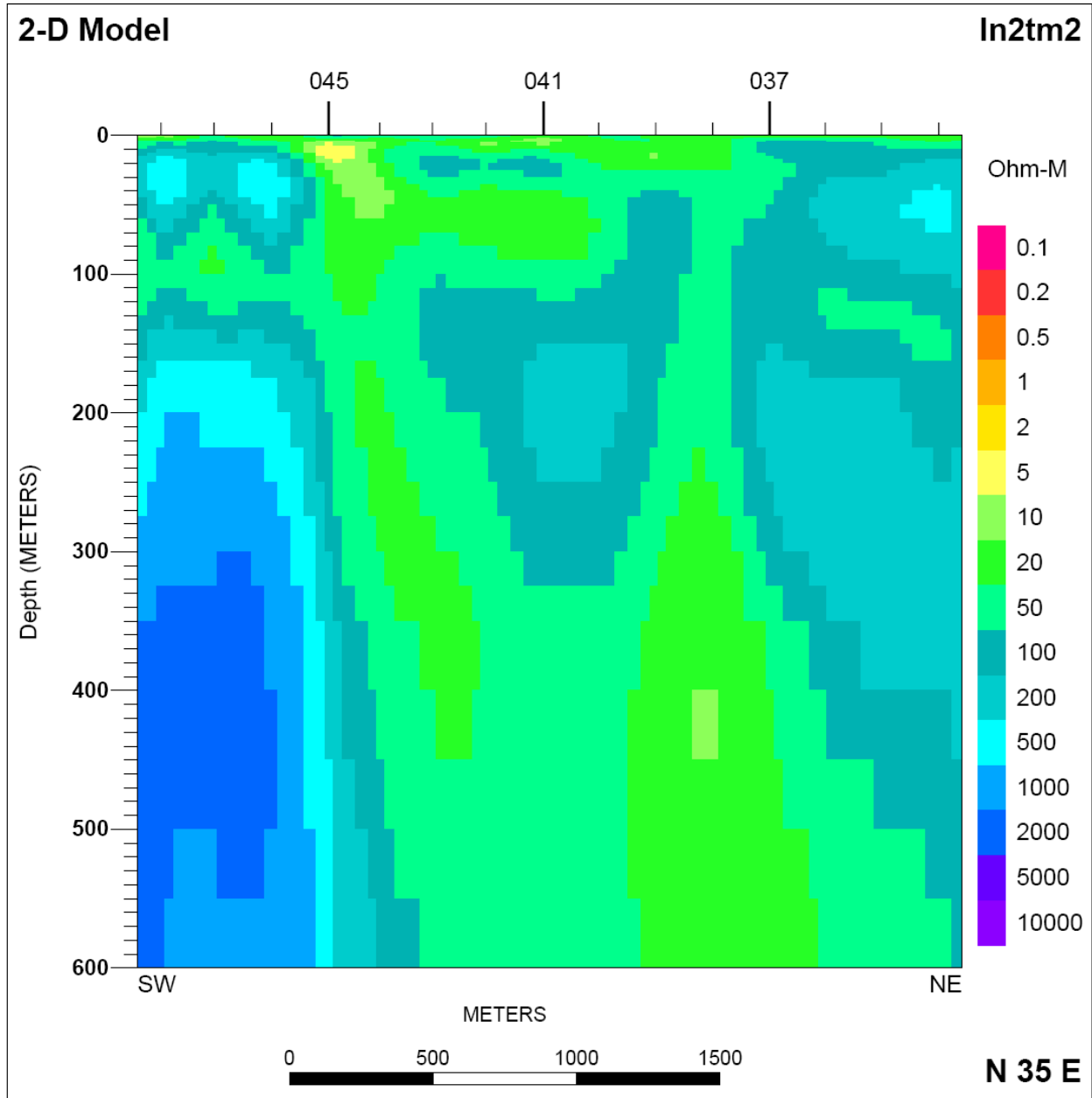


**Figure A1-182.** Line 2 2-D resistivity inversion modeling result for TM mode without model mesh lines. Tic marks at top of model are projected AMT station locations. Vertical exaggeration is 5:1.

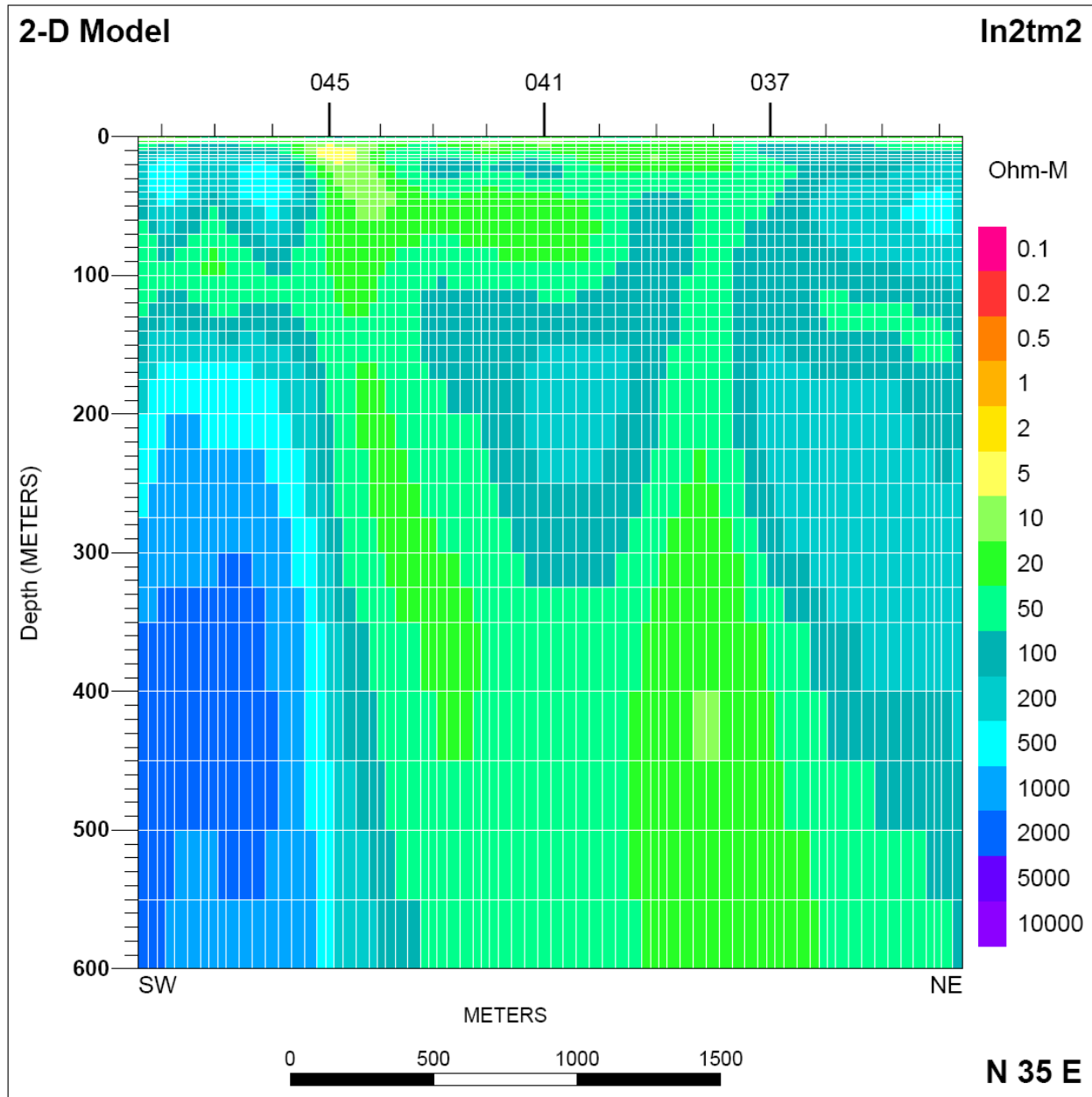


**Figure A1-183.** Line 2 2-D inversion modeling result for TM mode with white model mesh lines. Tic marks at top of model are projected AMT station locations. Vertical exaggeration is 5:1.

## Appendix 1 – Audio-Magnetotelluric Data and Models

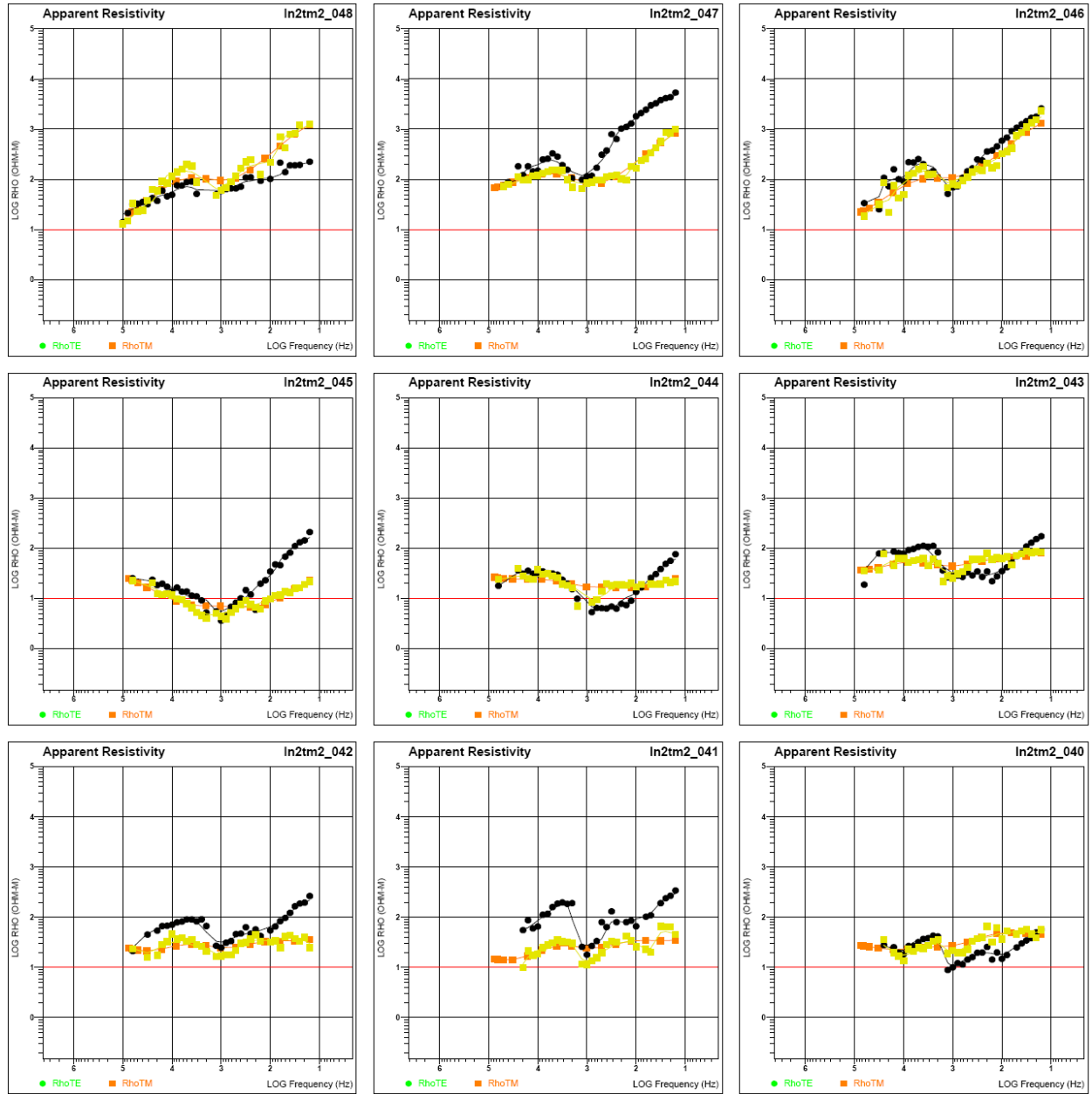


**Figure A1-184.** Line 2 impedance apparent resistivity data for TM mode inversion model, sites 40 - 48.

## Appendix 1 – Audio-Magnetotelluric Data and Models

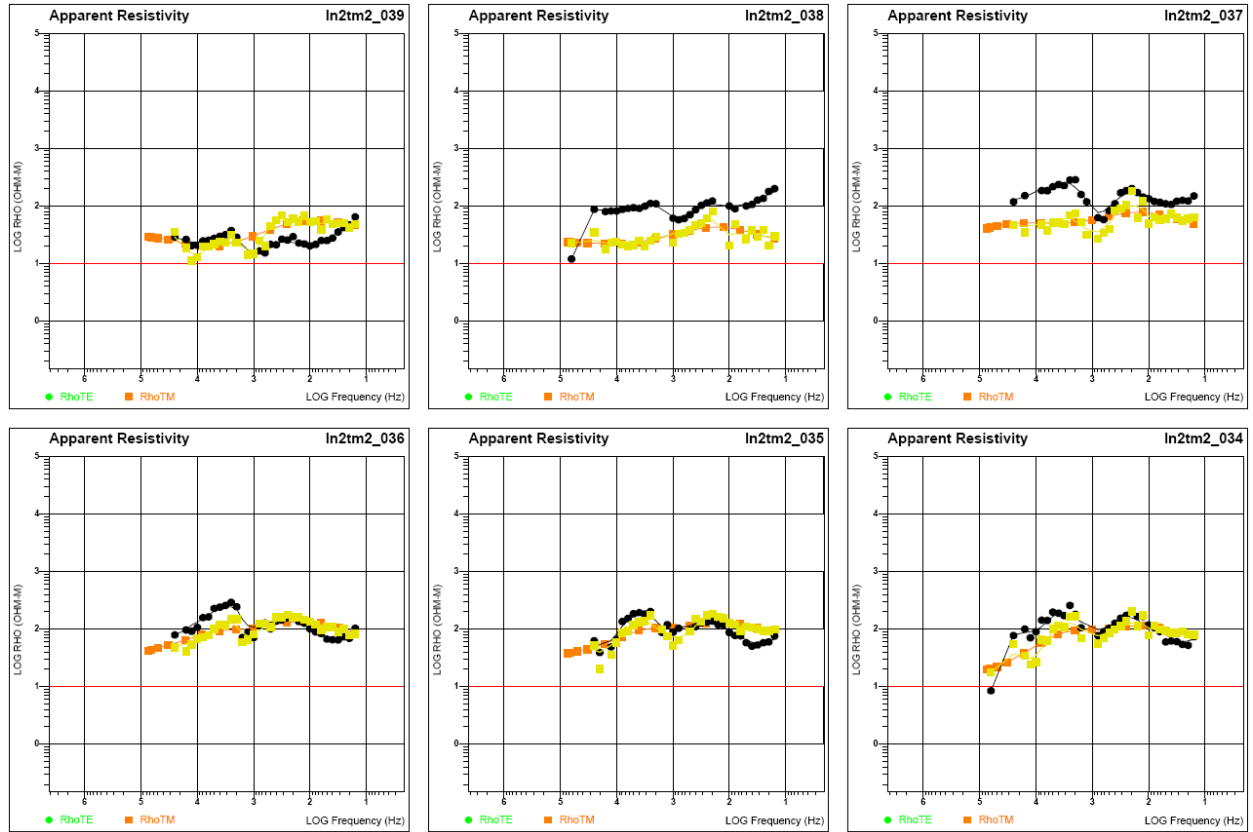


**Figure A1-185.** Line 2 impedance apparent resistivity data for TM mode inversion model, sites 34 - 39.

# Appendix 1 – Audio-Magnetotelluric Data and Models

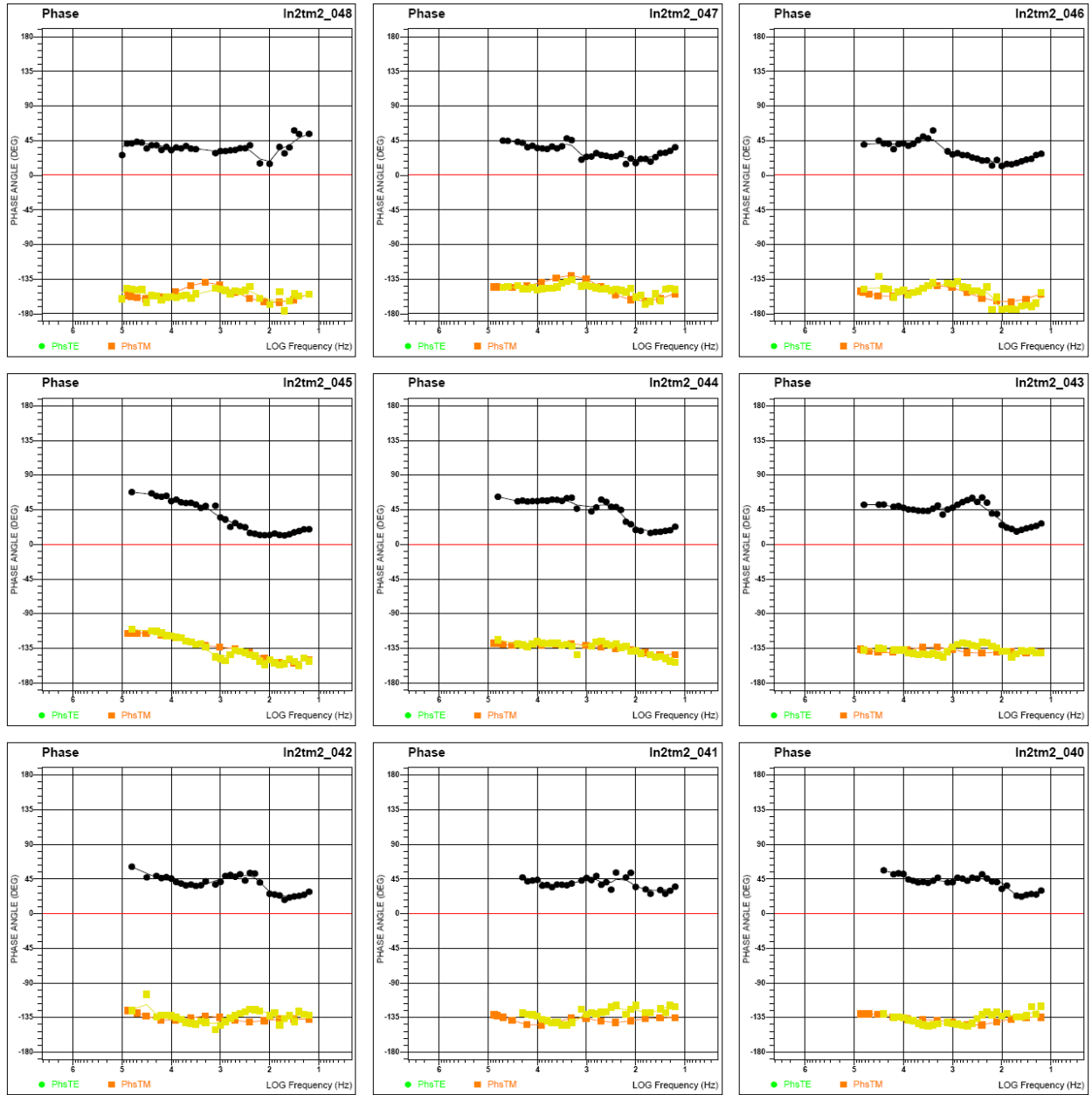


**Figure A1-186.** Line 2 impedance phase data for TM mode inversion model, sites 40 – 48.

## Appendix 1 – Audio-Magnetotelluric Data and Models

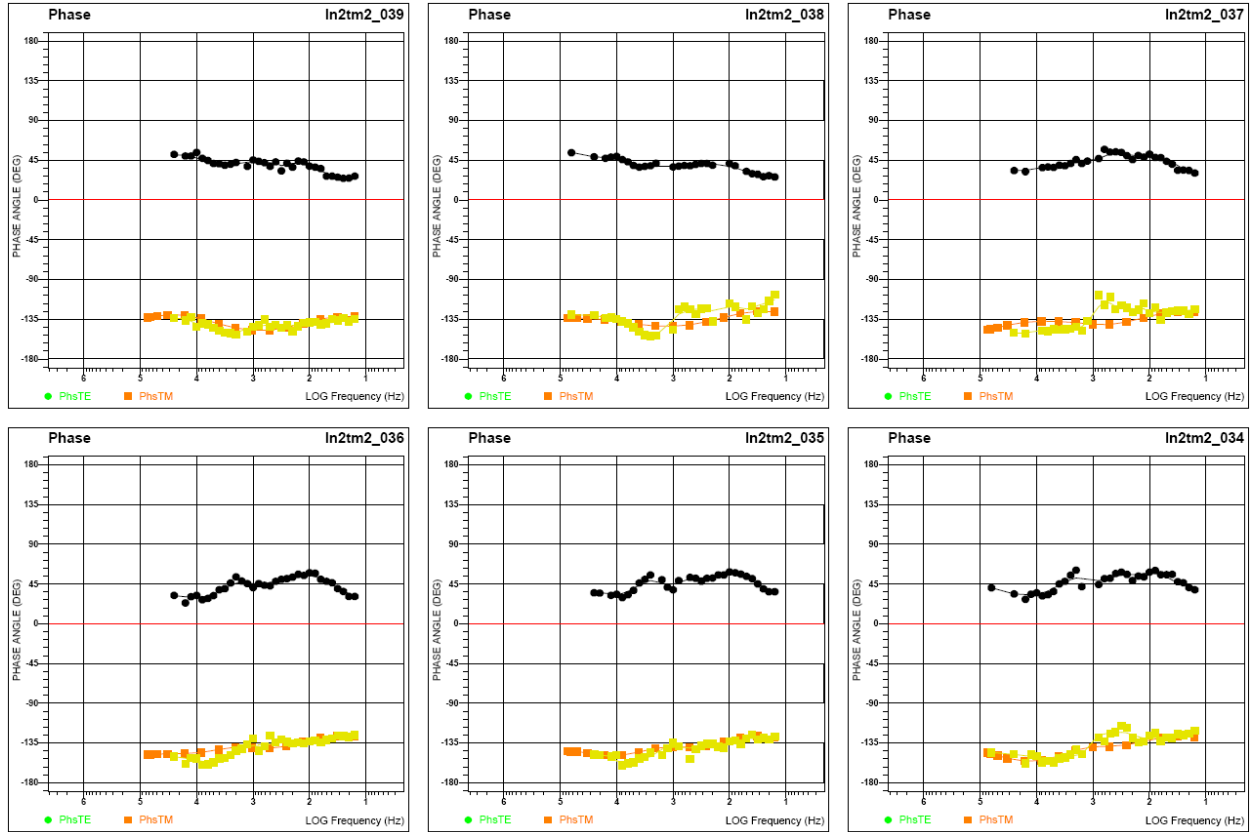


**Figure A1-187.** Line 2 impedance phase data for TM mode inversion model, sites 34 – 39.

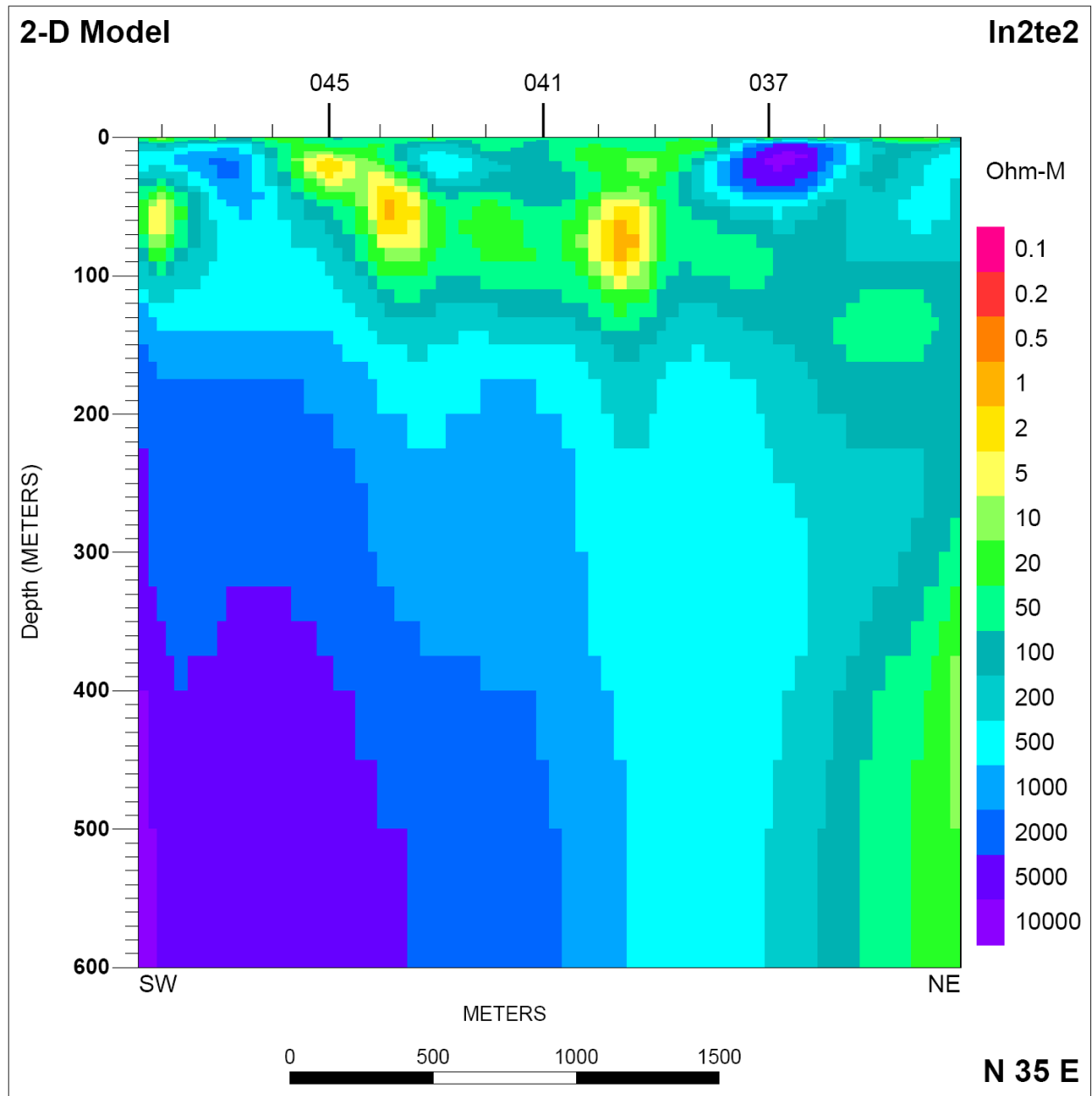


**Figure A1-188.** Line 2 2-D inversion modeling result for TE mode without model mesh lines. Tic marks at top of model are projected AMT station locations. Vertical exaggeration is 5:1.



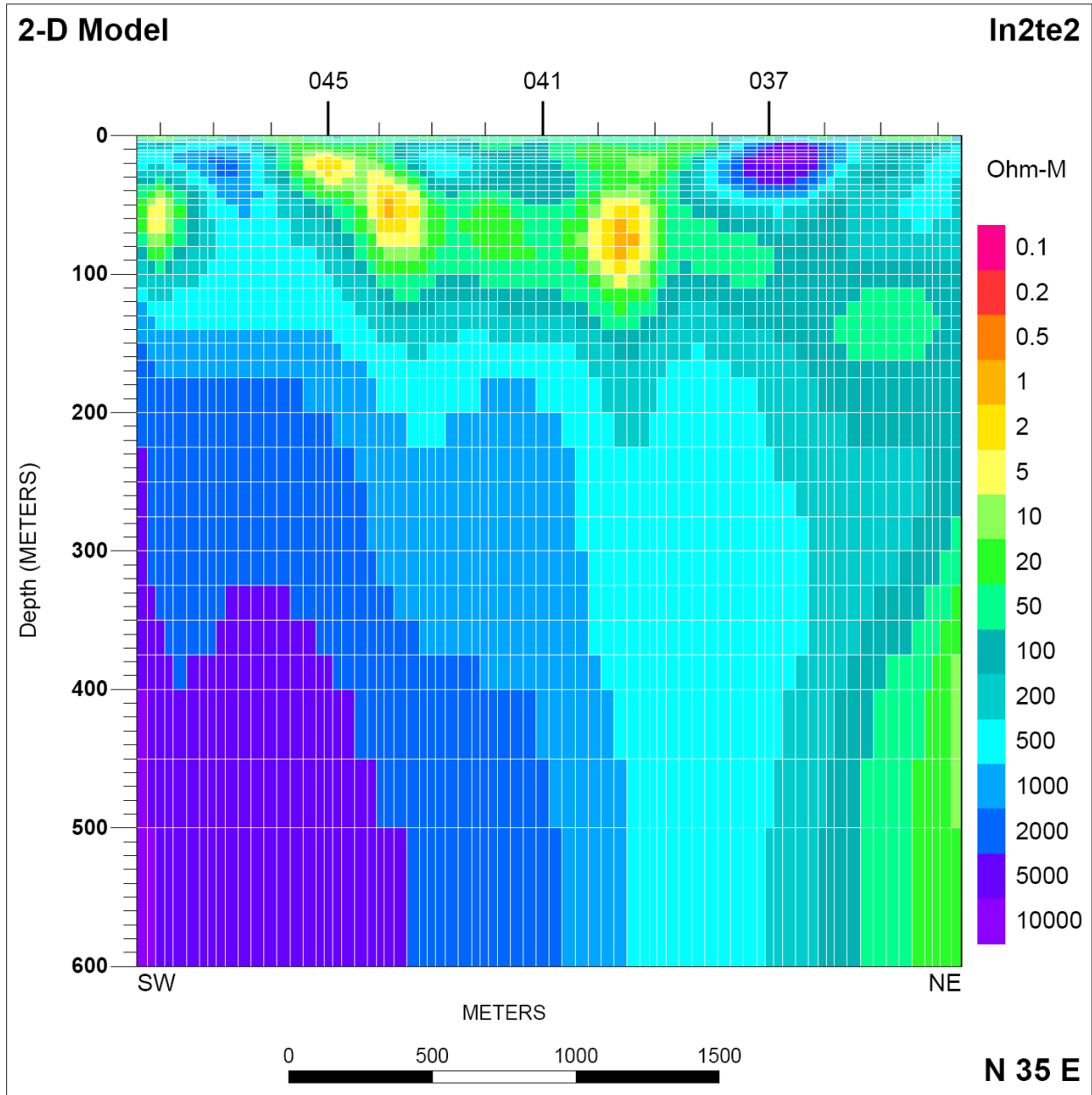


**Figure A1-189.** Line 2 2-D inversion modeling result for TE mode with white model mesh. lines. Tic marks at top of model are projected AMT station locations. Vertical exaggeration is 5:1.

## Appendix 1 – Audio-Magnetotelluric Data and Models

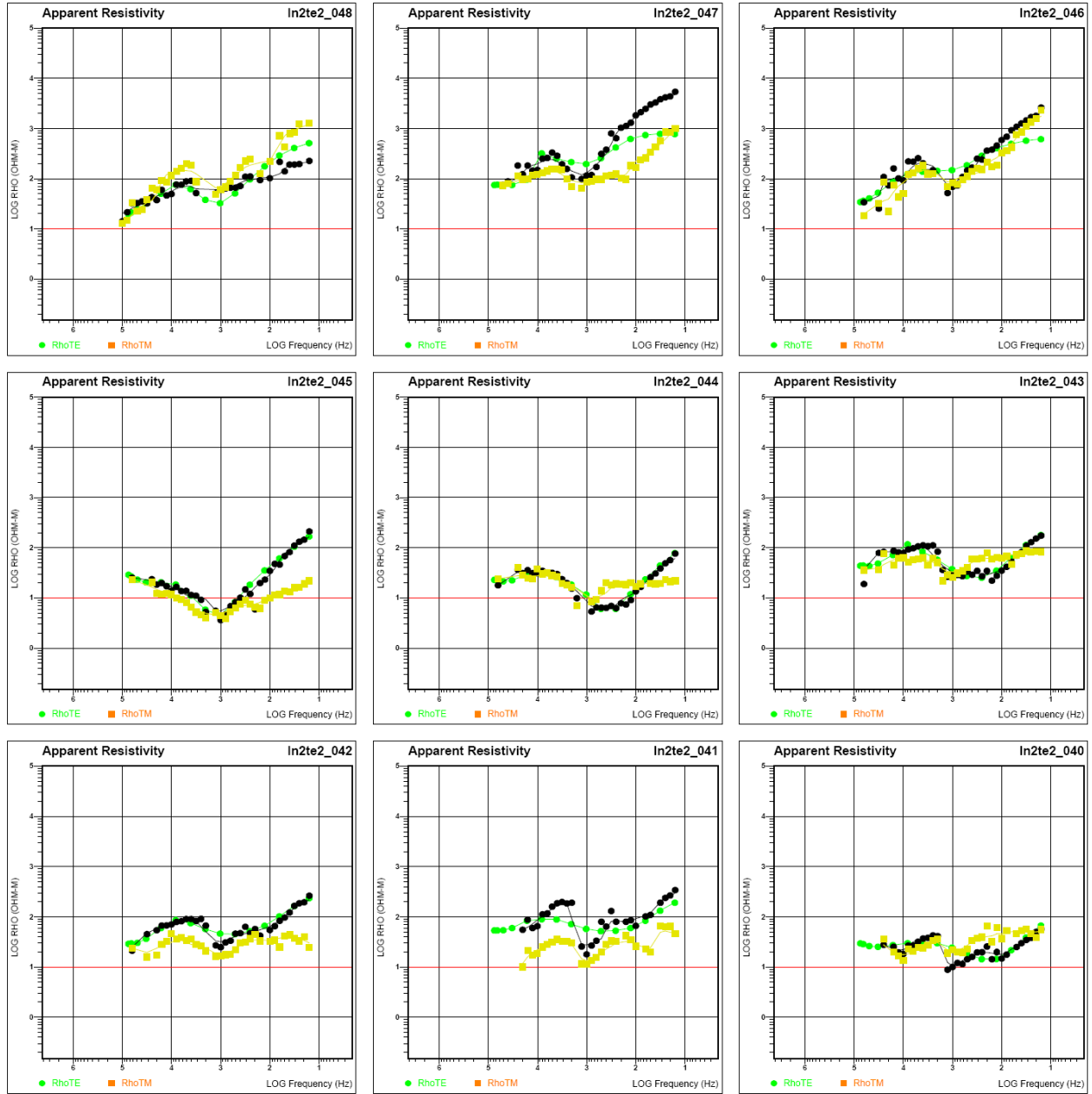
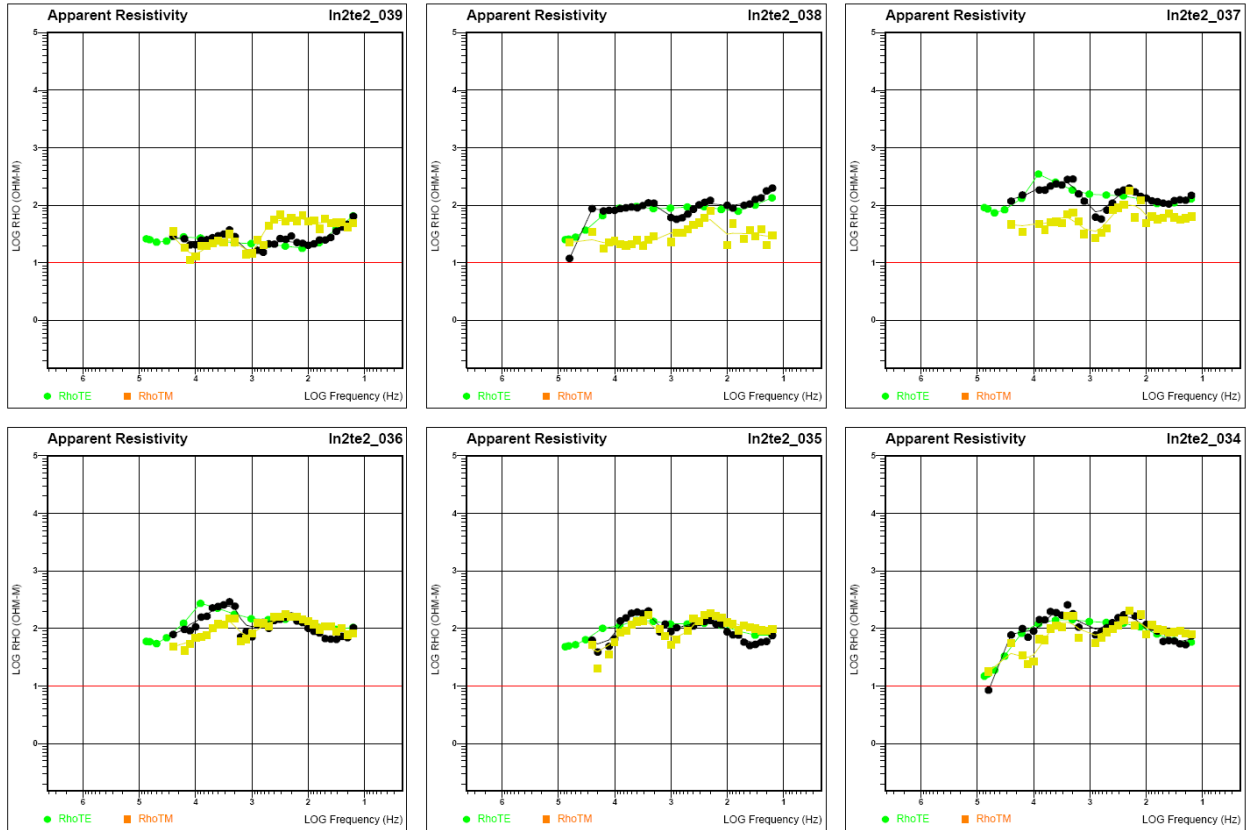


Figure A1-190. Line 2 impedance apparent resistivity data for TE mode inversion model, sites 40 - 48.

## Appendix 1 – Audio-Magnetotelluric Data and Models



**Figure A1-191.** Line 2 impedance apparent resistivity data for TE mode inversion model, sites 34 - 39.

## Appendix 1 – Audio-Magnetotelluric Data and Models

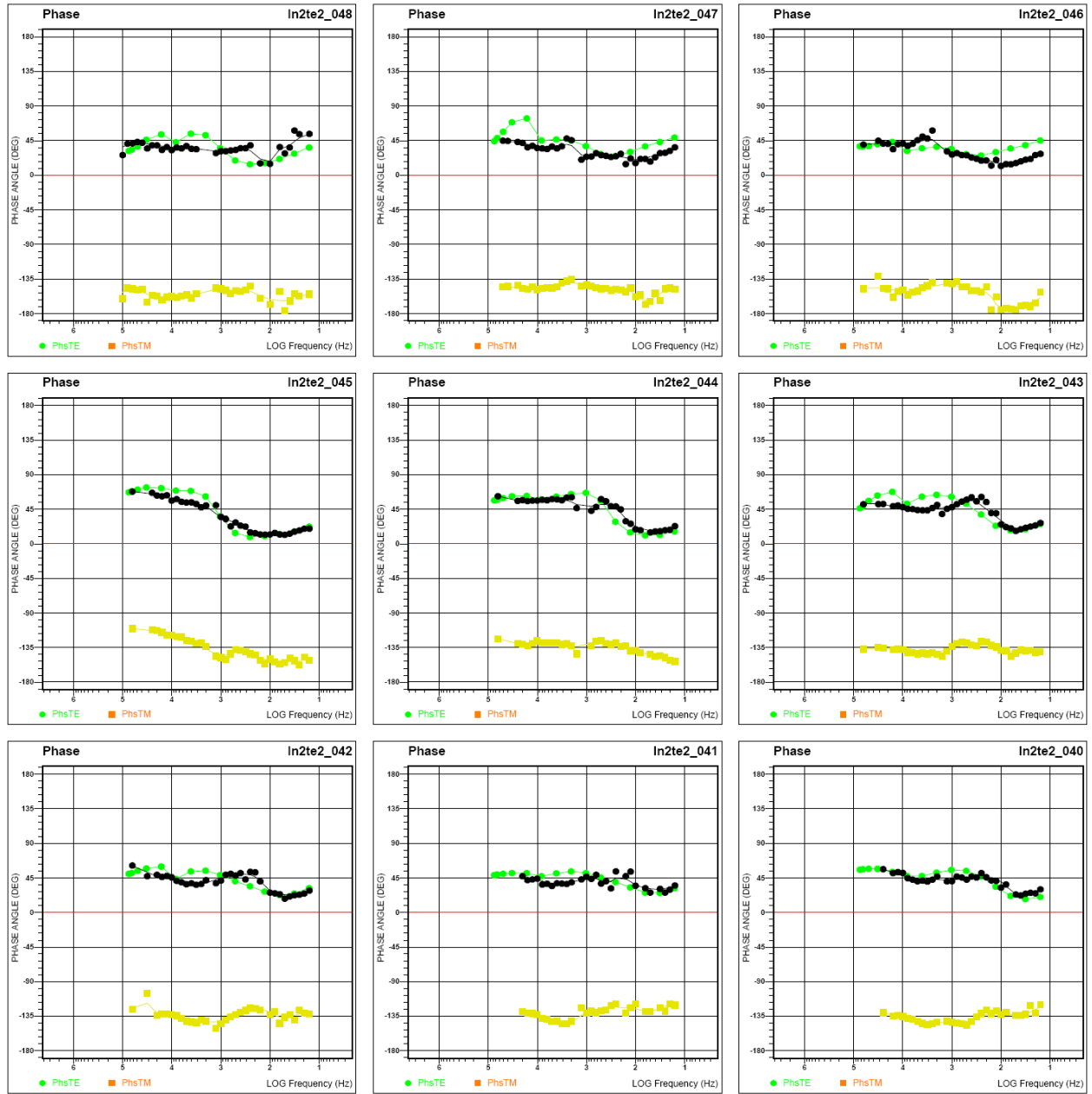


Figure A1-192. Line 2 impedance phase data for TE mode inversion model, sites 40 – 48.

## Appendix 1 – Audio-Magnetotelluric Data and Models

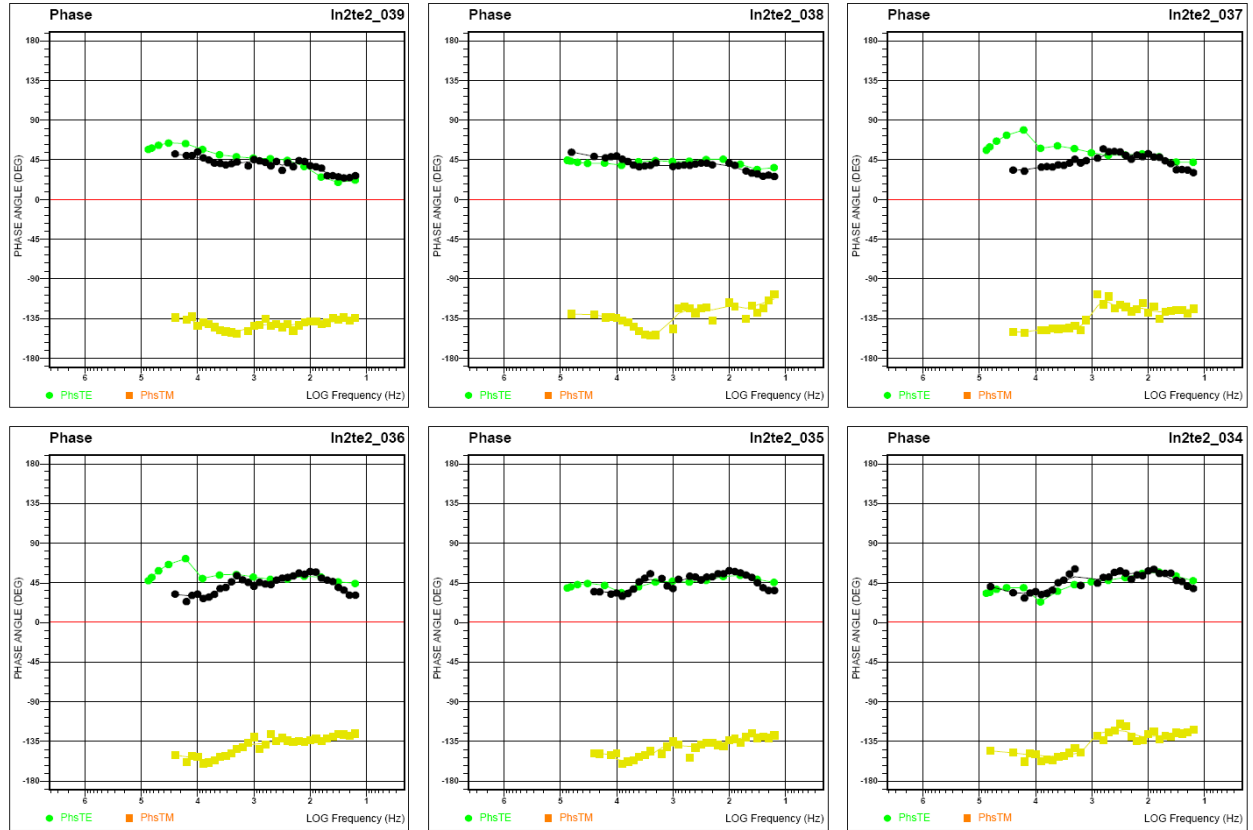
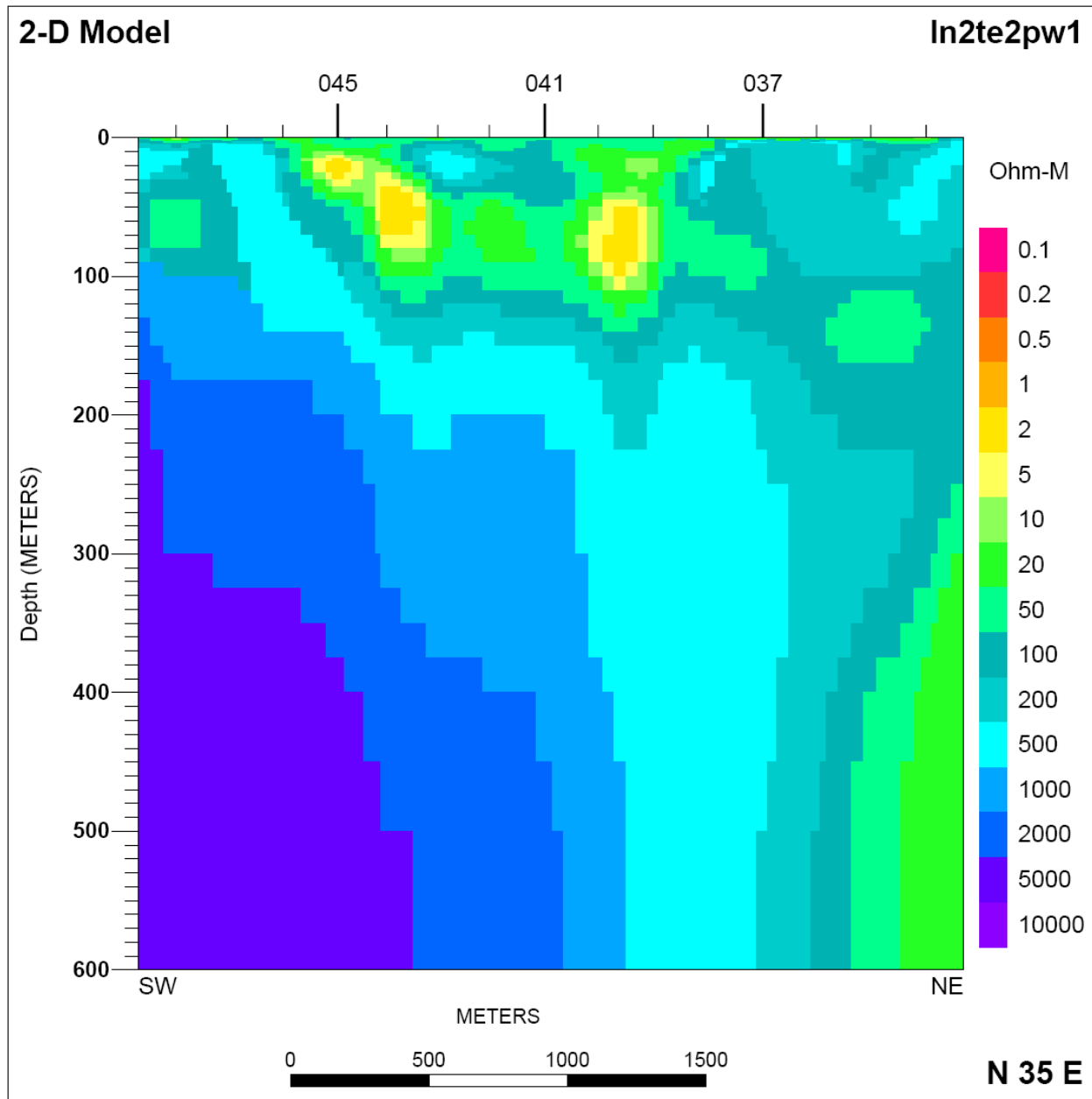
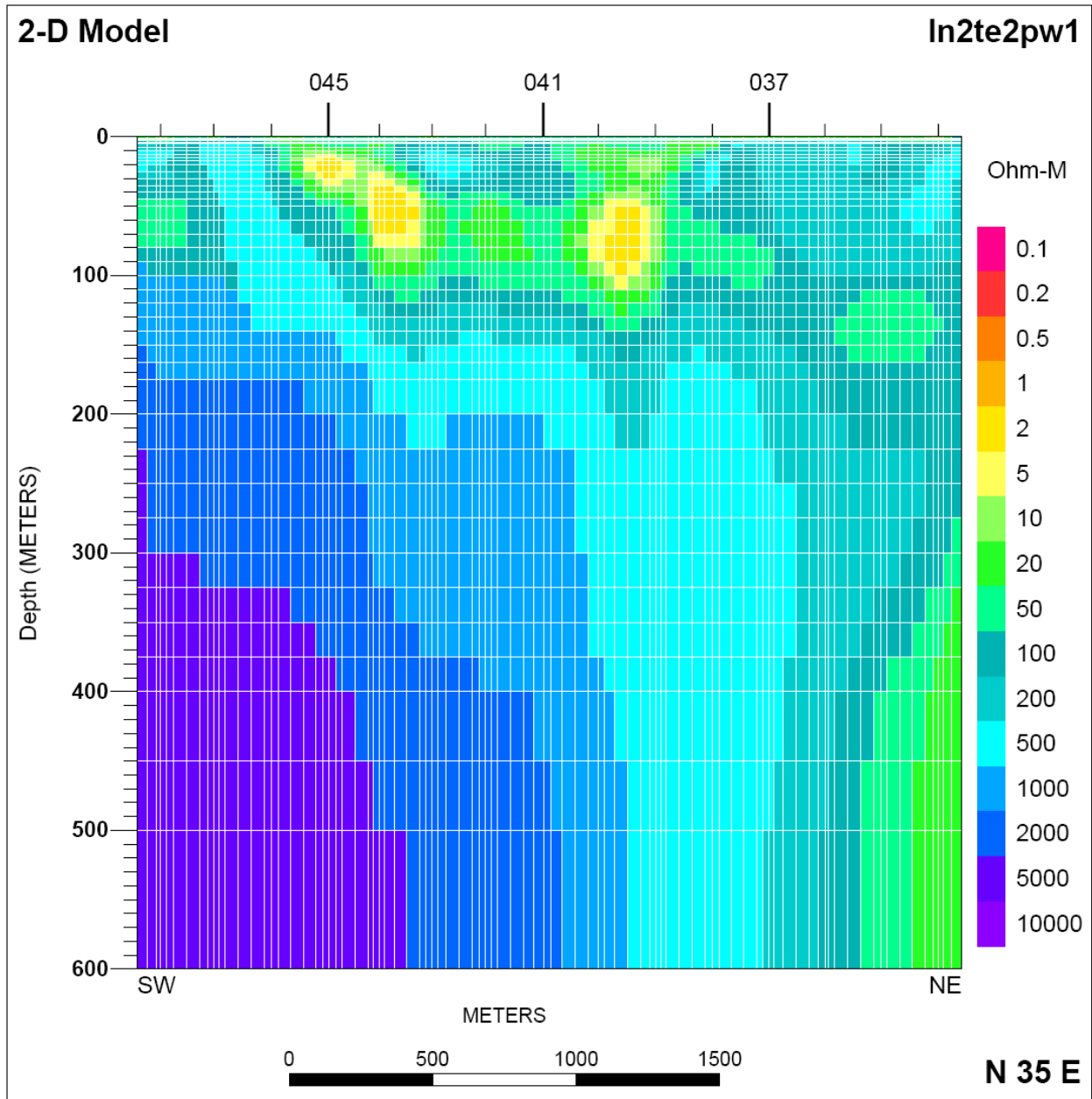


Figure A1-193. Line 2 impedance phase data for TE mode inversion model, sites 34 – 39.



**Figure A1-194.** Line 2 2-D forward modeling result for TE mode inversion result without model mesh lines. This forward model is built from ln2te2 in figure A1-188 and A1-189. Tic marks at top of model are projected AMT station locations. Vertical exaggeration is 5:1.



**Figure A1-195.** Line 2 2-D forward modeling result for TE mode with white model mesh lines. Tic marks at top of model are projected AMT station locations. Vertical exaggeration is 5:1.

## Appendix 1 – Audio-Magnetotelluric Data and Models

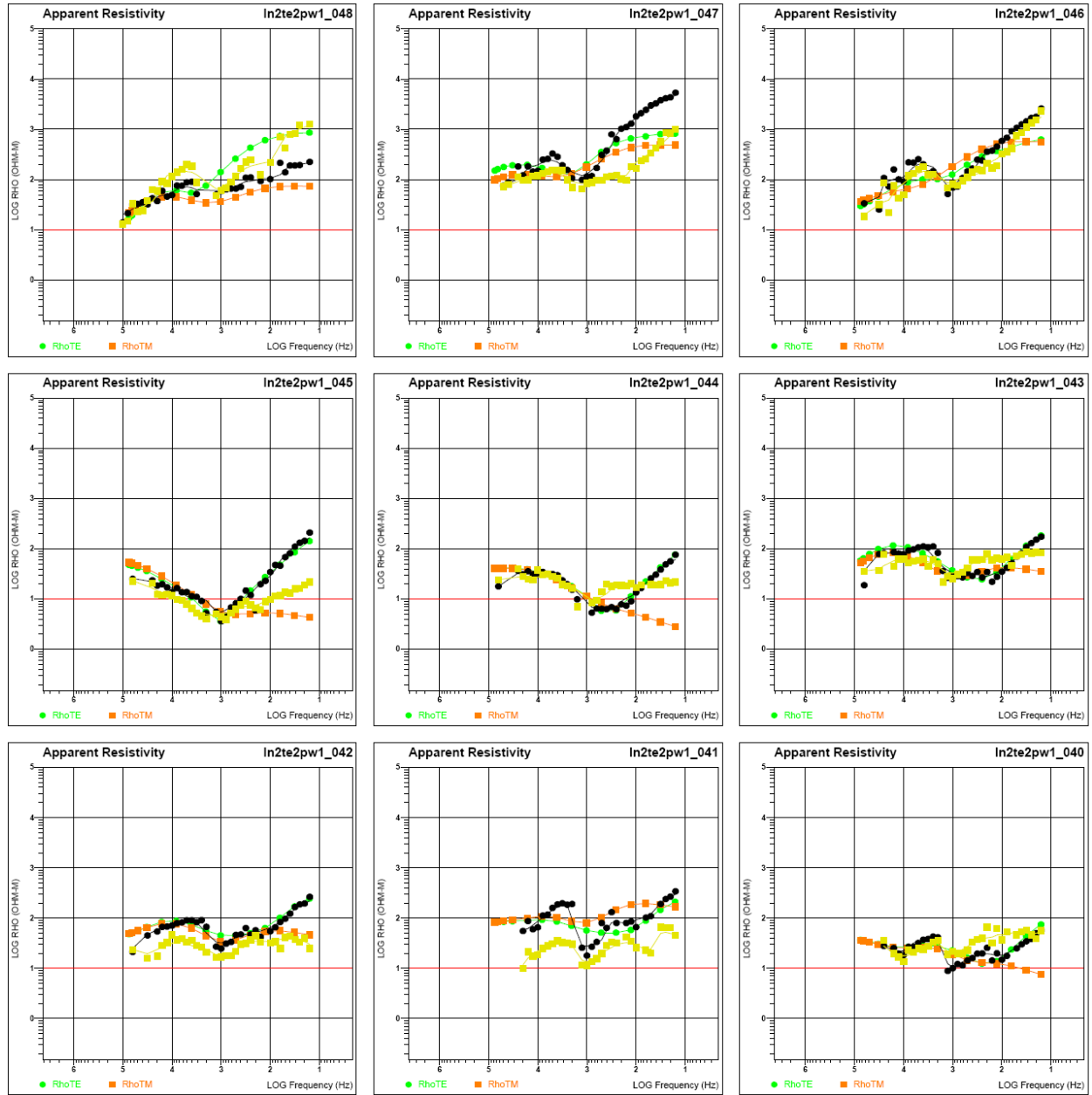
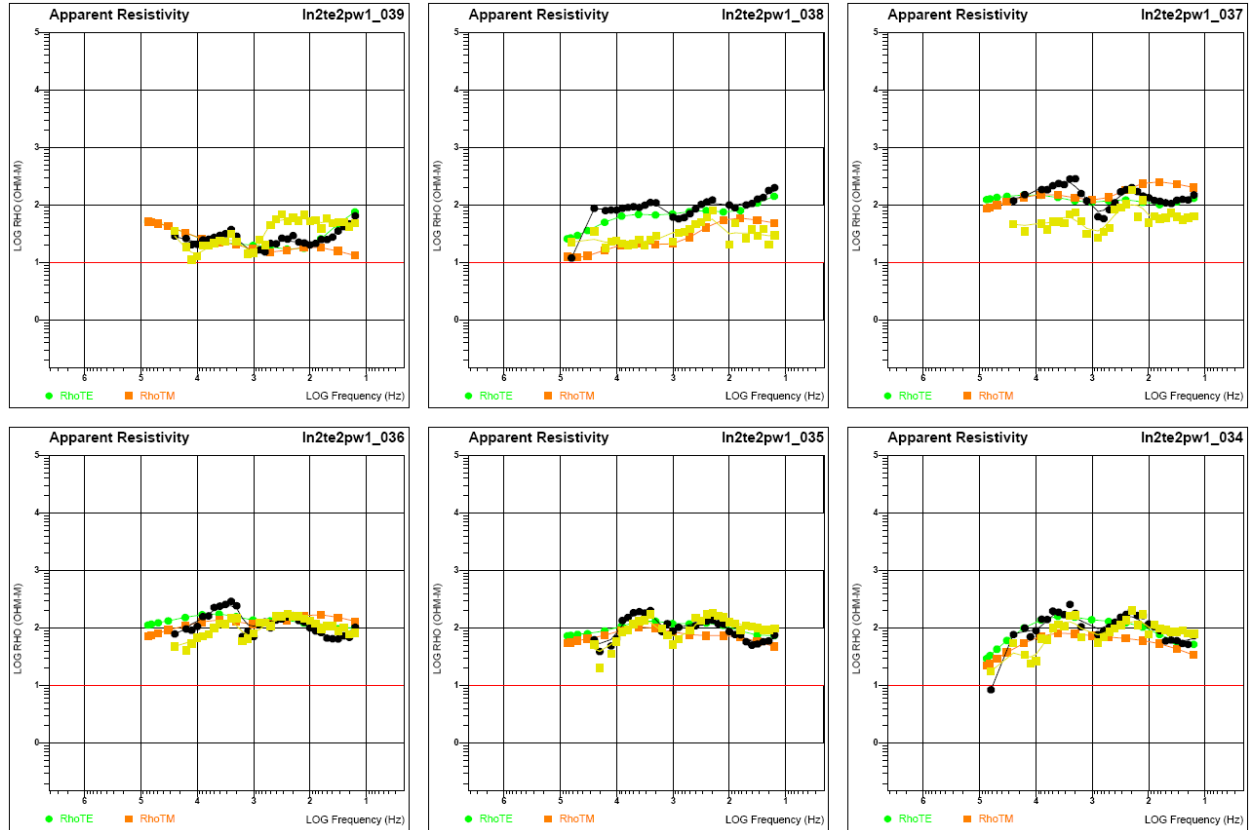


Figure A1-196. Line 2 impedance apparent resistivity data for TE mode forward model, sites 40 - 48.



## Appendix 1 – Audio-Magnetotelluric Data and Models



**Figure A1-197.** Line 2 impedance apparent resistivity data for TE mode forward model, sites 34 - 39.

## Appendix 1 – Audio-Magnetotelluric Data and Models

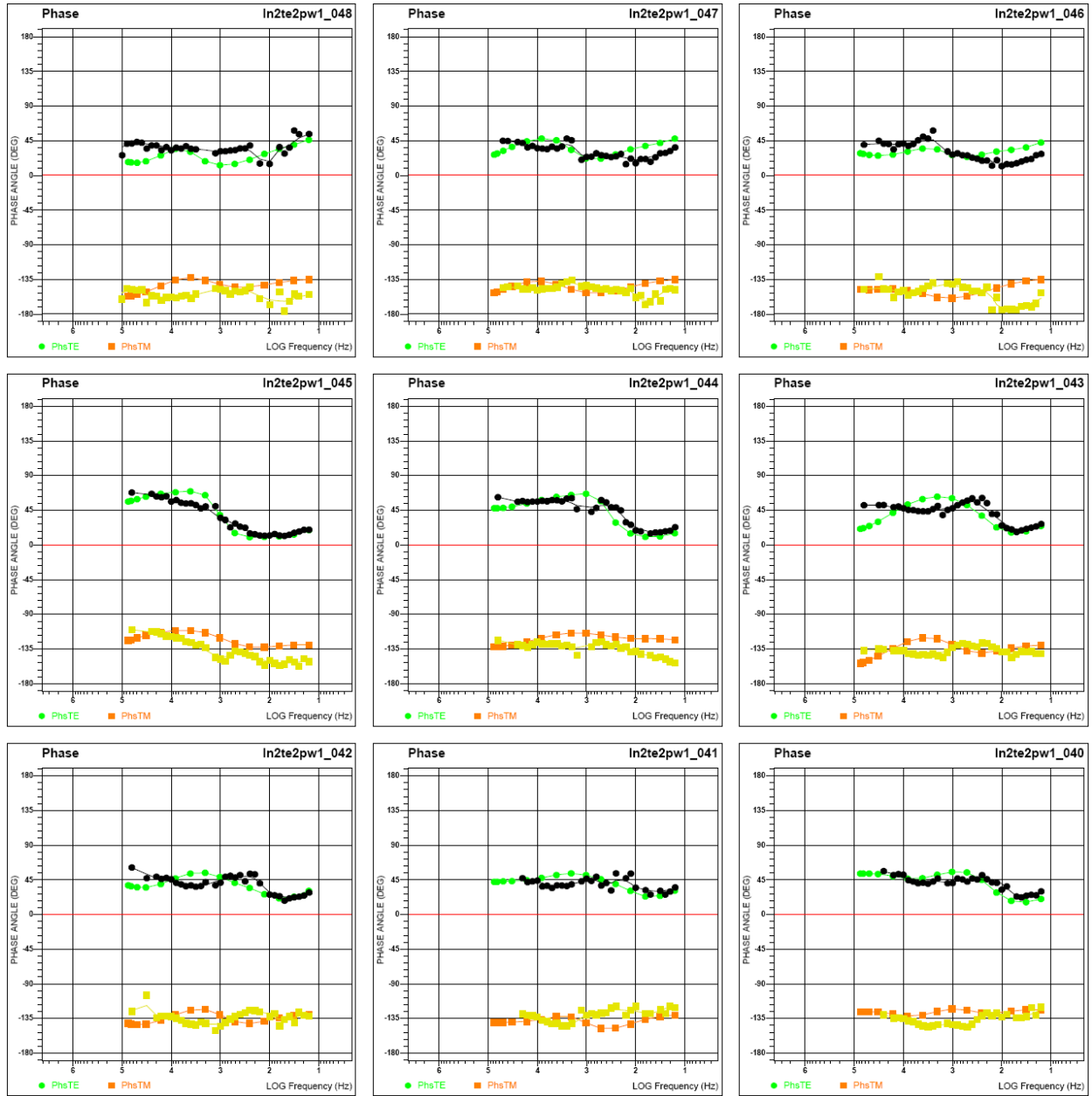


**Figure A1-198.** Line 2 impedance phase data for TE mode forward model, sites 40 – 48.

## Appendix 1 – Audio-Magnetotelluric Data and Models

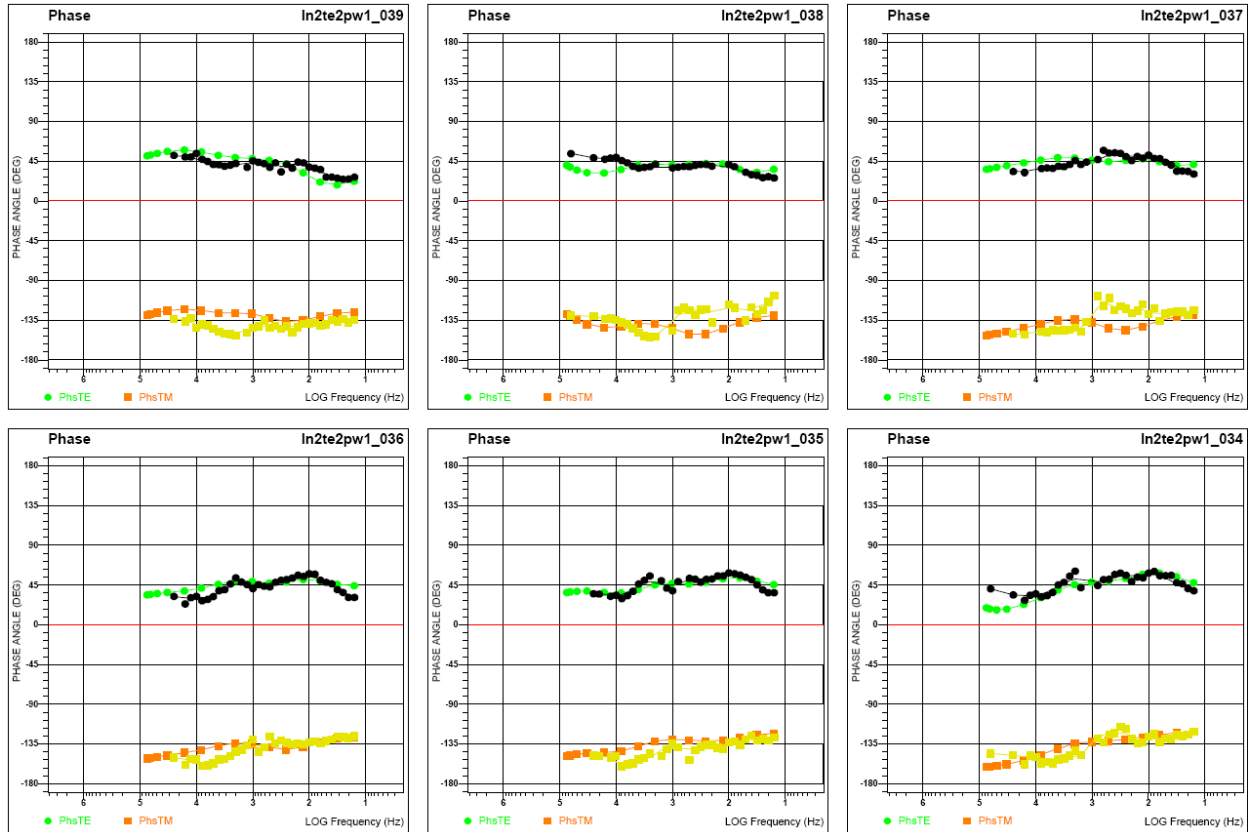


**Figure A1-199.** Line 2 impedance phase data for TE mode forward model, sites 34 – 39.

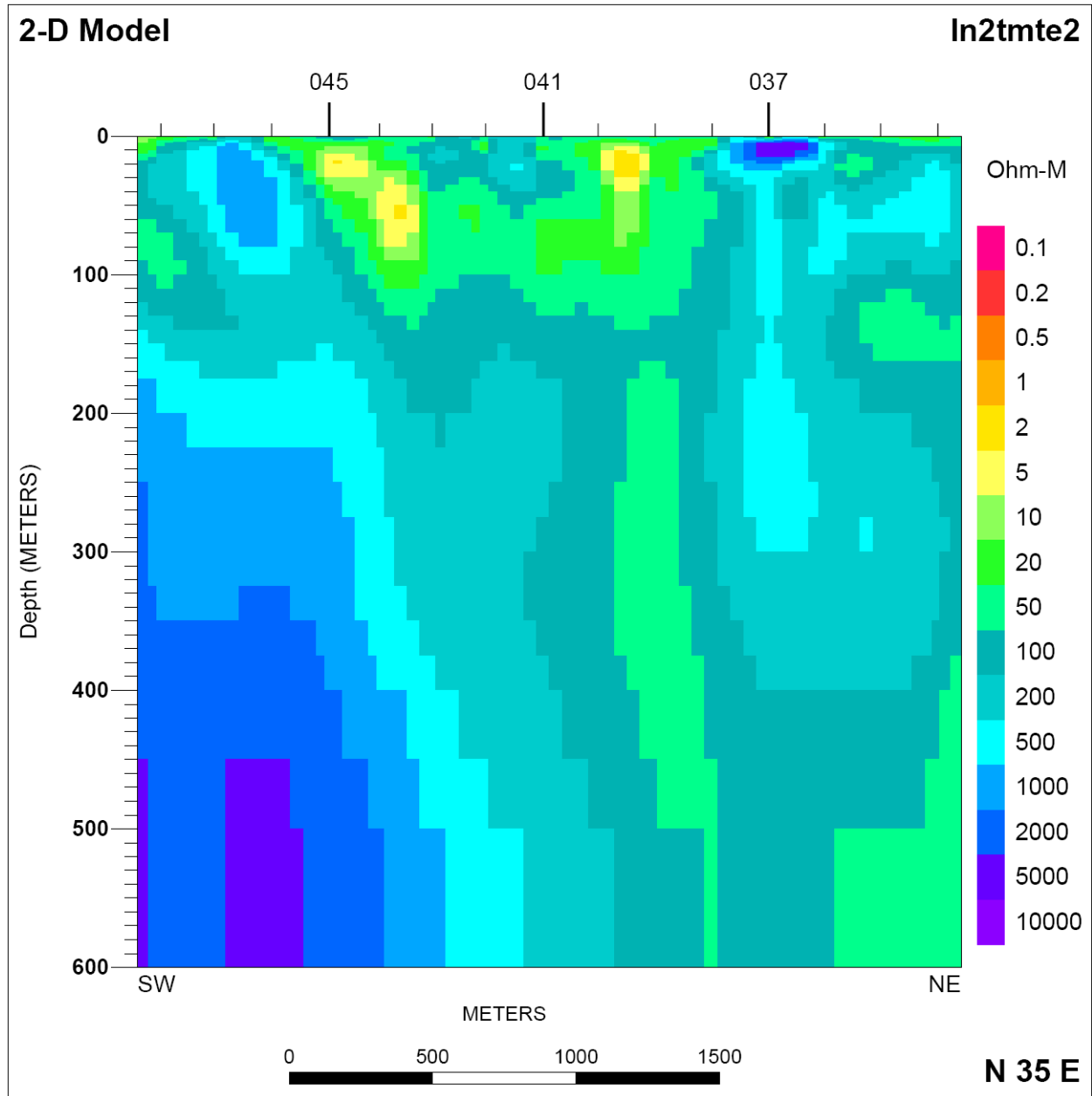


**Figure A1-200.** Line 2 2-D inversion modeling result for combined TM & TE modes without model mesh lines. Tic marks at top of model are projected AMT station locations. Vertical exaggeration is 5:1.

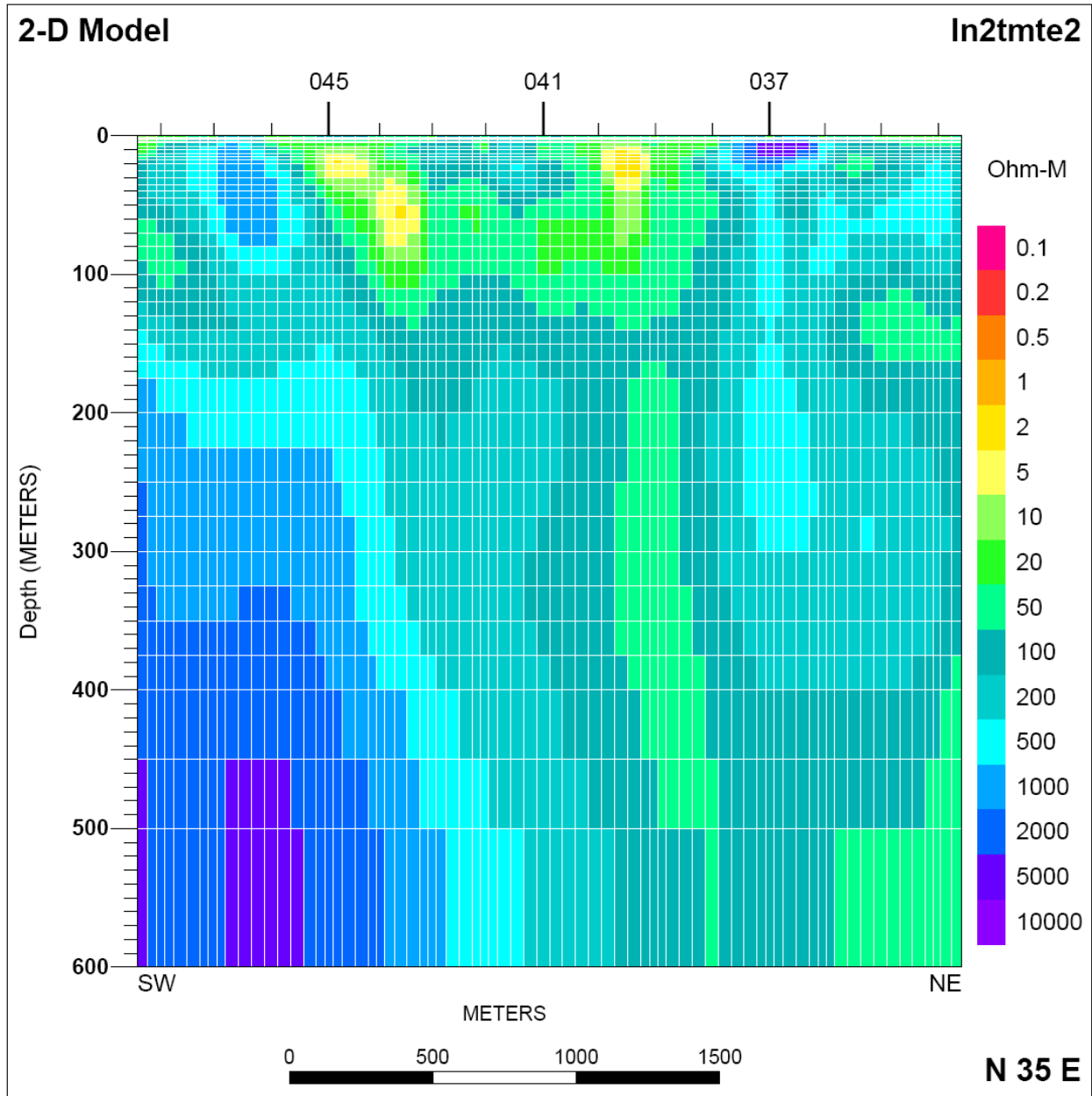


**Figure A1-201.** Line 2 2-D inversion modeling result for combined TM & TE modes with white model mesh lines. Tic marks at top of model are projected AMT station locations. Vertical exaggeration is 5:1.

## Appendix 1 – Audio-Magnetotelluric Data and Models

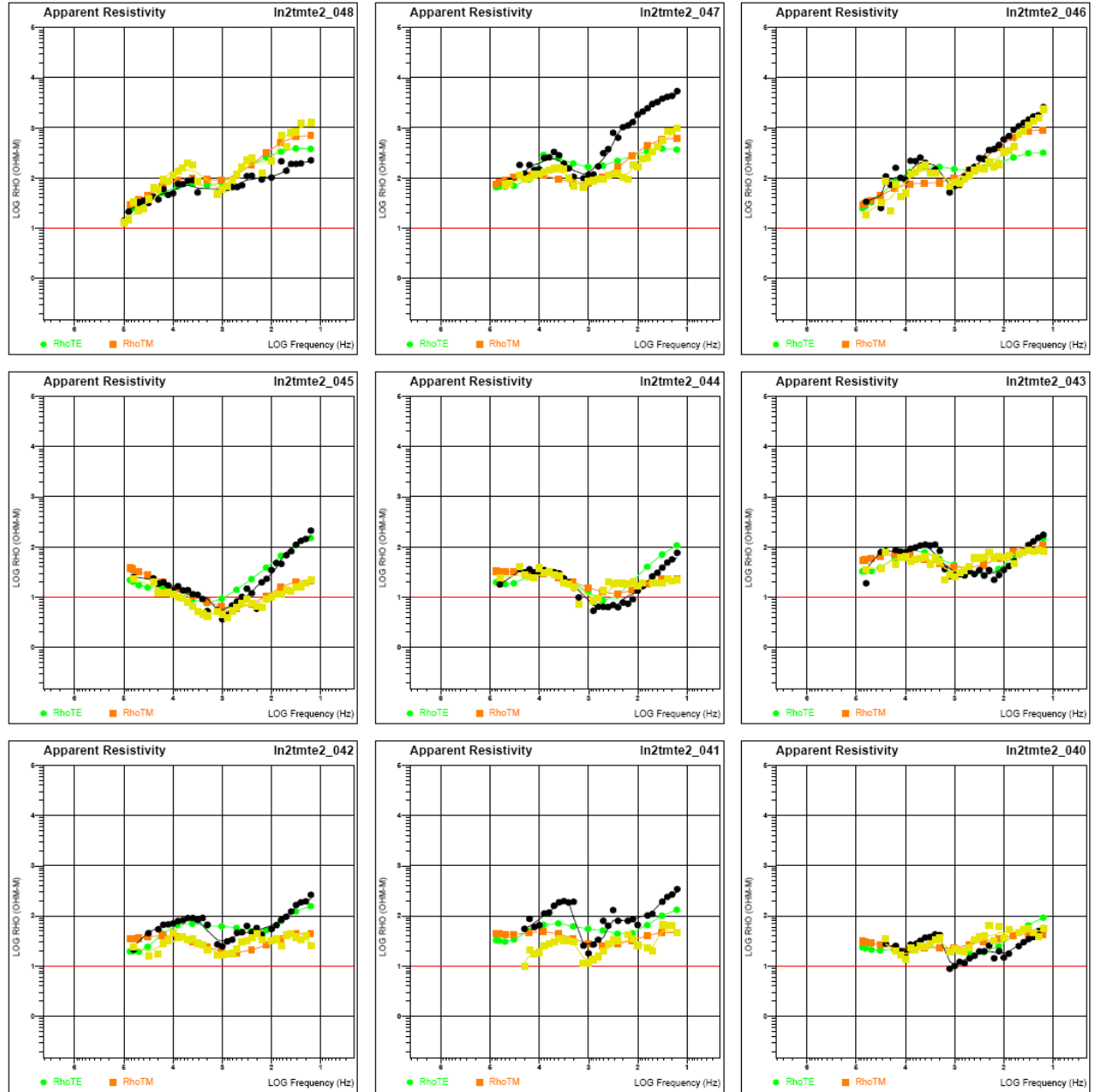


**Figure A1-202.** Line 2 impedance apparent resistivity data for TE mode forward model, sites 40 - 48.

## Appendix 1 – Audio-Magnetotelluric Data and Models

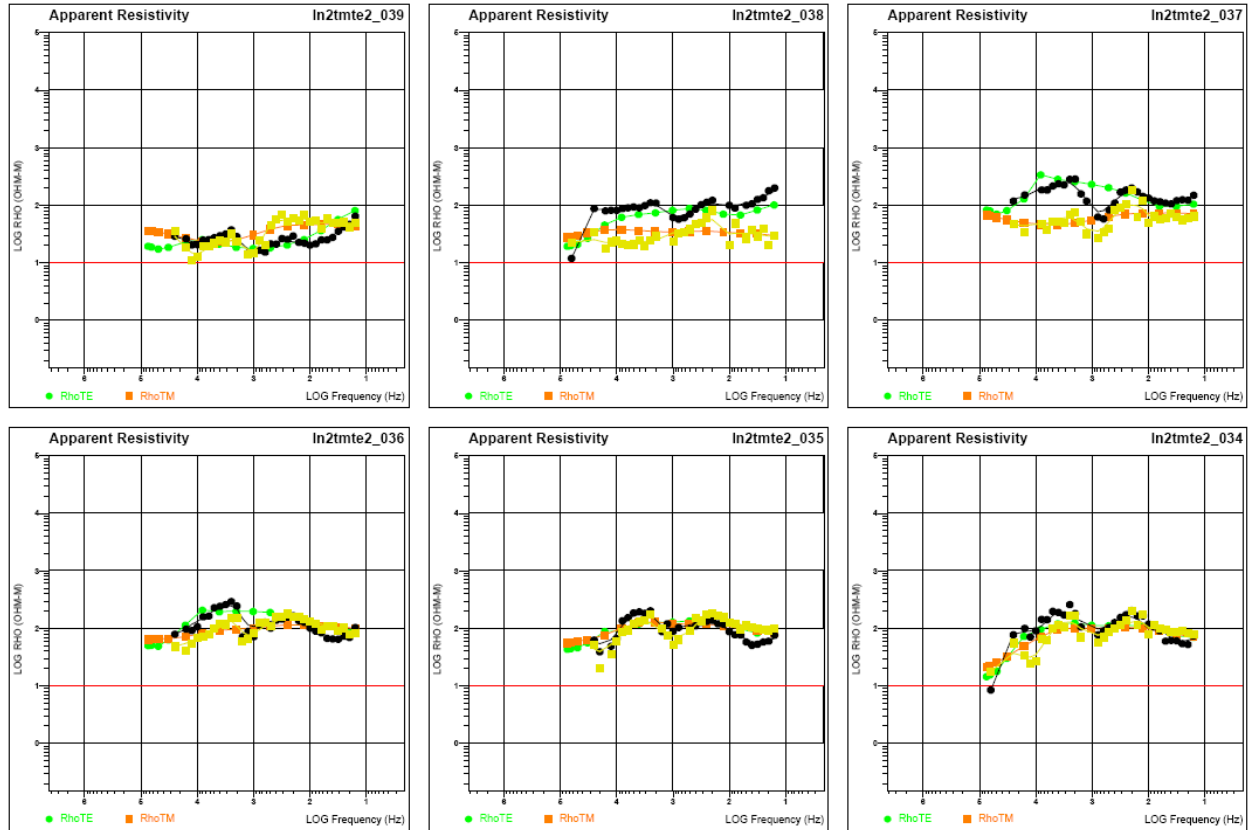


**Figure A1-203.** Line 2 impedance apparent resistivity data for TE mode forward model, sites 34 - 39.

# Appendix 1 – Audio-Magnetotelluric Data and Models

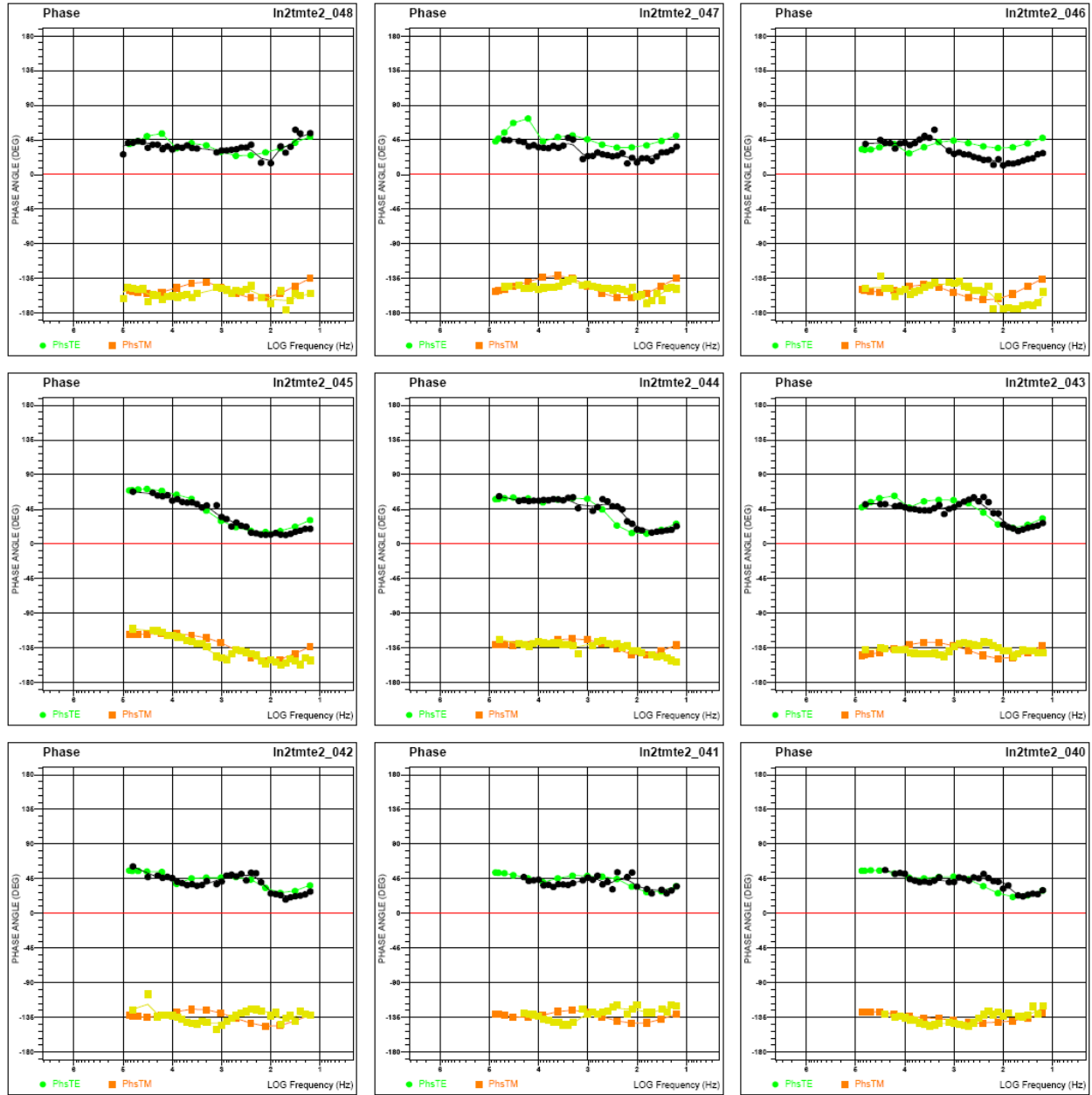


**Figure A1-204.** Line 2 impedance phase data for TE mode forward model, sites 40 – 48.



## Appendix 1 – Audio-Magnetotelluric Data and Models

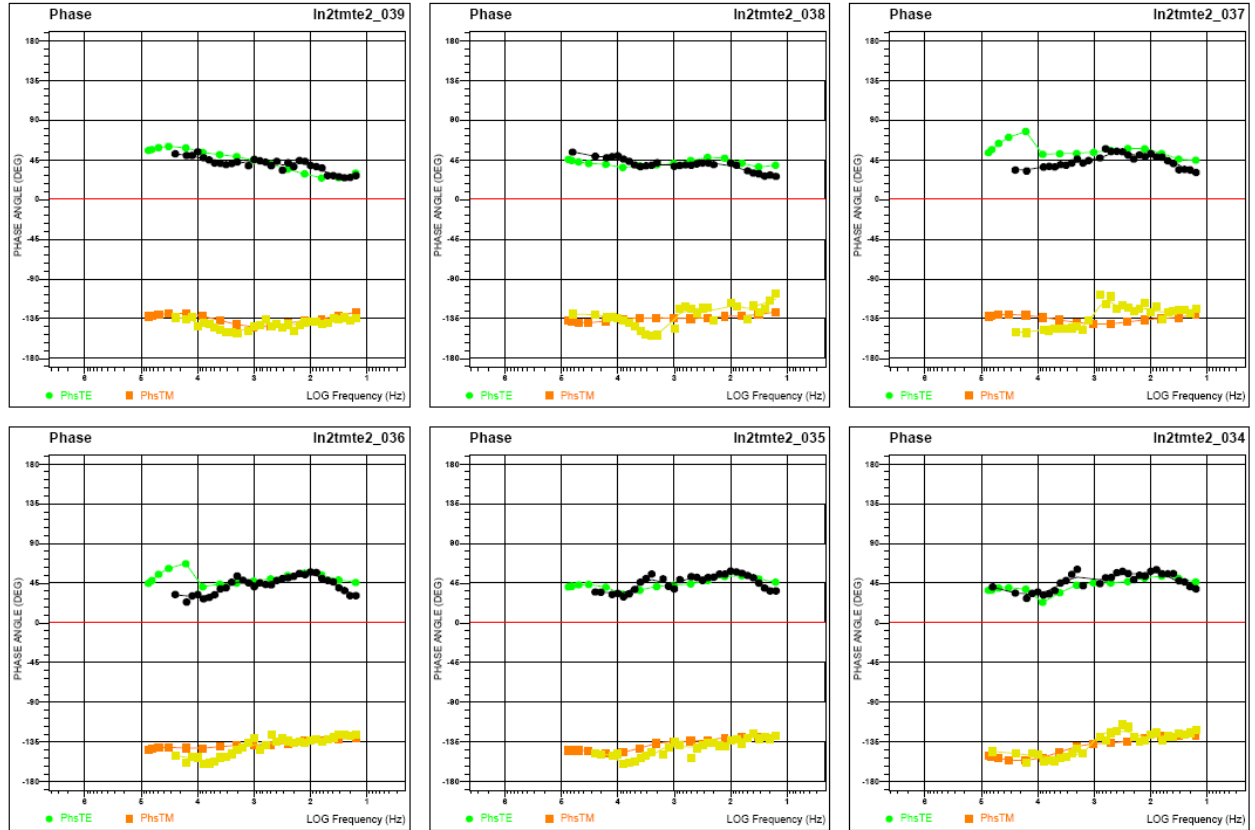


**Figure A1-205.** Line 2 impedance phase data for TE mode forward model, sites 34 – 39.

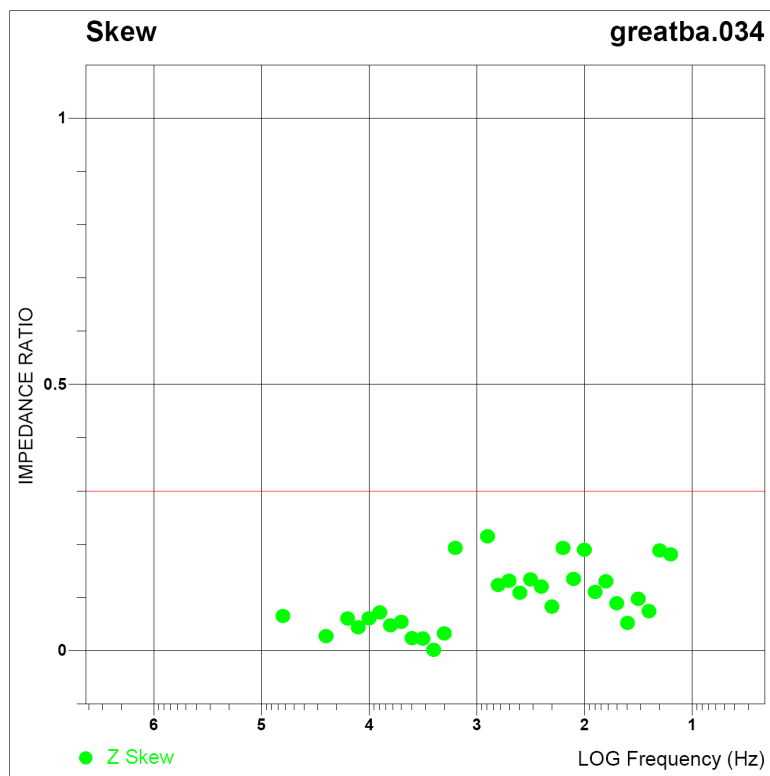


Figure A1-206. Line 2 impedance skew data for site 34.

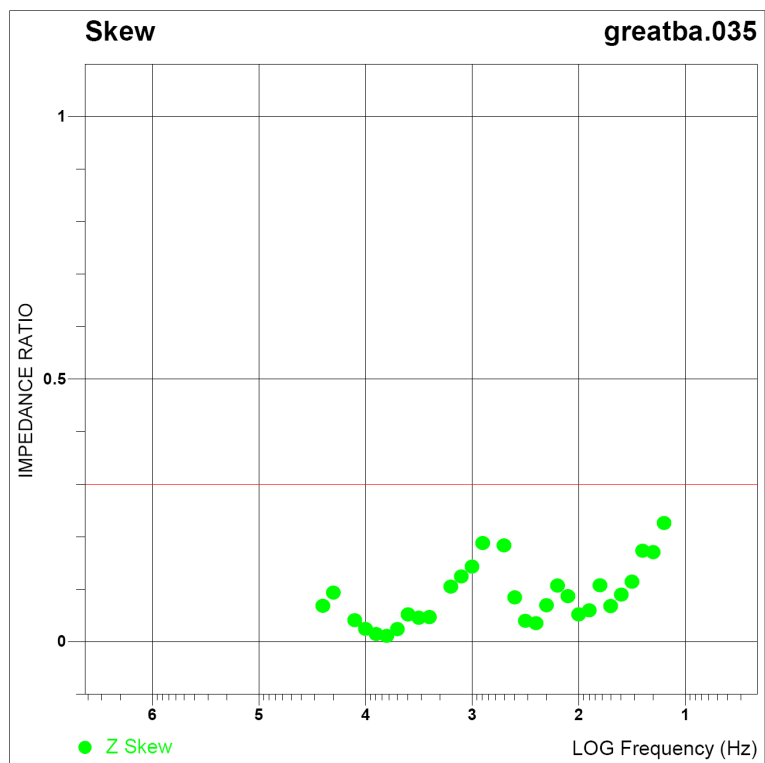


Figure A1-207. Line 2 impedance skew data for site 35.

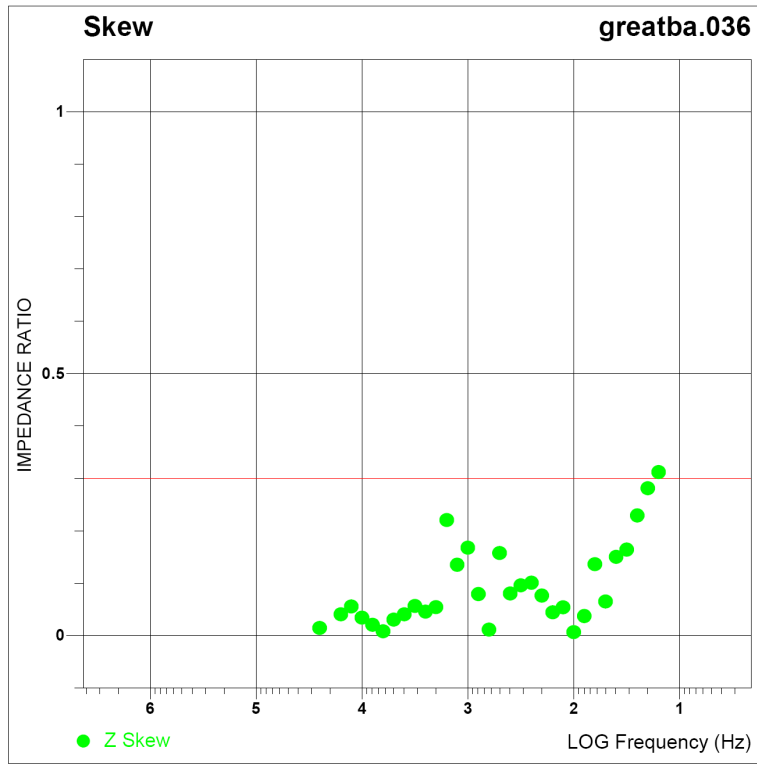


Figure A1-208. Line 2 impedance skew data for site 36.

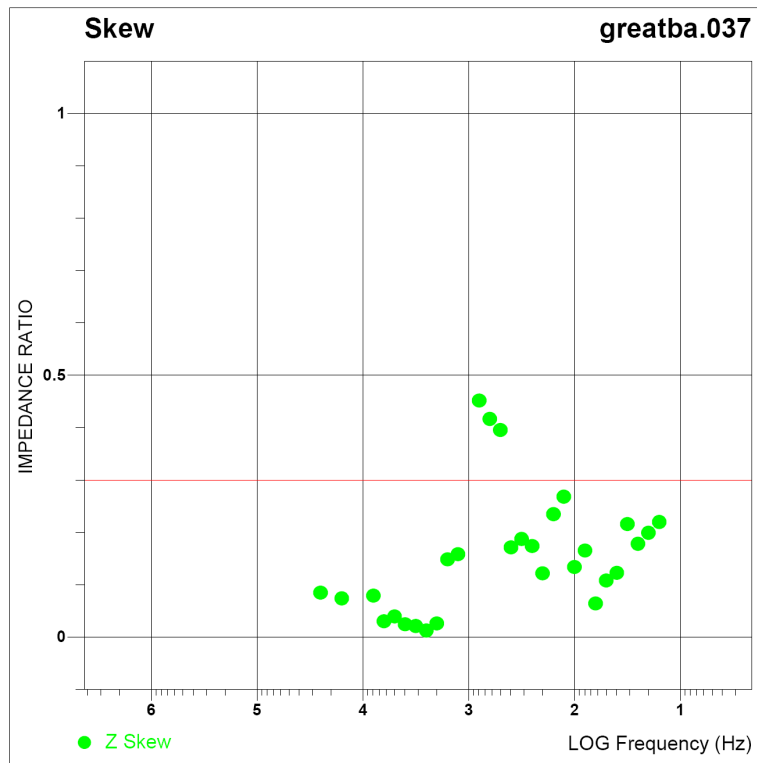


Figure A1-209. Line 2 impedance skew data for site 37.

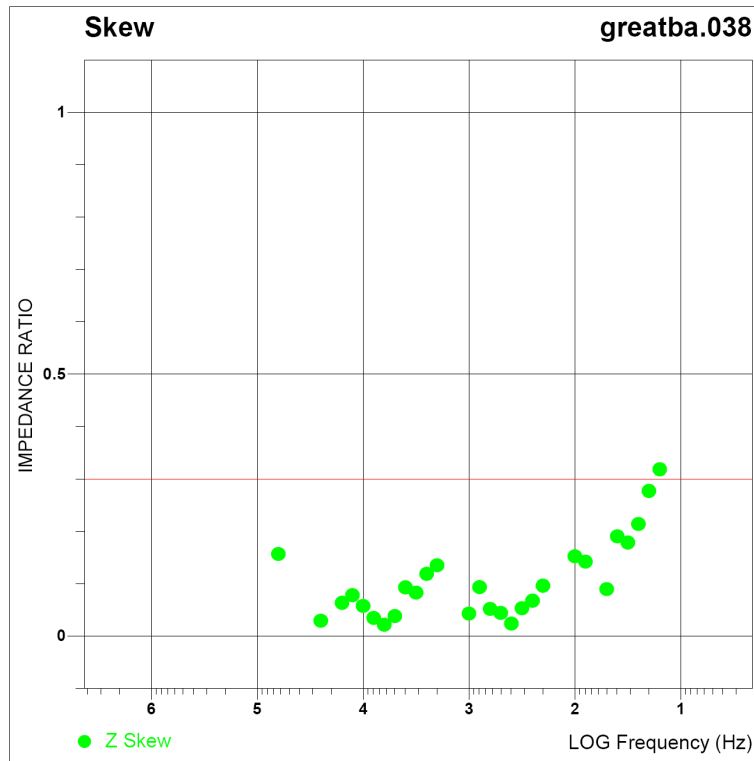


Figure A1-210. Line 2 impedance skew data for site 38.

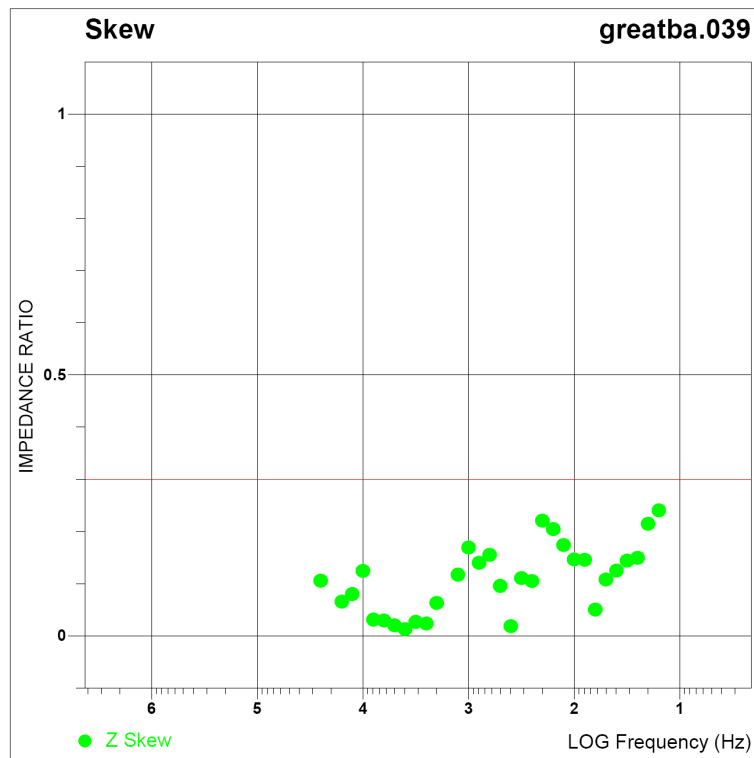


Figure A1-211. Line 2 impedance skew data for site 39.

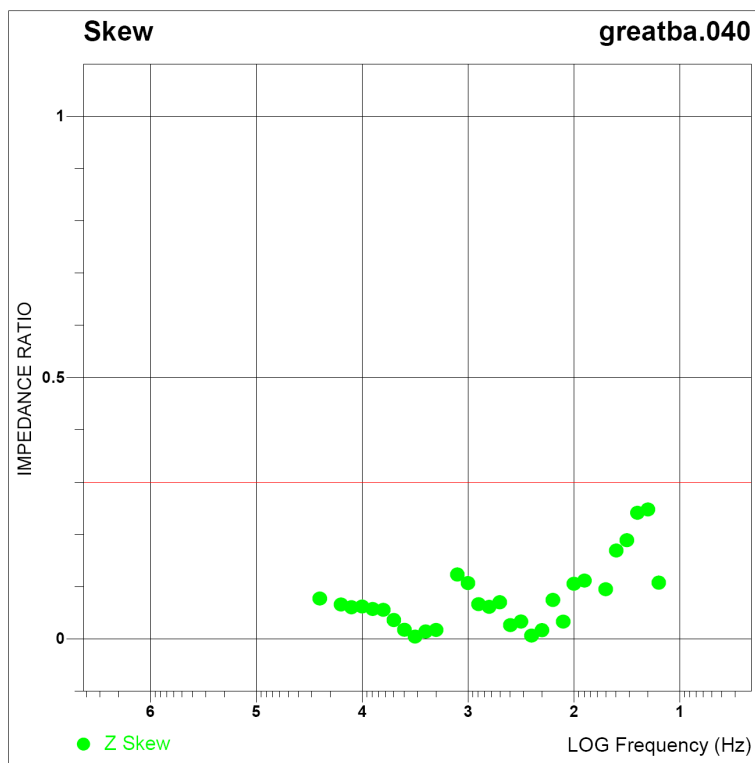


Figure A1-212. Line 2 impedance skew data for site 40.

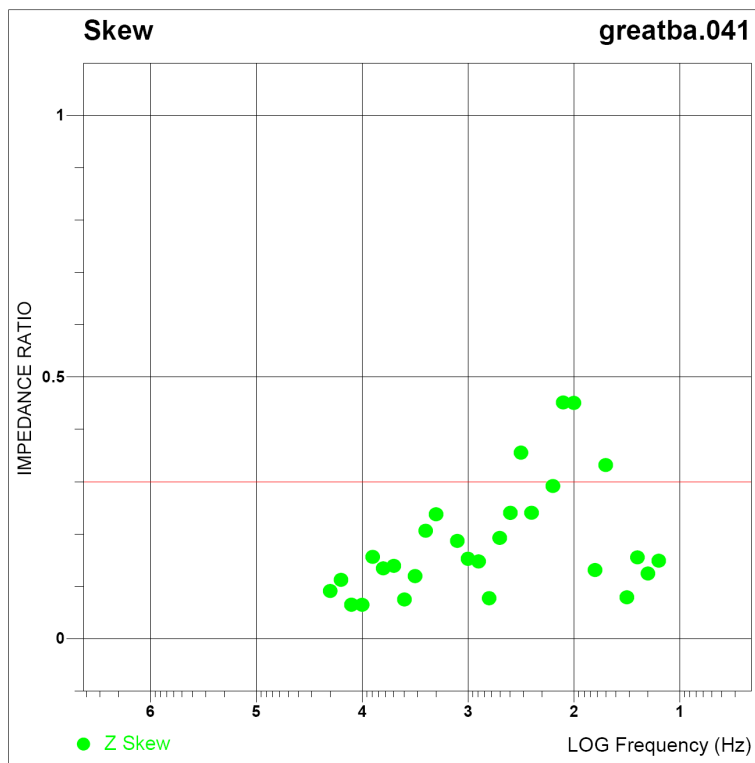


Figure A1-213. Line 2 impedance skew data for site 41.

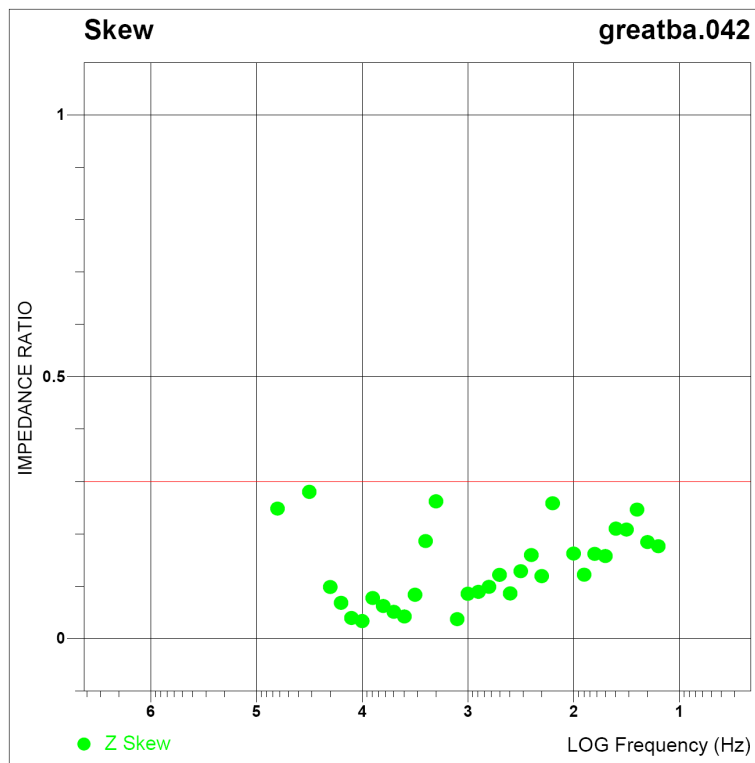


Figure A1-214. Line 2 impedance skew data for site 42.

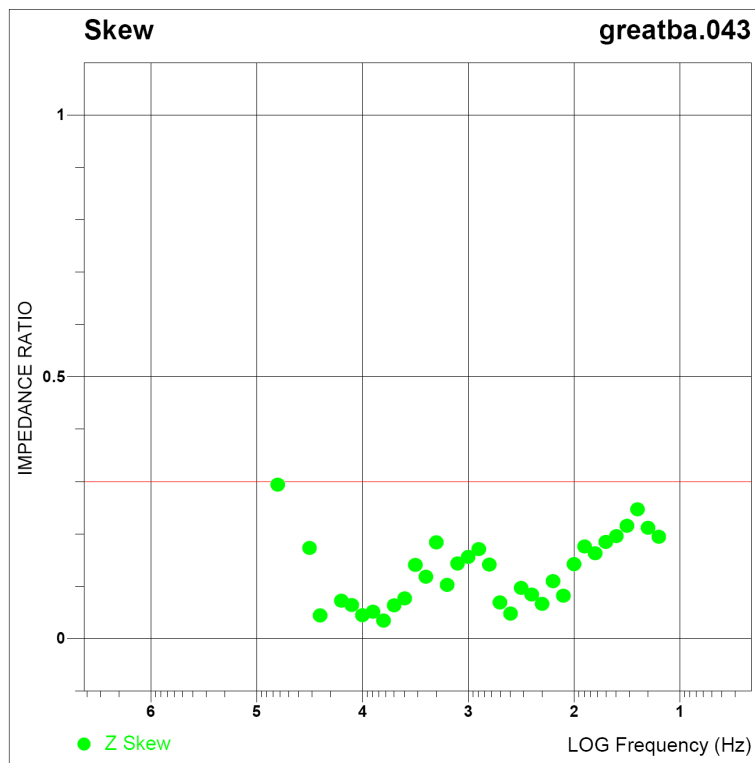


Figure A1-215. Line 2 impedance skew data for site 43.

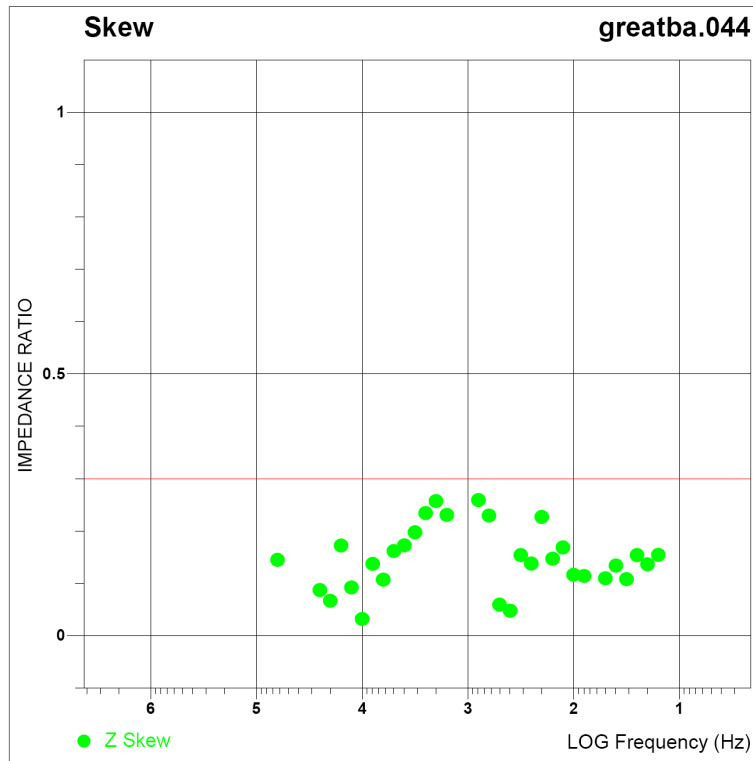


Figure A1-216. Line 2 impedance skew data for site 44.

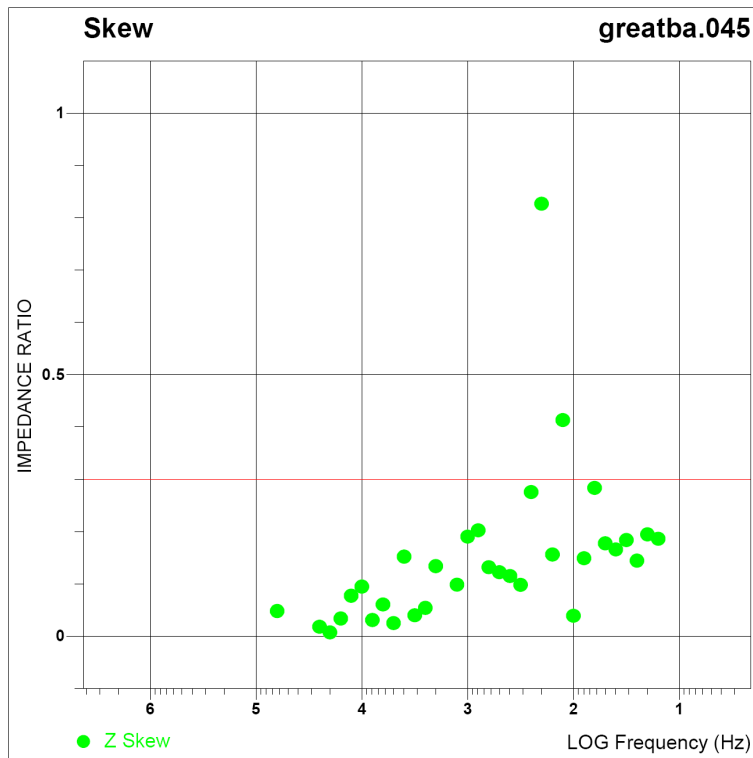


Figure A1-217. Line 2 impedance skew data for site 45.

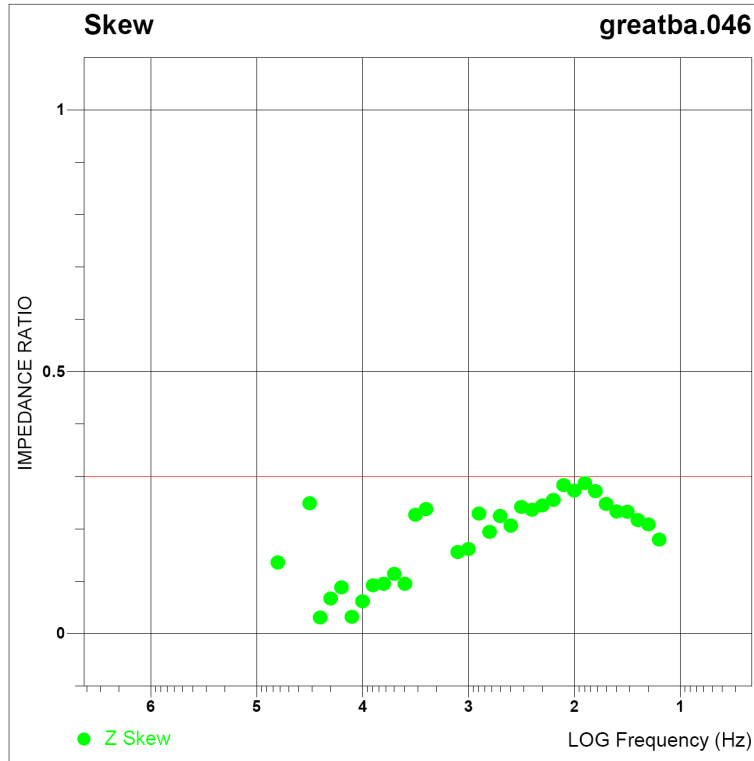


Figure A1-218. Line 2 impedance skew data for site 46.

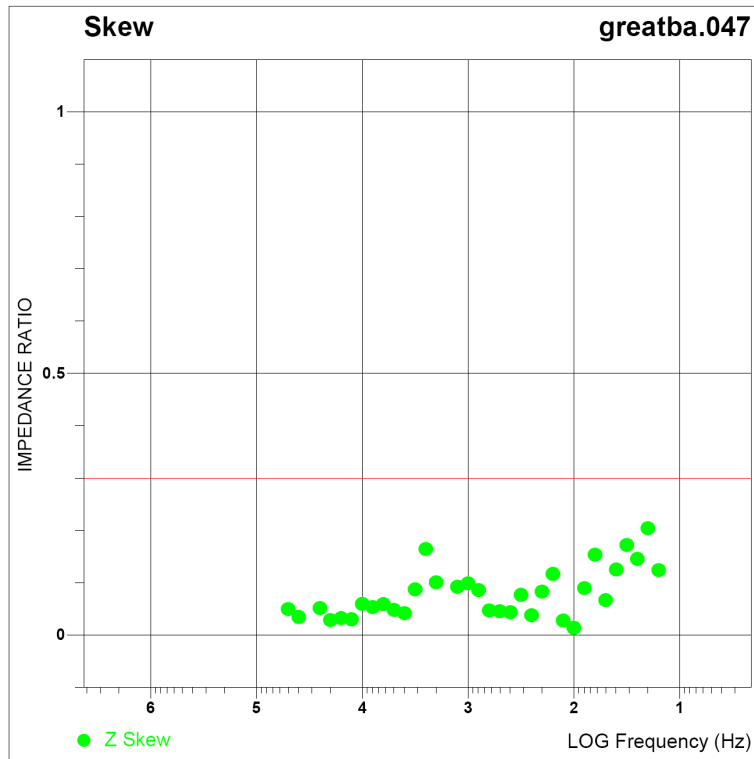


Figure A1-219. Line 2 impedance skew data for site 47.



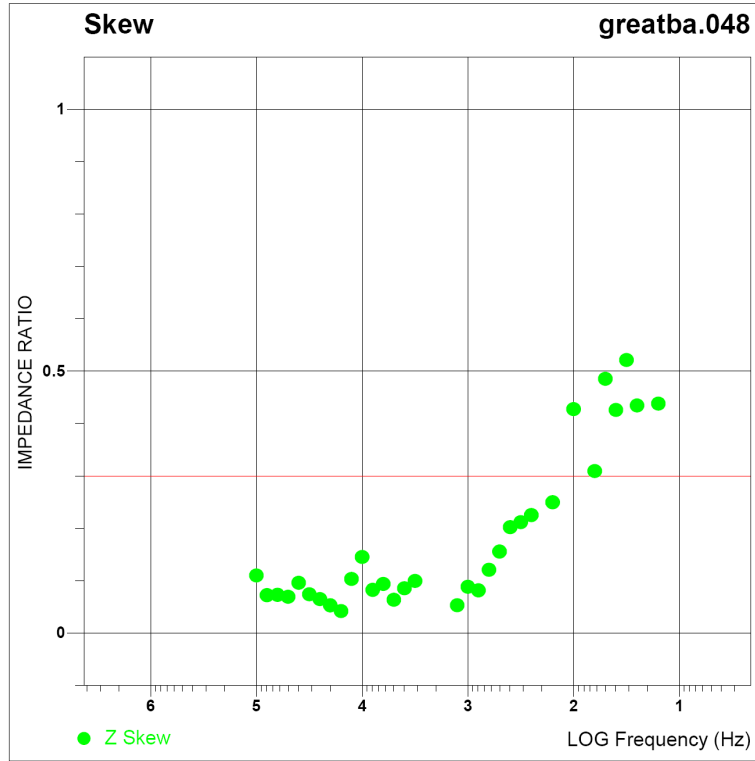


Figure A1-220. Line 2 impedance skew data for site 48.

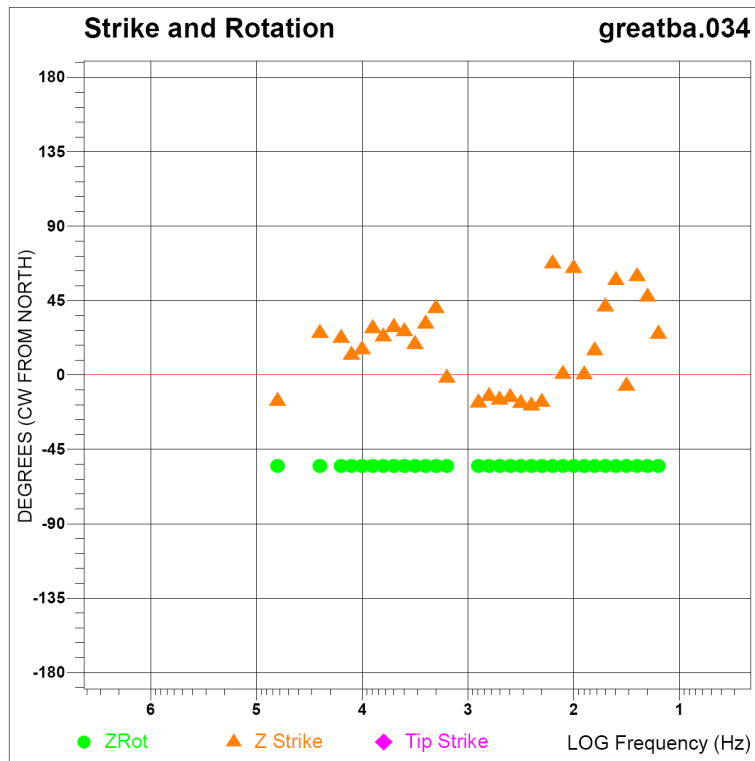


Figure A1-221. Line 2 impedance strike data for site 34.

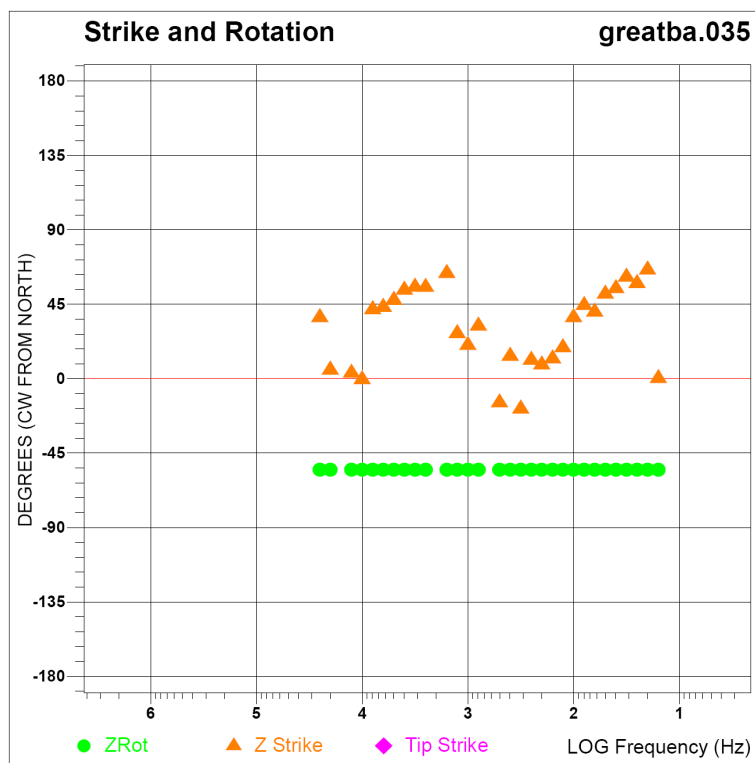


Figure A1-220. Line 2 impedance strike data for site 35.

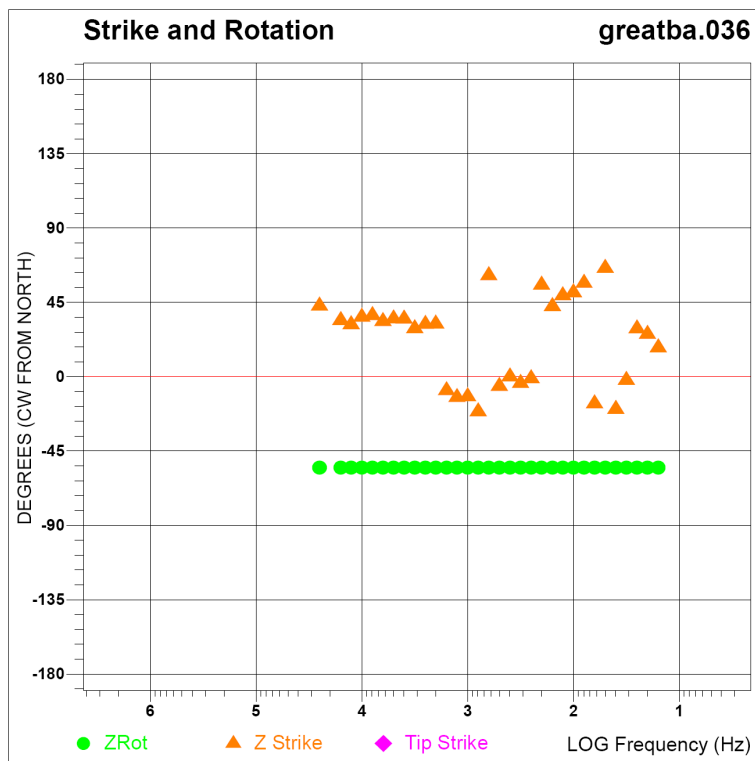


Figure A1-221. Line 2 impedance strike data for site 36.

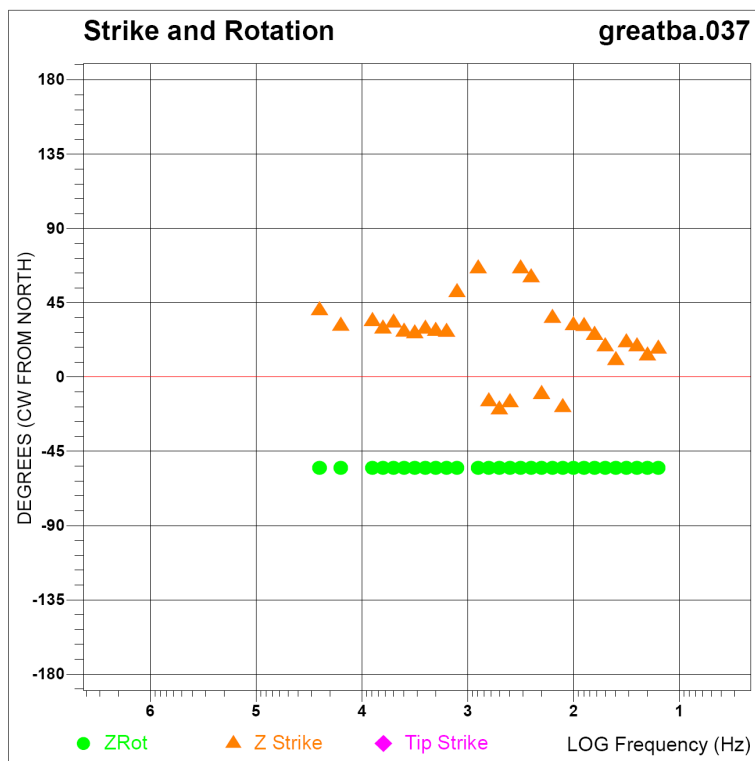


Figure A1-222. Line 2 impedance strike data for site 37.

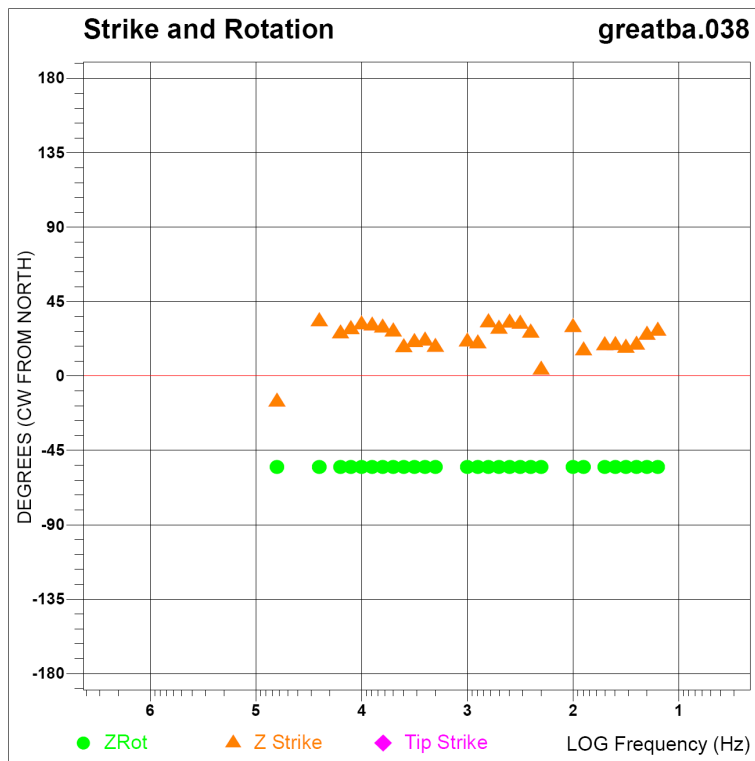


Figure A1-223. Line 2 impedance strike data for site 38.

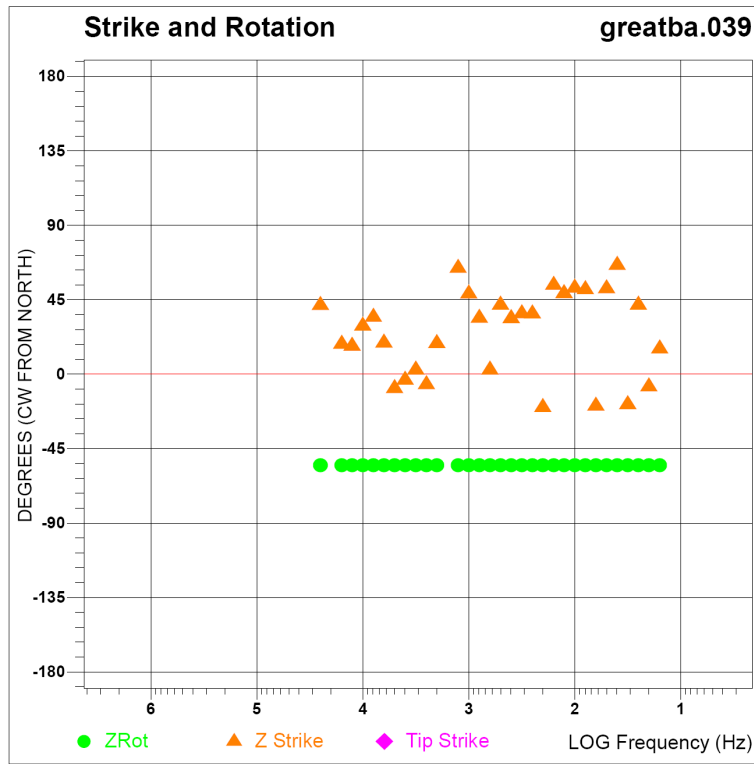


Figure A1-224. Line 2 impedance strike data for site 39.

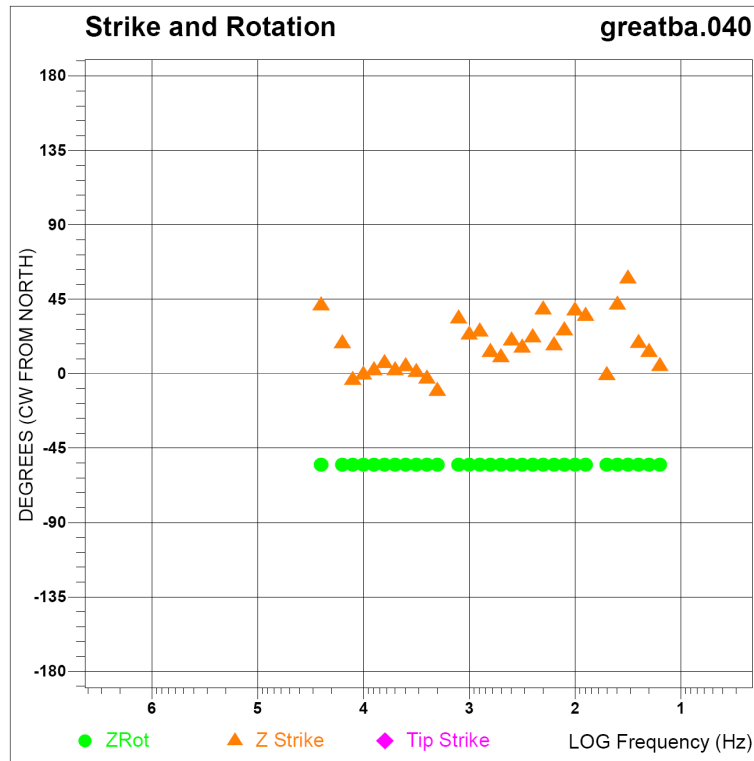


Figure A1-225. Line 2 impedance strike data for site 40.

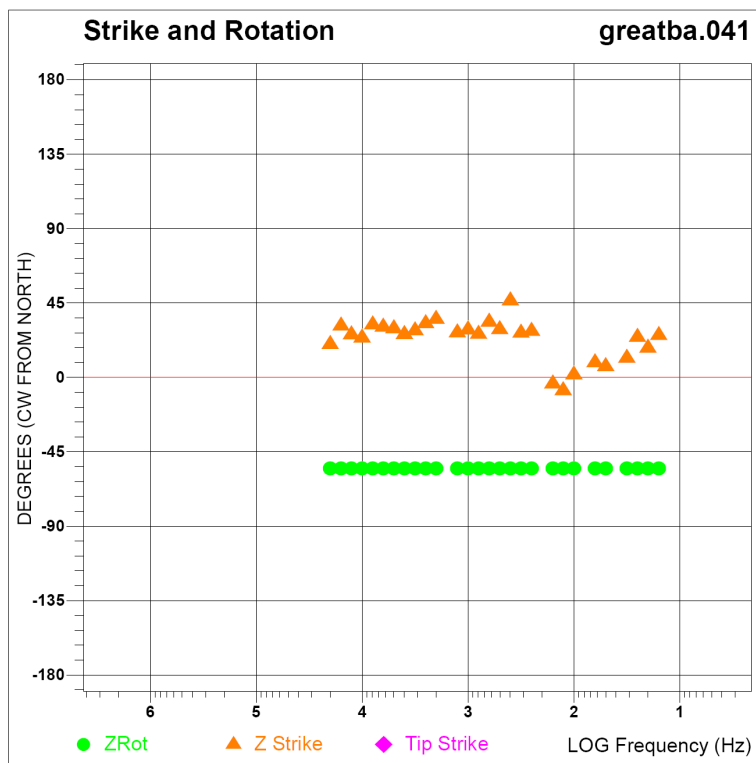


Figure A1-226. Line 2 impedance strike data for site 41.

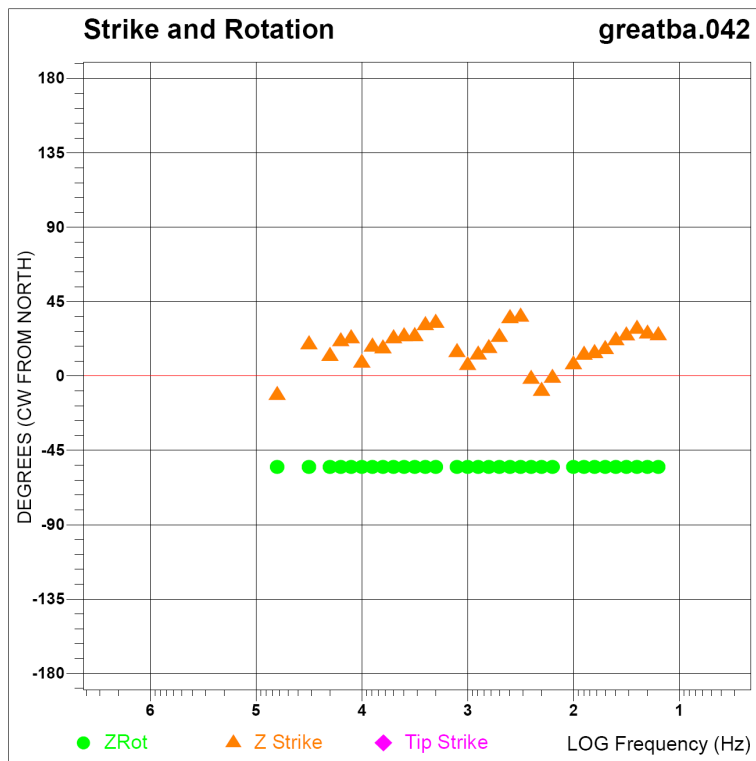


Figure A1-227. Line 2 impedance strike data for site 42.

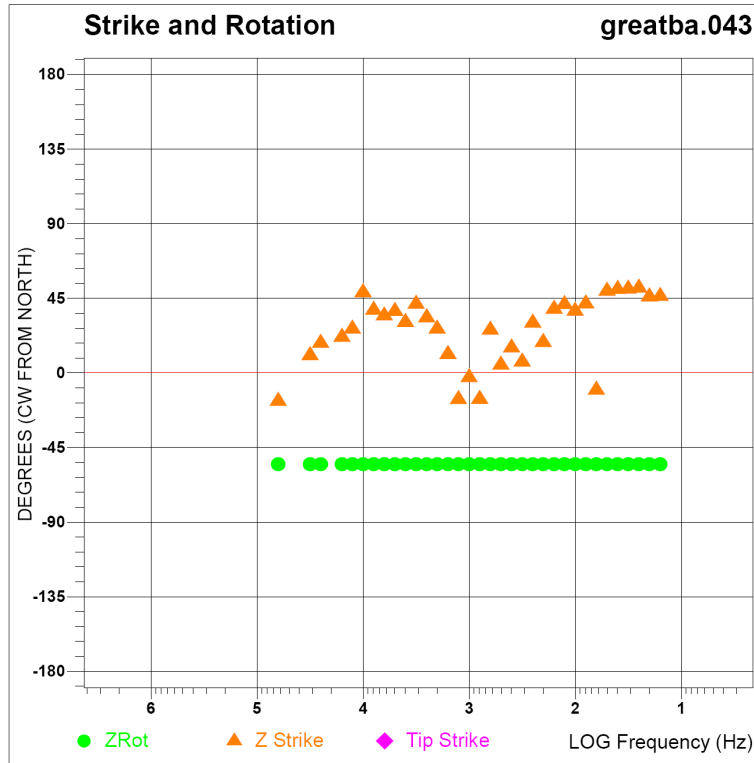


Figure A1-228. Line 2 impedance strike data for site 43.

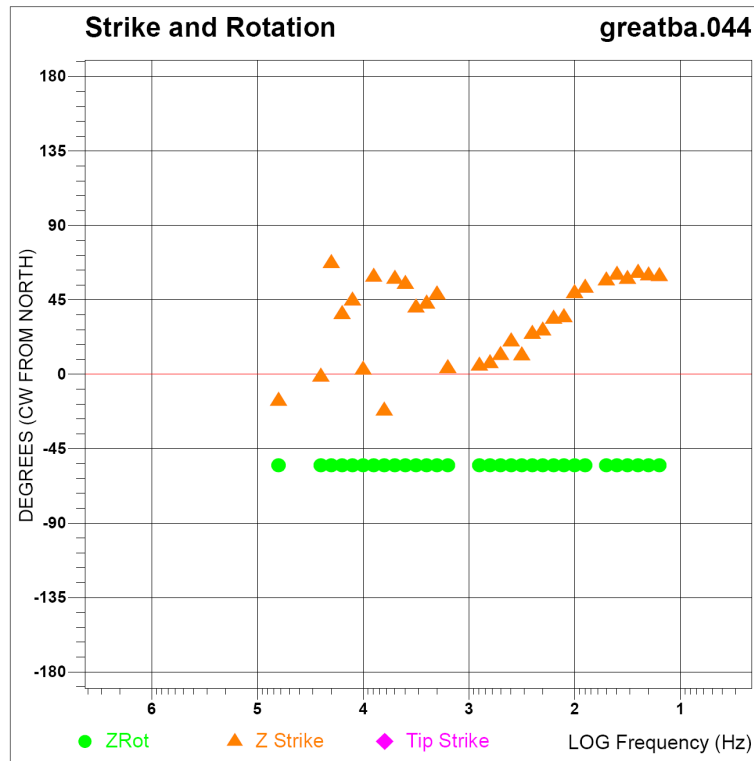


Figure A1-229. Line 2 impedance strike data for site 44.

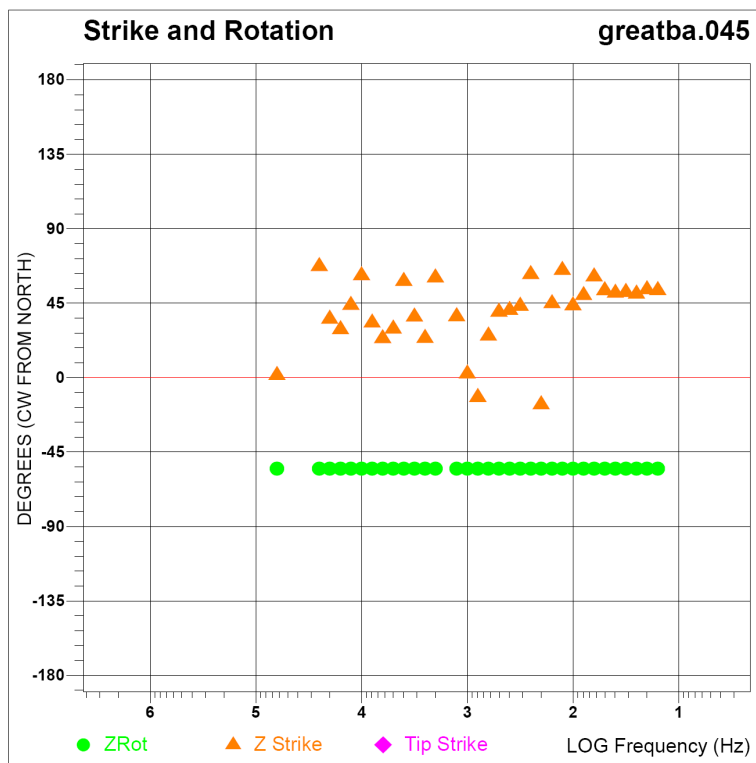


Figure A1-230. Line 2 impedance strike data for site 45.

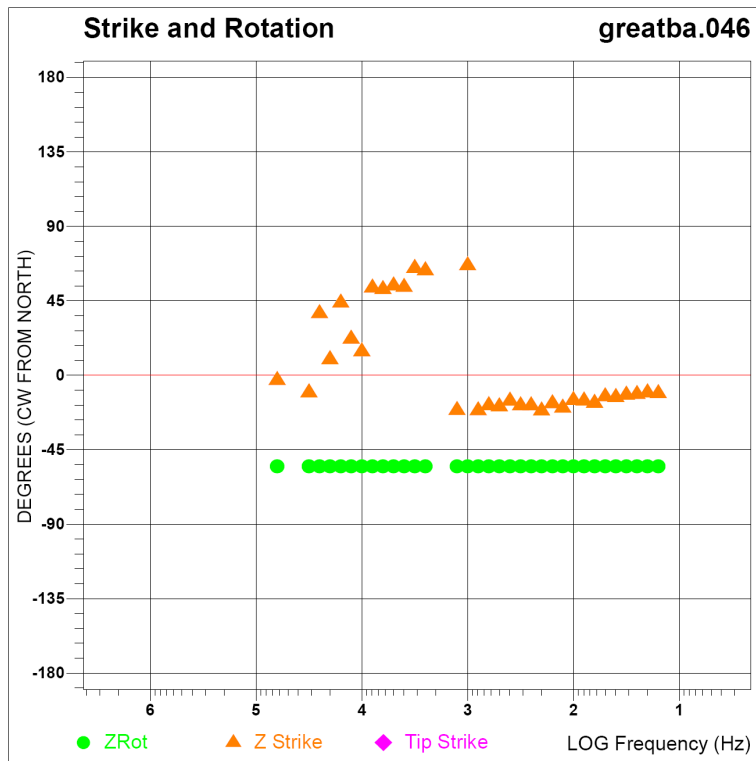


Figure A1-231. Line 2 impedance strike data for site 46.

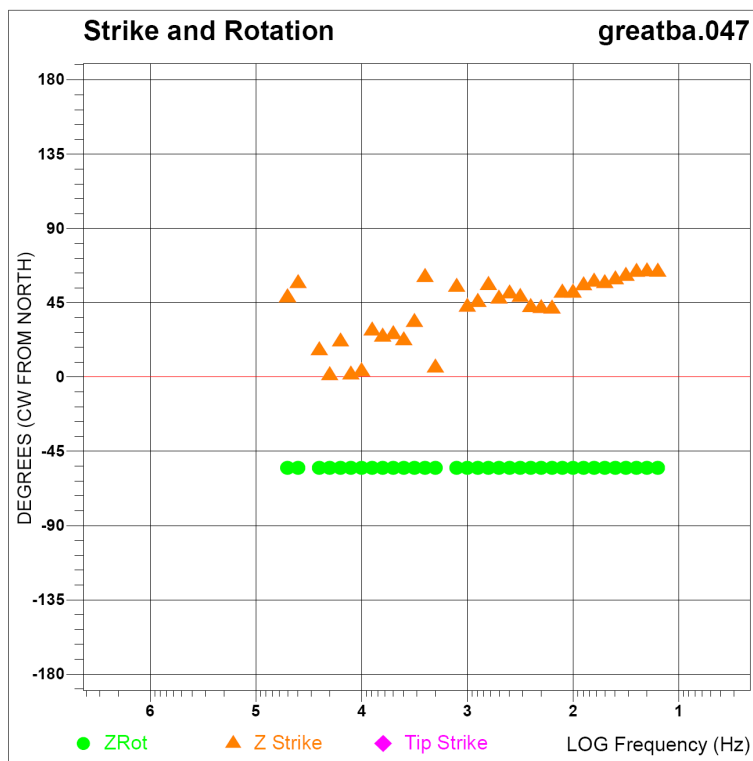


Figure A1-232. Line 2 impedance strike data for site 47.

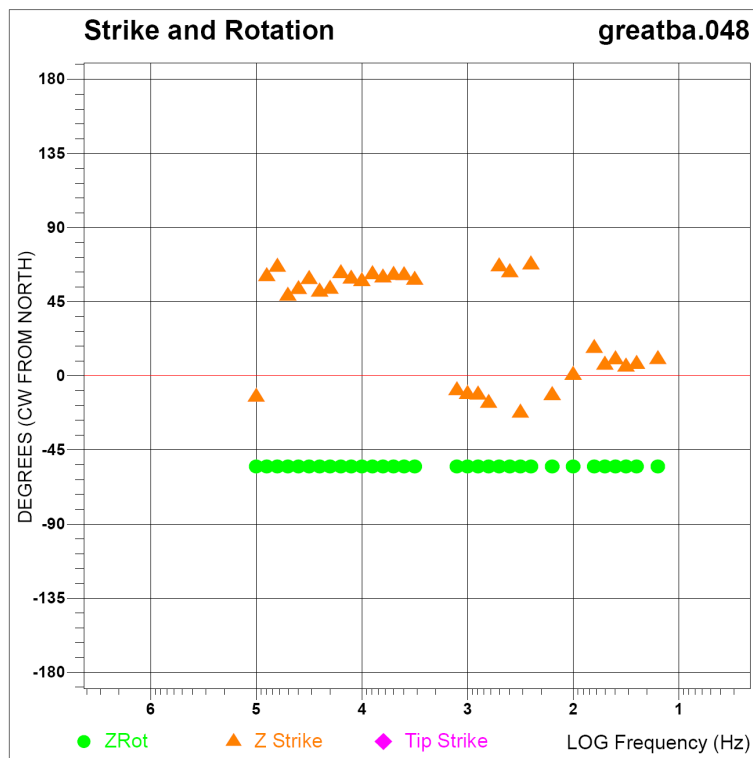
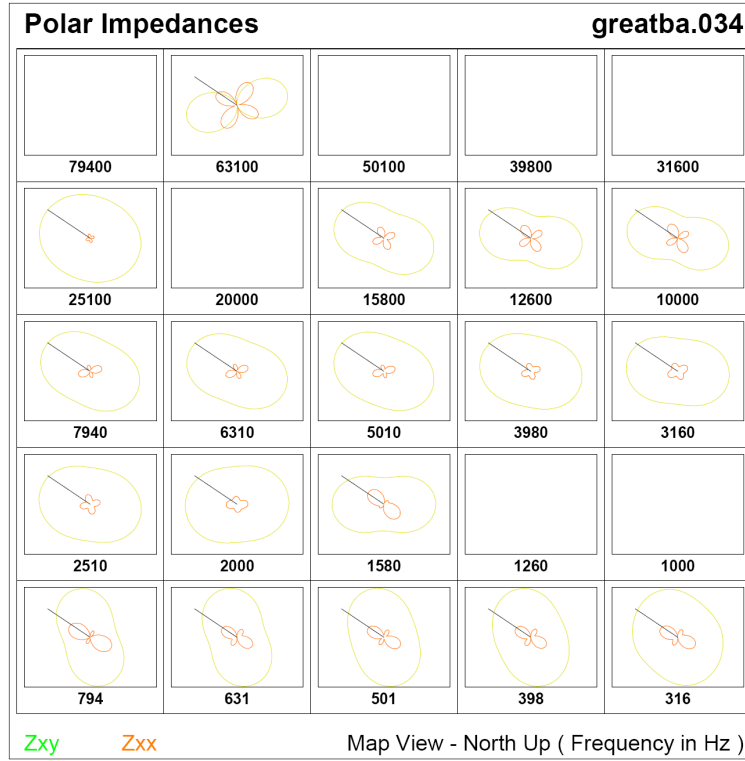
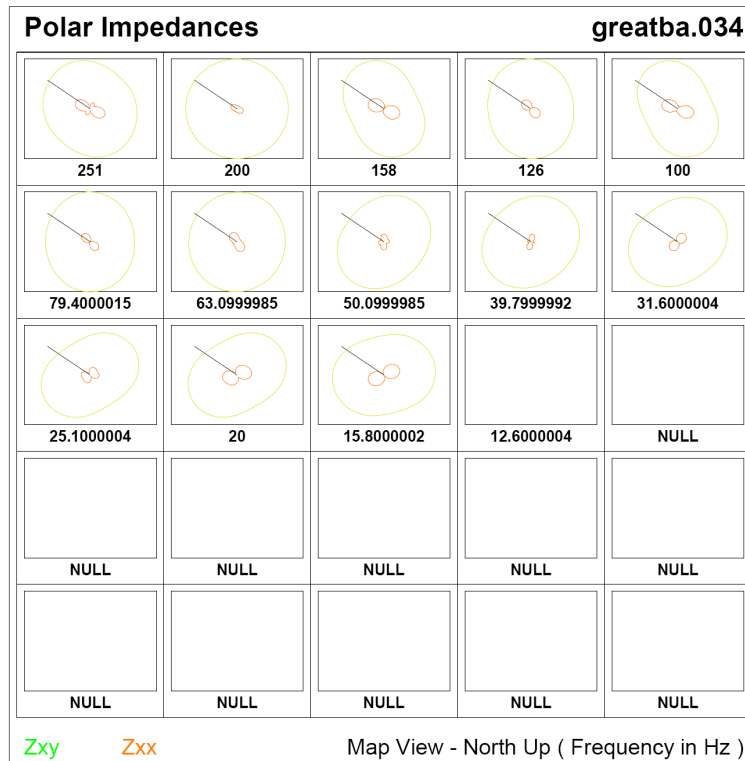


Figure A1-233. Line 2 impedance strike data for site 48.





**Figure A1-234.** Line 2 polar impedance data for site 34 for frequencies 316 Hz – 79 kHz.



**Figure A1-235.** Line 2 polar impedance data for site 34 for frequencies 12 Hz – 251 Hz.

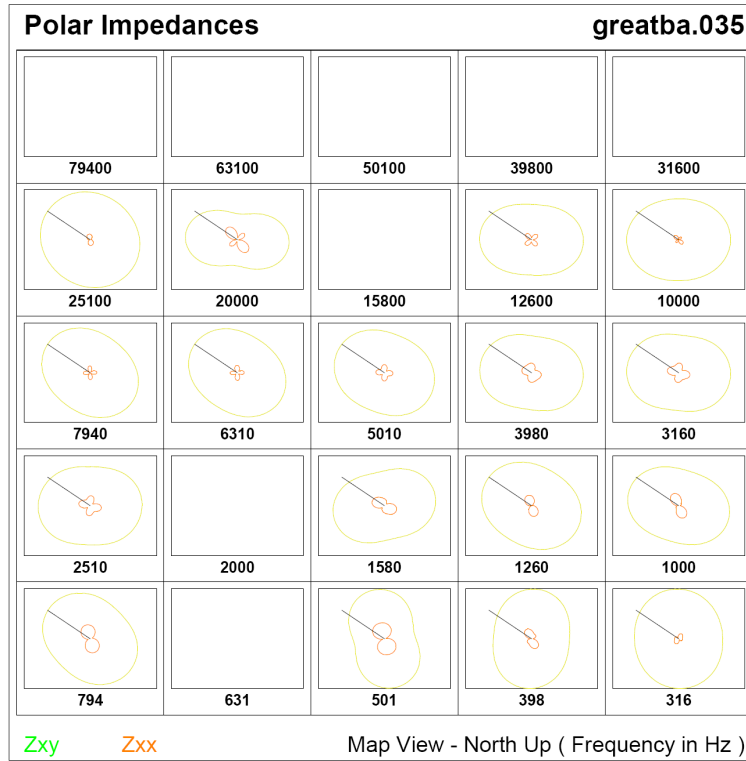


Figure A1-236. Line 2 polar impedance data for site 35 for frequencies 316 Hz – 79 kHz.

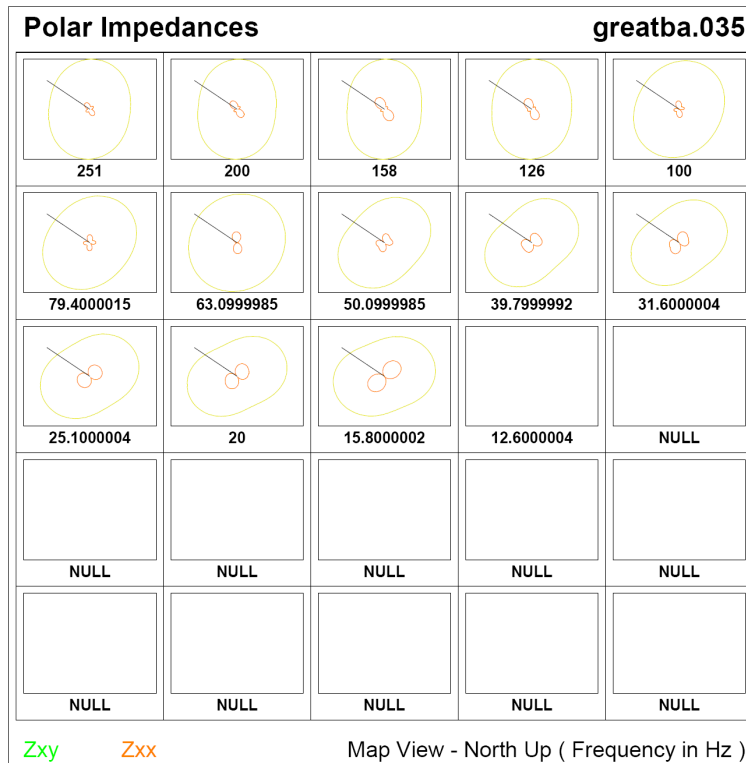


Figure A1-237. Line 2 polar impedance data for site 35 for frequencies 12 Hz – 251 Hz.

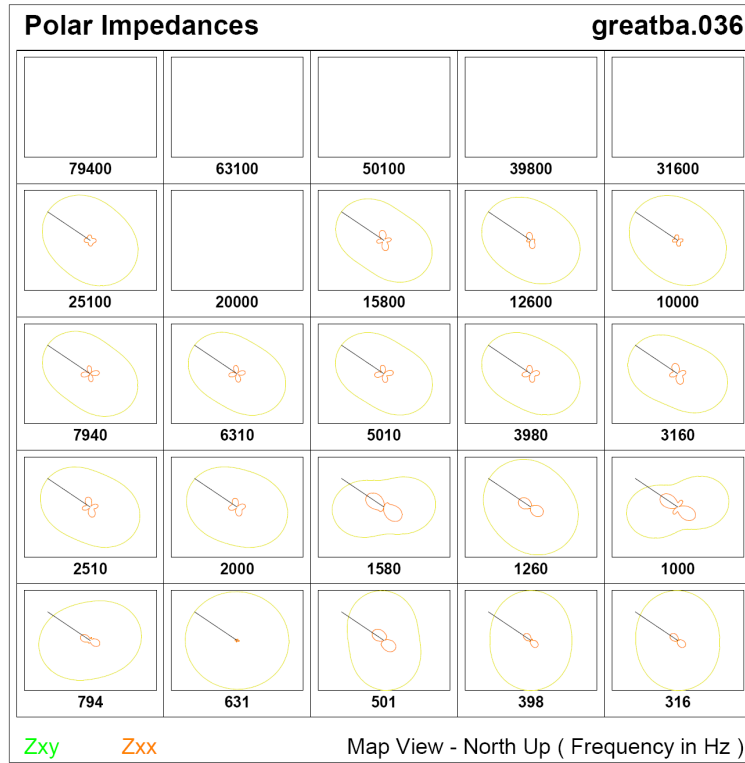


Figure A1-238. Line 2 polar impedance data for site 36 for frequencies 316 Hz – 79 kHz.

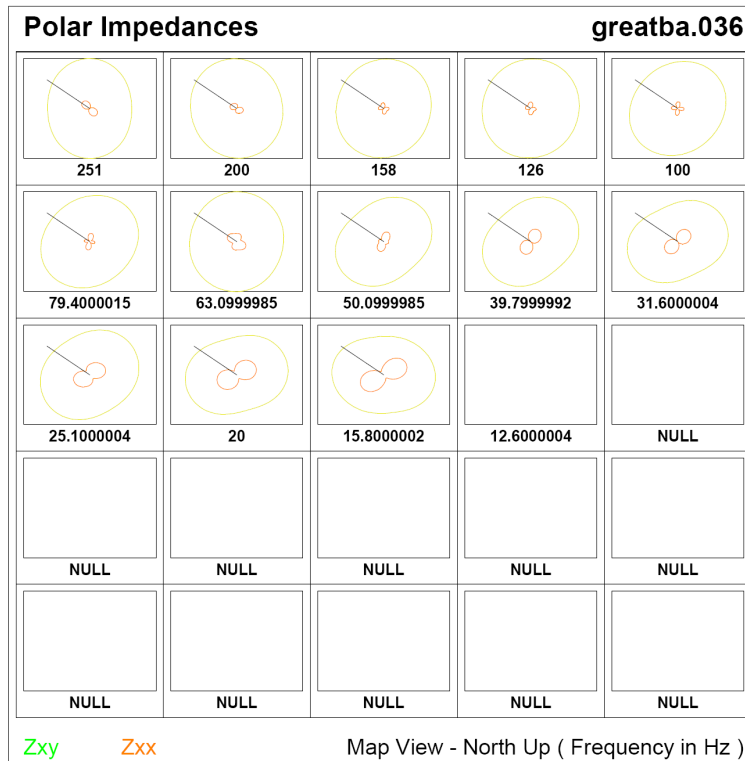


Figure A1-239. Line 2 polar impedance data for site 36 for frequencies 12 Hz – 251 Hz.

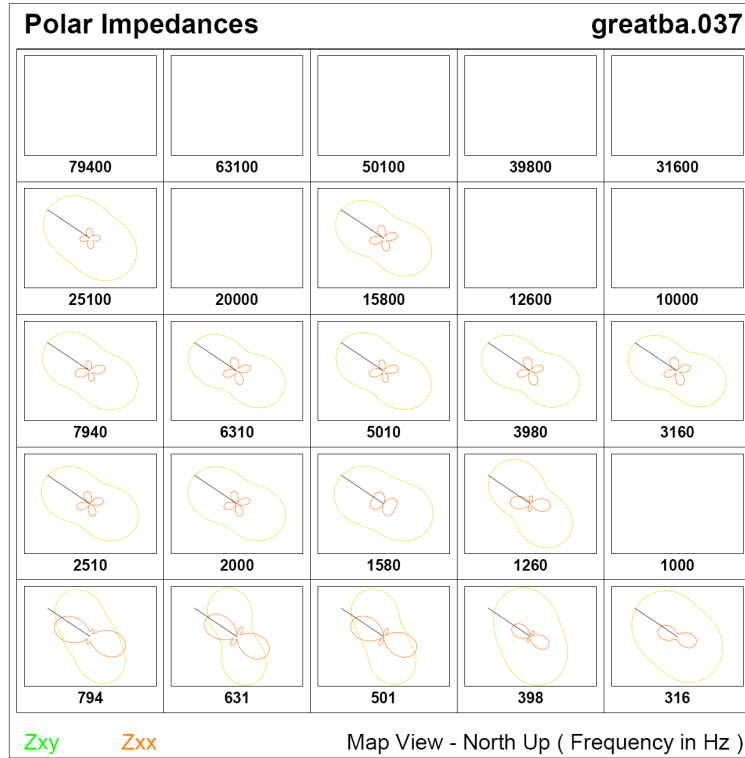


Figure A1-240. Line 2 polar impedance data for site 37 for frequencies 316 Hz – 79 kHz.

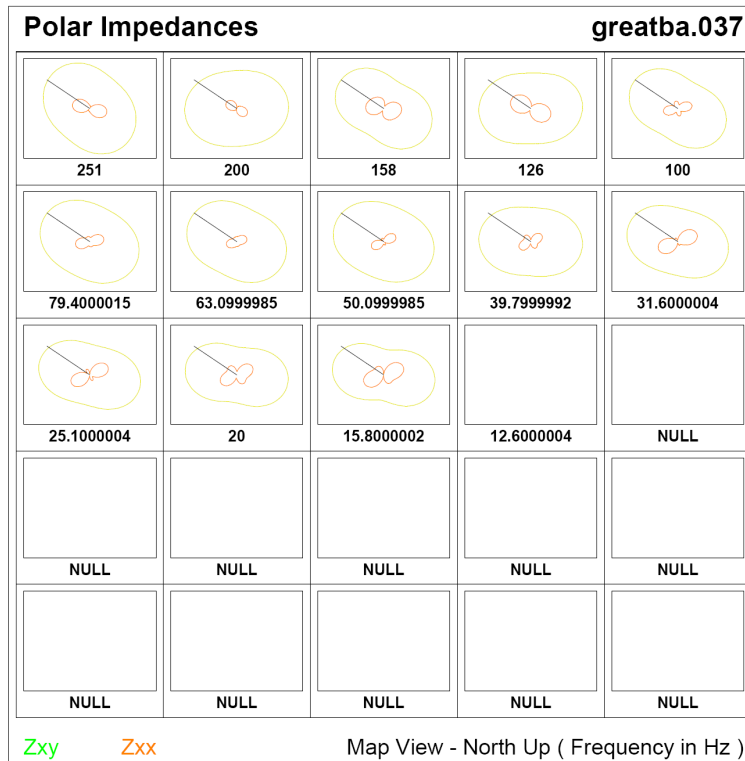


Figure A1-241. Line 2 polar impedance data for site 37 for frequencies 12 Hz – 251 Hz.

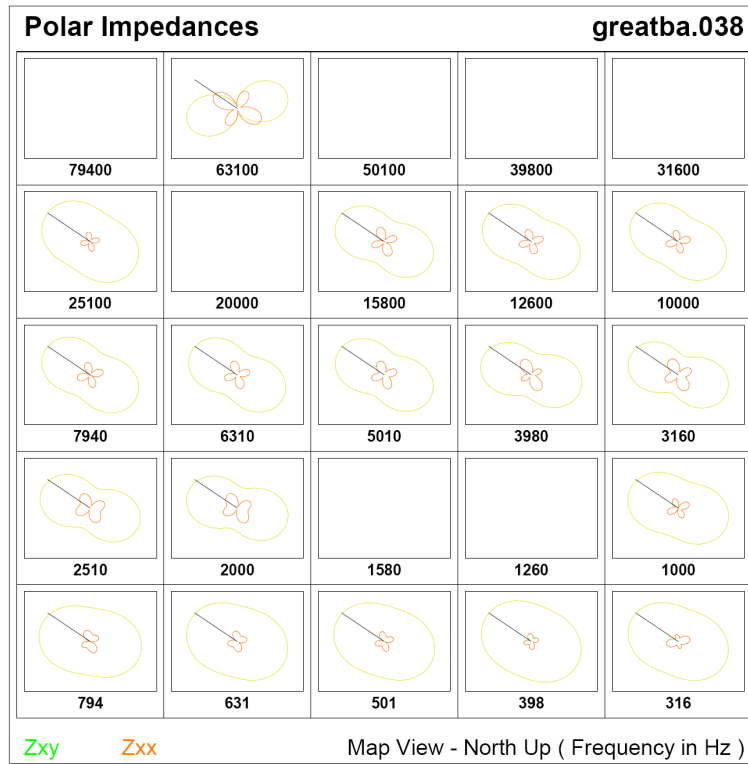


Figure A1-242. Line 2 polar impedance data for site 38 for frequencies 316 Hz – 79 kHz.

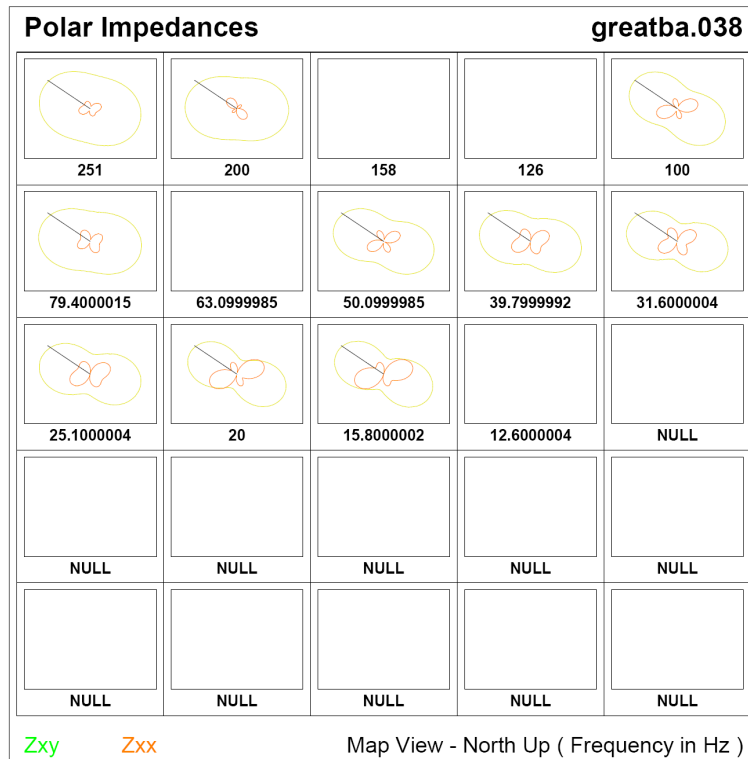
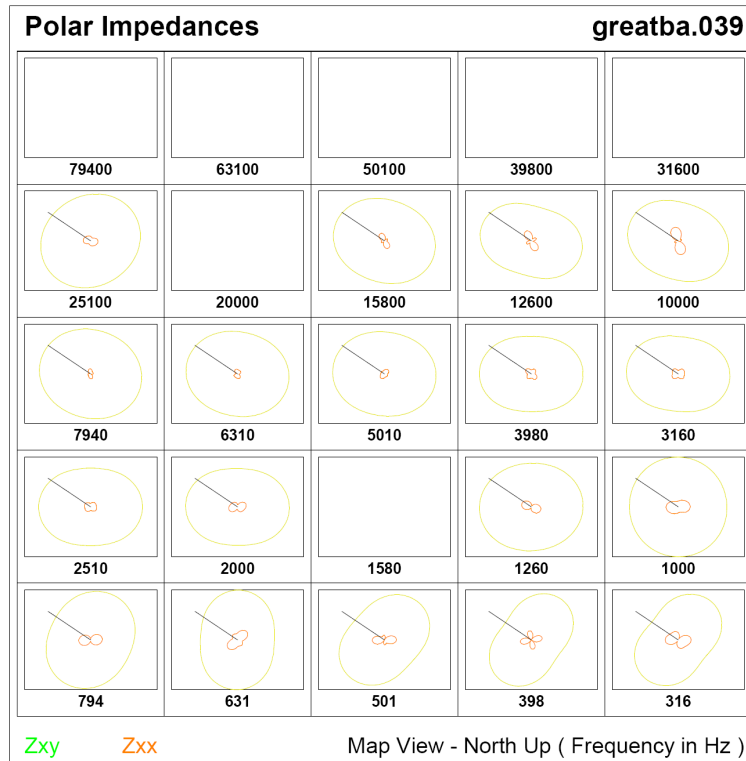
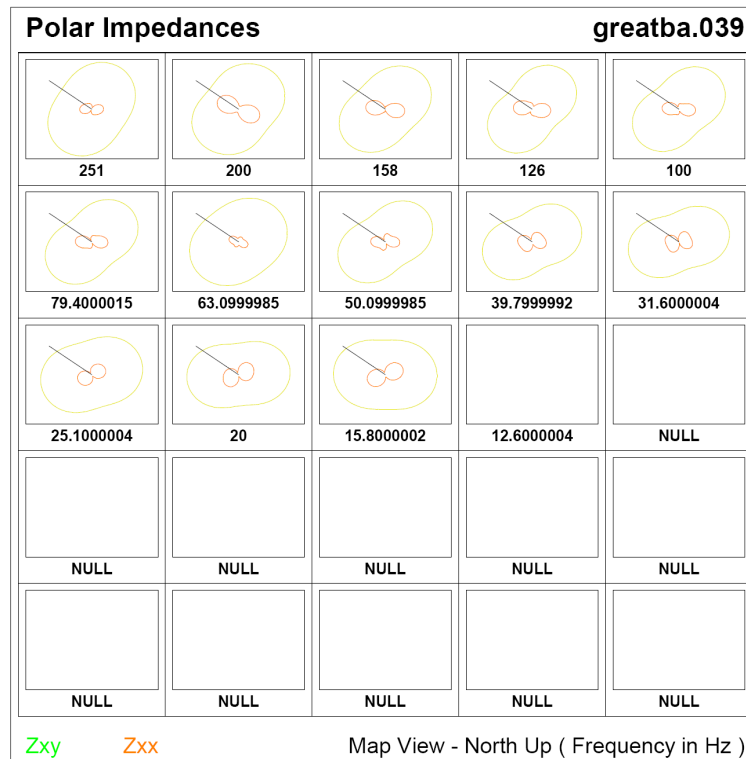


Figure A1-243. Line 2 polar impedance data for site 38 for frequencies 12 Hz – 251 Hz.



**Figure A1-244.** Line 2 polar impedance data for site 39 for frequencies 316 Hz – 79 kHz.



**Figure A1-245.** Line 2 polar impedance data for site 39 for frequencies 12 Hz – 251 Hz.

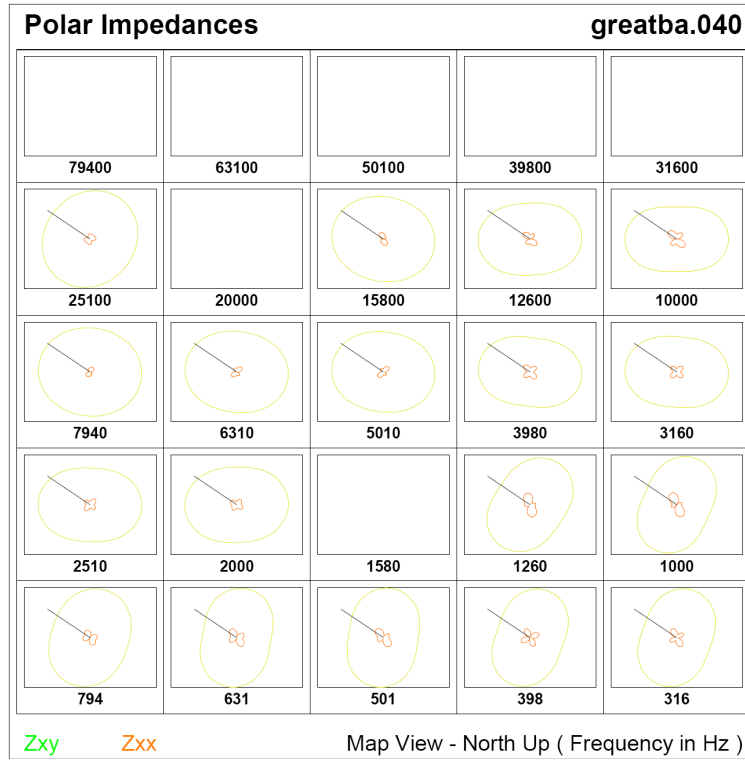


**Figure A1-246.** Line 2 polar impedance data for site 40 for frequencies 316 Hz – 79 kHz.

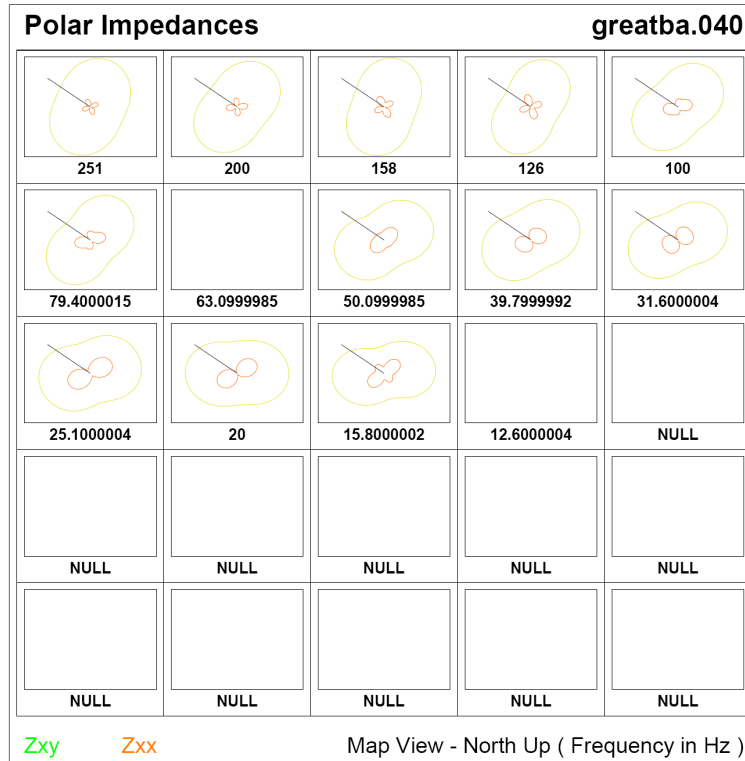


**Figure A1-247.** Line 2 polar impedance data for site 40 for frequencies 12 Hz – 251 Hz.

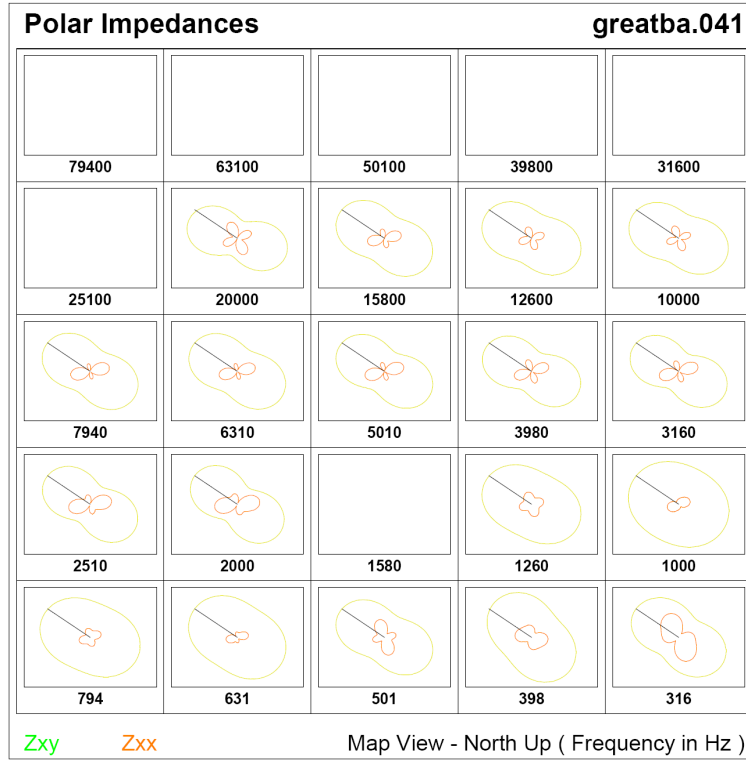


**Figure A1-248.** Line 2 polar impedance data for site 41 for frequencies 316 Hz – 79 kHz.

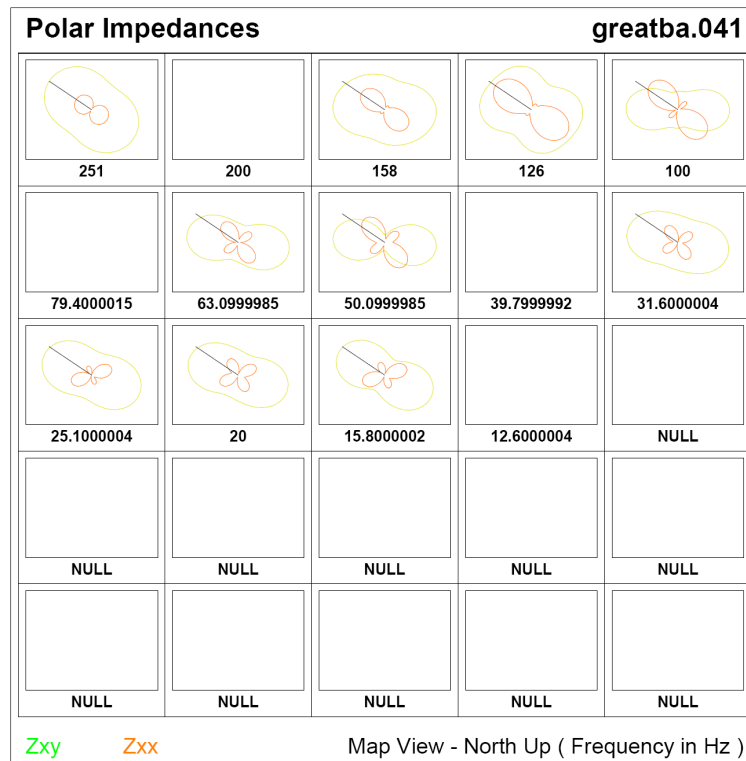


**Figure A1-249.** Line 2 polar impedance data for site 41 for frequencies 12 Hz – 251 Hz.



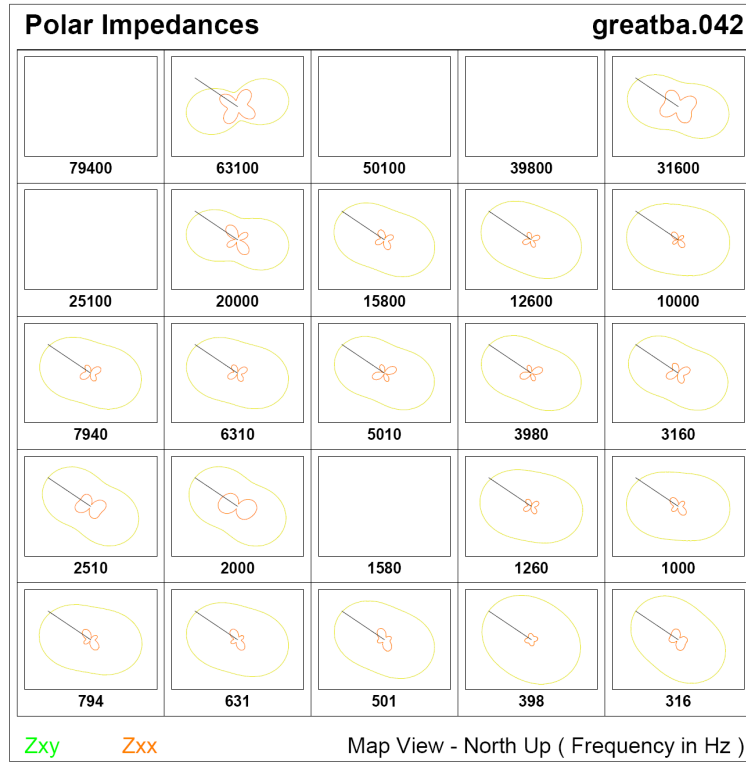


Figure A1-250. Line 2 polar impedance data for site 42 for frequencies 316 Hz – 79 kHz.

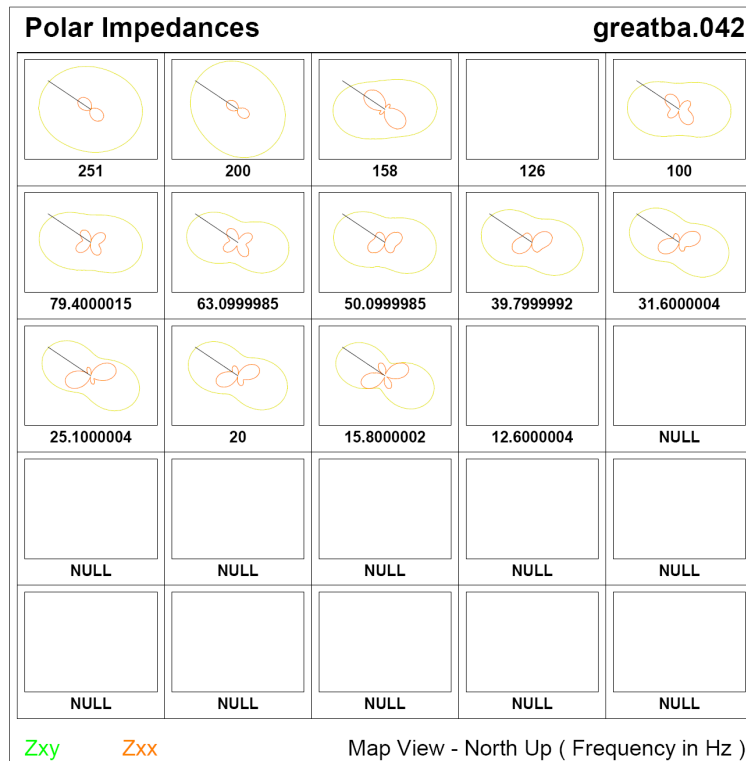


Figure A1-251. Line 2 polar impedance data for site 42 for frequencies 12 Hz – 251 Hz.

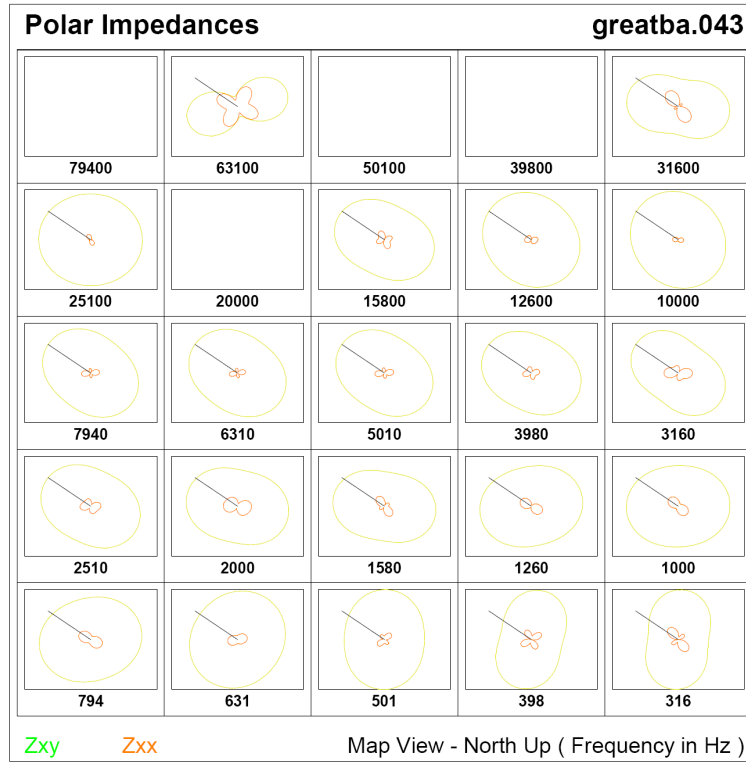


Figure A1-252. Line 2 polar impedance data for site 43 for frequencies 316 Hz – 79 kHz.

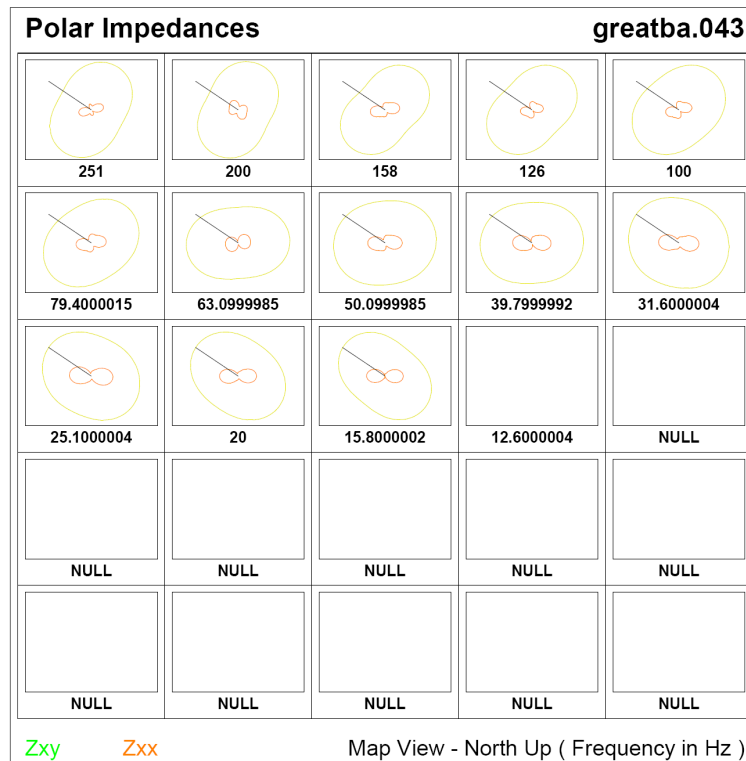
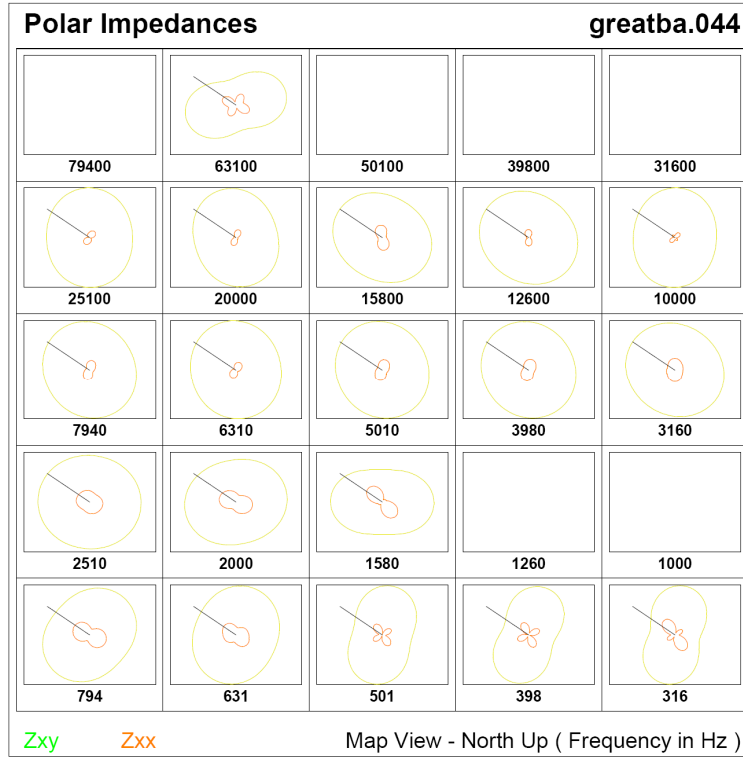
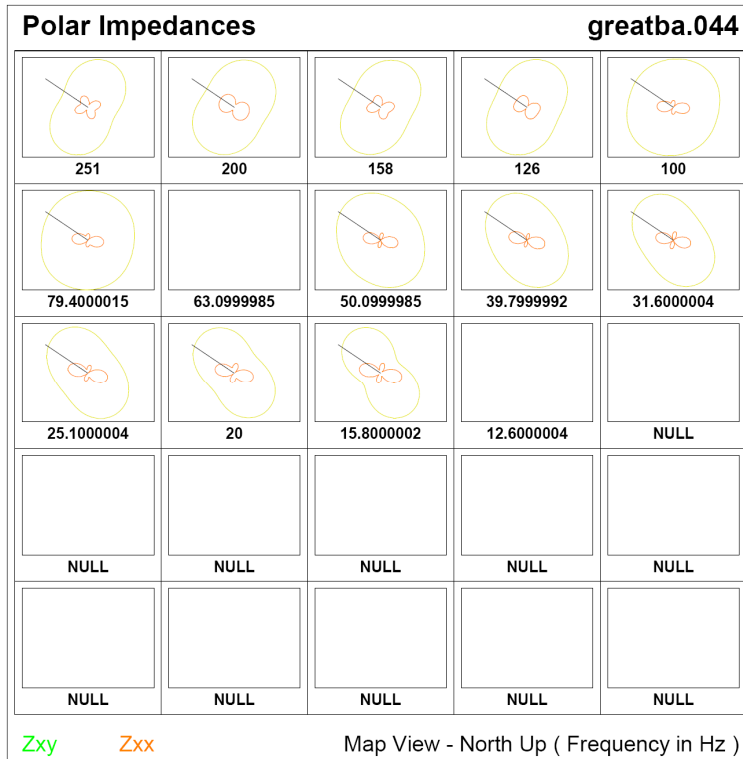


Figure A1-253. Line 2 polar impedance data for site 43 for frequencies 12 Hz – 251 Hz.



**Figure A1-254.** Line 2 polar impedance data for site 44 for frequencies 316 Hz – 79 kHz.



**Figure A1-255.** Line 2 polar impedance data for site 44 for frequencies 12 Hz – 251 Hz.

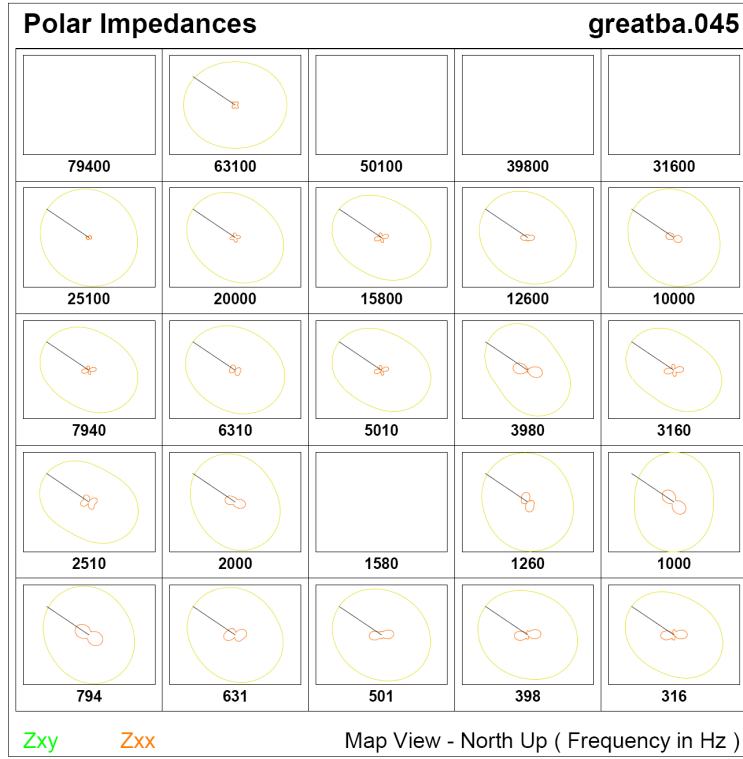


**Figure A1-256.** Line 2 polar impedance data for site 45 for frequencies 316 Hz – 79 kHz.

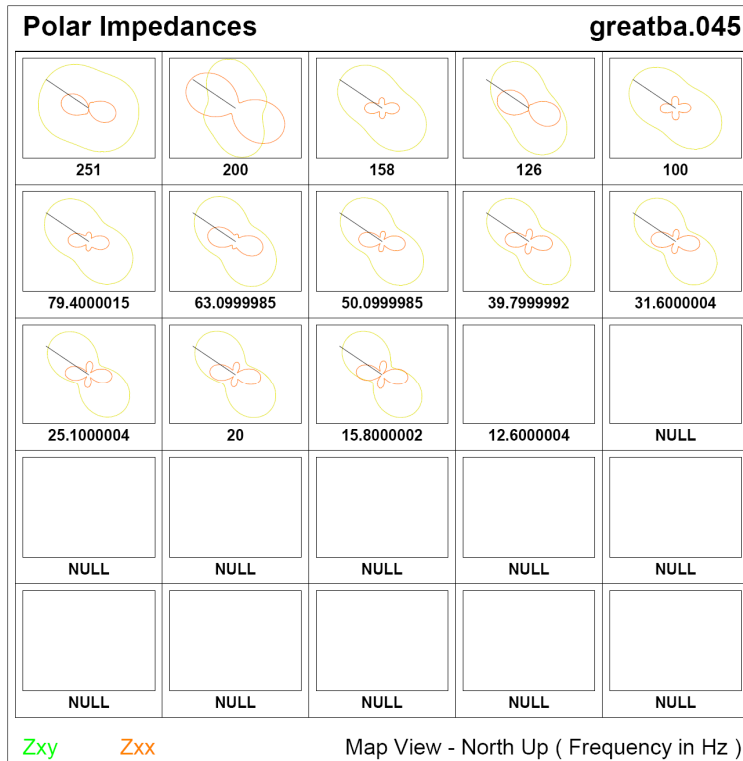


**Figure A1-257.** Line 2 polar impedance data for site 45 for frequencies 12 Hz – 251 Hz.

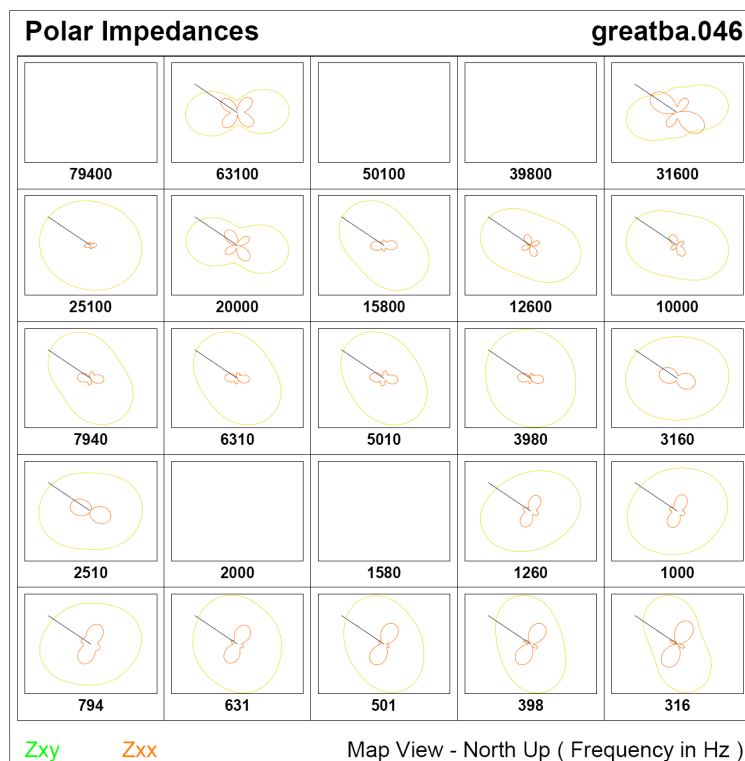


**Figure A1-258.** Line 2 polar impedance data for site 46 for frequencies 316 Hz – 79 kHz.

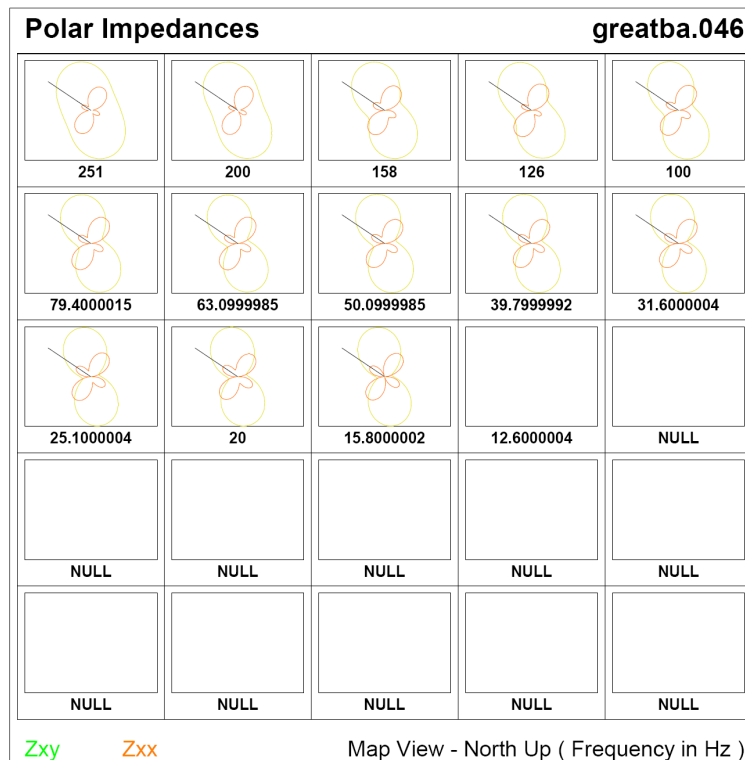


**Figure A1-259.** Line 2 polar impedance data for site 46 for frequencies 12 Hz – 251 Hz.

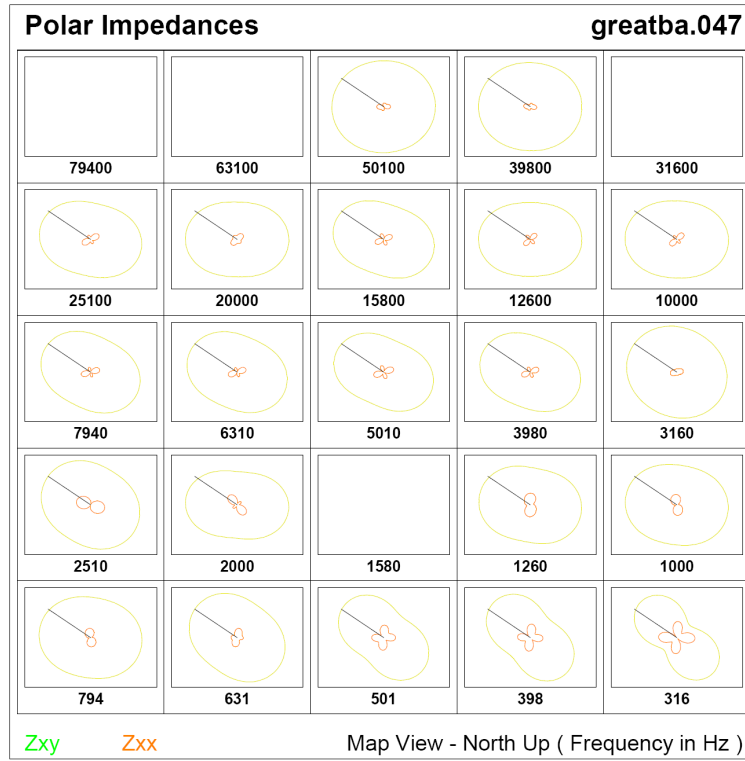


**Figure A1-260.** Line 2 polar impedance data for site 47 for frequencies 316 Hz – 79 kHz.

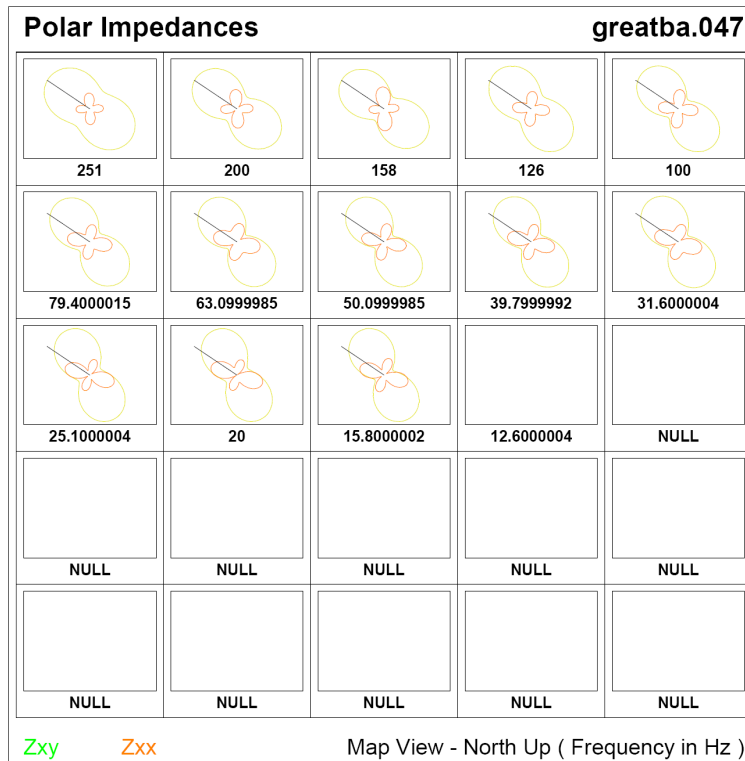


**Figure A1-261.** Line 2 polar impedance data for site 47 for frequencies 12 Hz – 251 Hz.

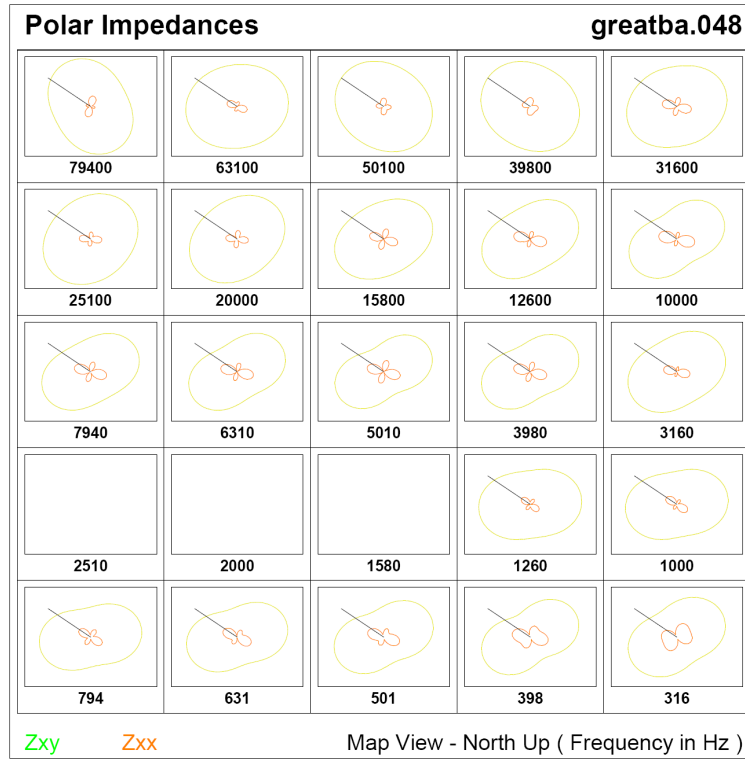


**Figure A1-262.** Line 2 polar impedance data for site 48 for frequencies 316 Hz – 79 kHz.

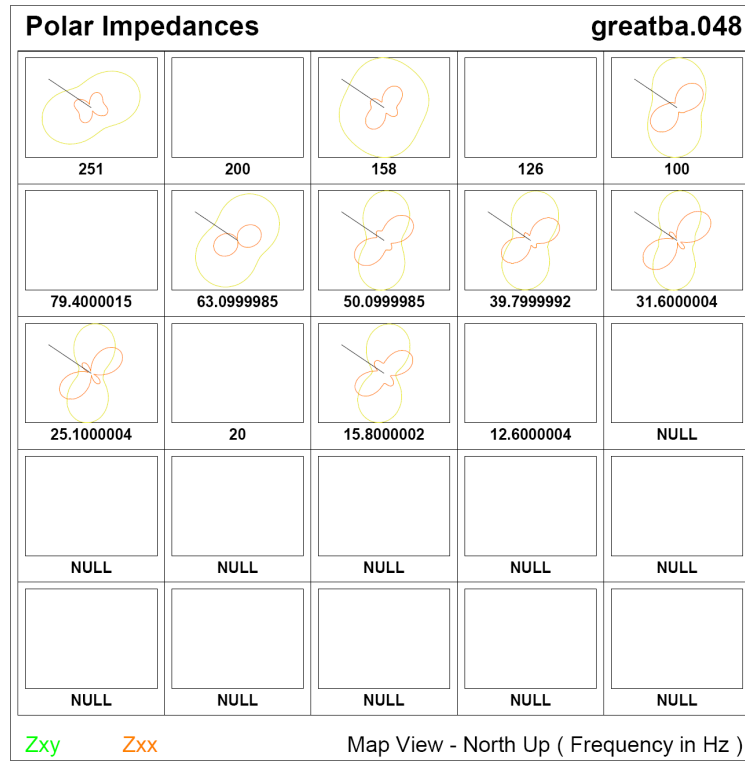


**Figure A1-263.** Line 2 polar impedance data for site 48 for frequencies 12 Hz – 251 Hz.

## **APPENDIX 2 - Survey Photographs**

**Figure A2-1.** STRATAGEM set up in field.

**Figure A2-2.** STRATAGEM set up in field.

**Figure A2-3.** STRATAGEM receiver layout.

**Figure A2-4.** STRATAGEM receiver layout.

**Figure A2-5.** Buffered electrode cables attached to STRATAGEM AFE receiver.

**Figure A2-6.** Stainless-steel electrode with amplification electronics attached.

**Figure A2-7.** EMI BF-6 induction coil magnetometers attached to STRATAGEM AFE receiver.

**Figure A2-8.** EMI BF-6 induction coil magnetometer.

**Figure A2-9.** EMI BF-6 induction magnetometer coil buried to prevent wind noise.

**Figure A2-10.** STRATAGEM AFE receiver with ground stake and console communication cable.

**Figure A2-11.** STRATAGEM Console, 12V battery power, and cable to AFE.

**Figure A2-12.** STRATAGEM Console.

**Figure A2-13.** Laying out the electric field dipoles in the brush along Line 1.

**Figure A2-14.** STRATAGEM transmitter set up.

**Figure A2-15.** STRATAGEM transmitter controller and 12V battery power source.

**Figure A2-16.** View of the trace of Line 1.

**Figure A2-17.** Aerial view of the traces of lines 1 and 2.

**Figure A2-18.** View to the southwest along the trace of Line 2 near station 36.

**Figure A2-19.** Trace of Quaternary fault scarp to the north of line 2.



## Appendix 2 – Survey Photographs



**Figure A2-1.** STRATAGEM audiomagnetotelluric equipment set up in field along Line 1 near Baker, Nevada.



**Figure A2-2.** STRATAGEM audiomagnetotelluric equipment set up in field near station 26 along Line 1.





**Figure A2-3.** STRATAGEM receiver layout.



**Figure A2-4.** STRATAGEM receiver layout.





**Figure A2-5.** Buffered electrode cables attached to STRATAGEM AFE receiver.



**Figure A2-6.** Stainless-steel electrode with amplification electronics attached.





**Figure A2-7.** EMI BF-6 induction coil magnetometer cables attached to STRATAGEM AFE receiver.



**Figure A2-8.** EMI BF-6 induction coil magnetometer.





**Figure A2-9.** EMI BF-6 induction coil magnetometer buried to minimize wind noise.



**Figure A2-10.** STRATAGEM AFE receiver with ground stake and console communication cable.





**Figure A2-11.** STRATAGEM Console, 12 volt battery power, and cable to AFE.



**Figure A2-12.** STRATAGEM Console.





**Figure A2-13.** Laying out the electric field dipoles in the brush near station 20 along Line 1.



**Figure A2-14.** STRATAGEM transmitter set up.



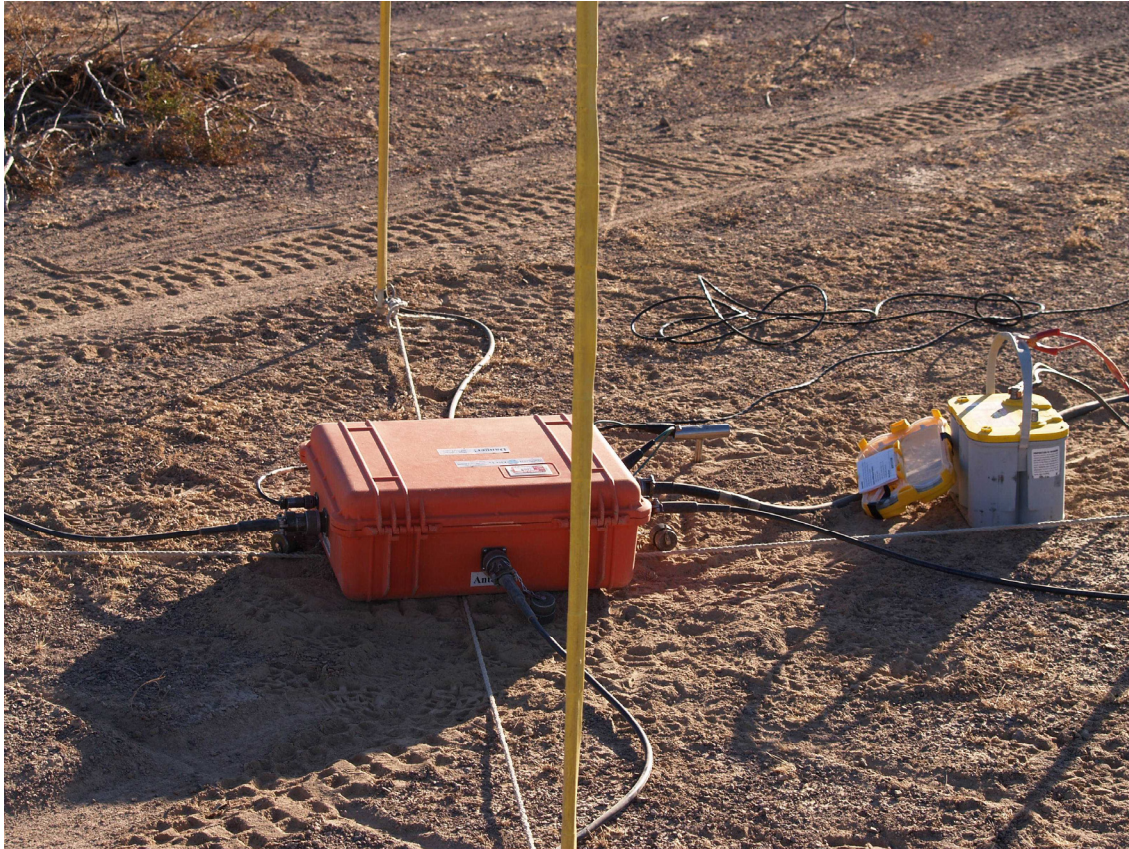


**Figure A2-15.** STRATAGEM transmitter controller and 12 volt battery power source.



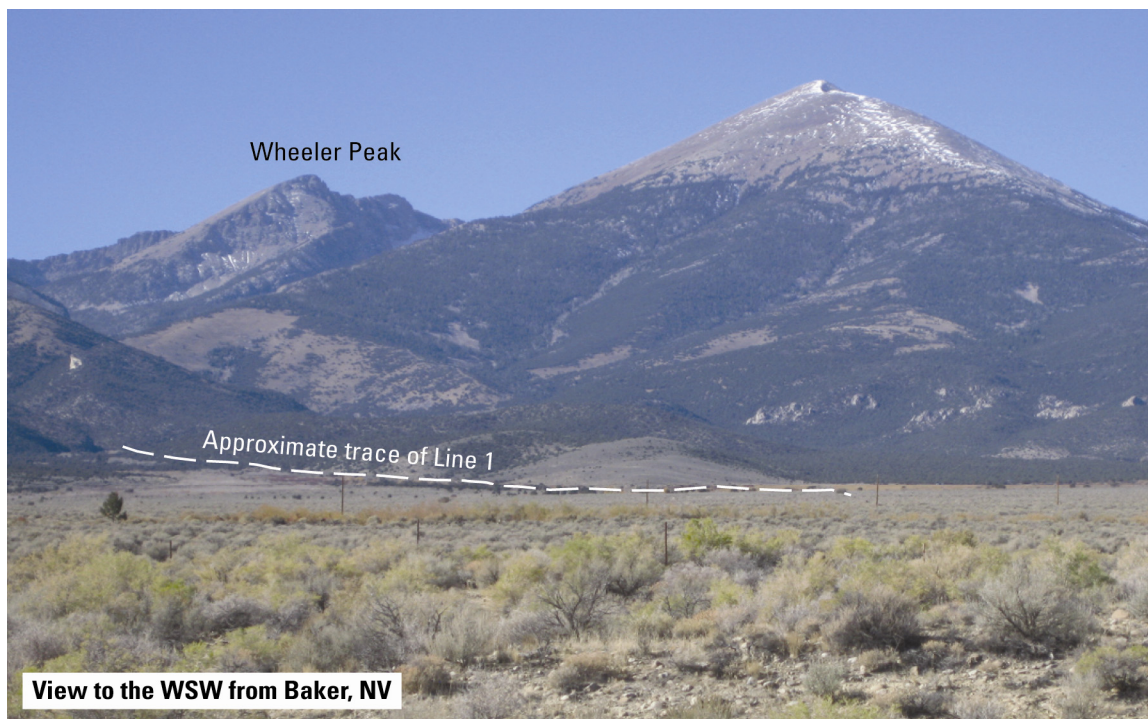


**Figure A2-16.** View of the trace of Line 1 near Baker, Nevada. Shape of line is distorted by perspective view.

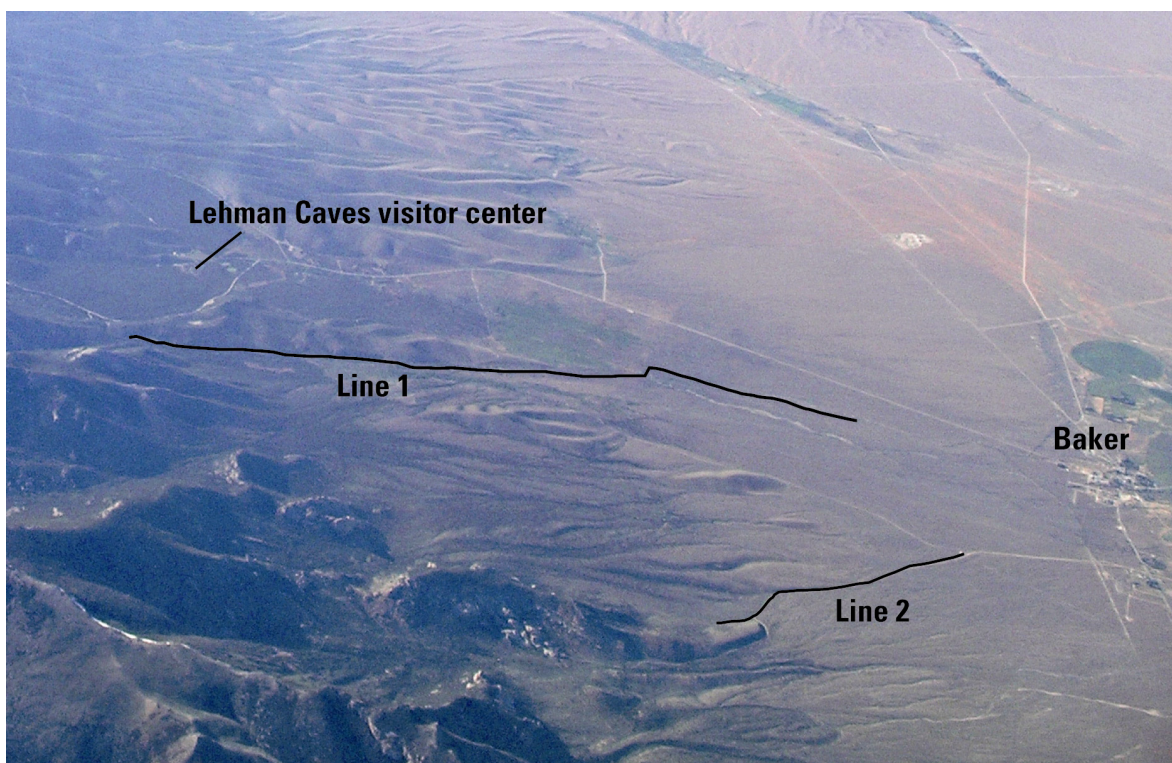


**Figure A2-17.** Aerial view of the traces of lines 1 and 2 near Baker, Nevada.





**Figure A2-18.** View to the southwest along the trace of Line 2 (the dirt road) near station 36. Dashed line shows bedrock trace of low-angle fault interpreted as the southern Snake Range detachment.



**Figure A2-19.** Trace of Quaternary fault scarp to the north of line 2.